



HAL
open science

Studying super star clusters in starburst galaxies in the era of JWST

Tung Lam Nguyen

► **To cite this version:**

Tung Lam Nguyen. Studying super star clusters in starburst galaxies in the era of JWST. Cosmology and Extra-Galactic Astrophysics [astro-ph.CO]. Sorbonne Université, 2021. English. NNT : 2021SORUS385 . tel-03644484

HAL Id: tel-03644484

<https://theses.hal.science/tel-03644484>

Submitted on 19 Apr 2022

HAL is a multi-disciplinary open access archive for the deposit and dissemination of scientific research documents, whether they are published or not. The documents may come from teaching and research institutions in France or abroad, or from public or private research centers.

L'archive ouverte pluridisciplinaire **HAL**, est destinée au dépôt et à la diffusion de documents scientifiques de niveau recherche, publiés ou non, émanant des établissements d'enseignement et de recherche français ou étrangers, des laboratoires publics ou privés.

SORBONNE UNIVERSITÉ
**LABORATOIRE D'ÉTUDES SPATIALES ET D'INSTRUMENTATION EN
ASTROPHYSIQUE**

École doctorale **Astronomie et Astrophysique d'Île de France (ED 127)**

Unité de recherche **Laboratoire d'Études Spatiales et d'Instrumentation en Astrophysique**

Thèse présentée par **NGUYEN TUNG LAM**

Soutenue le **29 janvier 2021**

En vue de l'obtention du grade de docteur de Sorbonne Université

Discipline **Sciences de la terre et de l'univers, espace**

Spécialité **Astronomie & Astrophysique**

Étudier les super amas d'étoiles dans les galaxies à flambées à l'époque du JWST

Thèse dirigée par Damien GRATADOUR directeur
Daniel ROUAN co-directeur

Composition du jury

<i>Rapporteurs</i>	Annie ZAVAGNO	professeur à l'Université d'Aix-Marseille & Laboratoire d'Astrophysique de Marseille	
	Ngoc Diep PHAM	directeur de recherche au Centre Spatial National du Vietnam (VNSC)	
<i>Examineurs</i>	Françoise COMBES	professeur au Collège de France & Observatoire de Paris-PSL, LERMA	président du jury
	Pierre Olivier LAGAGE	directeur de recherche au Service d'Astrophysique du CEA-IRFU	
	Benoit NEICHEL	chargé de recherche au Laboratoire d'Astrophysique de Marseille	
<i>Directeurs de thèse</i>	Damien GRATADOUR	maître de conférence à l'Université Paris Diderot et Observatoire de Paris-PSL, LESIA	
	Daniel ROUAN	directeur de recherche émérite à l'Observatoire de Paris-PSL, LESIA	

Mots clés : super amas d'étoiles, ligr, flambée d'étoiles, infrarouge, transfert radiatif, jwst
Keywords: super star clusters, ligr, starburst, infrared, radiative transfer, jwst

Cette thèse a été préparée au

Laboratoire d'Études Spatiales et d'Instrumentation en Astrophysique

Observatoire de Paris, Section de Meudon
5, place Jules Janssen
92195 MEUDON Cedex
France

☎ +33 1 45 07 77 01

Site <https://lesia.obspm.fr/>



To my beloved mother and father

Per aspera ad astra

The Force is what gives a Jedi his power. It's an energy field created by all living things. It surrounds us and penetrates us. It binds the galaxy together.

Obi-Wan Kenobi in Star Wars

It is difficult to say what is impossible, for the dream of yesterday is the hope of today and the reality of tomorrow.

Robert H. Goddard

ÉTUDE DES SUPER AMAS D'ÉTOILES DANS LES GALAXIES À FLAMBÉES À L'ÉPOQUE DU JWST**Résumé**

Les super amas d'étoiles (SSCs) sont des objets jeunes, massifs et compacts résultant d'une formation extrême d'étoiles, qui se produit souvent lorsque les galaxies interagissent, comme dans le cas des galaxies (ultra)-lumineuses en infrarouge ((U)LIRGs). Ils sont des éléments fondamentaux d'une hiérarchie globale de la formation des étoiles dans l'univers. Néanmoins, la majorité des populations des SSCs restent inexplorées en raison de leurs lointains. Par conséquent, leurs propriétés globales et leur cycle de vie ne sont pas entièrement compris et nécessitent des études plus approfondies, en particulier dans le domaine de l'infrarouge (IR) où ils rayonnent la plupart de leur puissance sous forme d'émission de poussières thermiques.

Nous avons étudié la population des SSCs dans l'IRAS 17138-1017, un LIRG typique, en utilisant des images en bandes JHK_s d'optique adaptative basées au sol. Un catalogue de 54 SSCs de m_{K_s} entre 16 mag et 21 mag avec une incertitude de 0,05 mag a été construit. À partir de diagrammes couleur-couleur et couleur-magnitude accompagné d'une trajectoire d'évolution stellaire théorique, nous avons déduit les âges, les masses et les extinctions des amas. La plupart des SSCs sont très éteintes et appartiennent à deux épisodes récents de flambées d'étoiles à 2,8 et 4,5 millions d'années. Leurs distributions de luminosité et de masse sont bien décrites par les lois de puissance mais avec des pentes moins profondes que celles généralement observées dans les LIRGs. À titre de comparaison, nous avons construit plusieurs modèles de SSCs à différents stades d'évolution en utilisant MontAGN, un code de transfert radiatif spécialisé dans l'IR. Ces modèles montrent que l'émission thermique de la poussière et la lumière diffusée sont insignifiantes dans la bande K et ne pourraient pas expliquer l'excès de rouge de certains SSCs.

En utilisant le code de transfert radiatif MontAGN, nous avons conçu des modèles de SSC consistant en une population stellaire centrale simple et une enveloppe de poussière sous la forme d'une structure hiérarchiquement fragmentée. Les modèles les mieux adaptés pour trois SSCs représentatifs dans l'IRAS 17138-1017 à des magnitudes lumineuses, médianes et faibles ont été obtenus, y compris leurs spectres dans l'IR moyen.

Compte tenu de la supériorité dans l'IR moyen du Télescope Spatial James Webb (JWST), nous avons créé une proposition pour observer les SSCs de l'IRAS 17138-1017 en utilisant l'instrument MIRI. Nous obtiendrons des données d'imagerie dans huit filtres F560W, F770W, F1000W, F1130W, F1500W, F1800W, F2100W, F2550W et des données Spectroscopiques à Moyenne Résolution (MRS) sur tous les canaux et dans toutes les gammes de longueurs d'onde de 4,9 à 28,3 μm , ainsi que des observations de fond dédiées et des images parallèles dans F560W, F770W et F1000W. Nous avons défini les paramètres d'exposition pour obtenir les rapports signal sur bruit les plus élevés possibles pour le SSC le plus faible sans saturer le SSC le plus brillant dans l'IRAS 17138-1017.

Enfin, nous avons utilisé MIRISim, un progiciel fourni par l'équipe MIRI, pour simuler les données du MIRI et les avons fait passer dans le pipeline d'étalonnage du JWST. Les analyses des données simulées réduites montrent que nos observations prévues sont capables de vérifier certaines prédictions du code de transfert radiatif MontAGN.

Mots clés : super amas d'étoiles, lirg, flambée d'étoiles, infrarouge, transfert radiatif, jwst

Laboratoire d'Études Spatiales et d'Instrumentation en Astrophysique

Observatoire de Paris, Section de Meudon – 5, place Jules Janssen – 92195 MEUDON Cedex
– France

Abstract

Super star clusters (SSCs) are young, massive and compact objects resulting from extreme star formation, which often occurs when galaxies interact, such as in the case of (ultra)luminous infrared galaxies ((U)LIRGs). They are fundamental parts of an overall star formation hierarchy throughout the universe. Nevertheless, a majority of SSC populations remain uncharted due to their large distances. Consequently, their global properties and lifecycle are not fully understood and require further studies, especially in the infrared (IR) range where they radiate most of their power in the form of thermal dust emission.

We studied the SSC population in IRAS 17138-1017, a typical LIRG, using ground-based adaptive optics JHK_s -band images. A catalogue of 54 SSCs of m_{K_s} between 16 mag and 21 mag with an uncertainty of 0.05 mag was constructed. From color-color and color-magnitude diagrams with a theoretical stellar evolutionary track, we derived the cluster ages, masses and extinctions. Most of the SSCs are highly extinct and belong to two recent starburst episodes at 2.8 and 4.5 Myr. Their luminosity and mass distributions are well described by power laws but with shallower slopes than those generally observed in LIRGs. For comparison, we constructed several SSC models at various evolution stages using MontAGN, a radiative transfer code specialized in the IR. These models show that dust thermal emission and scattered light are insignificant in K band and could not explain the red excess of some SSCs.

Using the radiative transfer code MontAGN, we designed SSC models consisting of a central simple stellar population and a dust envelope in the form of a hierarchically clumpy structure. Best-fit models for three representative SSCs in IRAS 17138-1017 at bright, median and faint magnitudes were obtained including their spectra in the mid-IR.

Given the superiority in the mid-IR of the James Webb Space Telescope (JWST), we created a proposal to observe the SSCs in IRAS 17138-1017 using the MIRI instrument. We will obtain imaging data in eight filters F560W, F770W, F1000W, F1130W, F1500W, F1800W, F2100W, F2550W and Medium Resolution Spectroscopic (MRS) data over all channels and wavelength ranges from 4.9 to 28.3 μm , along with dedicated background observations and parallel imaging in F560W, F770W and F1000W. We set the exposure parameters to achieve the highest possible signal-to-noise ratios for the faintest SSC without saturating the brightest SSC in IRAS 17138-1017.

Finally, we used MIRISim, a package provided by the MIRI team, to simulate MIRI data and passed them through the JWST calibration pipeline. Analyses of reduced simulated data show that our planned observations are able to verify some predictions from the radiative transfer code MontAGN.

Keywords: super star clusters, lirg, starburst, infrared, radiative transfer, jwst

Acknowledgement

Just like its subject, the super star clusters, this thesis has been formulated through extreme circumstances. From the beginning, it was a giant leap for me to go straight from a bachelor in banking and finance to a master and PhD in Astrophysics. In my second year, my mother suffered a severe illness and I had to go home for her, followed by months of pessimism and uncertainties and I almost quitted. After having come back to France, I spent most of my third year working from home, under lockdown due to the COVID-19 pandemic, which has caused great upheaval to the world. Against all odds, I could not have finished my thesis without the Force. It is created by all people surround me, giving me power to overcome hardships to reach for the stars.

First and foremost, I would like to express my sincerest gratitude to my supervisors, Damien Gratadour and Daniel Rouan. They have offered me valuable opportunities and mentored me on the interstellar journey since my Master. For many times, their support, encouragement and patience have aided me to overcome inertia and drag during my research. I am proud to be their academic descendant in astrophysics. It is also my honor to have my thesis reviewed by the jury members Annie Zavagno, Pham Ngoc Diep, Françoise Combes, Pierre Olivier Lagage and Benoit Neichel. Their comments, contributions and advice are valuable to my research.

Moreover, I am deeply indebted to my mother Do Thi Song Nga, my father Nguyen Tien Mau, my sister Nguyen Nga Mi and my extended family for their love and sacrifice. They have always done the best things for me, even during the hardest time when I should have been with them. My mother never gives up. My father encouraged me to continue my PhD and has been taking care of my mother together with her caregiver and my sister, which should have been my responsibility. I could not continue and finish my thesis without them behind me. *"Love is the one thing we are capable of perceiving that transcends dimensions of time and space."*, said my favorite quote in the Interstellar movie.

Besides, I would like to thank my colleagues at Paris Observatory, especially Lucas Grosset, for their assistance and support during my work, as well as joyous and savory parties. *"If you are lucky enough to have lived in Paris as a young man, then wherever you go for the rest of your life, it stays with you, for Paris is a moveable feast."*, said Ernest Hemingway. My life in France would be colorless without my friends sharing those joys and feasts both in life and work, but above all I truly appreciate who stood by me during my hard time. Their sympathy and encouragement have given me strength and hope.

Overall, I would like to acknowledge my almae matres. My love with physics started at the High School for Gifted Students in Physics, Hanoi University of Science (HUS HSGS), where I gained knowledge and inspiration from wonderful teachers. Meanwhile, the forum of Ho Chi Minh City Amateur Astronomy Club (HAAC) is the natal cocoon of my passion for astronomy in particular. Although my learning course deviated for a while when I went to university, my dream continued to be nurtured by Hanoi Amateur Astronomy Society (HAS), the Vietnamese community of Astrophysics enthusiasts (VLTV) and finally realized by the Department of Space

and Applications, University of Science and Technology of Hanoi (USTH) where I met my supervisors and other great lecturers. It was my honor to attend their classes, reaching for the stars and exploring the world. I am deeply grateful to professor Yannick-Giraud Heraud for his dedication to our department. I wish to see him back soon, as people in space always do incredible things!

"And, when you want something, all the universe conspires in helping you to achieve it.", said Paul Coelho in *The Alchemist*. Last but not least, I would like to thank all the conspirators that I may have not mentioned, because you know, it is not easy to constrain the universe.

Contents

Résumé	xi
Acknowledgement	xiii
Contents	xv
List of Tables	xix
List of Figures	xxi
List of Abbreviations	xxvii
1 Introduction	1
1.1 Super star clusters	1
1.1.1 Definition and fundamental characteristics	1
1.1.2 Cluster mass function	5
1.1.3 Cluster luminosity function	7
1.1.4 Cluster age distribution, formation and evolution	8
1.1.5 Cluster formation efficiency	11
1.2 Luminous infrared galaxies	13
1.2.1 Overview	13
1.2.2 Morphology	15
1.2.3 Extinction	17
1.2.4 Star formation rate	18
1.2.5 Starburst–active galactic nucleus connection	18
1.3 James Webb Space Telescope	20
1.3.1 Instrumentation	20
1.3.2 Science themes	21
1.3.3 Science planning	23
1.4 Thesis objectives	23
2 High angular resolution study of the super star cluster population in IRAS 17138 - 1017	25
2.1 Published paper	26
2.2 Analytical versus Starfinder PSF photometry	37

3	Modelling super star clusters with the radiative transfer code MontAGN	41
3.1	Radiative transfer code MontAGN	41
3.1.1	Input parameters	41
3.1.2	Photon propagation and interaction	42
3.1.3	Output	45
3.2	Hierarchically clumpy structure	45
3.2.1	Formulation	45
3.2.2	Implementation	46
3.3	Preliminary models	47
3.4	Modelling super star clusters in IRAS 17138-1017	52
3.4.1	SSC sample	52
3.4.2	Model grid	53
3.4.3	Model fitting	54
3.4.4	Results and discussions	56
4	Preparing a JWST Program: Observing extreme star formation in external galaxies	61
4.1	Scientific justification	61
4.2	Roadmap	63
4.3	Mid-Infrared Instrument (MIRI)	64
4.3.1	Imaging	64
4.3.2	Medium-resolution integral field unit spectroscopy	70
4.4	Feasibility of observations	75
4.4.1	JWST General Target Visibility Tool (GTVT)	75
4.4.2	JWST Interactive Sensitivity Tool (JIST)	76
4.4.3	JWST Backgrounds Tool (JBT)	76
4.5	Exposure Time Calculator (ETC)	79
4.5.1	Scenes and sources	79
4.5.2	Calculations	80
4.5.3	Results	83
4.6	JWST Astronomer’s Proposal Tool (APT)	86
5	MIRI data simulation and analysis	111
5.1	MIRISim	111
5.1.1	Introduction	111
5.1.2	Input scenes	114
5.1.3	Instrumental configuration	117
5.1.4	Simulator configuration	117
5.1.5	Output	117
5.2	Data reduction	122
5.2.1	Stage 1: Detector processing	122
5.2.2	Stage 2: Instrument-mode processing for imaging	126
5.2.3	Stage 3: Multiple exposure combination for imaging	129
5.2.4	Stage 2: Instrument-mode processing for spectroscopy	131
5.2.5	Stage 3: Multiple exposure combination for spectroscopy	135
5.3	Post-pipeline data analysis	136
5.3.1	MIRI imaging simulations	136
5.3.2	MIRI MRS simulations	139

6 Conclusions and prospectives	145
6.1 Observations and analyses in near-IR with adaptive optics	145
6.2 Simulations	146
6.3 Era of James Webb Space Telescope	147
6.3.1 Preparing the MIRI/JWST proposal	147
6.3.2 Perspective for SSC studies	148
Bibliography	151

List of Tables

3.1	Photon packet attributes	42
3.2	Properties of sampled SSCs in IRAS 17138-1017	53
3.3	Parameter grid for the sampled SSCs in IRAS 17138-1017	53
3.4	Fitted parameters of the sampled SSCs in IRAS 17138-1017	57
4.1	MIRI observing modes and their characteristics (STScI 2016–)	65
4.2	MIRI filter characteristics (STScI 2016–)	65
4.3	MIRI detector specifications (STScI 2016–)	66
4.4	MIRI subarrays (STScI 2016–)	66
4.6	MIRI dithering patterns (STScI 2016–)	67
4.7	MIRI IFU channels (STScI 2016–)	70
4.8	Performance of MIRI MRS dither patterns (STScI 2016–)	73
4.9	MIRI readout patterns (STScI 2016–)	82
4.10	MIRI imaging ETC calculation results	84
4.11	MIRI MRS ETC calculation results	85
5.1	Parameters for MSM-based cube building of individual MIRI bands	134
6.1	JWST post-pipeline data analysis tools already used frequently in this work	148

List of Figures

1.1	Known SSCs (indigo squares) in the Milky Way Galaxy with respect to the spiral arms from Vallée (2008). The Sun location (\odot), its Galactic orbit (dotted circle) and neighborhoods within radii of 1 kpc and 2 kpc (dashed circles) are also indicated (Portegies Zwart et al. 2010).	2
1.2	Central Molecular Zone of the Milky Way with the Arches, Quintuplet, and the Young Nuclear Star Cluster centered on the supermassive black hole. The Galactic plane is horizontal. The image combines infrared data from the Hubble NICMOS and Spitzer IRAC instruments. Image credit: NASA, ESA, D. Wang, S. Stolovy. Annotations by Lu (2018)	3
1.3	Super star cluster R136 in the 30 Doradus nebular of the LMC seen in the visible (left) and infrared (right). Data from the WFC3 instrument on HST. Illustration: NASA, ESA, and Z. Levay (STScI). Science: NASA, ESA, and F. Paresce (INAF-IASF, Bologna, Italy), R. O’Connell (University of Virginia, Charlottesville), and the Wide Field Camera 3 Science Oversight Committee.	4
1.4	Exponents α_M of CMFs in various galaxies (Krumholz et al. 2019). (a) The colored points indicate disk clusters with (open) and without (filled) morphological constraints. The solid and dashed black lines trace the evolved Schechter functions for GCs in the Milky Way and Virgo respectively. The horizontal bars represent the cluster mass ranges, with (straight dotted line) or without (downward dotted curve) detected truncations at the high-mass ends. For clarity, points are not centered on their mass ranges. (b) Distribution of the exponents α_M for disk clusters in the entire galaxy (blue) and independent subsamples (hatched), including Messa et al. (2018b).	5
1.5	Cluster mass functions of a galaxy sample (top) and their corresponding logarithmic slopes (bottom) (Krumholz et al. 2019). The sample includes the LMC, cluster-rich spirals, and cluster-poor spirals (Larsen 2009); M51 (Gieles 2009); Antennae galaxies (Zhang & Fall 1999); and M31 (Vansevičius et al. 2009). For comparison, Schechter (1976) functions for spirals ($M_* = 2.5 \times 10^5 M_\odot$, dashed curves) and Antennae ($M_* = 10^6 M_\odot$, dotted curve) are plotted.	6
1.6	Exponents α_T of the age distributions in various galaxy disks (Krumholz et al. 2019). The horizontal and vertical bars represent the measured age ranges and errors respectively, but points may be slightly displaced from the center for clarity. Panel (a) contains exclusive catalogs with clusters determined morphologically (open points). Panel (b) contains inclusive catalogs without morphological constraints on cluster selection (filled points). Subsamples of a galaxy are indicated by the same symbol. The gray curves are smoothed basis spline fits to the Piskunov et al. (2018) catalog of clusters within 2 kpc in the Solar neighborhood. Panel (c) shows the corresponding histograms of the exponent values.	9

1.7	Observed values of the CFE Γ versus cluster ages T (left panels (a,c)) and the SFR per unit area Σ_{SFR} (right panels (b,d)). Upper panels (a,b) contain exclusive catalogs with clusters determined morphologically. Lower panels (c,d) contain inclusive catalogs without morphological constraints on cluster selection. Dashed lines trace measurements at multiple age ranges for the same galaxy. Faded points indicate likely uncertain measurements (see text) (Krumholz et al. 2019).	12
1.8	Γ - Σ_{SFR} relations for $\tau \leq 10\text{Myr}$ (left) and $\tau > 10\text{Myr}$ (right). For comparison, the fiducial model by Kruijssen (2012) based on the Kennicutt-Schmidt law (Schmidt 1959; Kennicutt 1998) (solid line) and the Bigiel et al. (2008) Σ_{gas} - Σ_{SFR} conversion (dotted and dashed lines), as well as estimated constant Γ values the age range 1–10 and 10–100 Myr by Chandar et al. (2017) (horizontal dot-dashed lines) are plotted. Filled symbols indicate galaxy-wide measurements, while empty symbols denote sub-regions within the same galaxy (Adamo et al. 2020)	13
1.9	Sample of LIRGs at various merging stages (García-Marín et al. 2009). Data are obtained with HST/WFPC2 (F814W filter). The scales correspond to 5 arcsec. Some prominent SSCs on the galaxy disks are visible.	14
1.10	Example of LIRG visual morphological classification based on Larson et al. (2016) scheme	16
1.11	Interaction stages of LIRGs over IR luminosities (Larson et al. 2016)	16
1.12	Individual and combined distributions of spaxel A_V in a sample of LIRGs ($10^{12}L_{\odot} > L_{\text{IR}} > 10^{11}L_{\odot}$) and ULIRGs ($10^{13}L_{\odot} > L_{\text{IR}} > 10^{12}L_{\odot}$) with increasing L_{IR} (Piqueras López et al. 2013). Their interquartile ranges are covered by the corresponding boxes, with the 5th and 95th percentiles represented by the whiskers. The median and weighted mean values are marked by the horizontal blue and red lines respectively, while the nuclear extinctions are indicated by the black diamonds.	17
1.13	Observed (blue) and extinction-corrected (orange) spaxel Σ_{SFR} distributions of the LIRGs (<i>left</i>), the same physical regions in ULIRGs (<i>center</i>), and the whole ULIRGs (<i>right</i>) in a sample of Piqueras López et al. (2016). The median Σ_{SFR} values (dashed vertical lines) are expressed in $M_{\odot} \text{ yr}^{-1} \text{ kpc}^{-2}$	19
1.14	AGN bolometric contributions to the IR luminosities for the samples of local LIRGs from Alonso-Herrero et al. (2012) and local ULIRGs from Nardini et al. (2010).	19
1.15	James Webb Space Telescope and its major components. Image credit: NASA.	20
1.16	Imaging modes of the JWST instruments. Image credit: STScI.	21
1.17	Spectroscopic modes of the JWST instruments. Image credit: STScI.	22
1.18	JWST GO Cycle 1 schedule. TAC is the Telescope Allocation Committee. Image credit: STScI.	23
2.1	Original data, best-fit compound model, best-fit background and residual for a 2MASS source in K_s band.	37
2.2	Projection of original data (black dots), best-fit compound model (red line), Moffat PSF (blue line) and background (green line) for the same 2MASS source in K_s band as in Fig. 2.1.	37
2.3	Measured source (blue) and background (green) magnitudes using different window sizes for the same 2MASS source in K_s band as in Fig. 2.1. The 2MASS magnitude (red) is also plotted for comparison.	38
2.4	Photometric measurements of 109 extracted and cross-matched sources in Lam et al. (2020) using analytical PSF models versus STARFINDER.	39

3.1	Geometrical attributes of photon packets in MontAGN.	43
3.2	Averaged phase (<i>left</i>) and probability density (<i>right</i>) functions in the case of Mie scattering generated by MontAGN (400 000 photons) for MRN-distributed silicates (Grosset 2019).	44
3.3	Fractal dust shell of $R_{in} = 5$ pc, $R_{out} = 50$ pc, $N = 32$, $H = 5$ and $D = 2.6$ containing a total dust mass of $10^6 M_{\odot}$ with 75% silicate, 13.33% ortho-graphite, 6.67% para-graphite, 5% PAH and MRN size distribution.	47
3.4	JHK_s magnitudes of the SSC population in IRAS 17138-1017 (black circles) and their first principal component (magenta line). The red, green and blue circles represent the brightest, median and faintest SSCs respectively in terms of their projected values on the first principal component.	52
3.5	Input SB99 spectra used in the model grids for the sampled SSCs in IRAS 17138-1017	54
3.6	Total dust density maps of the model grid for the median SSC in IRAS 17138-1017. Darker colors represent thicker optical depth.	55
3.7	Spectral energy distributions equivalent to 100 000 photon packets of the bright SSC models with the largest shell inner radius R_{in} or highest clumpiness (99%). The position of the $BIJHK_s$ bands are denoted.	55
3.8	Spectral energy distributions of the bright (<i>top</i>), median (<i>middle</i>) and faint (<i>bottom</i>) SSC models generated using 1 000 000 photon packets. The observed fluxes in the JHK_s bands are marked as black circles.	56
3.9	Total dust density maps of the best-fit models for the bright (<i>left</i>), median (<i>middle</i>) and faint (<i>right</i>) sampled SSCs in IRAS 17138-1017. Darker colors represent thicker optical depth.	57
3.10	Spectral energy distributions of the best-fit models for the bright (red), median (green) and faint (blue) sampled SSCs in IRAS 17138-1017.	58
3.11	Temperature distributions inside the best-fit models for the bright (<i>top</i>), median (<i>middle</i>) and faint (<i>bottom</i>) sampled SSCs in IRAS 17138-1017.	59
3.12	Relation between the source luminosity and the median temperature in SSC models presented in Lam et al. (2020) with the same dust parameters.	60
4.1	MIRI imaging filter bandpasses (STScI 2016–).	66
4.2	Subarray arrangement on the MIRI imager detector (Ressler et al. 2015).	67
4.3	REULEAUX dither pattern (STScI 2016–).	68
4.4	Sets of 4-point dither pattern for extended sources on the BRIGHTSKY subarray (STScI 2016–).	69
4.5	Working principle of the MIRI MRS IFU (STScI 2016–).	71
4.6	Left: FOVs of IFU channels on the sky. Middle: Spectral dispersion onto the MRS detectors from IFU channels. Right: Reduced data cube containing two spatial and one spectral dimension (STScI 2016–).	72
4.7	MIRI MRS PSF and sampling (STScI 2016–).	72
4.8	Example dither pattern for the ALL, 4-point and extended source configuration. Circle sizes correspond to twice the PSF FWHM at 8 (blue) and 28 μm (red) (STScI 2016–).	74
4.9	Visibility of IRAS 17138-1017 for MIRI during Cycle 1.	75
4.10	SNRs for the faintest SSC assuming the minimum ($\log(\text{mJy}) \approx -2.5$, upper panel) and maximum ($\log(\text{mJy}) \approx -0.5$, lower panel) flux values in the wavelength range of the MIRI imaging mode. The exposure time is set at 50.55 seconds.	77

4.11	SNRs for the brightest SSC assuming the minimum flux value ($\log(\text{mJy}) \approx -0.9$) in the wavelength range of the MIRI imaging mode. The exposure time is set at 5.55 seconds.	78
4.12	Total background levels over one year at the sky position of IRAS 17138-1017 for the MIRI imaging filters.	78
4.13	Background intensity spectrum and its components on Day 63 at the sky position of IRAS 17138-1017.	79
4.14	Scenes of the bright (<i>left</i>) and faint (<i>right</i>) SSCs in IRAS 17138-1017 used in the ETC.	80
4.15	SEDs of the bright (cyan) and faint (yellow) SSCs in IRAS 17138-1017.	81
4.16	SEDs of the bright (brown) and faint (purple) galaxy backgrounds in IRAS 17138-1017.	82
4.17	MULTIACCUM readout scheme (Ressler et al. 2015).	83
4.18	SNR over the entire wavelength range of the MIRI MRS for the scene of the bright SSC.	84
4.19	SNR over the entire wavelength range of the MIRI MRS for the scene of the faint SSC.	86
4.20	Footprint of the MIRI imaging observation plotted on the 2MASS sky.	109
4.21	Footprint of the MIRI MRS observation and simultaneous imaging plotted on the 2MASS sky.	109
4.22	Footprint of the MIRI dedicated background observation and simultaneous imaging plotted on the 2MASS sky.	110
4.23	Visit schedule of our observations.	110
5.1	MIRISim Workflow for the imaging and LRS modes (MIRI European Consortium 2020)	112
5.2	MIRISim Workflow for the MRS mode (MIRI European Consortium 2020)	112
5.3	SCASim workflow (MIRI European Consortium 2020)	113
5.4	MIRI imaging simulation scene at $10 \mu\text{m}$. Six SSC models with their local galaxy backgrounds are depicted: the bright (red), median (green) and faint (blue) SSCs described in Chapter 3 and the SSCs from Lam et al. (2020) with the same inner radius for the dust envelope $R_{\text{in}} = 5 \text{ pc}$ and the ages $\tau = 1$ (magenta), 5 (yellow), 10 Myr (cyan). A Vega star (white) normalized at $m = 12.5$ is also added for calibration purposes.	114
5.5	Input SEDs of point sources for MIRISim.	115
5.6	Input SEDs of galaxy backgrounds for MIRISim.	115
5.7	MIRI MRS simulation scene at $10 \mu\text{m}$ containing the bright SSC (red dot) on its local galaxy background (white disk).	116
5.8	Detector image of the scene in Fig. 5.4 observed through the F560W filter. The last frame of the first exposure is shown for maximum signal levels.	118
5.9	Detector image of the scene in Fig. 5.7 for the 1 Myr SSC observed through channels 12SHORT. The last frame of the exposure is shown for maximum signal levels.	119
5.10	Illumination model through the F560W filter for the scene in Fig. 5.4.	120
5.11	Illumination model through channels 12SHORT for the scene in Fig. 5.7 with the 1 Myr SSC.	121
5.12	Count rate data retrieved from the detector image in Fig. 5.8.	126
5.13	Count rate data retrieved from the detector image in Fig. 5.9.	127

5.14	Calibrated data retrieved from the detector image in Fig. 5.8. The pixel values are in MJy/sr.	128
5.15	Resampled 2D data retrieved from the detector image in Fig. 5.8. The pixel values are in MJy/sr.	129
5.16	Resampled 2D data retrieved by processing and combining four dithered F560W exposures of the scene in Fig. 5.4.	131
5.17	Calibrated data retrieved from the detector image in Fig. 5.9. The pixel values are in MJy/sr.	133
5.18	Spectrum extracted from the detector image in Fig. 5.9 containing two disjointed segments for channels 1SHORT ($4.88 \mu\text{m} - 5.75 \mu\text{m}$) and 2SHORT ($7.48 \mu\text{m} - 8.76 \mu\text{m}$).	135
5.19	Recovered photometric measurements using pipeline (dots) and Vega (diamonds) calibrations compared to the input spectra (lines) of the bright (red), median (green) and faint (blue) SSCs described in Chapter 3.	136
5.20	Recovered photometric measurements using pipeline (dots) and Vega (diamonds) calibrations compared to the input spectra (lines) of the SSCs with the same inner radius for the dust envelope $R_{\text{in}} = 5\text{pc}$ and ages $\tau = 1$ (magenta), 5 (yellow), 10 Myr (cyan) described in Lam et al. (2020).	137
5.21	Relation between the mass-normalized $8 \mu\text{m}$ luminosity and the cluster age in our sample (<i>left</i>) compared to Lin et al. (2020) (<i>right</i>).	138
5.22	Spectral energy distributions of the bright (top), median (middle) and faint (bottom) SSC models generated by MontAGN using 1 000 000 photon packets. The observed fluxes in the mid-IR filters are marked as black circles.	138
5.23	Detected SSC and the extraction aperture in the 1SHORT median continuum image, which is retrieved from the detector image in Fig. 5.9.	139
5.24	Original (red) and background-subtracted (green) spectra extracted from the SSC in Fig. 5.23.	140
5.25	Extracted (solid lines) compared to the input spectra (dashed lines) of the SSCs with the same inner radius for the dust envelope $R_{\text{in}} = 5 \text{ pc}$ and ages $\tau = 1$ (magenta), 5 (yellow), 10 Myr (cyan) described in Lam et al. (2020).	141
5.26	Smoothed and joined (solid lines) compared to the input spectra (dashed lines) of the SSCs with the same inner radius for the dust envelope $R_{\text{in}} = 5 \text{ pc}$ and ages $\tau = 1$ (red), 5 (green), 10 Myr (blue) described in Lam et al. (2020).	141
5.27	$6.2 \mu\text{m}$ feature (red) of the 1 Myr SSC and its fitted local continuum (black). . .	142
5.28	Continuum-normalized and subtracted $6.2 \mu\text{m}$ feature (magenta) of the 1 Myr SSC and its Gaussian fit (blue).	142
5.29	Relation between the $11.3/7.7 \mu\text{m}$ and the $6.2/7.7 \mu\text{m}$ PAH ratios of the SSCs with the same inner radius for the dust envelope $R_{\text{in}} = 5 \text{ pc}$ and ages $\tau = 1$ (red), 5 (green), 10 Myr (blue) described in Lam et al. (2020).	143

List of Abbreviations

- 4QPM** 4-quadrant phase-mask
- AGN** active galactic nucleus
- AO** adaptive optics
- APT** Astronomer's Proposal Tool
- AR** Archival Research
- ASDF** Advanced Scientific Data Format
- BCD** blue compact dwarf
- CDP** Calibration Data Product
- CDS** correlated double sampling
- CFE** cluster formation efficiency
- CFR** cluster formation rate
- CLF** cluster luminosity function
- CMF** cluster mass function
- CMZ** Central Molecular Zone
- CRDS** Calibration Reference Data System
- CSA** Canadian Space Agency
- DD ERS** Director's Discretionary Early Release Science
- ESA** European Space Agency
- ET** Eastern Time
- ETC** Exposure Time Calculator
- FET** field effect transistor
- FITS** Flexible Image Transport System
- FOV** field of view
- FWHM** full width at half maximum
- GC** globular cluster
- GeMS** Gemini Multi-Conjugate Adaptive Optics System
- GENCI** Grand Équipement National de Calcul Intensif

- GMC** giant molecular cloud
GO General Observer
GOALS Great Observatories All-Sky LIRG Survey
GPU Graphical Processor Unit
GSAOI Gemini South Adaptive Optics Imager
GTO Guaranteed Time Observations
GTVT General Target Visibility Tool
- HRAA** Haute Résolution Angulaire en Astrophysique
HST Hubble Space Telescope
HWHM half width at half maximum
- ICRS** International Celestial Reference System
IFU integral field unit
IMF initial mass function
IR infrared
ISM interstellar medium
- JBT** JWST Backgrounds Tool
JIST JWST Interactive Sensitivity Tool
JWST James Webb Space Telescope
- LEGUS** Legacy Extragalactic UV survey
LESIA Laboratoire d'Études Spatiales et d'Instrumentation en Astrophysique
LMC Large Magellanic Cloud
LRS low-resolution spectrometer
LSF line spread function
- MAISIE** Multipurpose Astronomical Instrument Simulator
MAST Mikulski Archive for Space Telescopes
MDD mass-dependent destruction
MID mass-independent destruction
MIRI Mid-Infrared Instrument
MontAGN Monte Carlo for Active Galactic Nuclei
MRS medium-resolution spectrometer
MSM Modified Shepard's Method
- NASA** National Aeronautics and Space Administration
NED NASA/IPAC Extragalactic Database
NIRCam Near-Infrared Camera
NIRISS Near-Infrared Imager and Slitless Spectrograph
NIRSpec Near-Infrared Spectrograph

-
- OC** open cluster
- PA** position angle
- PAH** polycyclic aromatic hydrocarbon
- PCA** principal component analysis
- PSF** point spread function
- ReDCaT** Reference Data for Calibration and Tools
- RSCD** reset switch charge decay
- SB99** Starburst99
- SCA** Sensor Chip Assembly
- SED** spectral energy distribution
- SFE** star-forming efficiency
- SFR** star formation rate
- Si:As IBC** arsenic-doped silicon impurity band conduction
- SMC** Small Magellanic Cloud
- SMO** Spectrometer Main Optics
- SNR** signal-to-noise ratio
- SSC** super star cluster
- SSP** simple stellar population
- STScI** Space Telescope Science Institute
- TAC** Telescope Allocation Committee
- TSO** time-series observation
- (U)LIRG** (ultra)luminous infrared galaxy
- UV** ultraviolet
- VLT** Very Large Telescope
- WCS** world coordinate system
- YMC** young massive cluster
- YSO** young stellar object

Chapter 1

Introduction

1.1 Super star clusters

1.1.1 Definition and fundamental characteristics

Although clustered environments are major contributors to star formation (Portegies Zwart et al. 2010, and references therein), the definition and classification of star clusters remain fuzzy. Clusters may typically be identified based on morphological and dynamical criteria (Ascenso 2018, and references therein), but their classifications are essentially qualitative (Krumholz et al. 2019). Usually, gravitationally bound groups of stars are considered as clusters, while unbound systems are called associations instead. In the Milky Way, most of the star clusters in the disk have lower masses ($\lesssim 5000 M_{\odot}$) and younger ages ($\lesssim 6$ Gyr) compared to the halo population, which is more massive ($\gtrsim 10^4 M_{\odot}$) and older ($\gtrsim 6$ Gyr) (Kharchenko et al. 2013). They are classified as open clusters (OCs) and globular clusters (GCs) respectively. However, new observations at various spatial and temporal scales are revealing more and more similarities and connections among those populations in terms of their properties, formation and evolution. All of them may be parts of an overall hierarchy (Elmegreen & Efremov 1997) and follow a common life cycle.

Our work is focused on super star clusters (SSCs), which may also be called by a more descriptive name as young massive clusters (YMCs). These clusters are evolving through the violent mass-loss phase but long-term stellar dynamical processes have not become dominant. They are expected to last for at least 1 Gyr given their high masses and densities. For practical purposes, we have adopted the definitions of "young" as not more than about 100 Myr and "massive" as not less than $10^4 M_{\odot}$, as well as the assumption of being gravitationally bound from Portegies Zwart et al. (2010) since these are measurable quantities in our study. Basically these constraints distinguish SSCs from OCs with lower masses ($\lesssim 10^3 M_{\odot}$) and GCs with older ages ($\gtrsim 10$ Gyr). SSCs may be considered as the most massive and young OCs, and possibly young GCs. Furthermore, SSCs are highly compact with virial radii on the order of 1 pc and core densities $\rho_c \gtrsim 10^3 M_{\odot} \text{ pc}^{-3}$.

Adopting the above definition, there are only a few known YMCs in the Milky Way Galaxy (Fig. 1.1), which are all younger than 20 Myr and less massive than $\sim 5 \times 10^4 M_{\odot}$ (Portegies Zwart et al. 2010; Krumholz et al. 2019, and references therein). However, they may not reach the age of GCs as expected for SSCs. An observational selection bias likely exists since Galactic extinction, together with foreground and background contaminations limit detection of older and distant populations. Being the most massive young cluster ($\sim 5 \times 10^4 M_{\odot}$) at a relative close distance (~ 4.0 kpc) and with less extinction ($A_V \sim 10$) with respect to other Galactic YMCs,

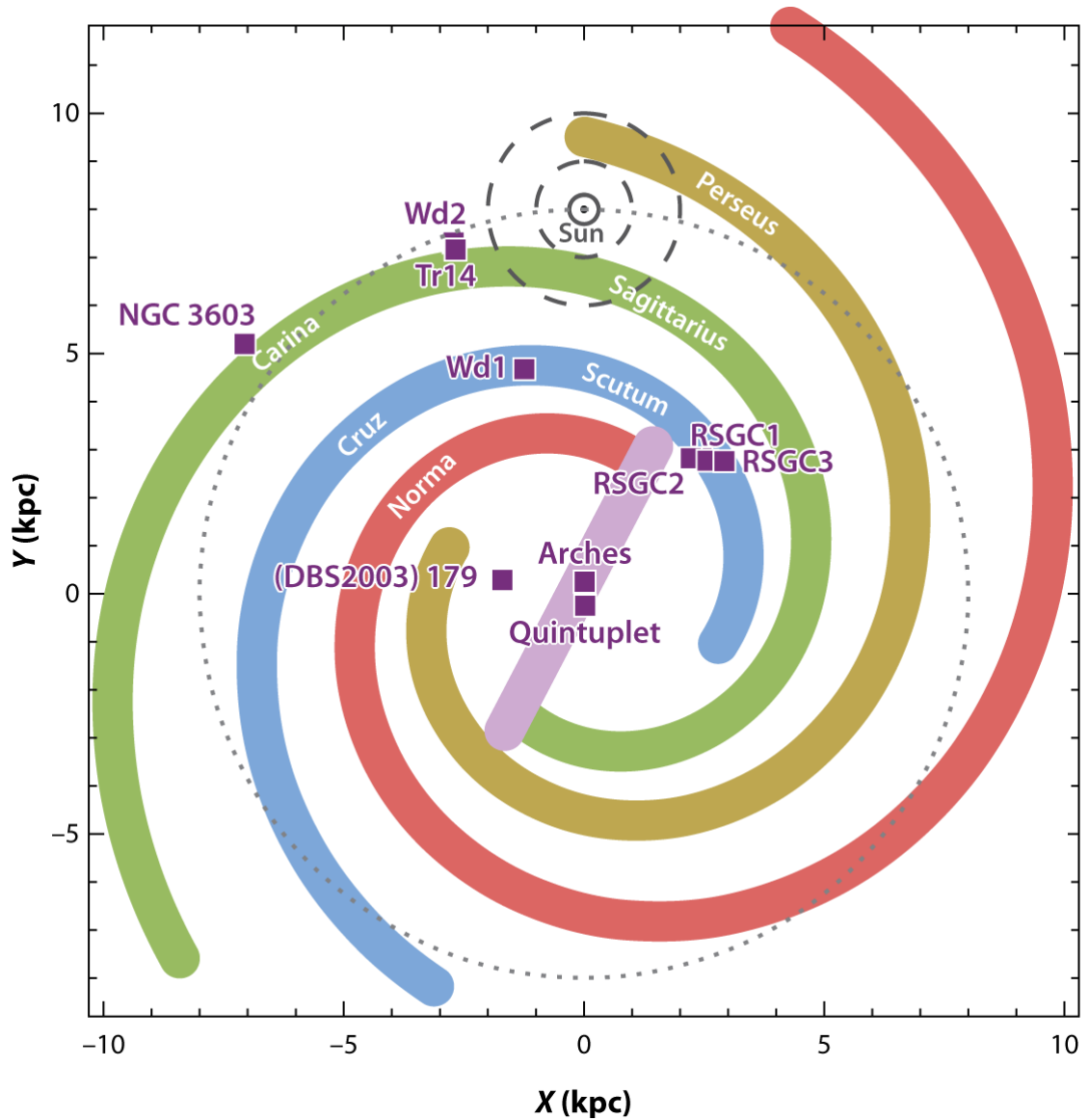


Figure 1.1 – Known SSCs (indigo squares) in the Milky Way Galaxy with respect to the spiral arms from Vallée (2008). The Sun location (\odot), its Galactic orbit (dotted circle) and neighborhoods within radii of 1 kpc and 2 kpc (dashed circles) are also indicated (Portegies Zwart et al. 2010).

Westerlund 1 represents an object of interest for the study of star formation and evolution in clustered environments (Gennaro et al. 2011). It hosts a rich population of massive and rare objects including Wolf–Rayet stars, evolved OB stars as well as luminous blue variables and yellow hypergiants, which are more concentrated in the central region. Observed mass segregation and elongation of Westerlund 1 suggest coeval subcluster merging during its formation. Other captivating Galactic YMCs close to the Galactic Center include the Arches, Quintuplet, and

the Young Nuclear Star Cluster (Lu 2018, and references therein). They are located in the Central Molecular Zone (CMZ), an extreme environment in terms of temperatures, stellar and gas densities, magnetic fields, tidal fields, turbulent pressures and gravitational gradient within 200 pc from the central supermassive black hole. The formation and evolution of these clusters and their stellar contents in such extreme conditions are essential issues to be addressed. Specifically, the initial mass functions (IMFs) in the Galactic Center seem to deviate from the one in the solar neighborhood (Lu 2018, and references therein). Nevertheless, the accompanying crowding and extinction effects remain significant challenges for more comprehensive studies.

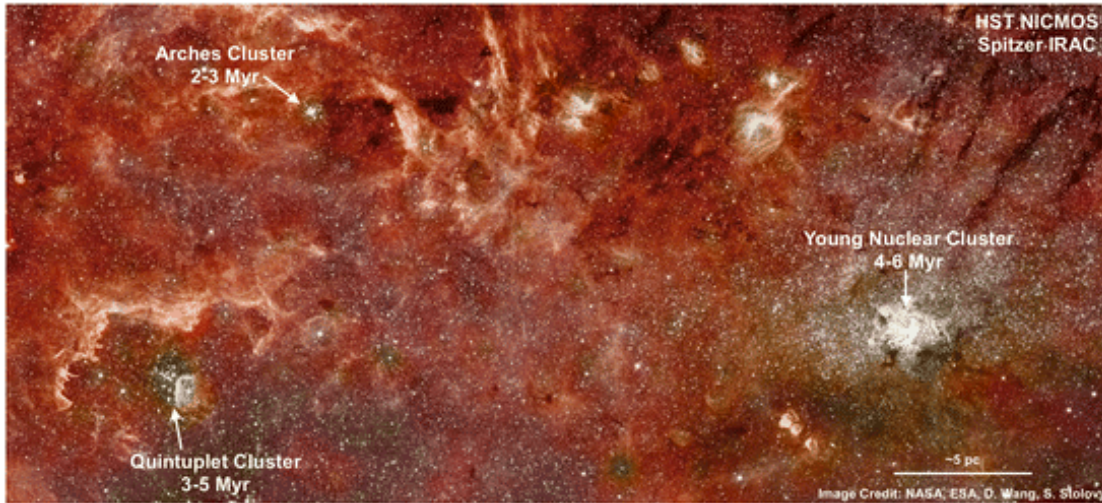


Figure 1.2 – Central Molecular Zone of the Milky Way with the Arches, Quintuplet, and the Young Nuclear Star Cluster centered on the supermassive black hole. The Galactic plane is horizontal. The image combines infrared data from the Hubble NICMOS and Spitzer IRAC instruments. Image credit: NASA, ESA, D. Wang, S. Stolovy. Annotations by Lu (2018)

More diverse populations of SSCs are found in nearby galaxies from the Local Group, notably the Magellanic Clouds and M31 (Portegies Zwart et al. 2010, and references therein). They may also be resolved spatially but are less affected by extinction and stellar contaminations than Milky Way clusters, thus being ideal observing targets. The Magellanic Clouds’ SSCs are generally older (> 10 Myr) than the Milky Way counterparts. Compared to the Milky Way OCs of similar ages, these clusters are also much more massive and denser. Furthermore, the Magellanic Clouds represent metal-poor environments similar to high redshift galaxies, where the formation and evolution of clusters and their stellar contents have also received much attention (Adamo et al. 2020, and references therein). Various studies find typical values of $0.5 Z_{\odot}$ and $1/3$ of the Milky Way dust-to-gas ratio in the Large Magellanic Cloud (LMC), $0.25 Z_{\odot}$ and $1/6$ of the Milky Way dust-to-gas ratio in the Small Magellanic Cloud (SMC) (e.g., Russell & Dopita 1992; Rolleston et al. 1999; Lee et al. 2005; Roman-Duval et al. 2014). Since metal line absorption transfers photon momentum to the stellar atmosphere plasma and affects stellar winds, as a consequence these environments exhibit higher effective stellar temperatures and luminosities, especially in the ultraviolet (UV), faster stellar evolution and lower mass-loss rates (Kudritzki & Puls 2000). Low extinctions ($A_V^{\text{LMC}} \sim 0.4$, $A_V^{\text{SMC}} \sim 0.3$) also facilitate UV observations (e.g., Górski et al. 2020). Notably the closest archetype of SSC that may evolve into a GC ($\gtrsim 10^5 M_{\odot}$, see Portegies Zwart et al. 2010) is the cluster R136 in the LMC (Fig. 1.3). As determined from Hubble Space Telescope (HST) UV spectroscopy, the central 1 pc of R136 is dominated by extremely young

(~ 1.5 Myr), massive ($50 M_{\odot}$, assuming a [Salpeter 1955](#) IMF) and luminous ($m_{F555W} < 16.0$) O2-3 stars ([Crowther et al. 2016](#)). On the other hand, the outer population up to a radius of 7 pc has been studied using HST infrared (IR) and optical imaging data ([Andersen et al. 2009](#)). The cluster mass is estimated to be $5 \times 10^4 M_{\odot}$ over the mass range of $2.1\text{--}25 M_{\odot}$ assuming an age of 3 Myr. A [Salpeter \(1955\)](#) IMF over a mass range of $1.1\text{--}20 M_{\odot}$ is observed outside the radius of 5 pc, together with stars down to $0.5 M_{\odot}$. Applying this IMF down to $0.5 M_{\odot}$ and to the entire cluster will double its estimated mass. Combining this with a low velocity dispersion ($4\text{--}5 \text{ km s}^{-1}$, [Hénault-Brunet et al. 2012](#)), R136 may evolve into a proto-globular cluster. However, based on N-body computations, [Banerjee & Kroupa \(2018\)](#) argue that R136 has undergone violent gas expulsion following an episodic or monolithic formation, but still achieves dynamical equilibrium. Recent observations ([Schneider et al. 2018](#)) and simulations ([Banerjee & Kroupa 2012](#); [Banerjee et al. 2012](#)) also indicate top-heavy (shallower at high mass) IMFs instead.

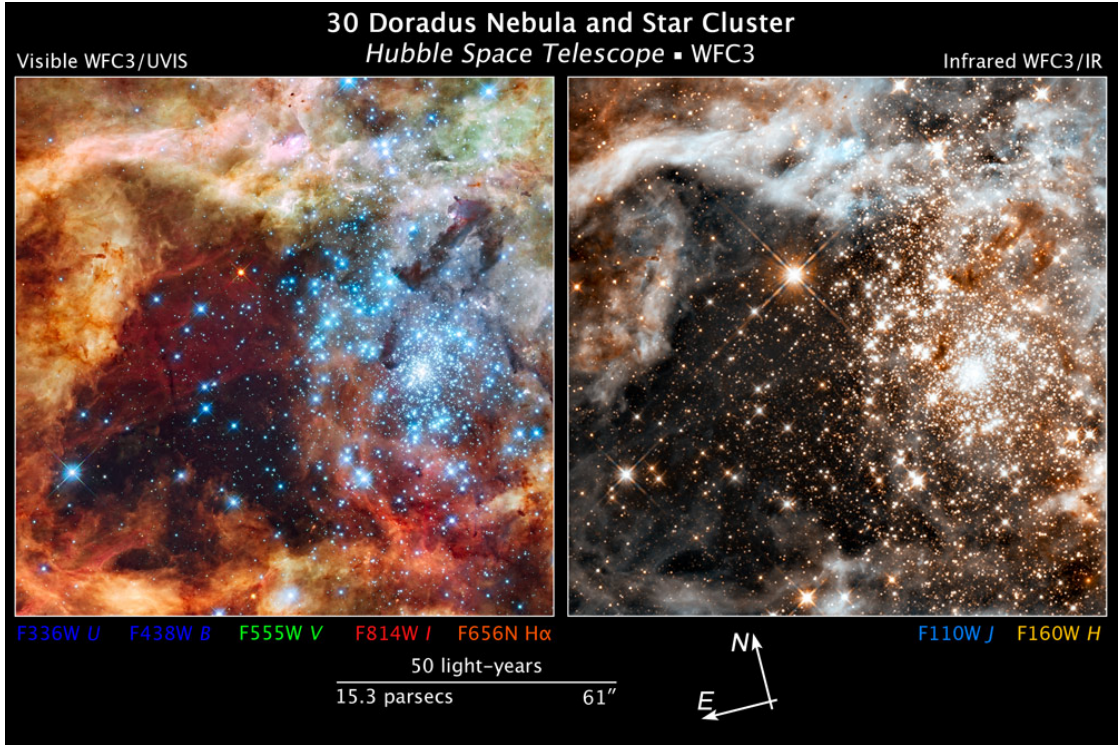


Figure 1.3 – Super star cluster R136 in the 30 Doradus nebular of the LMC seen in the visible (left) and infrared (right). Data from the WFC3 instrument on HST. Illustration: NASA, ESA, and Z. Levay (STScI). Science: NASA, ESA, and F. Paresce (INAF-IASF, Bologna, Italy), R. O’Connell (University of Virginia, Charlottesville), and the Wide Field Camera 3 Science Oversight Committee.

Beyond the Local Group, SSCs may be luminous enough to be detected at large distances (e.g., $M_V = -15.5$, [Östlin et al. 2007](#); $-18 < M_{K_s} \leq -13$, [Lam et al. 2020](#)). However most of them are unresolved and may also be blended. Exhibiting extreme star formation, SSCs are often located in interacting and merging systems and other star-forming galaxies, such as (ultra)luminous infrared galaxies ((U)LIRGs; e.g., [Vavilkin 2011](#); [Miralles-Caballero et al. 2011](#); [Randriamanakoto et al. 2013a,b](#); [Linden et al. 2017](#); [Lam et al. 2020](#)), blue compact dwarves

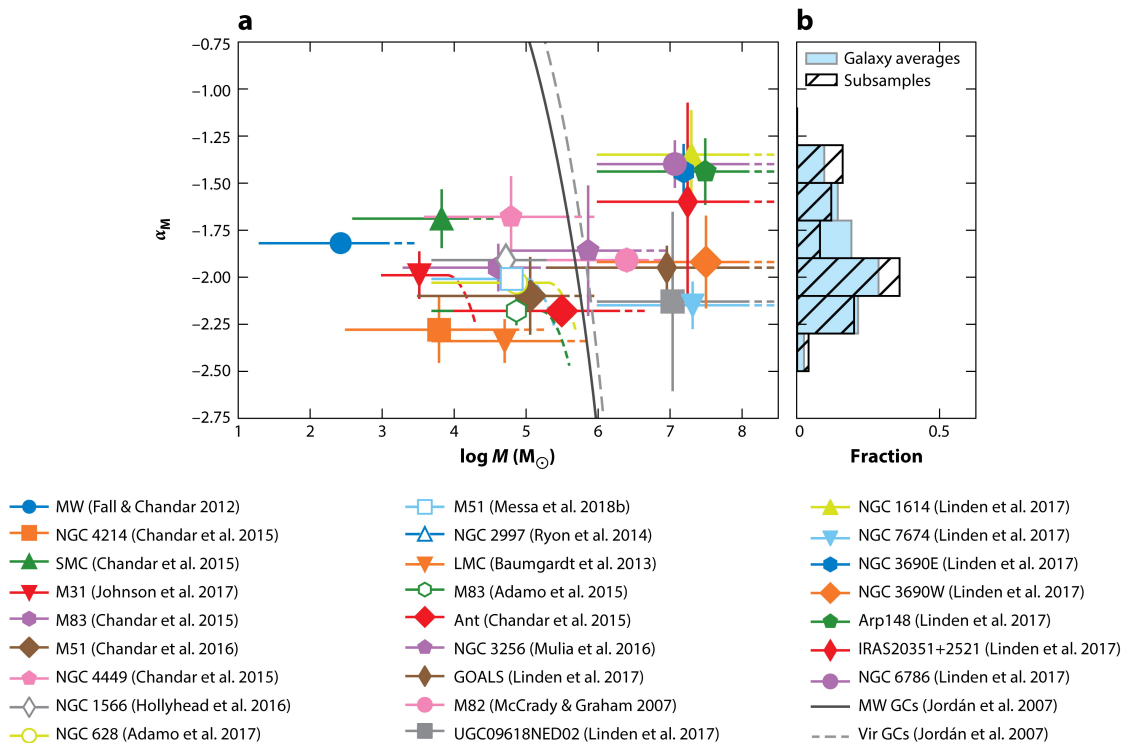
(BCDs; e.g., Adamo et al. 2010, 2011a,b) and spirals, even quiescent ones (e.g., Gieles et al. 2005; Bastian 2008; Grosbøl & Dottori 2008, 2012; Haas et al. 2008; Larsen 2009). Some global properties of SSCs are observed across different environments, as discussed below.

1.1.2 Cluster mass function

Previous work on SSCs in various galaxies shows that the cluster mass function (CMF), which describes the number of clusters N over bins of masses M , generally follows a power law :

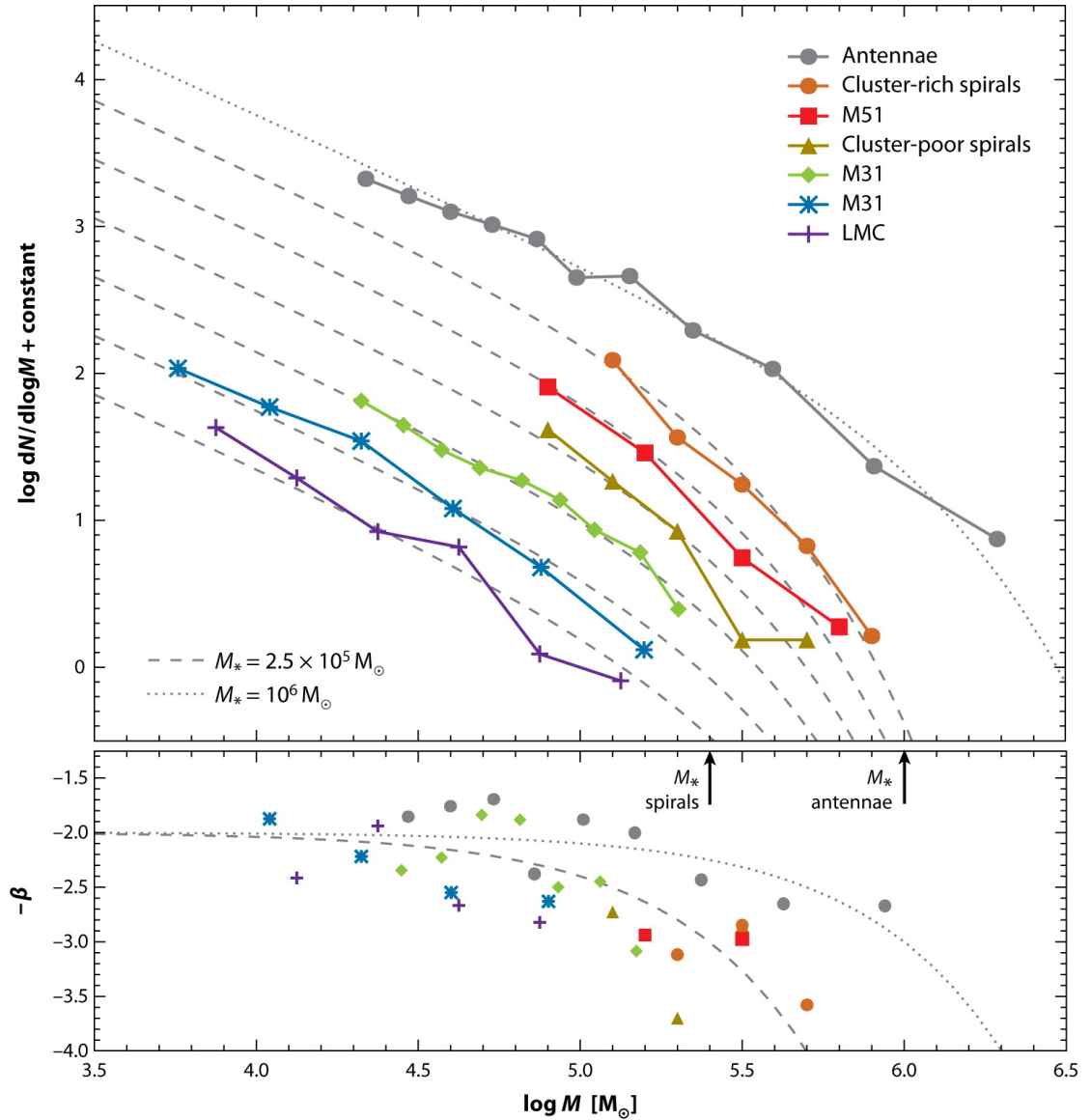
$$\frac{dN}{dM} \propto M^{\alpha_M} \quad (1.1)$$

where $\alpha_M \sim -2$ (Portegies Zwart et al. 2010; Adamo & Bastian 2018; Krumholz et al. 2019, and references therein, see Fig.1.4). Compared to quiescent spirals, the CMFs of starburst galaxies may be flattened due to blending effects (Krumholz et al. 2019).



Krumholz MR, et al. 2019.
Annu. Rev. Astron. Astrophys. 57:227–303

Figure 1.4 – Exponents α_M of CMFs in various galaxies (Krumholz et al. 2019). (a) The colored points indicate disk clusters with (open) and without (filled) morphological constraints. The solid and dashed black lines trace the evolved Schechter functions for GCs in the Milky Way and Virgo respectively. The horizontal bars represent the cluster mass ranges, with (straight dotted line) or without (downward dotted curve) detected truncations at the high-mass ends. For clarity, points are not centered on their mass ranges. (b) Distribution of the exponents α_M for disk clusters in the entire galaxy (blue) and independent subsamples (hatched), including Messa et al. (2018b).



AR Zwart SFP, et al. 2010.
 Annu. Rev. Astron. Astrophys. 48:431–93

Figure 1.5 – Cluster mass functions of a galaxy sample (top) and their corresponding logarithmic slopes (bottom) (Krumholz et al. 2019). The sample includes the LMC, cluster-rich spirals, and cluster-poor spirals (Larsen 2009); M51 (Gieles 2009); Antennae galaxies (Zhang & Fall 1999); and M31 (Vansevičius et al. 2009). For comparison, Schechter (1976) functions for spirals ($M_* = 2.5 \times 10^5 M_{\odot}$, dashed curves) and Antennae ($M_* = 10^6 M_{\odot}$, dotted curve) are plotted.

This slope value may be explained by a hierarchical formation process under supersonic turbulence and self-gravity (e.g., Fleck 1996; Elmegreen & Falgarone 1996; Elmegreen 2006,

2011; Hopkins 2013), which is self-similar and scale-free. Consequently, for any hierarchy level (i.e. logarithmic bin $\log M$ of constant size $\Delta \log M$) containing N objects, the total mass MN remains constant. The resulting mass distribution is:

$$\frac{dN}{dM} \approx \frac{N}{\Delta M} \approx \frac{1}{M^2} \frac{MN}{\Delta \log M \ln 10} \propto \frac{1}{M^2} \quad (1.2)$$

Different mass ranges are measured across studies. The lower limits merely reflect observational constraints, while truncations at the high-mass end are still a matter of debate, which may be better described using a Schechter (1976) function instead (Portegies Zwart et al. 2010; Adamo & Bastian 2018; Krumholz et al. 2019; Adamo et al. 2020, and references therein):

$$\frac{dN}{dM} \propto \left(\frac{M}{M_*}\right)^{\alpha_M} \exp\left(-\frac{M}{M_*}\right) \quad (1.3)$$

The Schechter (or characteristic, truncation) mass M_* seems to depend on the galactic environment, as seen in Fig. 1.5. Correlations between M_* , α_M and the star formation rate (SFR) surface density Σ_{SFR} has also been observed by Adamo et al. (2020). Multiple theories have been established to explain these truncations (Adamo et al. 2020, and references therein). Kruijssen (2014) suggests a connection between M_* and the Toomre (1964) mass, which corresponds to the maximum size for a giant molecular cloud (GMC) to remain bound in a rotating galaxy disk. This limit particularly depends on the gas surface density and the velocity dispersion caused by shearing motions and centrifugal forces. Additionally, Reina-Campos & Kruijssen (2017) take into account the disruption caused by stellar feedback and recover the observed maximum masses of GMCs, clumps and clusters in the Milky Way, the Local Group galaxy M31, the spiral galaxy M83 and the high-redshift galaxy zC406690. This model has been incorporated into the E-MOSAICS project (Pfeffer et al. 2018; Kruijssen et al. 2019) and subsequently reproduced the $M_*-\Sigma_{\text{SFR}}$ and $\alpha_M-\Sigma_{\text{SFR}}$ relations above (Pfeffer et al. 2019). Another analytical model from Elmegreen (2018) provides the maximum cluster mass sustained by the cloud-core pressure as a function of Σ_{SFR} , assuming parameter values from observations. Results for local galaxies are in good agreement with the observed M_* ranging from $10^{3.9} M_\odot$ to $10^{6.3} M_\odot$.

1.1.3 Cluster luminosity function

The cluster luminosity function (CLF) (i.e. the number of clusters N over bins of luminosities L) may be derived directly from observations without fitting models. Similar to the CMF, observations show that the CLF may also be described by a power-law:

$$\frac{dN}{dL} \propto L^{\alpha_L} \quad (1.4)$$

with $\alpha_L \sim -2$. Yet steeper slopes at brighter end and compared to the CMF have been detected (e.g., Portegies Zwart et al. 2010; Adamo & Bastian 2018, and references therein). The value of α_L seems to vary across different galactic environments. In ULIRGs, LIRGs and BCDs $\alpha_L \approx -1.87 \pm 0.3$ (Randriamanakoto et al. 2013b; Vavilkin 2011; Miralles-Caballero et al. 2011; Adamo et al. 2010, 2011a,b). More quiescent star-forming galaxies and normal spirals have steeper distributions with $\alpha_L \approx -2.2 \pm 0.3$ (Elmegreen & Efremov 1997; Gieles et al. 2006a; Bastian 2008; Haas et al. 2008; Larsen 2009). However, CLFs may deviate from power law due to uncorrected reddening (Megeath 1996). Fall (2006) shows the analytical relations between the CLF, CMF and the cluster age distribution. Assume that the cluster mass-to-light ratios μ only depends on their ages τ :

$$\frac{M}{L} = \mu(\tau) \quad (1.5)$$

Thus the joint luminosity-age and mass-age distributions of clusters are related by:

$$\frac{\partial^2 N}{\partial L \partial \tau} dL d\tau = \frac{\partial^2 N}{\partial M \partial \tau} dM d\tau = dN(L, M, \tau) \quad (1.6)$$

$$\implies \frac{\partial^2 N}{\partial L \partial \tau} dL d\tau = \frac{\partial^2 N}{\partial M \partial \tau} \left| \frac{\partial M}{\partial L} \right| dL d\tau \quad (1.7)$$

$$\implies \frac{\partial^2 N}{\partial L \partial \tau} d\tau = \frac{\partial^2 N}{\partial M \partial \tau} \mu(\tau) d\tau \quad (1.8)$$

If we assume that the cluster masses and ages are distributed independently, then the mass distribution is the same in all age bins and vice versa. The joint mass-age distribution may be decomposed as:

$$\frac{\partial^2 N}{\partial M \partial \tau} = \frac{1}{\Sigma N} \frac{dN}{dM} \frac{dN}{d\tau} \quad (1.9)$$

where ΣN is the total number of clusters. The CLF is calculated as:

$$\frac{dN}{dL} = \int_{\tau=0}^{\infty} \frac{\partial^2 N}{\partial L \partial \tau} d\tau \quad (1.10)$$

$$= \frac{1}{\Sigma N} \int_{\tau=0}^{\infty} \frac{dN}{dM} \frac{dN}{d\tau} \mu(\tau) d\tau \quad (1.11)$$

If the CMF is a power-law with an exponent α_M :

$$\frac{dN}{dM} = A_M M^{\alpha_M} \quad (1.12)$$

then the CMF follows a distribution with the same exponent:

$$\frac{dN}{dL} = \frac{A_M L^{\alpha_M}}{\Sigma N} \int_{\tau=0}^{\infty} \frac{dN}{d\tau} \mu^{\alpha_M+1}(\tau) d\tau \propto L^{\alpha_M} \quad (1.13)$$

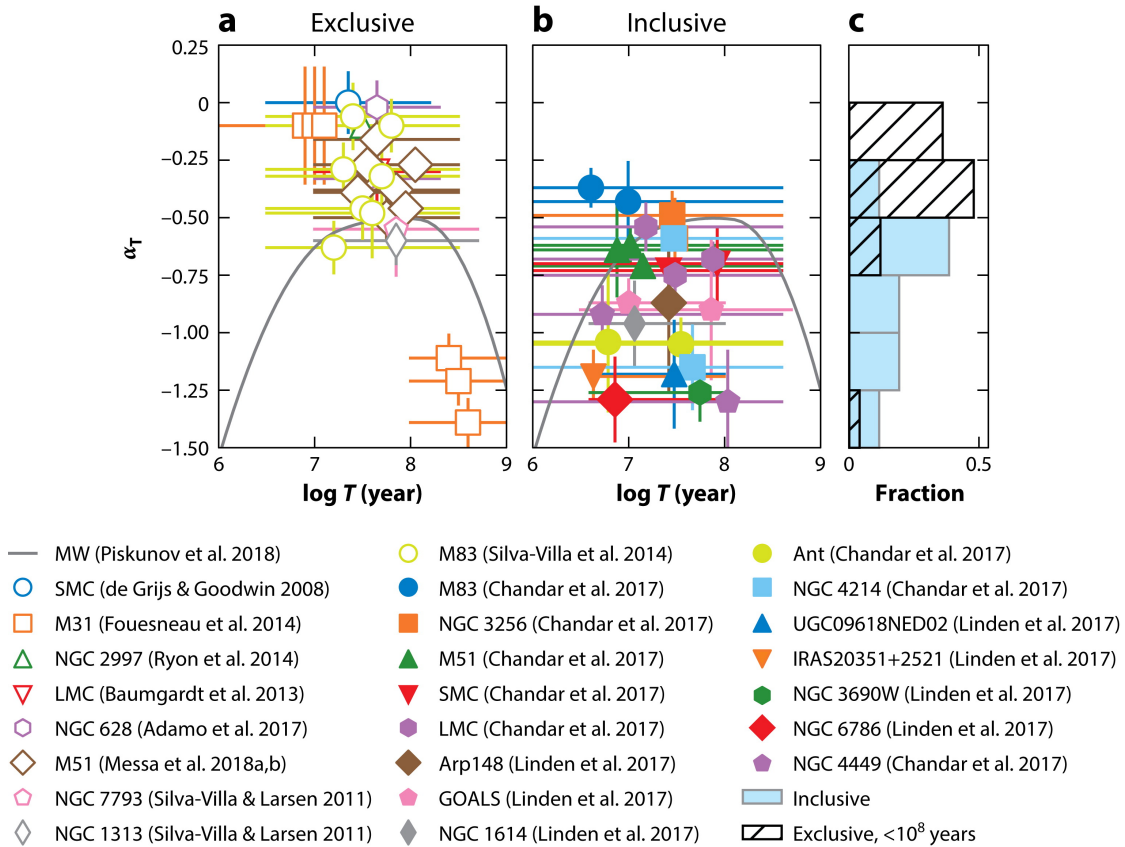
1.1.4 Cluster age distribution, formation and evolution

The formation histories and evolution of clusters may be inferred from their age distributions. The distribution of star clusters over bins of ages τ also follow a power law in general:

$$\frac{dN}{d\tau} = \tau^{\alpha_\tau} \quad (1.14)$$

where α_τ depends strongly on the galactic environment (e.g., [Adamo & Bastian 2018](#); [Krumholz et al. 2019](#), and references therein, see Fig. 1.6). Exclusive catalogs strictly containing bound clusters have $\alpha_\tau \approx -0.3$ to -0.2 . In contrast, inclusive catalogs without morphological considerations have $\alpha_\tau \approx -1$ to -0.7 , indicating shorter survival times. Starburst, GMC-rich galaxies, especially where strong tidal forces are present tend to have α_τ closer to -1 compared to normal spirals and dwarfs ($\alpha_\tau \approx -0.7$), which implies more intense disruption. Some grand-design spirals also have steeper α_τ toward their centers (e.g., [Bastian et al. 2012](#); [Silva-Villa et al. 2014](#);

Messa et al. 2018a). In addition, α_τ may also increase with the cluster mass (e.g., Silva-Villa et al. 2014; Adamo et al. 2017; Messa et al. 2018b).



Krumholz MR, et al. 2019.
Annu. Rev. Astron. Astrophys. 57:227–303

Figure 1.6 – Exponents α_τ of the age distributions in various galaxy disks (Krumholz et al. 2019). The horizontal and vertical bars represent the measured age ranges and errors respectively, but points may be slightly displaced from the center for clarity. Panel (a) contains exclusive catalogs with clusters determined morphologically (open points). Panel (b) contains inclusive catalogs without morphological constraints on cluster selection (filled points). Subsamples of a galaxy are indicated by the same symbol. The gray curves are smoothed basis spline fits to the Piskunov et al. (2018) catalog of clusters within 2 kpc in the Solar neighborhood. Panel (c) shows the corresponding histograms of the exponent values.

Initially, clusters are born in hierarchically structured GMCs under supersonic turbulence and self-gravity (see Sect. 1.1.2 and Sect. 3.2). There are two proposed mechanisms of cluster formation: *monolithic*, *episodic* or *in situ* (top-down) formation and *conveyor belt* (bottom-up) formation (e.g., Longmore et al. 2014; Banerjee & Kroupa 2018; Krumholz et al. 2019, and references therein). In the *in situ* formation scenario, sufficient mass of gas is accumulated locally before a single starburst occurs and quickly disperses the cloud. Such scenario is consistent with the Galactic Center environment and the observed properties of gas-free SSCs such as R136,

NGC 3603 and the Orion Nebula Cluster. On the other hand, the *conveyor belt* mechanism implies gas inflows and subcluster merging along the star formation process due to local gravitational potential. This formation mode may explain the formation of SSCs in the Galactic disk where there is a lack of starless gas clouds of $10^5 M_\odot$ and 1 pc scales (e.g., Peretto & Fuller 2009), as well as substructures within clusters (e.g., Kuhn et al. 2014). Nevertheless, similar fundamental cluster properties may result from different initial conditions. Afterwards clusters evolve through three stages characterized by the embedding natal cloud, stellar mass loss and stellar dynamical evolution as detailed below (see e.g., Portegies Zwart et al. 2010; Adamo & Bastian 2018; Krumholz et al. 2019).

At their early ages, clusters are embedded in their natal clouds of dust and gas (see e.g., Lada & Lada 2003; Portegies Zwart et al. 2010; Longmore et al. 2014; Ascenso 2018; Krumholz et al. 2019, and references therein). As a result, SSCs are often optically obscured but prominent in the IR because of the thermal emission from heated dust. Eventually, gas exhaustion and gas expulsion due to stellar feedback terminate star formation, exposing the cluster. If gas expulsion becomes dominant and violent enough, it may cause early disruption of clusters, which are no longer self-gravitationally sustained (*infant mortality*; Lada & Lada 2003), manifested as sharp decreases in the age distributions during the first Myr. In fact, over 90% of clusters may not survive the embedded phase (Lada & Lada 2003; Portegies Zwart et al. 2010). Given a short gas removal timescale of 1–5 Myr (e.g., Leisawitz et al. 1989; Eggleton 2006; Portegies Zwart et al. 2010; Morales et al. 2013), stellar age spreads within clusters are insignificant. Thus SSCs can be considered as coeval simple stellar populations (SSPs).

After becoming gas-free, clusters continue to experience mass loss due to stellar evolution and tidal perturbations and may be disrupted during their first 100 Myr (see e.g., Portegies Zwart et al. 2010; Adamo & Bastian 2018; Krumholz et al. 2019). Especially, tidal shocks due to GMC encounters play an important role (Spitzer 1958), even the clusters' own natal environments can be destructive (*cruel cradle effect*; Elmegreen & Hunter 2010; Kruijssen et al. 2011). There are two proposed models of cluster disruption: mass-independent destruction (MID; e.g., Fall et al. 2005, 2009; Whitmore et al. 2007) and mass-dependent destruction (MDD; e.g., Boutloukos & Lamers 2003; Lamers et al. 2005, 2010). The mass-independent destruction (MID) model states that cluster disruption processes primarily depend on their internal densities and concentrations, which are uncorrelated to their masses or local environments. A cluster mortality rate of $\sim 90\%/\log(\tau/\text{yr})$ corresponding to $\alpha_\tau \sim -1$ is observed regardless of CMF (see also Eq.1.9), although minor variations may be present due to different cluster formation histories, GMC encounters or spatial scales. On the other hand, the mass-dependent destruction (MDD) model relates the cluster dissolution timescales with their masses and environments. The cluster age distribution is interpreted in terms of evolutionary fading and cluster disruption (Boutloukos & Lamers 2003), in the following we will only focus on the latter effect. Let us assume that clusters disrupt quickly at an age t_{dis} depending on their masses M :

$$t_{\text{dis}} \propto M^\gamma \quad (1.15)$$

where $\gamma = 0.62$, but the scaling factor varies with the tidal field (Lamers et al. 2005) and the GMC density (Gieles et al. 2006b). Thus at age τ only clusters more massive than M_{dis} are observable:

$$M_{\text{dis}} \propto \tau^{1/\gamma} \quad (1.16)$$

Let us assume that in a particular galactic environment, clusters are formed at a constant rate S and fixed power-law CMF of exponent $\alpha_M > 1$, then the observed age distribution is:

$$\frac{dN}{d\tau} \propto \int_{M_{\text{dis}}}^{\infty} S M^{-\alpha_M} dM = \frac{S}{\alpha_M - 1} M_{\text{dis}}^{1-\alpha_M} \quad (1.17)$$

$$\propto \tau^{\frac{1-\alpha_M}{\gamma}} \quad (1.18)$$

Controversies between these theories have arisen and they are complicated by the definition of clusters themselves, particularly the application of morphological criteria in different cluster catalogs. Whether the dissolution timescale t_{dis} depends on the cluster mass M is the central issue between the two models. For a cluster density ρ , calculations show that $t_{\text{dis}} \propto \rho$ (e.g., [Portegies Zwart et al. 2010](#); [Krumholz et al. 2019](#)). However the relation between ρ and M has not been firmly established.

Over timescales much longer than 100 Myr, along with external tidal perturbations, stellar dynamical processes govern the cluster evolution (see [Portegies Zwart et al. 2010](#); [Krumholz et al. 2019](#)). In particular, stellar kinetic energies tend to follow a Maxwellian velocity distribution. However in the high-velocity tail a fraction of the stars attains enough kinetic energy to escape from the cluster. Eventually gravitational interactions between stars cause the velocity distribution to relax back to a Maxwellian, repopulating the tail and the cycle continues. As a result, cluster members steadily evaporate, especially the low-mass ones.

Given their masses and expected lifetimes, SSCs may finally evolve into GCs (see [Portegies Zwart et al. 2010](#); [Krumholz et al. 2019](#)). However, there are major differences between these two populations that still need to be reconciled. First of all, the mass functions of globular clusters follow a lognormal distribution with a turnover mass of $\approx 2 \times 10^5 M_{\odot}$, corresponding to a luminosity function peaking at $M_V \approx -7.5$ (e.g., [Harris 2001](#); [Brodie & Strader 2006](#); [Jordán et al. 2007](#)), as opposed to the power law or the Schechter function in the case of SSCs. This discrepancy may be linked to the selective disruption of low-mass clusters during their evolution as presented above. There is an ongoing debate on the dominant disruption mechanism: either early gas expulsion (e.g., [Baumgardt et al. 2008](#)), subsequent stellar mass loss (e.g., [Vesperini & Zepf 2003](#)) or long-term dynamical evolution (e.g., [Elmegreen & Efremov 1997](#); [Vesperini & Heggie 1997](#); [Baumgardt 1998](#); [Fall & Zhang 2001](#); [Jordán et al. 2007](#); [McLaughlin & Fall 2008](#)). Furthermore, GCs possess two unique features that do not appear in SSCs: anticorrelations in certain light elements (e.g., Na-O, Mg-Al) and multiple stellar populations which are not well understood (see e.g., [Bastian & Lardo 2018](#); [Gratton et al. 2019](#)). Nevertheless, if we only define GCs as old massive clusters without any other constraint, SSCs are likely their progenitors.

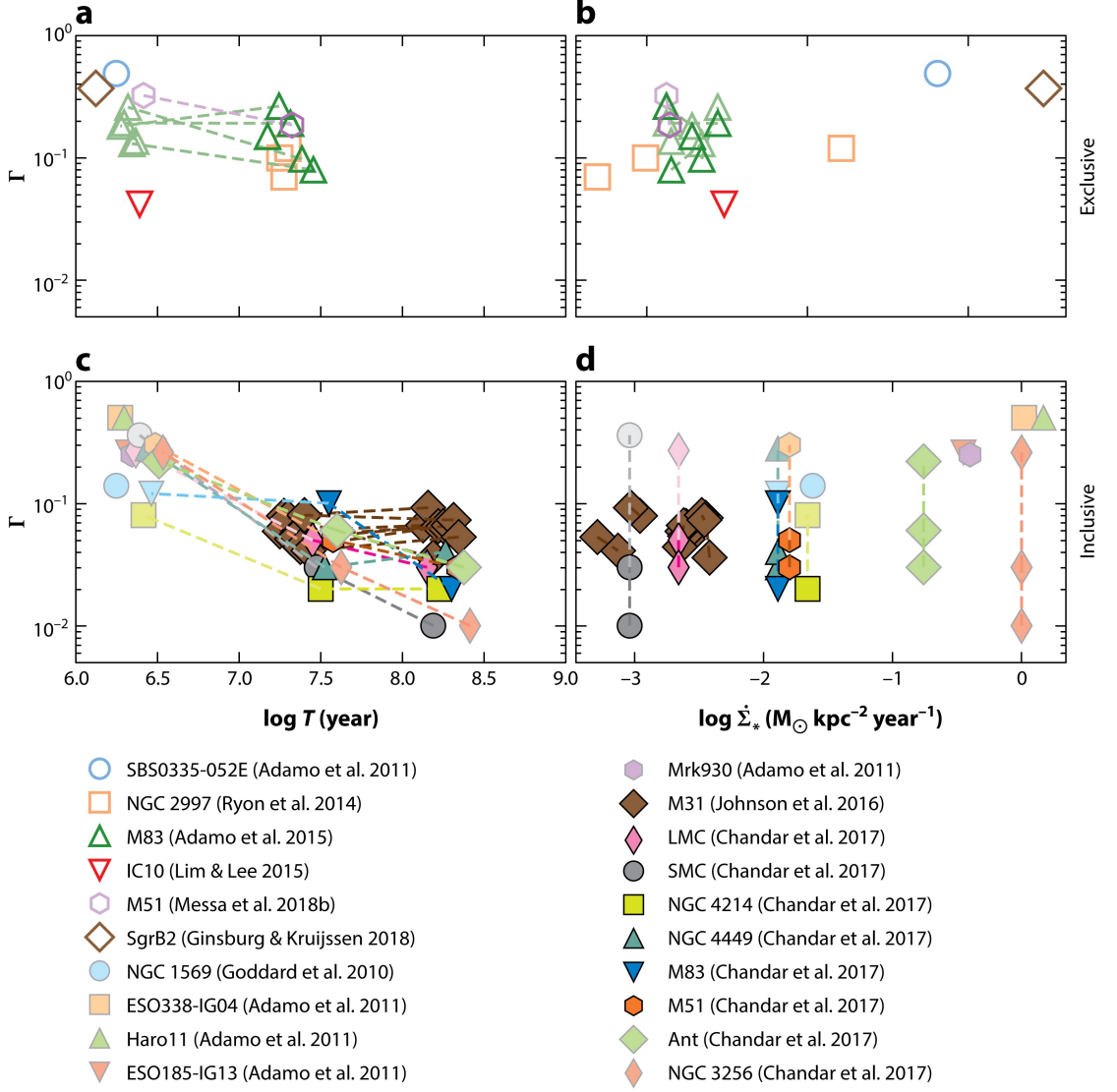
1.1.5 Cluster formation efficiency

The role of SSCs in star formation is also reflected in the fraction of stellar mass formed in bound clusters, which is defined by [Bastian \(2008\)](#) as the cluster formation efficiency (CFE or Γ):

$$\Gamma = \frac{CFR}{SFR} \quad (1.19)$$

where CFR and SFR are cluster and star formation rates respectively. The former quantity can be calculated as:

$$CFR = \frac{\Sigma_{\Delta\tau} M}{\Delta\tau} \quad (1.20)$$




 Krumholz MR, et al. 2019.
Annu. Rev. Astron. Astrophys. 57:227–303

Figure 1.7 – Observed values of the CFE Γ versus cluster ages T (left panels (a,c)) and the SFR per unit area Σ_{SFR} (right panels (b,d)). Upper panels (a,b) contain exclusive catalogs with clusters determined morphologically. Lower panels (c,d) contain inclusive catalogs without morphological constraints on cluster selection. Dashed lines trace measurements at multiple age ranges for the same galaxy. Faded points indicate likely uncertain measurements (see text) (Krumholz et al. 2019).

where $\Sigma_{\Delta\tau}M$ is the total stellar mass formed during an age range of $\Delta\tau$. Values of Γ measured at various $\Delta\tau$ vary widely (e.g., Adamo & Bastian 2018; Krumholz et al. 2019; Adamo et al. 2020, and references therein, see Fig. 1.7). Robust values of $\Gamma \approx 0.01$ – 0.1 are retrieved from star-forming galaxies with $\alpha_{\tau} \sim 0$ at $\tau \gtrsim 10$ Myr, agreeing with the *infant mortality* scenario.

At younger ages, unbound associations may not have dispersed, while bound clusters have not relaxed, thus estimations should be considered as upper or lower limits only (Kruijssen & Bastian 2016). Nevertheless, it is challenging to measure older populations in high-SFR galaxies due to their complicated star formation histories or magnitude limits at large distance (Chandar et al. 2017).

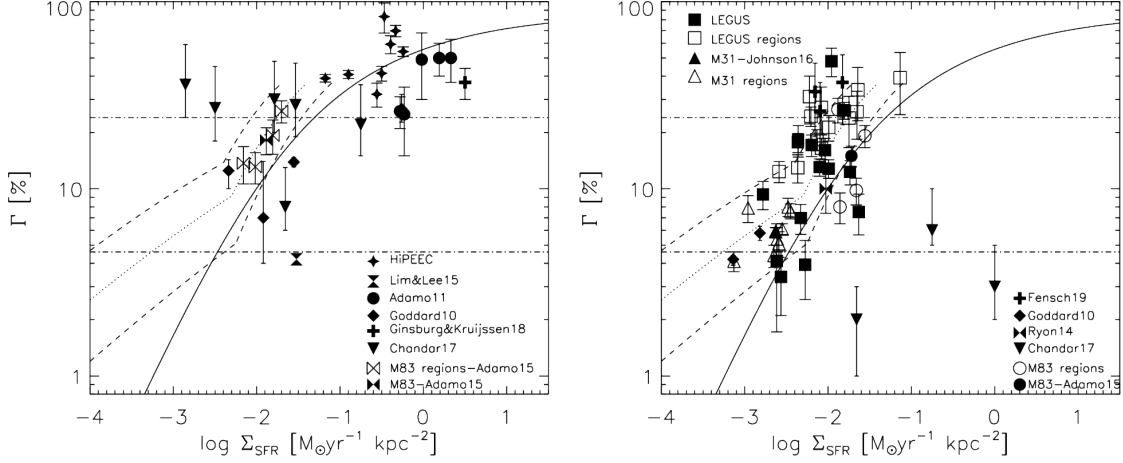


Figure 1.8 – Γ – Σ_{SFR} relations for $\tau \leq 10 \text{ Myr}$ (left) and $\tau > 10 \text{ Myr}$ (right). For comparison, the fiducial model by Kruijssen (2012) based on the Kennicutt-Schmidt law (Schmidt 1959; Kennicutt 1998) (solid line) and the Bigiel et al. (2008) Σ_{gas} – Σ_{SFR} conversion (dotted and dashed lines), as well as estimated constant Γ values the age range 1–10 and 10–100 Myr by Chandar et al. (2017) (horizontal dot-dashed lines) are plotted. Filled symbols indicate galaxy-wide measurements, while empty symbols denote sub-regions within the same galaxy (Adamo et al. 2020)

To verify the relation between the CFE (Γ) and the SFR per unit area Σ_{SFR} , Adamo et al. (2020) separate measurements based on their age ranges: either younger or older than 10 Myr and plot them in Fig. 1.8. Most of the measurements at $\tau \leq 10 \text{ Myr}$ do not impose morphological constraints on cluster selection, as opposed to the measurements at $\tau > 10 \text{ Myr}$ which are largely based on these constraints. Nonetheless, both age ranges show the purported Γ – Σ_{SFR} relation (Kruijssen 2012), as well as similar ranges of Γ within uncertainties. Several numerical simulations also confirm this relation (e.g., Li et al. 2018; Pfeffer et al. 2019). In summary, cluster formation is facilitated by high-SFR environments.

1.2 Luminous infrared galaxies

1.2.1 Overview

To better understand SSCs, it is essential to study the typical environments in which they are found in abundance. (ultra)luminous infrared galaxies ((U)LIRGs, hereafter LIRGs in general) are prominent targets since most of these objects are interacting systems and mergers exhibiting extreme starburst and active galactic nucleus (AGN) activities, along with intense IR emission from heated dust ($L_{\text{IR}} > 10^11 L_{\odot}$, Sanders & Mirabel 1996). A sample of LIRGs is illustrated in Fig. 1.9.

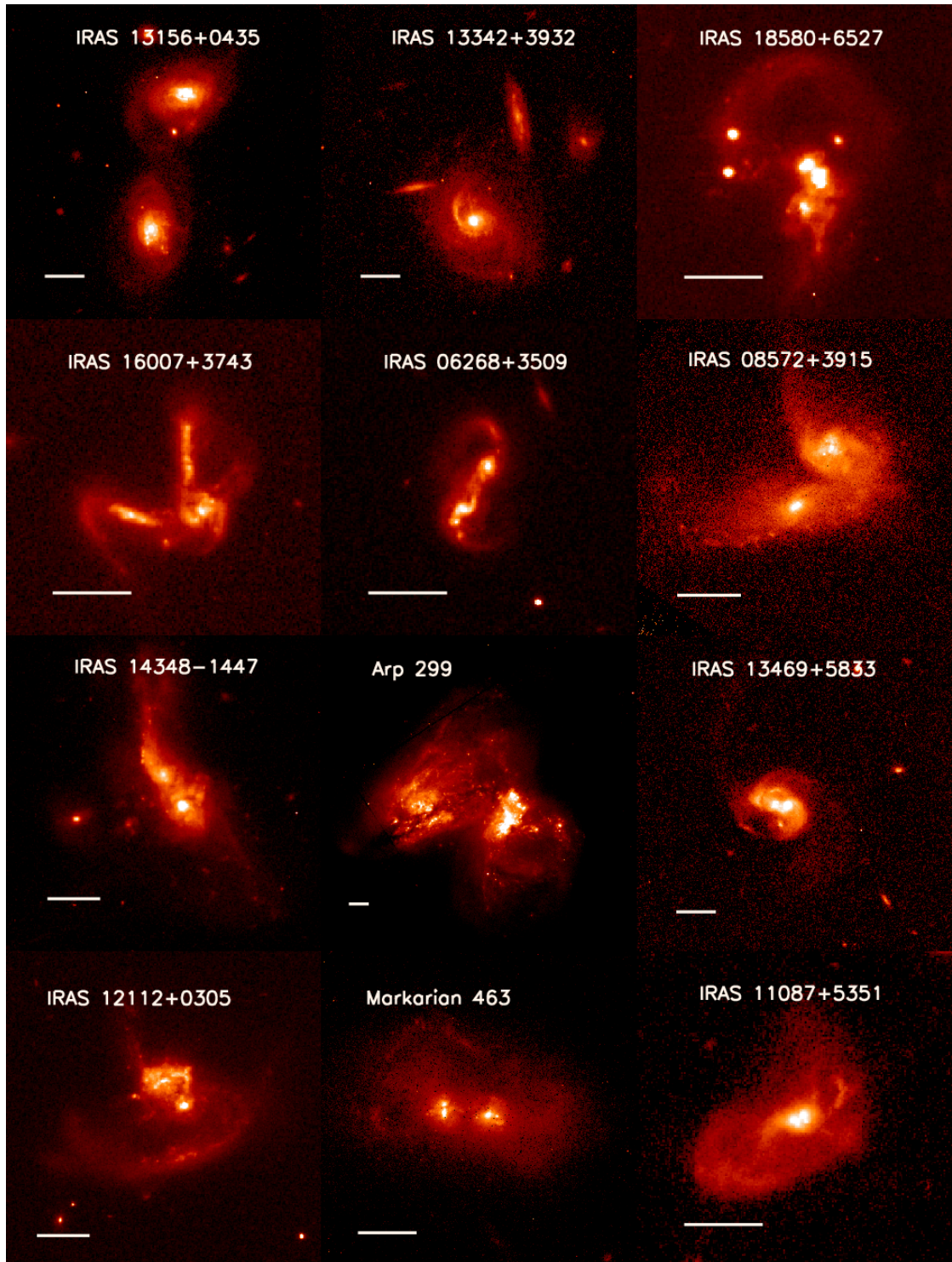


Figure 1.9 – Sample of LIRGs at various merging stages (García-Marín et al. 2009). Data are obtained with HST/WFPC2 (F814W filter). The scales correspond to 5 arcsec. Some prominent SSCs on the galaxy disks are visible.

Although in the local universe LIRGs are rare, at $z \sim 1-2$ they become much more prevalent and dominate in terms of IR luminosity and SFR densities (e.g., [Elbaz et al. 2002](#); [Le Floch et al. 2005](#); [Pérez-González et al. 2005](#); [Caputi et al. 2007](#); [Magnelli et al. 2009](#); [Béthermin et al. 2011](#)). Nevertheless, SSC populations at high redshift are almost inaccessible, except for some objects detected through gravitational lensing (e.g., [Vanzella et al. 2017](#)). Even for local LIRGs, distance remains a challenge, making individual SSCs unresolved. As a consequence, while many LIRG surveys exist, only few of them include analyses of their SSC populations. For example, [Linden et al. \(2017\)](#) study SSCs in a subsample of 27 individual LIRGs at the mean distance of 115 Mpc, among a total of 291 individual galaxies in the Great Observatories All-Sky LIRG Survey (GOALS; [Armus et al. 2009](#)). In the following sections, we consider some relevant features of LIRGs in the context of SSC surveys.

1.2.2 Morphology

Since the formation of SSCs is triggered by the interaction of galaxies, their merging stages and morphologies are of interest. Based on previous works on the GOALS sample (e.g., [Surace et al. 1998](#); [Haan et al. 2011](#); [Kim et al. 2013](#); [Stierwalt et al. 2013](#)), [Larson et al. \(2016\)](#) introduce a visual morphological classification scheme of LIRGs, accounting for velocity and spatial separation. The merging sequence is divided into the following stages (Fig. 1.10):

- Single galaxy (**s**): No interaction or merging is observed.
- Minor merger (**m**): Interacting pairs with mass ratios over 4:1.
- Major merger - stage 1 (**M1**): Closing in galaxy pairs with line of sight velocities $\Delta V < 250 \text{ km s}^{-1}$ and projected nuclear separations $n_{\text{sep}} < 75 \text{ kpc}$ and no visible tidal bridge or tail.
- Ambiguous (**amb**): Close galaxy pairs without velocity information to confirm their interaction.
- Major merger - stage 2 (**M2**): Disturbed pairs showing clear tidal features ([Toomre & Toomre 1972](#)) or other perturbations.
- Major merger - stage 3 (**M3**): Merging galaxies with separate nuclei, blending disks and tidal tails.
- Major merger - stage 4 (**M4**): Galaxies showing coalesced nuclei ($n_{\text{sep}} \lesssim 2 \text{ kpc}$) and tidal tails.
- Major merger - stage 5 (**M5**): Evolved merger remnants containing only one single nucleus, likely deviated from the center, without any prominent tidal tails. Diffuse shells or other fine structures may be present ([Schweizer & Seitzer 1992](#)).

In conjunction with the above scheme, there are extended categories for interacting triplets: TM1, TM2, TM3 corresponding to M1, M2 and M3, where the most recent interaction is adopted. Projection effects may still alter classifications but only to some limited extent. Alternatively, more sophisticated quantitative methods exist but they do not allow simple and robust classifications of LIRGs (e.g., [Psychogyios et al. 2016](#)).

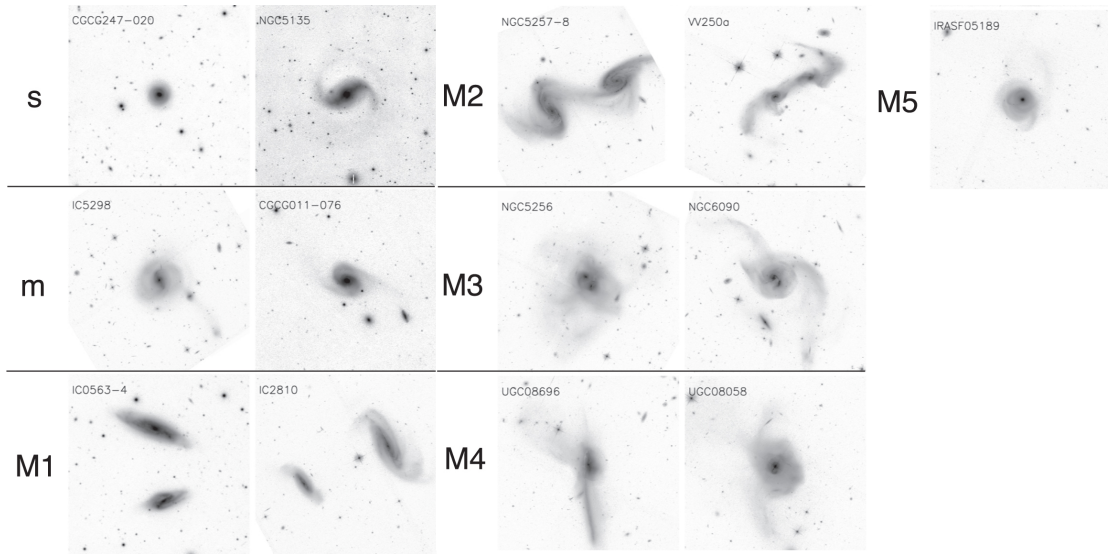


Figure 1.10 – Example of LIRG visual morphological classification based on [Larson et al. \(2016\)](#) scheme

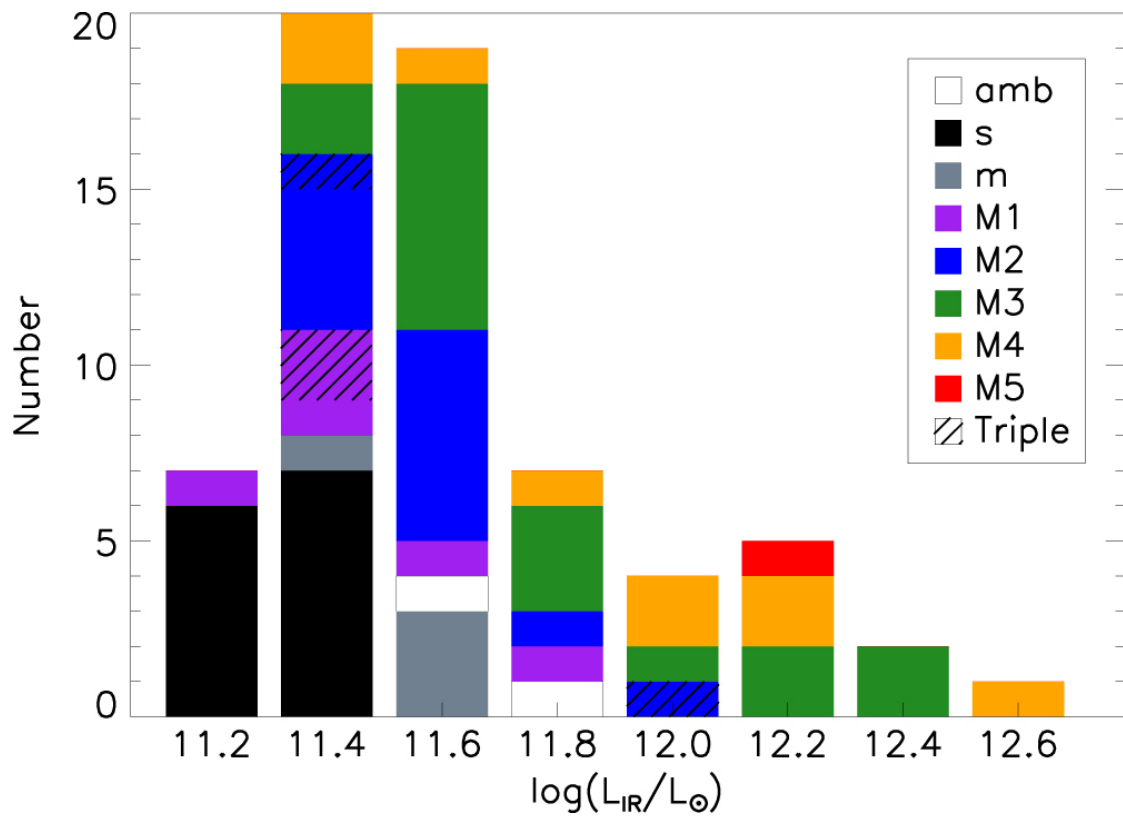


Figure 1.11 – Interaction stages of LIRGs over IR luminosities ([Larson et al. 2016](#))

Larson et al. (2016) applied this classification scheme to a complete sample from the GOALS survey. Consequently, the majority of LIRGs at $L_{\text{IR}} \leq 10^{11.5} L_{\odot}$ are normal galaxies and minor mergers (Fig. 1.11). Galaxies brighten to $L_{\text{IR}} > 10^{11.5} L_{\odot}$ when major merging starts, and reach $L_{\text{IR}} > 10^{12} L_{\odot}$ at final stages. The molecular gas fraction also increases during the merging until the stage M3, as atomic gas (HI) in the outer regions converge at the center and transforms into molecular gas (H_2). Afterwards, it is consumed or ionized by the starburst and AGN activities.

1.2.3 Extinction

Typically LIRGs are obscured by dust, resulting in substantial and non-uniform extinctions, especially the nucleus region may have elevated values up to $A_V > 10$ (e.g., Alonso-Herrero et al. 2006; García-Marín et al. 2009; Pereira-Santaella et al. 2010; Piqueras López et al. 2013, see Fig. 1.12). Therefore it is important to observe LIRGs in IR and longer wavelengths, as well as construct 2D extinction maps to better constrain their properties, including the SFRs and the SSC populations.

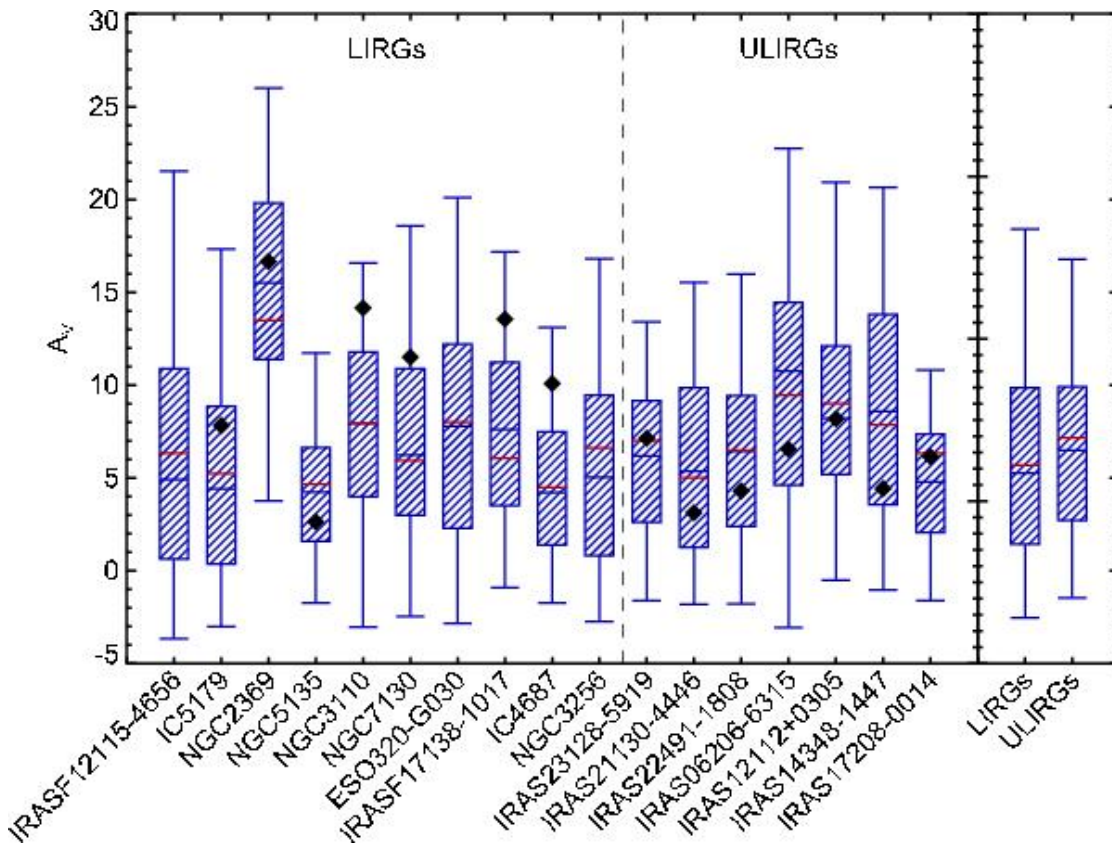


Figure 1.12 – Individual and combined distributions of spaxel A_V in a sample of LIRGs ($10^{12} L_{\odot} > L_{\text{IR}} > 10^{11} L_{\odot}$) and ULIRGs ($10^{13} L_{\odot} > L_{\text{IR}} > 10^{12} L_{\odot}$) with increasing L_{IR} (Piqueras López et al. 2013). Their interquartile ranges are covered by the corresponding boxes, with the 5th and 95th percentiles represented by the whiskers. The median and weighted mean values are marked by the horizontal blue and red lines respectively, while the nuclear extinctions are indicated by the black diamonds.

From a sample of LIRGs, [Calzetti et al. \(2000\)](#) derive the following extinction law for starburst galaxies:

$$k(\lambda) = \frac{A_\lambda}{E(B-V)} = \begin{cases} 2.659(-2.156 + 1.509/\lambda - 0.198/\lambda^2 + 0.011/\lambda^3) + R_V & \text{for } 0.12 \mu\text{m} \leq \lambda \leq 0.63 \mu\text{m} \\ 2.659(-1.857 + 1.040/\lambda) + R_V & \text{for } 0.63 \mu\text{m} \leq \lambda \leq 2.20 \mu\text{m} \end{cases}$$

where $R_V = A_V/E(B-V) = 4.05 \pm 0.80$.

1.2.4 Star formation rate

For LIRGs, SFR is an essential parameter characterizing their star formation process, including their CFEs (see Sect. 1.1.5). There are various methods to estimate SFR (e.g., [Kennicutt 1998](#); [Kennicutt & Evans 2012](#); [Brown et al. 2017](#), and references therein). Although spectral energy distribution (SED) fitting may be used if multiwavelength data are available (e.g., [Herrero-Illana et al. 2017](#)), in general SFRs are calibrated against spectral measurements in the form of:

$$\log \frac{\text{SFR}}{M_\odot \text{ yr}^{-1}} = a + b \log L_\lambda \quad (1.21)$$

where a and b are calibration constants and L_λ is the luminosity of interest, which may correspond to a single spectral range or combine multiple wavelengths. Given the dusty and luminous nature of LIRGs, IR and radio diagnostics are often adopted. For example, the global SFRs of LIRGs can be calculated as ([Kennicutt 1998](#)):

$$\frac{\text{SFR}}{M_\odot \text{ yr}^{-1}} = 4.5 \times 10^{-44} \frac{L_{\text{IR}}}{\text{erg s}^{-1}} \quad (1.22)$$

assuming a [Salpeter \(1955\)](#) IMF, a continuous star formation over the timescale of 10–100 Myr based on [Leitherer & Heckman \(1995\)](#) and total dust obscuration of young stars whose luminosity is fully transformed into IR radiation emitted by heated dust.

For resolved galaxies, SFR measurements are usually expressed in terms of surface density Σ_{SFR} . On a global scale, the relation between Σ_{SFR} and the gas surface density Σ_{gas} is described by the Kennicutt-Schmidt law ([Schmidt 1959](#); [Kennicutt 1998](#)):

$$\frac{\Sigma_{\text{SFR}}}{M_\odot \text{ yr}^{-1} \text{ kpc}^{-2}} = 2.5 \times 10^{-4} \left(\frac{\Sigma_{\text{gas}}}{M_\odot \text{ pc}^{-2}} \right)^{1.4} \quad (1.23)$$

On sub-kpc scales, Σ_{SFR} may vary across the galaxy disks. For example, Fig. 1.13 shows the Σ_{SFR} distributions of a LIRG sample from [Piqueras López et al. \(2016\)](#).

1.2.5 Starburst–active galactic nucleus connection

Along with star formation, AGNs are also an interesting feature in LIRGs. Various methods to detect and quantify their luminosity contributions have been established (see e.g., [Veilleux et al. 2009](#); [Alonso-Herrero et al. 2012](#); [Herrero-Illana et al. 2017](#), and references therein). Although AGN presence is common in LIRGs, their luminosity contributions are generally modest compared to starburst activities except for the most luminous sources (e.g., [Nardini et al. 2008, 2010](#); [Veilleux et al. 2009](#); [Petric et al. 2011](#); [Alonso-Herrero et al. 2012](#); [Herrero-Illana et al. 2017](#),

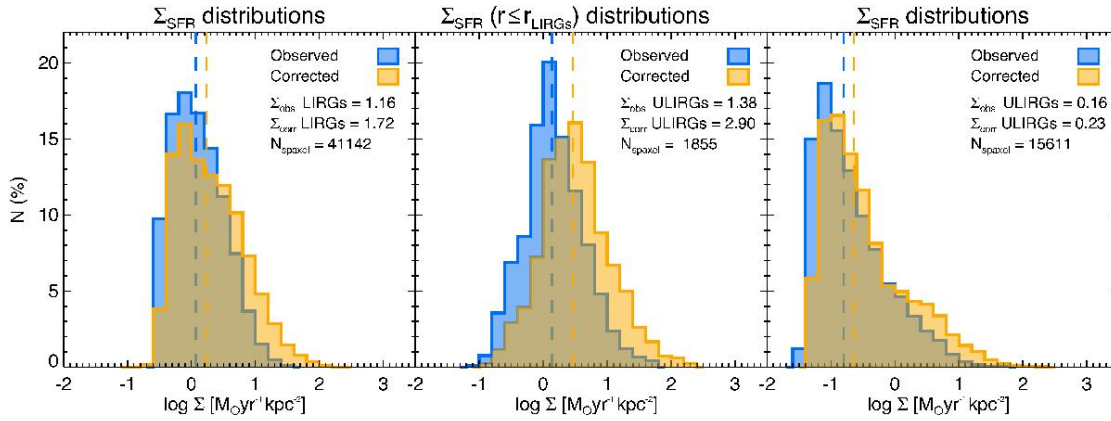


Figure 1.13 – Observed (blue) and extinction-corrected (orange) spaxel Σ_{SFR} distributions of the LIRGs (*left*), the same physical regions in ULIRGs (*center*), and the whole ULIRGs (*right*) in a sample of Piqueras López et al. (2016). The median Σ_{SFR} values (dashed vertical lines) are expressed in $M_{\odot} \text{ yr}^{-1} \text{ kpc}^{-2}$.

see Fig. 1.14). Nevertheless, AGNs may have some influence on the star formation activity. In particular, SFR seems to be correlated with AGN luminosity, but has lower values compared to galaxies without AGNs (e.g., Alonso-Herrero et al. 2013; Stemo et al. 2020). The starburst-AGN connection requires further studies, as for example the proposal by Armus et al. (2017) which utilizes the state-of-the-art James Webb Space Telescope.

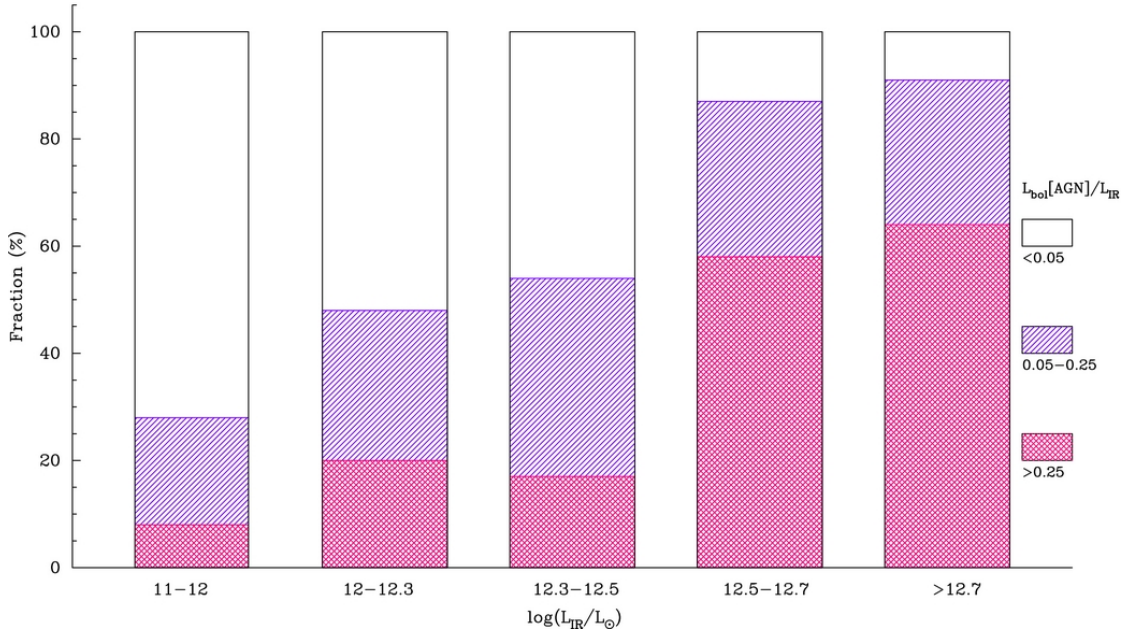


Figure 1.14 – AGN bolometric contributions to the IR luminosities for the samples of local LIRGs from Alonso-Herrero et al. (2012) and local ULIRGs from Nardini et al. (2010).

1.3 James Webb Space Telescope

1.3.1 Instrumentation

Characterizing SSC populations in LIRGs requires high resolution and sensitivity in the near and mid-IR, which would be met in the next decade by a game changer. The James Webb Space Telescope (JWST; [STSci 2016](#)–) is an international project between the National Aeronautics and Space Administration (NASA), the European Space Agency (ESA) and the Canadian Space Agency (CSA). With a segmented primary mirror of 6.5 m diameter and unprecedented sensitivity in the IR (0.6–28.8 μm), it will be the next generation observatory complementing and extending the legacy of HST. To avoid IR instrumental background interference, JWST must be kept at $\sim 40\text{K}$ by orbiting about the Lagrange point L2 1.5 million km from Earth, with a multi-layer shield facing towards the Sun and the Earth. Fig. 1.15 presents some major components of JWST:

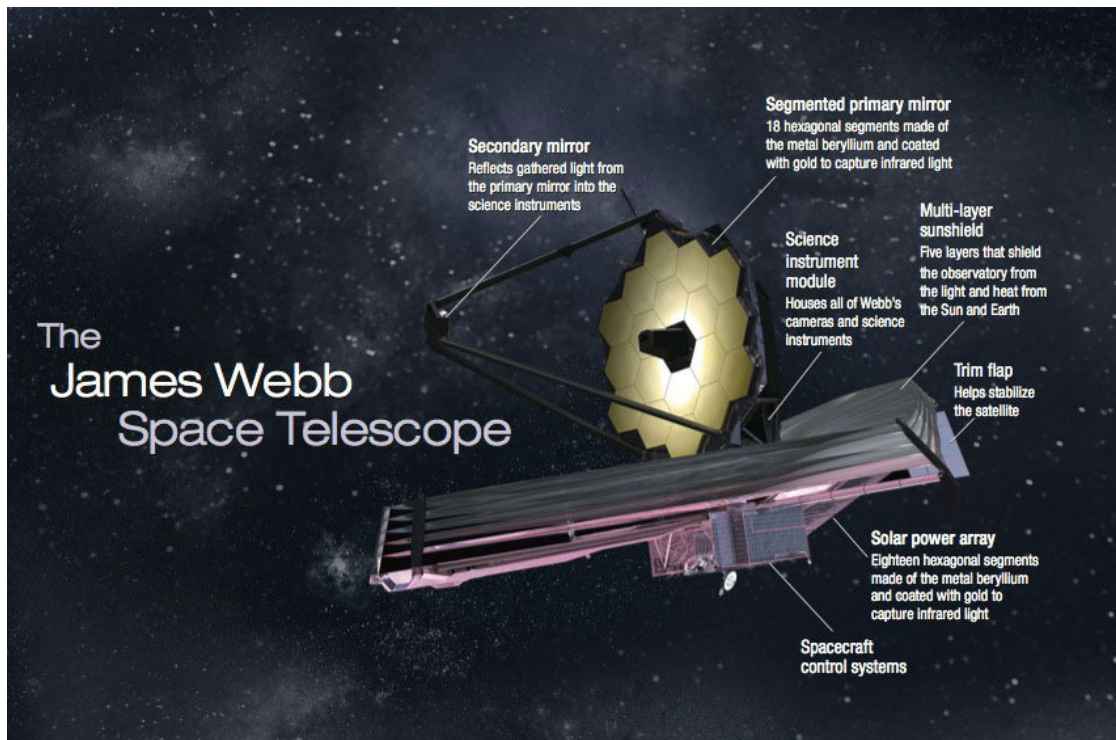


Figure 1.15 – James Webb Space Telescope and its major components. Image credit: NASA.

There are four science instruments onboard JWST with a variety of observing modes:

- Mid-Infrared Instrument (MIRI): Standard Imaging, Coronagraphic Imaging, Medium Resolution Spectroscopy, Low Resolution Spectroscopy and Time-Series Observations
- Near-Infrared Camera (NIRCam): Standard Imaging, Coronagraphic Imaging, Time-Series Observations and Wide Field Slitless Spectroscopy
- Near-Infrared Imager and Slitless Spectrograph (NIRISS): Wide Field Slitless Spectroscopy,

Single Object Slitless Spectroscopy, Aperture Masking Interferometry, and Standard Imaging

- Near-Infrared Spectrograph (NIRSpec): Multi-Object Spectroscopy, Integral Field Unit Spectroscopy, Fixed Slits Spectroscopy and Bright Object Time-Series Spectroscopy

The capabilities of their imaging and spectroscopic modes are summarized in Fig. 1.16 and Fig. 1.17 respectively. Specifically, the MIRI instrument will be presented in detailed in Chapter 4.

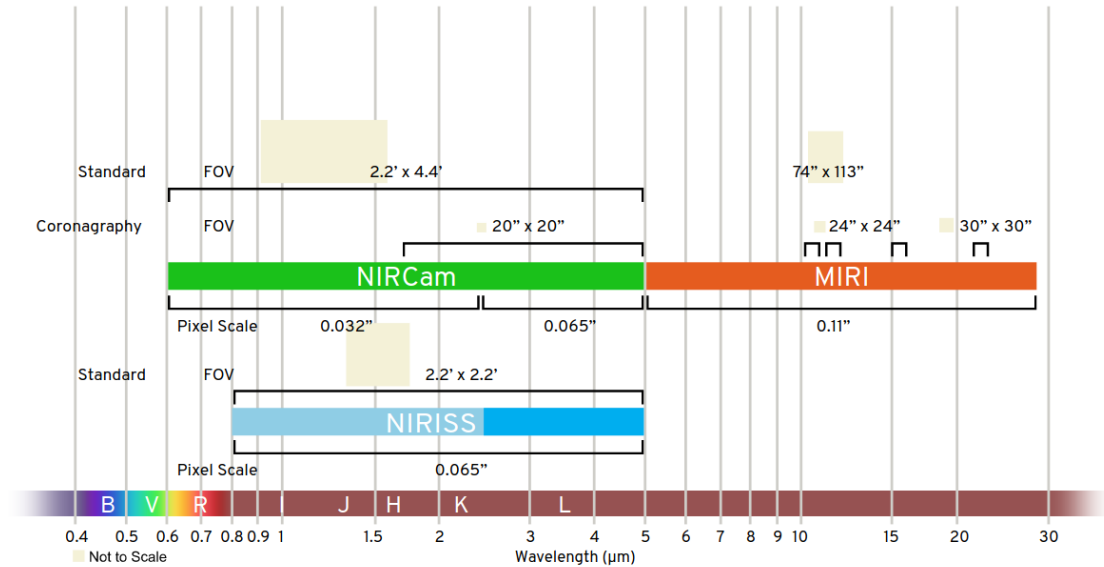


Figure 1.16 – Imaging modes of the JWST instruments. Image credit: STScI.

1.3.2 Science themes

With cutting-edge technologies in the IR regime, JWST aims to address four major science themes (Mather 2012):

- The End of the Dark Ages: First Light and Reionization

About 180 million years after the Big Bang, the universe expanded and cooled, allowing molecular hydrogen to be formed and collapse into the first stars. With masses of 30–300 M_{\odot} and luminosities of $\sim 10^6 L_{\odot}$, they quickly burnt out in a few Myr and ended up as core-collapse supernovae or black holes. The supernovae seeded the future stellar generations with heavier elements. On the other hand, the black holes subsequently grew into mini-quasars and supermassive black holes found at galaxy centers. JWST is expected to observe these supernovae and mini-quasars, which may be the origins of gamma ray and gravity wave bursts. Afterwards, the reionization of molecular hydrogen occurs. JWST aims to investigate the sources, epochs and mechanisms of reionization, which might involve the first galaxies.

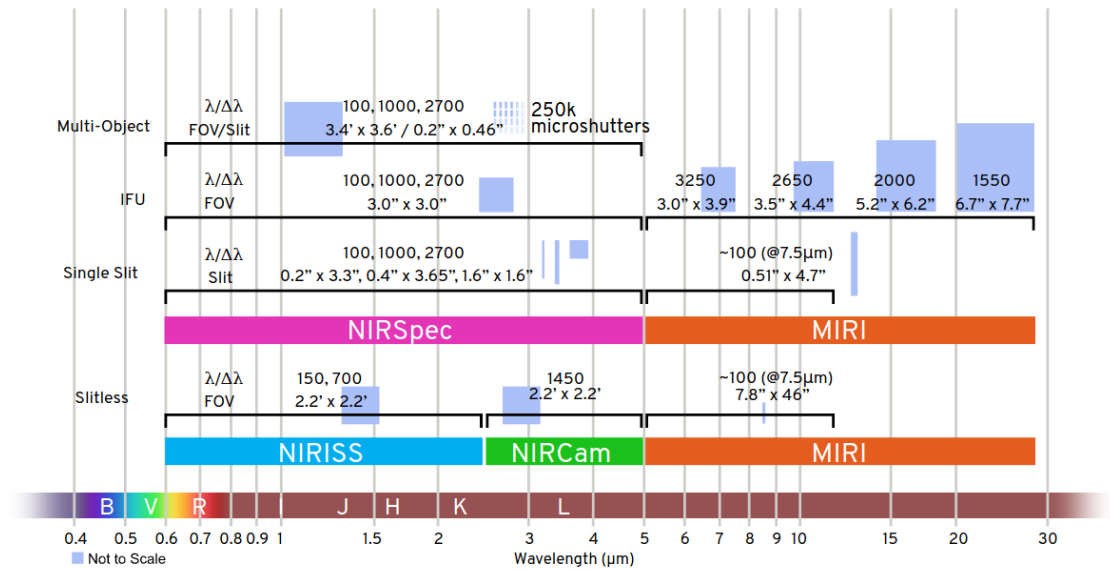


Figure 1.17 – Spectroscopic modes of the JWST instruments. Image credit: STScI.

— Assembly of Galaxies:

Being the fundamental constituents of the universe, galaxies are hierarchically assembled from smaller objects. However, there are still many open questions on their formation process, their morphological evolution, the formation and generation of heavy elements, the roles of ULIRGs, central black holes and AGNs in galaxy evolution, the origin of the global scaling relations... JWST observations of galaxy ancestors are required to unveil those mysteries.

— Birth of Stars and Protoplanetary Systems:

Although stars is a central subject of astronomy, our knowledge about them is still primitive. For example, the collapse of protostellar clouds, the formation of star and planetary systems, the interactions between stars and their environments, the low-mass stellar IMF are not known in details. With high resolution and sensitivity in the near- and mid-IR, JWST will help us observe these objects and address the unknowns.

— Planetary Systems and the Origins of Life:

The origins of life remain a mystery. From an astronomical perspective, the answer may lie in the physical and chemical histories of planetary systems, where the vital conditions for life can be found. They will be studied in details with JWST, from Solar System objects to exoplanets.

1.3.3 Science planning

The science mission of JWST is expected to be at least five years, with a 10-year goal lifetime. After many delays, the current target launch date for JWST is October 31, 2021. During its science operation, the Space Telescope Science Institute (STScI) releases Calls for Proposal to the astronomical community in annual cycles. During Cycle 1, JWST offers three categories of science program:

- Director’s Discretionary Early Release Science (DD ERS) program:

To prepare the science community for the maximum exploitation of JWST, STScI and the JWST Advisory Committee offered $\sim 450\text{h}$ to 13 teams whose programs are illustrative, profitable and open to the community. These programs have been selected in November 2017 and will be implemented during the first 5 months of JWST science operations.

- Guaranteed Time Observations (GTO) program:

This program is dedicated to key scientists involved in the JWST project. They will be allocated 16% of total observing time during the first three cycles. Cycle 1 GTO proposals were finalized in June 2019.

- General Observer (GO) program:

This program is accessible by the international observers. Up to 6000h available are offered in this cycle, including of 3500h for Small programs ($\leq 25\text{h}$), 1500h for Medium programs (25–75h), and 1000h for Large programs ($> 75\text{h}$). The most recent schedule for GO Cycle 1 is illustrated in Fig. 1.18.

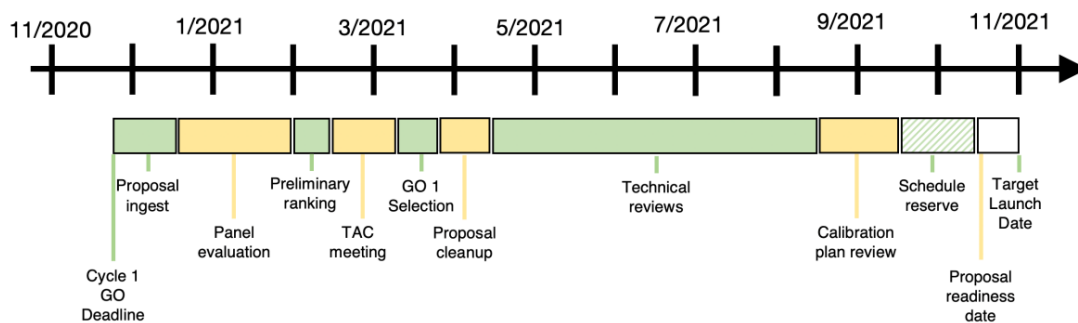


Figure 1.18 – JWST GO Cycle 1 schedule. TAC is the Telescope Allocation Committee. Image credit: STScI.

1.4 Thesis objectives

The goal of this thesis is to characterize the SSC populations in LIRGs using ground-based near-IR imaging at high angular resolution and to take advantage of the upcoming JWST, which will open a new era for mid-IR studies with its unprecedented angular resolution and sensitivity.

Chapter 2 presents our study of SSCs in a typical LIRG using ground-based adaptive optics JHK_s -band images. We extracted the SSC photometry, constructed color-color diagrams then compared results with a theoretical stellar evolutionary model to derive cluster properties. Finally we simulated SSC models at different stages of evolution using our radiative transfer code MontAGN, which is especially tuned to the mid-IR, and compared results to observations.

In Chapter 3, we describe our radiative transfer code Monte Carlo for Active Galactic Nuclei (MontAGN) and the design of SSC models in details. From the SSC catalogue extracted in Chapter 2, we selected three SSCs representing different magnitudes, then created corresponding model grids to fit cluster parameters. The best-fit models provided SSC spectra that would be used in the following chapters.

Based on the analyses in the previous chapters, in Chapter 4 we elaborated a JWST proposal to observe the SSCs in the same LIRG as in Chapter 2 using MIRI. At first we justified our need for new observations in the mid-IR with JWST. After studied the instrument in details, we selected the best configurations and showed the feasibility of the proposal. The complete submitted proposal is attached at the end of the chapter.

To support our proposal, based on the observations in Chapter 2 and SSC models from Chapter 3, in Chapter 5 we simulated MIRI data using MIRISim, a package provided by the JWST community. Then we reduced the simulated data using the JWST calibration pipeline. We showed that some predictions of MontAGN can be indeed verified with the planned observations.

Finally in Chapter 6, we provide conclusions from our work and present some prospectives for the future studies of SSCs, particularly in the era of the JWST.

Chapter 2

High angular resolution study of the super star cluster population in IRAS 17138 - 1017

In this chapter we present our near-IR study of the SSC population in IRAS 17138-1017, a typical LIRG merger, using the ground-based adaptive optics on the Gemini telescope. The observations were obtained as part of a proposal by a team including members of the division of Haute Résolution Angulaire en Astrophysique (HRAA, High Angular Resolution in Astrophysics) in the Laboratoire d'Études Spatiales et d'Instrumentation en Astrophysique (LESIA, Laboratory of Space Studies and Instrumentation in Astrophysics). They consist of several sets of near-IR images in the J , H and K_s filters, acquired during several nights of April 2014, using the Gemini South Adaptive Optics Imager (GSAOI) fed by the Gemini Multi-Conjugate Adaptive Optics System (GeMS) on the Gemini South telescope. Since the seeing conditions were changing from night to night, a first selection of the best datasets was necessary.

After a classical data processing of near-IR images, I have been asked to analyze the dataset for detection, extraction and photometry of the sources belonging to the three bands. Concerning the photometric method, I compared various algorithms either available on the web or developed by the team, performing tests on artificial sources introduced on the actual images. Because of the strong structured background due to the galaxy itself, it took a rather long time to reach eventually a satisfactory result. The second step was to separate background sources (stars and distant galaxies) from the actual SSCs. The main result of these first steps is the detection with a fair degree of confidence of 54 SSCs of m_{K_s} between 16 mag and 21 mag with an uncertainty of 0.05 mag.

By de-reddening the measurements with respect to a theoretical evolutionary track predicted for a young stellar cluster, I built a color-color diagram and a color-magnitude diagram, which revealed that most of the sources are very much extinct. The de-reddened colors point unambiguously to two distinct and very recent starburst episodes at 2.8 and 4.5 Myr which are among the youngest starbursts ever revealed by similar studies. The derived luminosity and mass functions present the expected power-law behavior, although with shallower slopes than generally observed in LIRGs.

Finally, using the radiative transfer code MontAGN, I tried to explain the few very red SSCs that could not be de-reddened safely, hypothesizing that dust thermal emission and scattered light may become significant in K band. However those two effects are shown to be negligible.

This chapter essentially reproduces the paper published in *Astronomy and Astrophysics*, completed with a short study comparing the STARFINDER photometry with an analytical point spread function (PSF) fitting procedure using Moffat functions.

2.1 Published paper

High angular resolution study of the super star cluster population in IRAS 17138–1017[★]

N. T. Lam¹, D. Gratadour¹, D. Rouan¹, and L. Grosset^{1,2}

¹ LESIA, Observatoire de Paris, Université PSL, CNRS, Sorbonne Université, Univ. Paris Diderot, Sorbonne Paris Cité, 5 place Jules Janssen, 92195 Meudon, France
e-mail: lam.nguyen@obspm.fr

² SOFIA Science Center, USRA, NASA Ames Research Center, Moffett Field, CA 94035, USA

Received 17 February 2020 / Accepted 22 April 2020

ABSTRACT

Aims. Currently, the global characteristics and evolution of super star clusters (SSCs) are not well understood, due to the large distances to their host galaxies. We aim to study the population of SSCs in IRAS 17138-1017, a luminous infrared galaxy (LIRG), in terms of age, extinction, mass, and luminosity distribution.

Methods. We analyzed imaging data in the near-infrared from the GeMS/GSAOI instrument on the Gemini telescope and generated simulations with the radiative transfer code MontAGN. The extraction of SSCs from the images and their photometry in J , H , and K_s allowed us to derive color-color and color-magnitude diagrams. Comparison with a theoretical stellar evolutionary track gives a first hint into the extinction towards each SSC, as well as their ages, despite some degeneracy between those two quantities. Spectra given by our radiative transfer code MontAGN, which includes dust emission, also provide insightful predictions and comparisons.

Results. We detect with a fair degree of confidence 54 SSCs of m_K , between 16 mag and 21 mag with a median instrumental uncertainty of 0.05 mag. When plotted on a color–color diagram and a color–magnitude diagram, it appears that most of the sources are very much extinct with respect to an intrinsic theoretical evolutionary track. Once de-reddened, the colors point unambiguously to two distinct and very recent starburst episodes at 2.8 and 4.5 Myr. While the SSCs in the 4.5 Myr starburst are distributed along the spiral arms, the 2.8 Myr SSCs are concentrated in the central region. The luminosity and mass functions present a classical power-law behavior, although with shallower slopes than generally observed in LIRGs. Comparison with radiative transfer simulations shows that, the dust thermal emission and scattered light are negligible and could not explain the few very red SSCs that could not be de-reddened safely.

Key words. galaxies: individual: IRAS 17138-1017 – galaxies: starburst – galaxies: star clusters: general – radiative transfer – infrared: galaxies – instrumentation: high angular resolution

1. Introduction

The interaction of galaxies, even if it does not end in merging, generally triggers extreme star formation. This is evidenced prominently in (ultra)luminous infrared galaxies ((U)LIRGs), where the star formation rate (SFR) can exceed 1000 times the one of a quiescent galaxy like the Milky Way. These objects radiate most of their energy in the infrared (IR; $\log(L_{\text{IR}}/L_{\odot}) > 11$), as the dust of the dense star-forming clouds is heated by the ultraviolet (UV) light. Its major sources are luminous massive stars dominating the starburst activity (Sanders & Mirabel 1996). Found in abundance in (U)LIRGs are very young (< 100 Myr), massive ($\geq 10^4 M_{\odot}$), and dense ($\geq 10^3 M_{\odot} \text{pc}^{-1}$ at core) stellar clusters called super star clusters (SSCs). They play a fundamental role in star formation history throughout the universe, yet their global characteristics and evolution are not well constrained due to a limited number of nearby samples. Notably, their connection with the globular clusters, which are thought to be their remnants, has not been established in detail (Portegies Zwart et al. 2010). Although extensive surveys of LIRGs do exist (e.g., the Great Observatories All-sky LIRG

Survey (GOALS); Armus et al. 2009), studying their SSC populations remains challenging because of the large distances. For instance, the GOALS sample in Haan et al. (2011) has a median distance of ~ 140 Mpc. To resolve, or at least separate SSC complexes in the near IR with ground-based telescopes, adaptive optics (AO) is usually required. The goal of this paper is precisely to exploit AO-assisted near-IR images of the LIRG IRAS 17138-1017, in order to study its SSC population in terms of luminosity function, age distribution, spatial distribution, extinction, and dust content with the help of a radiative transfer code, as well as theoretical evolutionary tracks. The question of the possible effect of hot dust emission in the K band and the way it can affect the location of SSCs on the color–color diagram (C–CD) is examined in particular.

Our target IRAS 17138-1017 is a late-stage merger (Stierwalt et al. 2014), deeply extincted LIRG (Depoy et al. 1988), with $\log(L_{\text{IR}}/L_{\odot}) = 11.42$ at a luminosity distance of 75.9 Mpc (Sanders et al. 2003). Although optical spectroscopy (Yuan et al. 2010) and spectral energy distribution (SED) fitting (Herrero-Illana et al. 2017) suggest some active galactic nucleus (AGN) activities, mid-IR tracers (Herrero-Illana et al. 2017) and X-ray observations (Ricci et al. 2017; Torres-Albà et al. 2018) confirm the domination of starburst in IRAS 17138-1017, as originally proposed by Depoy et al. (1988) based

[★] Full Table 1 is only available at the CDS via anonymous ftp to cdsarc.u-strasbg.fr (130.79.128.5) or via <http://cdsarc.u-strasbg.fr/viz-bin/cat/J/A+A/639/A28>

on multiwavelength observations. [Herrero-Illana et al. \(2017\)](#) also suggested the existence of a 23.0 Myr starburst, along with a star formation rate (SFR) of $58.8 M_{\odot} \text{ yr}^{-1}$, consistent with other indicators. Several highly extinct supernovae have been detected in IRAS 17138-1017 (e.g. [Kankare et al. 2008](#); [Kool et al. 2018](#)), as expected for a core-collapse supernova (CCSN) rate of 0.75 SN yr^{-1} ([Herrero-Illana et al. 2017](#)). The SSC population in IRAS 17138-1017 has been characterized in *B* and *I* band by [Miralles-Caballero et al. \(2011\)](#), in *K_s* band by [Randriamanakoto et al. \(2013a,b\)](#), and in *BIK_s* bands all together by [Randriamanakoto \(2015\)](#) as part of their survey of local LIRGs. In this paper, we present an in-depth study of the SSC population in IRAS 17138-1017 with AO images in *J*, *H* and *K_s* bands, using multiconjugate adaptive optics that allow wide field imaging.

2. Observations and data reduction

We observed IRAS 17138-1017 in *J*, *H*, and *K_s* bands on 15 April 2014 (PID: GS-2014A-Q-21; PI: Olivier Lai), using GSAOI, the Gemini South Adaptive Optics Imager ([McGregor et al. 2004](#); [Carrasco et al. 2012](#)) fed by GeMS, the Gemini Multi-Conjugate Adaptive Optics System ([Rigaut et al. 2014](#); [Neichel et al. 2014](#)). The GSAOI detector consists of 2×2 mosaic Rockwell HAWAII-2RG 2048×2048 arrays, covering a $85'' \times 85''$ field of view with a pixel scale of $0.02''$. In total, 20, 12, and 8 frames of 120s were obtained in *J*, *H*, and *K_s* bands, respectively, following a 2×2 dithering pattern with $15'' \times 20''$ offsets. The observations used five sodium laser guide stars (LGSs) to correct for the atmospheric distortion and three natural guide stars (NGSSs) to compensate for the tip-tilt and plate-scale modes. A temporary misalignment in the Laser Guide Star Wave-Front Sensor (LGSWFS) from November 2013 to June 2014 causing point-spread function (PSF) distortions was reported (e.g. [Monty et al. 2018](#)). However, since a software patch was introduced in February 2014, our data only suffers from limited degradation.

Firstly, nonlinear correction, flat division, and sky subtraction were performed on the raw data with the standard IRAF/PYRAF package for Gemini's GSAOI ([Tody et al. 1986, 1993](#)). To correct for the distortion and subsequently align and stack the images, we used DISCO-STU¹, a standalone utility provided by Gemini. The static distortion was calculated from a lookup table taking the telescope pointing and instrument position angle into account, while the variable distortion was determined by matching sources between images. After stacking, bad pixels were rejected, and pixels received inverse-variance-weighted average values. Finally, we resampled and rescaled the *J* and *H* band images to match the *K_s* band image using the IRAF tasks GEOMAP and GEOTRAN. The world coordinate system (WCS) was calibrated with the IRAF task CCMAP. Using field stars from the 2MASS catalogue ([Skrutskie et al. 2006](#)), we obtain an average astrometric error of $0.2''$. The final trimmed images in *J*, *H* and *K_s* are displayed in Fig. 1.

3. Construction of the super star cluster catalog

3.1. Source extraction

We identified cluster candidates using STARFINDER ([Diolaiti et al. 2000](#)), a code developed for the analysis of

¹ http://www.gemini.edu/sciops/data-and-results/processing-software#disco_stu

crowded fields in AO images. An empirical PSF template was first constructed from several bright, non-saturated stars in the subfield, then decontaminated by a preliminary detection at 5σ level. Post-processing including circular masking, principal component extraction, halo smoothing and normalisation were applied. Finally, the sources were iteratively extracted twice at 3σ level. The correlation thresholds were set at 0.7 for *J* and *K_s* bands, and 0.8 for *H* band. These parameters were tuned to recover the faintest objects while limiting spurious detections. After cross-matching all three bands, we detect 109 objects in total with $15 \text{ mag} \leq m_{K_s} < 22 \text{ mag}$. Most of them exist in the central region of the galaxy. However, several sources in the outer parts may still be true SSCs belonging to some tidal tails. Section 3.3 details how we proceed to discriminate between actual SSCs and possible foreground field stars or background galaxies to obtain a final sample that would be populated by SSCs with a fair degree of confidence.

3.2. Point-spread function photometry

For high background variation and crowding, aperture photometry of extragalactic clusters is prone to contamination from neighboring sources and nebular emission ([Bastian et al. 2014](#)), while PSF photometry performs more robustly, as already demonstrated with GeMS/GSAOI by [Turri et al. \(2017\)](#). Thus, we used the photometric measurements from STARFINDER provided together with the extracted sources. The instrumental photometric errors were calculated from the variance associated with the science data, with median values in *J*, *H*, and *K_s* of 0.05 mag, 0.03 mag, and 0.04 mag, respectively. [Chavez et al. \(2019\)](#) estimate photometric zero points for Gemini's GeMS/GSAOI at various epochs of observation, including the one when the present images were recorded. However, those zero points were derived from standard star observations under natural seeing conditions, and they give colors that are clearly strongly biased when applied to our dataset. We thus preferred to establish zero points directly from multiple non-saturated 2MASS stars within the original fields instead, using the 2MASS calibration ([Skrutskie et al. 2006](#)). The corresponding errors for *J*, *H*, and *K_s* band zero points are 0.04 mag, 0.09 mag, and 0.11 mag. Finally, we corrected the foreground Galactic extinction using the [Fitzpatrick \(1999\)](#) reddening law and [Schlafly & Finkbeiner \(2011\)](#) measurements from the NASA/IPAC Extragalactic Database (NED).

3.3. Cluster selection

To evaluate the potential contamination from foreground stars and background galaxies, we analyzed a nearby control field of the same area in which 42 objects are detected. This is not consistent with the theoretical expectation, since in a field of view of $32'' \times 32''$ at the same galactic coordinates of IRAS 17138-1017 and in the apparent *K*-band magnitude range of $15 \text{ mag} \leq m_K < 22 \text{ mag}$, the Besançon model ([Robin et al. 2003](#)) expects negligible Milky Way star count (< 1), while the GALAXYCOUNTER program ([Ellis & Bland-Hawthorn 2007](#)) estimates 12 ± 4 galaxies only, assuming completeness of detection. Now, we cannot exclude a local density that is actually higher than predicted, especially when GALAXYCOUNTER is based on galaxy surveys without AO correction, and thus are less sensitive to low surface brightness. Moreover, [Ellis & Bland-Hawthorn \(2007\)](#) also advise using their models with caution for star-counting observations with unknown numbers of galaxies. In fact, the *Hubble* Source Catalog version 2 ([Whitmore et al. 2016](#)) contains all of these objects and even some additional sources in this field.

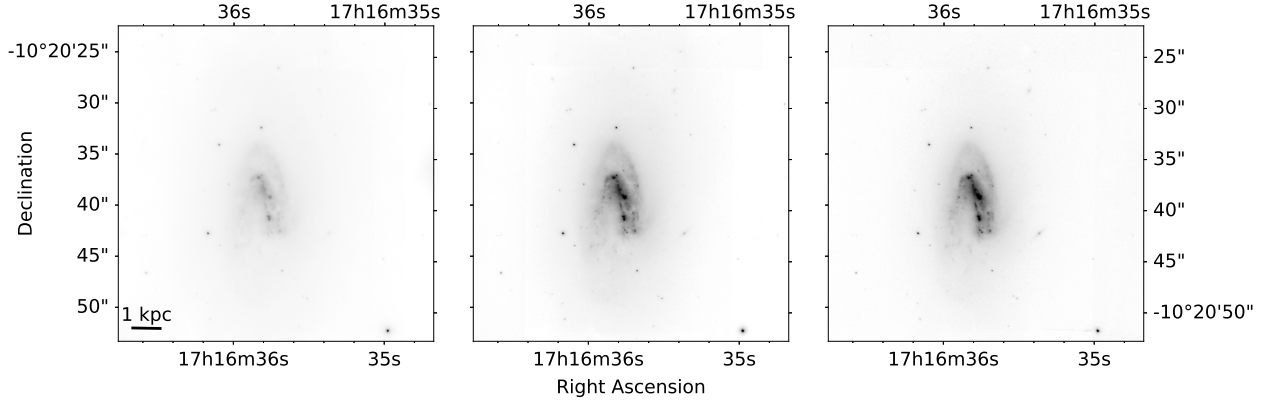


Fig. 1. GeMS/GSAOI images of IRAS 17138-1017 in J (left), H (middle), and K_s (right) plotted in square root scale. The field of view is $32'' \times 32''$ and the horizontal bar represents 1 kpc at the estimated distance of IRAS 17138-1017.

Nevertheless, we visually inspected and removed 42 sources outside the galaxy at a median distance of $10.7''$ corresponding to ~ 3.9 kpc to minimize contamination, and we also excluded the nucleus (identified unambiguously on the SINFONI velocity map of Piqueras López et al. 2012), leaving us with 66 SSC candidates. The consistency of the catalog is later confirmed in the $(H - K_s)$ versus $(J - H)$ C-CD (Fig. 2) through comparison with the control field, which reveals clearly distinct locations of both samples. The objects in the control field are well grouped in the area expected for field galaxies, as illustrated by the red stars, which corresponds to the average and standard deviation of near-IR colors of the sample of 100 galaxies from the 2MASS survey, studied by Jarrett et al. (2003). About the same area of the $(J - H)$ versus $(H - K)$ diagram is found in Fig. 5 of Foster et al. (2008). However, we notice some variations in the colors of these objects in other nearby control fields, which may be related to the existence of a local galaxy cluster, as mentioned above, and is beyond the scope of our study. Table 1 lists the final sample of detected SSCs with their coordinates, their derived extinctions, ages, and masses as described in the next section, and finally the J , H , and K_s magnitudes with their instrumental uncertainties. For comparison, Randriamanakoto et al. (2013b) detect 60 SSCs in K_s band with photometric errors $\sigma_m \leq 0.25$ and a 50% completeness limit of $m_K = 20.0$, while Randriamanakoto (2015) detects 104 SSCs in B , I and K_s bands with photometric errors $\sigma_m \leq 0.35$ in each filter.

4. Analyses and results

4.1. Color and magnitude distributions

The $(H - K_s)$ versus $(J - H)$ C-CD of selected clusters is presented in Fig. 2. For comparison, we also plot an evolutionary track calculated using Starburst99 (SB99, Leitherer et al. (1999, 2014)) with the following setup: a simple stellar population (SSP) of $10^6 M_\odot$ with a Kroupa et al. (2008) initial mass function (IMF) ranging from $0.1 M_\odot$ to $100 M_\odot$ and a solar metallicity ($Z = 0.014$). We assume the Calzetti et al. (2000) extinction law for starburst galaxies with $R_V = 4.05$ and draw on the C-CD the corresponding reddening vector. With respect to the sources in the control field, the sample occupies a well-separated area in the upper-right region of the diagram, and by comparison with the evolutionary track, we can safely assume that most of the sources are highly extinct. However, some of them (the ones with rather large $(H - K_s)$ colors) cannot be directly de-reddened to match the evolutionary model, since the

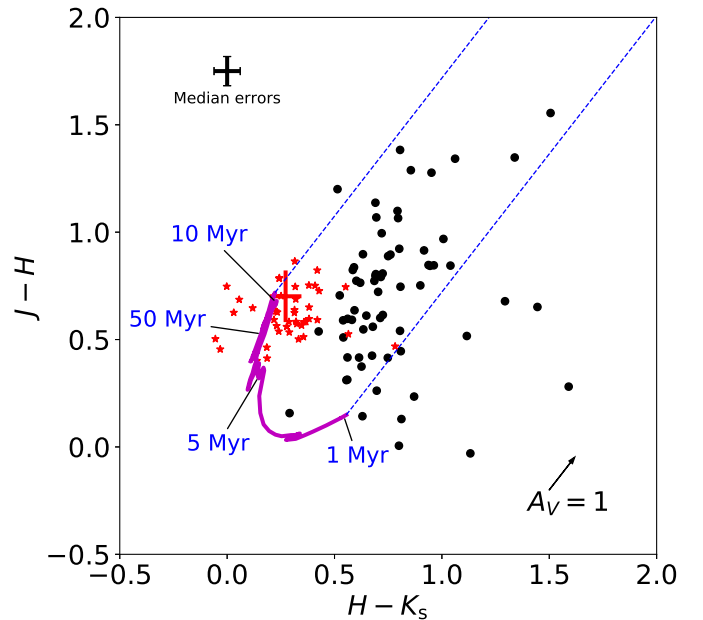


Fig. 2. Color-color diagram $(J - H)$ versus $(H - K_s)$ for the selected sample of SSCs (black dots). The theoretical stellar evolution track given by SB99 is shown for solar metallicity as the solid magenta line. The reddening vector corresponding to $A_V = 1$ is shown. The red stars are the sources detected in the control field, and the cross corresponds to the average color indices of the sample of 100 galaxies from the 2MASS survey, studied by Jarrett et al. (2003), with the length of the arms being equal to the standard deviations of those indices. The black cross represents the median errors of the cluster colors.

line parallel to the reddening vector does not cross the theoretical track. Although we think that a large fraction of those peculiar sources do not correspond to an erroneous photometry, but to an additional reddening different from the one due to dust extinction, as discussed in Sect. 5, we consider them as outliers in the de-reddening process that we use. In any case, it appears that for the vast majority of the SSCs we detected, the age is clearly below 5 Myr, as discussed in more detail below.

We also calculated the reddening-independent color index $Q = (H - K_s) - E(H - K_s)/E(J - H) \times (J - H)$, which does not depend on the extinction A_V , for both the actual data and the theoretical evolutionary track. As demonstrated by Santos et al. (2013), this type of color index is a powerful tool for age diagnostics of young star clusters. A color-magnitude diagram

Table 1. Catalog of SSC candidates in IRAS 17138-1017.

Source	RA	Dec	m_J (mag)	m_H (mag)	m_{K_s} (mag)	A_V (mag)	$\log(\tau/\text{yr})$	$\log(M/M_\odot)$
1	17h16m35.4845s	-10°20'38.2563"	17.87 ± 0.04	17.07 ± 0.02	16.38 ± 0.02	5.35 ^{+0.10} _{-0.33}	6.62 ^{+0.02}	7.26 ^{+0.01} _{-0.16}
2	17h16m35.5043s	-10°20'38.3885"	18.48 ± 0.04	17.19 ± 0.02	16.34 ± 0.02	7.35 ^{+0.35} _{-0.63}	6.81 ^{+0.02} _{-0.19}	7.02 ^{+0.14} _{-0.18}
3	17h16m35.7577s	-10°20'39.3936"	18.22 ± 0.04	17.62 ± 0.03	16.90 ± 0.03	4.40 ^{+0.20} _{-0.62}	6.46 ^{+0.22}	6.99 ^{+0.22} _{-0.08}
4	17h16m35.4999s	-10°20'38.2209"	18.47 ± 0.04	18.05 ± 0.03	17.37 ± 0.03	2.75 ^{+0.65} _{-0.53}	6.42 ^{+0.04} _{-0.04}	6.73 ^{+0.07} _{-0.06}
5	17h16m35.7750s	-10°20'39.0856"	18.96 ± 0.04	18.08 ± 0.02	17.33 ± 0.02	5.80 ^{+0.33} _{-0.10}	6.63 ^{-0.02}	6.82 ^{+0.16} _{-0.01}

Notes. The full catalog is available at the CDS.

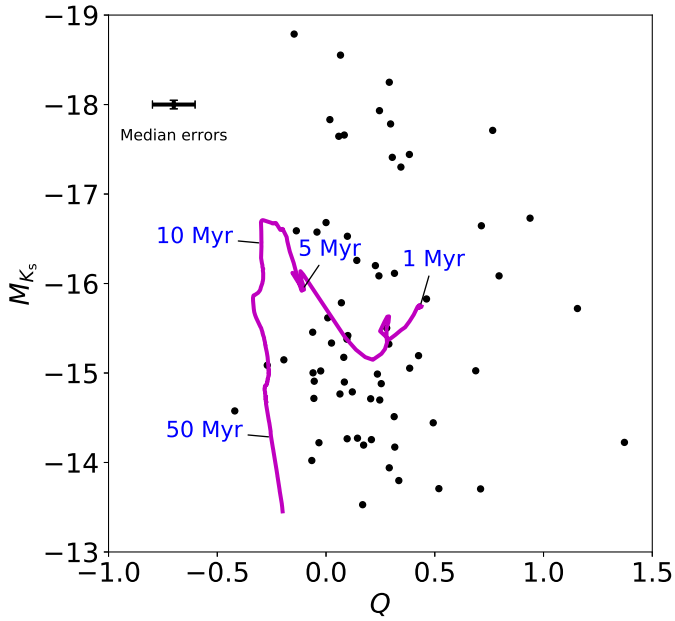


Fig. 3. Color–magnitude Q versus K_s diagram using the absolute K_s magnitude and the Q index, which in principle is not affected by the extinction. The same theoretical stellar evolution track as in Fig. 2 is shown. The black cross represents the median errors of the cluster colors and magnitudes.

(C–MD) using this index and the absolute de-reddened K_s -band magnitude is shown in Fig. 3 with the same evolutionary track and extinction vector as in the C–CD. This confirms that most of the clusters are very young. Age-reddening degeneracy occurs on both diagrams on the most evolved part of the evolutionary track, because on this portion (i) the track is practically parallel to the reddening vector, and (ii) there are several foldings of the track, so that the lines parallel to the reddening vector may cross the track on several locations, however the impact is weak, because as we already stated, the majority of SSCs are young. We note that in the upper part of the diagram (close to the SB99 track shifted by ~ -2 mag), corresponding to the brightest SSCs, the distribution of points tends to be more uniform along the Q axis, as if the brightest SSCs were more evenly distributed along an age sequence than the fainter ones. This could translate into the fact that the most massive SSCs are less subjected to disruption (see discussion in the next section).

4.2. Age, mass, and extinction calculation

To derive the age (τ), mass (M), and extinction (A_V) of each cluster, we looked for the age and extinction that minimize the

quantity (cf., [Parmentier et al. 2003](#)):

$$\chi^2(\tau, A_V) = \sum_{C=J-H,H-K_s} \frac{(C_{\text{obs}} - C_{\text{SB99}})^2}{\sigma_C^2}, \quad (1)$$

where C_{obs} and C_{SB99} are the de-reddened colors from the observations and from the SB99 model, respectively, and σ_C are the estimated errors of the observed colors, using age steps of 0.1 Myr and A_V steps of 0.05 mag. Cluster masses were estimated from extinction-corrected J , H , and K_s -band luminosities, assuming mass-to-light ratios from the model, then the median value among the three bands was adopted. We calculated the effects of each band’s photometric errors on the estimated parameters separately, then quadratically summed the resulting increments or decrements to determine the corresponding upper or lower variances of the parameters.

For validation, we also performed a semi-independent SED fitting taking into account cluster masses by minimizing the following quantity (cf., [Bik et al. 2003](#); [Anders et al. 2004](#)):

$$\chi^2(\tau, A_V, M) = \sum_{\lambda=J,H,K_s} \frac{(m_{\text{obs},\lambda} - m_{\text{SB99},\lambda} + 2.5 \log \frac{M}{10^6})^2}{\sigma_\lambda^2}, \quad (2)$$

where $m_{\text{obs},\lambda}$ and $m_{\text{SB99},\lambda}$ are the de-reddened apparent magnitudes from the observations and the SB99 model, respectively, and σ_λ are the photometric errors, using the same age and A_V steps as for the color fitting and mass steps of 0.01 dex. The two methods provide consistent results, as shown in Fig. 4, except for one distinct outlier visible in the age plot. For the analyses below, we excluded the peculiar sources that cannot be directly de-reddened to match the evolutionary model (including the outlier above), leaving us with 54 cluster candidates.

Table 1 gives the estimated extinctions, ages, masses and apparent magnitudes of the final sample with the associated instrumental errors.

4.3. Age distribution and star formation history

Figure 5 plots the age distribution of the clusters as an histogram with bins of 0.1 dex in age. We identify two clear peaks at $\tau = 2.8$ and 4.5 Myr. Although rapid changes in the energy distributions and colors of clusters have been known to cause similar statistical artefacts (e.g., [Bik et al. 2003](#); [Bastian et al. 2005](#)), in our case, we believe they are real physical patterns given the very fine age steps of 0.1 Myr in our models. The ages corresponding to both peaks are consistent with [Randriamanakoto \(2015\)](#) who find a broad distribution peaking around 6 Myr and extending to younger ages, but that does not separate into two peaks. Nevertheless, comparisons are limited because they use larger age

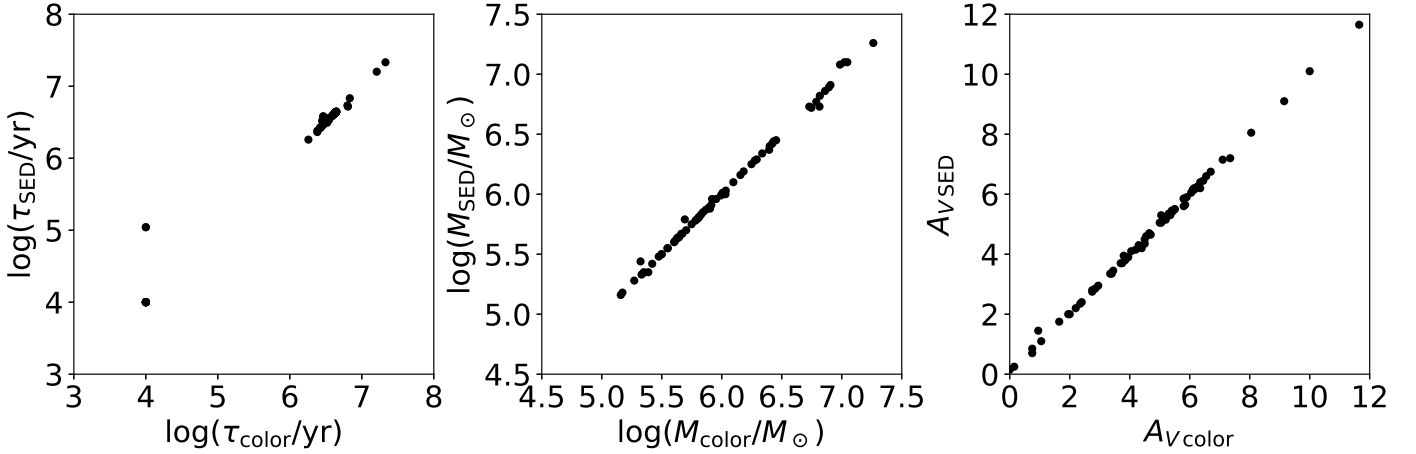


Fig. 4. Comparison between the three quantities age, mass and extinction derived for each cluster using color fitting versus the same quantities derived from SED fitting.

steps and cannot break the age-extinction degeneracy with BIK_s -data only. These two peaks in age are particularly prominent, indicating that two very recent bursts occurred and in fact dominate the detected population of SSCs. Such young ages for starbursts are not often observed, but have been measured in a few other galaxies, for instance in M51 where Gieles et al. (2005) find two peaks: one being at 5.5 Myr, or in the dwarf merger ESO 185-IG13 (Adamo et al. 2011a) where the histogram peaks at 3 Myr.

Figure 6 shows the estimated masses of the clusters versus their ages. The bimodal distribution on the two bursts is especially clear on this plot. Disruption of clusters by interaction with giant molecular clouds (GMCs) in their vicinity has been the subject of many works and debates (Longmore et al. 2014; Adamo et al. 2018). The characteristic disruption time generally follows the relation $t_{\text{dis}} \approx t_4 (M_{\text{cl}}/10^4 M_{\odot})^{0.62}$ (e.g., Boutloukos & Lamers 2003; de Grijs et al. 2003), where t_4 is the disruption time of a $10^4 M_{\odot}$ cluster, which depends on the specific conditions of the galaxy, especially the surface density of molecular clouds. For the non-LIRG star-forming galaxy M51, Gieles et al. (2005) derived a disruption time $t_{\text{dis}} \approx 100.0 (M_{\text{cl}}/10^4 M_{\odot})^{0.62}$ Myr. If the law is universal, no SSC less massive than $10^4 M_{\odot}$ and with an age older than 0.1 Gyr would be detectable in IRAS 17138-1017. This is in fact what we observe, but the lowest mass we detect would also be compatible with $t_4 = 6$ Myr. However in a subsequent paper, Gieles et al. (2006) proposed a more detailed relation where the surface density of GMCs is taken into account, since it may vary by large amounts from one galaxy to another. They find that $t_{\text{dis}} = 2.0 (M_c/10^4 M_{\odot})^{0.62} (5.1 M_{\odot}^2 \text{pc}^{-5}) (\Sigma_n \rho_n)^{-1}$ Gyr, where the surface density of individual GMC (Σ_n) and the global GMC density (ρ_n) are scaled to the solar neighborhood. To reach $t_4 = 6$ Myr, we need an increase of the product $\Sigma_n \rho_n$ of 300 with respect to the solar neighborhood, a value that is not exceptional in an LIRG galaxy. For instance, ALMA observations of the LIRG IRAS 13120-5453 reveal a surface density $\Sigma_n = 2.0 \times 10^4 M_{\odot} \text{pc}^{-2}$ (Privon et al. 2017) which, if combined with a density of GMC twice that of the solar neighborhood ($\rho_n = 0.03 M_{\odot} \text{pc}^{-3}$, Solomon et al. 1987), would provide this factor. IRAS 17138-1017 is well known for its very high obscuration (Depoy et al. 1988, this work). This is also demonstrated by the detection of the most extinct supernovae so far, with $A_V = 15.7$ mag for SN2008cs (Kankare et al. 2008), supporting such high value of Σ_n . Finally, Piqueras López et al. (2016)

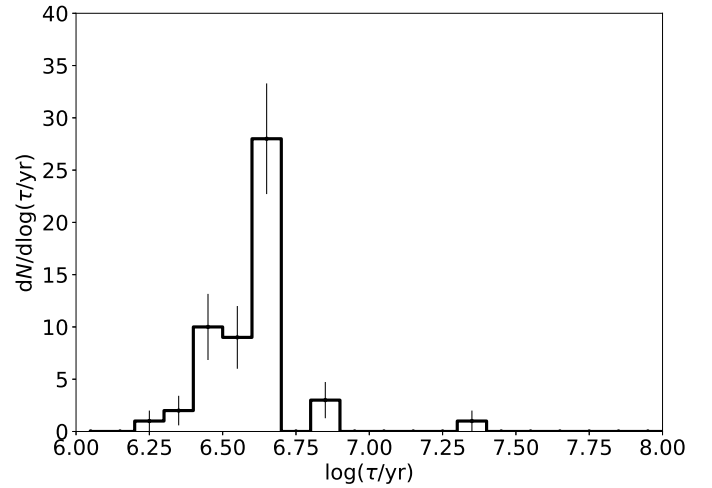


Fig. 5. Age distribution of SSCs in IRAS 17138-1017. The error bars assume Poisson uncertainties.

find that the star formation rate per unit surface, Σ_{SFR} of IRAS 17138-1017 is the second highest in a sample of 17 LIRGs and ULIRGs. Considering the well-established Kennicutt-Schmidt law $\Sigma_{\text{SFR}} \propto (\Sigma_{\text{gas}})^{1.4 \pm 0.15}$, this is an additional hint of a high Σ_n .

We also calculated the cluster formation efficiency (CFE or Γ), defined by Bastian (2008) as the fraction of stellar mass formed in bound clusters $\Gamma = \text{CFR}/\text{SFR}$, where CFR is the cluster formation rate, meaning the total cluster mass in a certain age range divided by the corresponding time interval, and SFR is the star formation rate of the host galaxy during that period. Adopting an SFR of $44.7 M_{\odot} \text{yr}^{-1}$ derived from the IR luminosity (Kennicutt 1998) and an age range between 1 and 10 Myr, we obtain $\Gamma \approx 33.4\%$. Given the similar SFR, Randriamanakoto (2015) found a value of 17% for the age range between 10 and 100 Myr. These values are consistent with the ones observed for starburst galaxies (Adamo et al. 2018, and references therein) and could be evidence of infant mortality: clusters are disrupted quickly during the first 10 Myr due to the gas expulsion process (Lada & Lada 2003). Our Γ value and the Σ_{SFR} of $8.9 M_{\odot} \text{yr}^{-1} \text{kpc}^2$ measured by Piqueras López et al. (2016) are also in agreement with the Γ - Σ_{SFR} relation established by Kruijssen (2012). Nevertheless, our estimation of Γ at an early age should only be viewed as an upper limit, due to the possible inclusion of unbound associations in our catalog (Kruijssen & Bastian 2016).

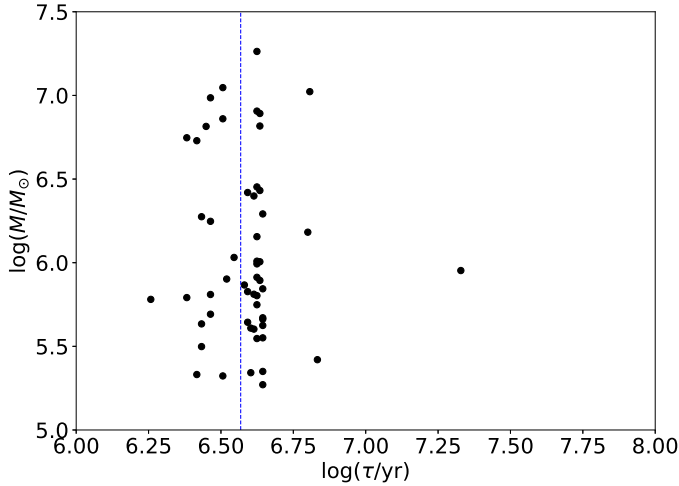


Fig. 6. Cluster age-mass plane for the sample of SSCs in IRAS 17138-1017. The blue dash line marks the age of 3.7 Myr splitting two bursts.

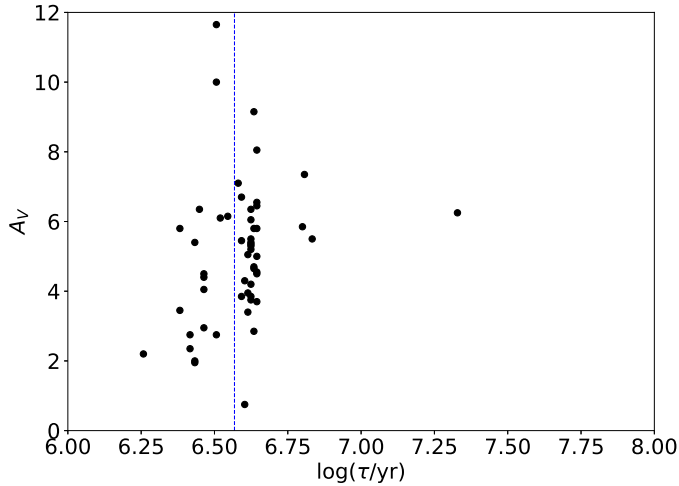


Fig. 7. Age versus extinction for the sample of SSCs. The blue dash line marks the age of 3.7 Myr separating the two identified bursts.

4.4. Extinction

To further examine the relation between the cluster age and extinction as shown in Fig. 7, in Fig. 8 we plot the histograms of A_V splitting the SSCs into two groups corresponding to the identified bursts, meaning younger or older than 3.7 Myr. In particular, the bottom plot showing the relative distribution of extinction in each population reveals a clear tendency to have fewer extinct SSCs in the most recent burst, with more than 60% of the SSCs having $A_V < 5$, while the 4.5 Myr burst has more than 60% of the SSCs with $A_V > 5$. Nevertheless, the two most extinct SSCs belong to the young burst. The intuitive idea that “the younger an SSC is, the more embedded it should be”, is not confirmed here. Given the narrow time period between the two bursts, it might be that the first generation had consumed or expelled a part of the interstellar medium (ISM) so that the next generation was born in a less dense medium. Another tentative explanation could be that the most recent burst was triggered by the first one and occurred in a less dense component of the GMC within the galaxy, which had not collapsed at the moment of the first burst.

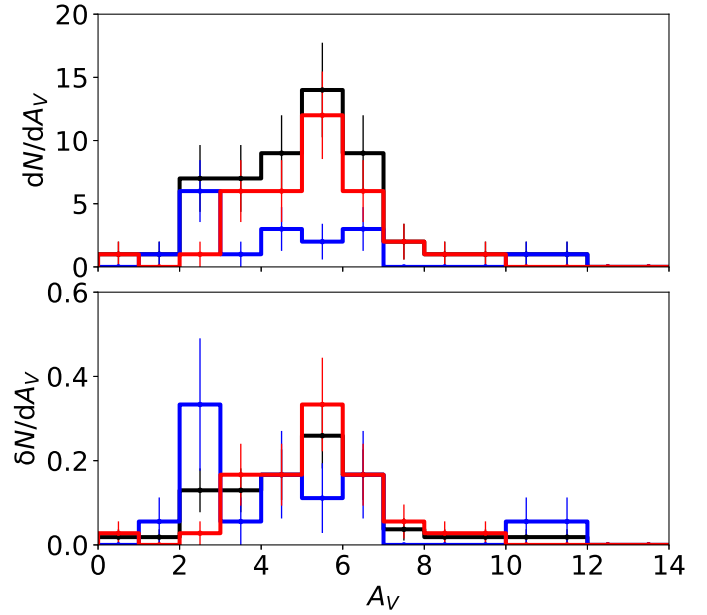


Fig. 8. Frequency distribution of the extinction. The black line represents the entire sample, and the blue and red lines correspond to the populations of the 2.8 Myr burst and 4.5 Myr burst, respectively. *Top*: absolute numbers. *Bottom*: relative numbers. The error bars assume Poisson uncertainties.

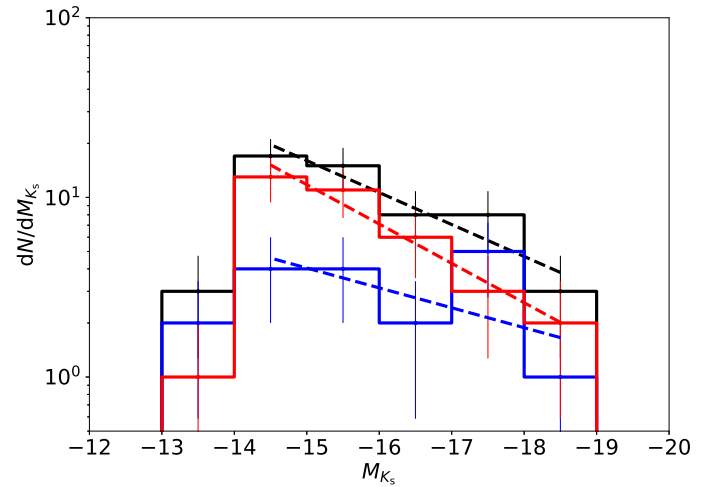


Fig. 9. Luminosity function (dN/dL versus M_{K_s}) of the entire sample of SSCs (black) and for the subsamples of age $\tau \leq 3.7$ Myr (blue) and age $\tau \geq 3.7$ Myr (red), in bins of 1 mag. The black, blue, and red dash lines are corresponding linear regressions. The error bars assume Poisson uncertainties.

4.5. Luminosity and mass functions

Figures 9 and 10, respectively, plot the intrinsic (de-reddened) K_s -band cluster luminosity function (CLF) and the cluster mass function (CMF) of IRAS 17138-1017, expressed as the number of objects per bin of 1 mag and 0.5 dex of mass, respectively. Each of them can be approximated by a power-law distribution (plotted as the dashed line on each figure) in the forms of $dN/dL \propto L^\alpha$ and $dN/dM \propto M^\beta$, with $\alpha = -1.44$ and $\beta = -1.58$. For clusters with age $\tau \leq 3.7$ Myr, we obtain $\alpha = -1.28$ and $\beta = -1.48$. Clusters with age $\tau > 3.7$ Myr have $\alpha = -1.55$ and $\beta = -1.67$. As can be seen on the plots, the flattening of

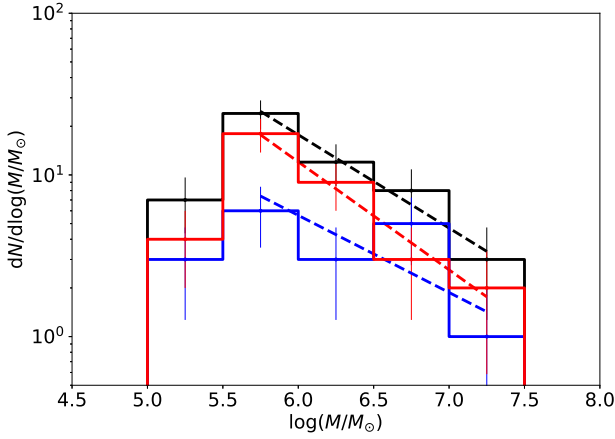


Fig. 10. Mass function of the entire sample of SSCs (black) and for the subsamples of age $\tau \leq 3.7$ Myr (blue) and age $\tau > 3.7$ Myr (red), in bins of 0.5 dex. The black, blue, and red dash lines are corresponding linear regressions. The error bars assume Poisson uncertainties.

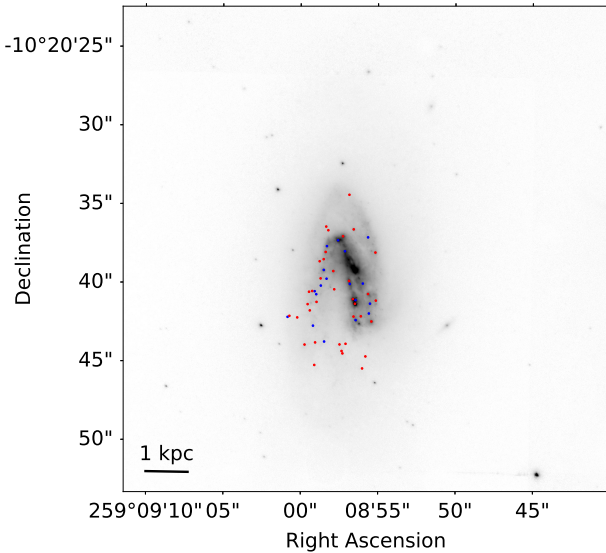


Fig. 11. Locations of the SSCs on the K_s image of IRAS 17138-1017. The colors of the open circles indicate the age category (blue for age $\tau \leq 3.7$ Myr burst and red for age $\tau > 3.7$ Myr).

the young age CLF and CMF is caused by a spike of heavy ($6.5 \leq \log(M/M_\odot) < 7$) and bright ($-18 < M_{K_s} \leq -17$) SSCs.

In general, these values of the CLF are at the lower end of the observed range ($\alpha \approx -1.87 \pm 0.3$) for SSCs in ULIRGs and LIRGs (including blue compact dwarves) (Randriamanakoto et al. 2013b; Vavilkin 2011; Miralles-Caballero et al. 2011; Adamo et al. 2010a, 2011a,b). For comparison, normal spiral galaxies, or even star-forming galaxies though not yet LIRGs exhibit significantly steeper distribution, where $\alpha \approx -2.2 \pm 0.3$ (Elmegreen & Efremov 1997; Gieles et al. 2006; Bastian 2008; Haas et al. 2008; Larsen 2009). However, many authors might not de-redden their estimated magnitudes when the effect of extinction could be significant and lead to CLFs deviating from power law (Megeath 1996). For IRAS 17138-1017, without de-reddening we find that $\alpha = -1.57$, which matches the Randriamanakoto et al. (2013b) values of $\alpha = -1.53$ and -1.64 for constant and variable bin widths, respectively.

In terms of the CMF, our indices are shallower than the canonical $\beta \approx -2$ found in the literature (Krumholz et al. 2019), as well as the average value of $\beta = -1.95 \pm 0.11$

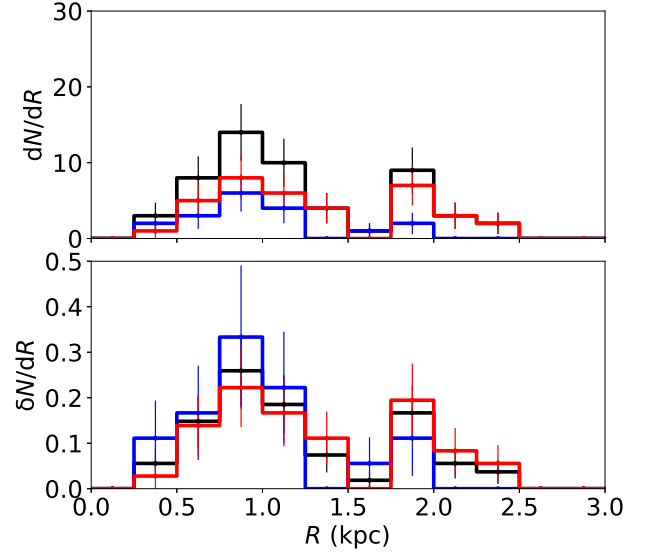


Fig. 12. Number of SSCs per ring of increasing diameters centered on the nucleus. The black line represents the entire sample, the blue and red lines correspond to the populations of the 2.8 Myr burst and 4.5 Myr burst, respectively. *Top:* absolute numbers. *Bottom:* relative numbers in each category.

for LIRGs in the GOALS survey (Linden et al. 2017), yet they still fall in the observed range. Starburst galaxies at large distances tend to have flatter CMFs, which might result from a blending effect (Krumholz et al. 2019). For comparison, Randriamanakoto (2015) obtained values of $\beta = -1.86$ for clusters younger than 30 Myr, and $\beta = -1.61$ for clusters of ages between 30 Myr and 1 Gyr in IRAS 17138-1017, but she also warned of an overestimation of cluster masses and the age-extinction degeneracy.

Because IRAS 17138-1017 is distant, the mass and luminosity functions are only significant for the SSCs more massive than $\sim 3.0 \times 10^5 M_\odot$, which is the range used to fit the power law. Comparison with the CLFs or CMFs of nearby galaxies is thus meaningful only for this range. The observed slopes of both CLF and CMF are linked to the shape of the underlying IMF and to the evolution and disruption of the SSC population. The relatively flatter luminosity distribution of IRAS 17138-1017, with respect to other LIRGs may again be an evidence for the disruption of lower mass SSCs due to tidal shock heating by dense gas, as proposed by Kruijssen et al. (2012). This cruel cradle effect could be more efficient here than in similar galaxies because of its high surface density of GMCs.

Several studies have pointed out that the CMF tends to be steeper than the power law at the high-mass end due to a truncation effect (Adamo et al. 2018). At first sight, such a steepening seems to be present in Fig. 8, the two last bins of the CMF being well below the power law. However, this is actually not significant, due to the very low number of SSCs in those bins.

4.6. Spatial distribution

Figure 11 shows the K_s image of IRAS 17138-1017 with the detected SSCs superimposed and colored in accordance with their ages. There is a clear tendency to find the younger SSCs closer to the center. This can be confirmed by plotting the number of SSCs in successive rings on Fig. 12: the youngest burst mainly populates the central region ($R < 1.25$ kpc) rather than

the more peripheral one. The spatial distribution of the SSCs is also consistent with the cruel cradle effect: older clusters are able to survive early disruption because they have escaped into more quiescent regions, only young clusters are present in the gas-rich environments (Kruijssen et al. 2012).

Figure 13 plots the relation between the masses of the clusters and their distances to the galactic center. In general, the cluster mass decreases as the galactocentric distance increases. Pflamm-Altenburg et al. (2013), Sun et al. (2016), Randriamanakoto et al. (2019) also find a similar relation for the most massive clusters in their samples, yet Sun et al. (2016) showed that it is mostly caused by size-of-sample effects, and they supported the stochastic cluster formation scenario. We find this trend pertaining to the entire sample of SSCs and less likely affected by any size-of-sample effect. Adamo et al. (2015) also showed that the cluster formation efficiency Γ declines over galactocentric distance in M83, following the $\Gamma - \Sigma_{\text{SFR}}$ relation of Kruijssen (2012). A radial decrease of Σ_{SFR} is also observed in IRAS 17138-1017 (Piqueras López et al. 2016). We conclude that the formation of star clusters depends on the host galaxy environment.

5. Modeling super star clusters with the radiative transfer code MontAGN

Until now, to interpret observations, most cluster studies assumed that evolutionary models such as SB99 can fairly simulate the spectra of SSCs at different ages. However, we have seen that in several cases it is not possible to de-redden the cluster colors along the reddening vector to reach a point on the evolutionary track. Many other authors also face similar problems without definitive explanations, particularly outliers in color space or near-IR excesses in SED fitting (e.g. Grosbøl & Dottori 2008, 2012; Reines et al. 2008a,b; Adamo et al. 2010a, 2011a,b). For instance, the presence of evolved stellar populations was hypothesized to cause extra reddening (e.g. Grosbøl & Dottori 2008, 2012). However using the COLIBRI code (Pastorelli et al. 2019) with an accurate processing of the thermally-pulsing asymptotic giant branch (TP-AGB) phase, we find that a 1 Gyr synthetic stellar population only produces $(H - K) = 0.06$. Low spatial resolution and large photometric aperture may also introduce nebular emission and nearby stellar contamination into the near-IR flux, resulting in redder colors (Bastian et al. 2014), yet our study should not be susceptible. Other proposed mechanisms include nebular emission (e.g. Reines et al. 2010; Adamo et al. 2010b) and hot dust emission (e.g. Adamo et al. 2010a, 2011a,b). In our study, SB99 only considers the stellar and nebular emission and no other sources of radiation. Because SSCs are formed within dense cocoons of gas and dust, we expected some contribution of the hot dust emission at least in the K -band. In addition, we wondered whether scattered radiation in a highly clumpy medium might lead to a different behavior of the extinction with respect to the wavelength rather than classical reddening laws representing point sources behind a screen. This may be a concern for SSCs, because a significant portion of the light scattered in the cocoon is also collected in the beam². To quantify the role of these two effects, we generated a series of simulations using the radiative transfer code MontAGN developed by our team (Grosset et al. 2018).

² To illustrate this, we can consider hypothetical dust grains with a very high albedo (say 0.95): the extinction efficiency Q_{ext} would be totally dominated by the scattering term Q_{sca} . However, most of the light from the source would be collected in a beam encompassing the cocoon.

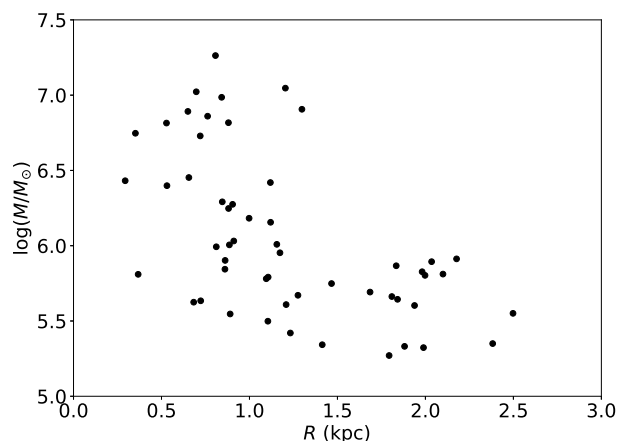


Fig. 13. Mass-galactocentric radius relation for the sample of SSCs.

5.1. Model description

To simulate embedded SSCs in the IR, we developed additional features for our three-dimensional radiative transfer code MontAGN (Monte Carlo for Active Galactic Nuclei), which was originally designed for the study of AGNs (Grosset et al. 2016, 2018; Marin et al. 2016). We added polycyclic aromatic hydrocarbons (PAHs) as a component of the ISM following the absorption and emission scheme of Draine & Li (2007), with the absorption cross sections from Siebenmorgen et al. (2014). We also introduced the fractal dust distribution to simulate the hierarchically clumpy ISM within the cluster (Elmegreen 1997). The algorithm followed Mathis et al. (2002). (1) Initially, we selected N random cells in the simulation grid. (2) For each previously selected cell, we selected N other random cells within a distance of $S/2L$ along each Cartesian axis. We recursively selected N^H cells in total. Here, S is the grid size, L is the fractal length giving the fractal dimension $D = \log_L N$, and H is the number of hierarchical levels. (3) We shifted each cell by multiples of S on three Cartesian axes until it was inside the grid. (4) We only kept cells inside the predefined envelope and filled appropriate dust densities. Our code provides matching results (Lam et al. 2019) to the SSC models from Whelan et al. (2011).

Our SSC models consist of a central point source enshrouded in a spherical dust envelope, with the outer radius fixed at 50 pc. The inner radius increases as the cluster evolves, similarly to Whelan et al. (2011). The source radiates an SB99 spectrum with the following parameters: a $10^6 M_\odot$ SSP with a Kroupa et al. (2008) IMF ($0.1 M_\odot - 100 M_\odot$), Geneva evolutionary tracks (Ekström et al. 2012) at solar metallicity ($Z = 0.014$), and an instantaneous starburst. The dust envelope has a mass composition of 75% silicate, 13.33% ortho-graphite, 6.67% para-graphite, and 5% PAH (Draine 2011) with a classical MRN grain size distribution (Mathis et al. 1977). Apart from a smooth distribution, 50% of the dust is distributed fractally. We adopted $N = 32$, $D = 2.6$, $H = 5$ for the hierarchically clumpy distribution, a standard dust-to-gas ratio of 0.01 as suggested by Whelan et al. (2011), and a representative star-forming efficiency (SFE) of 33% following Banerjee & Kroupa (2017). The SFE sets the mass of residual ISM and thus of dust, after stars have been formed.

5.2. Results and discussions

Figure 14 displays the SEDs for several sets of parameters where combinations of the inner radius of the envelope and the age are considered. We can see that the models with thin envelopes leak

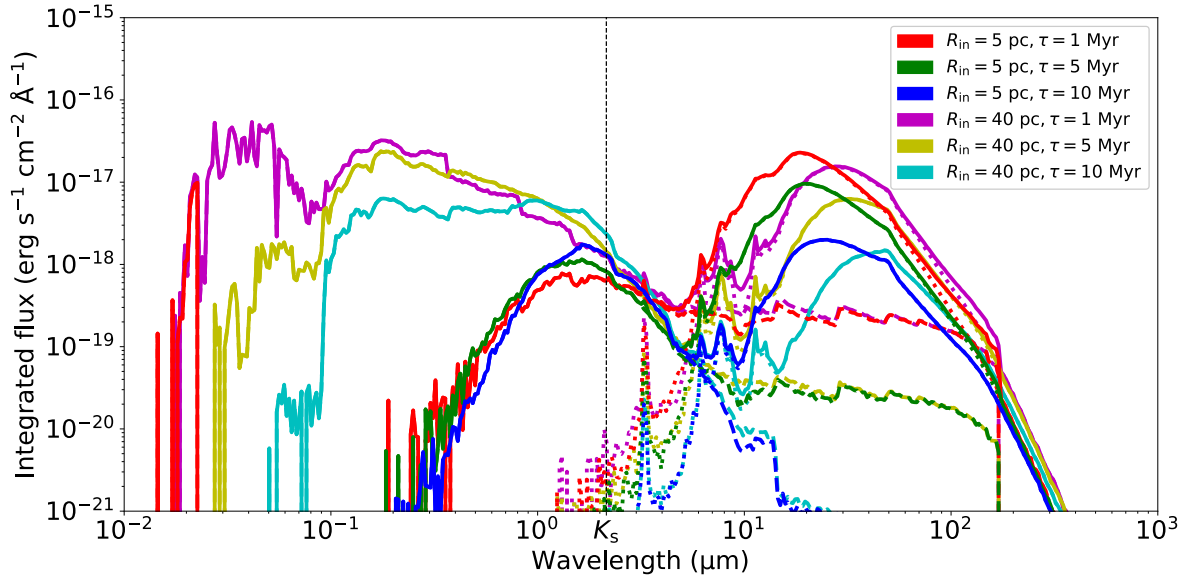


Fig. 14. Spectral energy distributions obtained with MontAGN for various sets of age τ and inner radius R_{in} of the dust envelope. The thick lines represent the total flux, the dotted lines indicate the dust emission, and the dashed lines indicate the stellar emission. The position of the K_s -band is denoted.

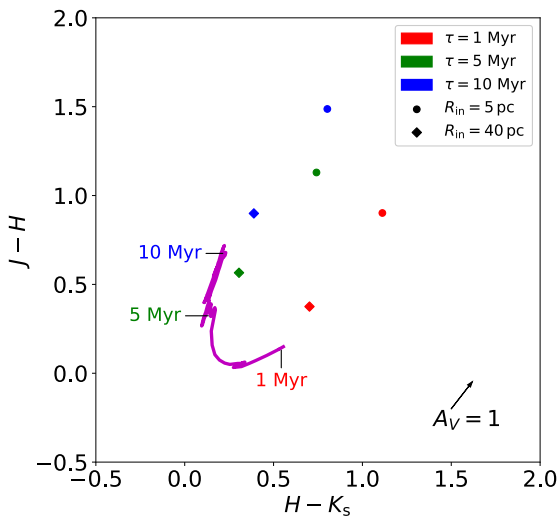


Fig. 15. Color-color diagram ($J - H$) versus ($H - K_s$) for the simulated SSCs with various conditions of age and inner radius of the dust envelope. The same theoretical track and reddening vector as in Fig. 2 are shown.

out significant star light and are much brighter in the visible than in the near IR, which is not the case for IRAS 17138-1017. They must be disregarded for this reason. The dust thermal emission in K_s -band is lower than the total flux by at least two orders of magnitude in all considered cases, which is negligible. The same conclusion also applies to the scattered radiation because most of the grains have very low albedo values. We find that the extra reddening brought by thermal and scattered photons is $\Delta K_s = -0.015$ at maximum. Figure 15 plots the corresponding points on the C-CD, derived by integrating the flux in each filter band. We also show the reddening vector conforming to the Calzetti et al. (2000) extinction law for starburst galaxies like in Fig. 2, but it is for comparison purposes only and not used in the numerical code. Nevertheless, the colors can be de-reddened along this vector without significant deviations in the estimated ages. As a consequence, the extra reddening could not be explained by the thermal emission or scattered radiation. Assuming good uncer-

tainty estimates, an extra source of reddening affecting a small number of SSCs has yet to be identified.

6. Conclusions

The excellent quality of the AO-assisted near-IR images in J , H , and K_s obtained with GeMS on Gemini allows us to identify 54 SSCs in the LIRG IRAS 17138-1017 and to extract their photometry. Most of them appear highly extinct compared to an evolutionary track provided by SB99. Using the Calzetti et al. (2000) extinction law to directly de-redden the clusters and derive their ages, we show that most of them are very young and distributed in two narrow bins of ages of around 2.8 and 4.5 Myr. Thus, IRAS 17138-1017 is a noticeably interesting object for studying the actual IMF of SSCs since disruption could not have played a significant role at those ages. Their luminosity and mass functions follow the classical power-law behavior, however with somewhat shallower slopes than are usually observed in LIRGs. This is a possible indication of the cruel cradle effect: lower mass SSCs are produced less efficiently in an environment with a high surface density of GMCs (Kruijssen et al. 2012), a very likely characteristic of IRAS 17138-1017 where the most extinct SNe have been observed. The SSCs belonging to the youngest starburst episode primarily gather near the central area, while the older ones from the 4.5 Myr starburst are scattered along the spiral arms. In addition, the extinction of the 2.8 Myr SSCs is generally lower than the 4.5 Myr episode, yet some highly extinct SSCs are found in the first group. Even though being separated by only 2 Myr, the two episodes appear to be distinct, probably triggered by different causes and in different populations of molecular clouds. By comparing the observed photometry with the output from realistic radiative transfer models of young SSCs, we conclude that hot dust emission, as well as scattered photons in the K_s band remain negligible even for the thickest envelopes.

Acknowledgements. The authors would like to thank the referee for helpful comments and suggestions. This study is based on observations obtained at the Gemini Observatory processed using the Gemini IRAF package, which is operated by the Association of Universities for Research in Astronomy, Inc., under

a cooperative agreement with the NSF on behalf of the Gemini partnership: the National Science Foundation (United States), National Research Council (Canada), CONICYT (Chile), Ministerio de Ciencia, Tecnología e Innovación Productiva (Argentina), Ministério da Ciência, Tecnologia e Inovação (Brazil), and Korea Astronomy and Space Science Institute (Republic of Korea). IRAF is distributed by the National Optical Astronomy Observatories, which are operated by the Association of Universities for Research in Astronomy, Inc., under cooperative agreement with the National Science Foundation. PyRAF is a product of the Space Telescope Science Institute, which is operated by AURA for NASA. This research has made use of the NASA/IPAC Extragalactic Database (NED), which is funded by the National Aeronautics and Space Administration and operated by the California Institute of Technology. This research has made use of the SIMBAD database, operated at CDS, Strasbourg, France. This research made use of Astropy (<http://www.astropy.org>), a community-developed core Python package for Astronomy (Astropy Collaboration 2013, 2018) and Matplotlib, a 2D graphics package used for Python for application development, interactive scripting, and publication-quality image generation across user interfaces and operating systems (Hunter 2007).

References

- Adamo, A., & Bastian, N. 2018, in *The Lifecycle of Clusters in Galaxies*, ed. S. Stahler, *Astrophys. Space Sci. Libr.*, 424, 91
- Adamo, A., Östlin, G., Zackrisson, E., et al. 2010a, *MNRAS*, 407, 870
- Adamo, A., Zackrisson, E., Östlin, G., & Hayes, M. 2010b, *ApJ*, 725, 1620
- Adamo, A., Östlin, G., Zackrisson, E., & Hayes, M. 2011a, *MNRAS*, 414, 1793
- Adamo, A., Östlin, G., Zackrisson, E., et al. 2011b, *MNRAS*, 415, 2388
- Adamo, A., Kruijssen, J. M. D., Bastian, N., Silva-Villa, E., & Ryon, J. 2015, *MNRAS*, 452, 246
- Anders, P., Bissantz, N., Fritze-v. Alvensleben, U., & de Grijs, R. 2004, *MNRAS*, 347, 196
- Armus, L., Mazzarella, J. M., Evans, A. S., et al. 2009, *PASP*, 121, 559
- Astropy Collaboration (Robitaille, T. P., et al.) 2013, *A&A*, 558, A33
- Astropy Collaboration (Price-Whelan, A. M., et al.) 2018, *AJ*, 156, 123
- Banerjee, S., & Kroupa, P. 2017, *A&A*, 597, A28
- Bastian, N. 2008, *MNRAS*, 390, 759
- Bastian, N., Gieles, M., Lamers, H. J. G. L. M., Scheepmaker, R. A., & de Grijs, R. 2005, *A&A*, 431, 905
- Bastian, N., Adamo, A., Schirmer, M., et al. 2014, *MNRAS*, 444, 3829
- Bik, A., Lamers, H. J. G. L. M., Bastian, N., Panagia, N., & Romaniello, M. 2003, *A&A*, 397, 473
- Boutloukos, S. G., & Lamers, H. J. G. L. M. 2003, *MNRAS*, 338, 717
- Calzetti, D., Armus, L., Bohlin, R. C., et al. 2000, *ApJ*, 533, 682
- Carrasco, E. R., Edwards, M. L., McGregor, P. J., et al. 2012, in *Adaptive Optics Systems III*, SPIE Conf. Ser., 8447, 84470N
- Chavez, J., Carrasco Damele, E. R., & Thomas-Osip, J. 2019, *Am. Astron. Soc. Meeting Abstr.*, 233, 170.01
- de Grijs, R., Bastian, N., & Lamers, H. J. G. L. M. 2003, *MNRAS*, 340, 197
- Depoy, D. L., Wynn-Williams, C. G., Hill, G. J., & Becklin, E. E. 1988, *AJ*, 95, 398
- Diolaiti, E., Bendinelli, O., Bonaccini, D., et al. 2000, *A&AS*, 147, 335
- Draine, B. T. 2011, in *EAS Publications Series*, eds. C. Joblin, & A. G. G. M. Tielens, 46, 29
- Draine, B. T., & Li, A. 2007, *ApJ*, 657, 810
- Ekström, S., Georgy, C., Eggenberger, P., et al. 2012, *A&A*, 537, A146
- Ellis, S. C., & Bland-Hawthorn, J. 2007, *MNRAS*, 377, 815
- Elmegreen, B. G. 1997, *ApJ*, 477, 196
- Elmegreen, B. G., & Efremov, Y. N. 1997, *ApJ*, 480, 235
- Fitzpatrick, E. L. 1999, *PASP*, 111, 63
- Foster, J. B., Román-Zúñiga, C. G., Goodman, A. A., Lada, E. A., & Alves, J. 2008, *ApJ*, 674, 831
- Gieles, M., Bastian, N., Lamers, H. J. G. L. M., & Mout, J. N. 2005, *A&A*, 441, 949
- Gieles, M., Portegies Zwart, S. F., Baumgardt, H., et al. 2006, *MNRAS*, 371, 793
- Grosbøl, P., & Dottori, H. 2008, *A&A*, 490, 87
- Grosbøl, P., & Dottori, H. 2012, *A&A*, 542, A39
- Grosset, L., Marin, F., Gratadour, D., et al. 2016, *SF2A-2016: Proceedings of the Annual meeting of the French Society of Astronomy and Astrophysics*, 57
- Grosset, L., Rouan, D., Gratadour, D., et al. 2018, *A&A*, 612, A69
- Haan, S., Surace, J. A., Armus, L., et al. 2011, *AJ*, 141, 100
- Haas, M. R., Gieles, M., Scheepmaker, R. A., Larsen, S. S., & Lamers, H. J. G. L. M. 2008, *A&A*, 487, 937
- Herrero-Illana, R., Pérez-Torres, M., Rand Riamanakoto, Z., et al. 2017, *MNRAS*, 471, 1634
- Hunter, J. D. 2007, *Comput. Sci. Eng.*, 9, 90
- Jarrett, T. H., Chester, T., Cutri, R., Schneider, S. E., & Huchra, J. P. 2003, *AJ*, 125, 525
- Kankare, E., Mattila, S., Ryder, S., et al. 2008, *ApJ*, 689, L97
- Kennicutt, R. C., Jr 1998, *ARA&A*, 36, 189
- Kool, E. C., Ryder, S., Kankare, E., et al. 2018, *MNRAS*, 473, 5641
- Kroupa, P. 2008, in *Pathways Through an Eclectic Universe*, eds. J. H. Knapen, T. J. Mahoney, & A. Vazdekis, *ASP Conf. Ser.*, 390, 3
- Kruijssen, J. M. D. 2012, *MNRAS*, 426, 3008
- Kruijssen, J. M. D., & Bastian, N. 2016, *MNRAS*, 457, L24
- Kruijssen, J. M. D., Maschberger, T., Moeckel, N., et al. 2012, *MNRAS*, 419, 841
- Krumholz, M. R., McKee, C. F., & Bland-Hawthorn, J. 2019, *ARA&A*, 57, 227
- Lada, C. J., & Lada, E. A. 2003, *ARA&A*, 41, 57
- Lam, N. T., Grosset, L., Rouan, D., & Gratadour, D. 2019, in *Astronomical Society of the Pacific Conference Series*, eds. K. Werner, C. Stehle, T. Rauch, & T. Lanz, *ASP Conf. Ser.*, 519, 273
- Larsen, S. S. 2009, *A&A*, 494, 539
- Leitherer, C., Schaerer, D., Goldader, J. D., et al. 1999, *ApJS*, 123, 3
- Leitherer, C., Ekström, S., Meynet, G., et al. 2014, *ApJS*, 212, 14
- Linden, S. T., Evans, A. S., Rich, J., et al. 2017, *ApJ*, 843, 91
- Longmore, S. N., Kruijssen, J. M. D., Bastian, N., et al. 2014, in *Protostars and Planets VI*, eds. H. Beuther, R. S. Klessen, C. P. Dullemond, & T. Henning, 291
- Marin, F., Grosset, L., Goosmann, R., et al. 2016, *SF2A-2016: Proceedings of the Annual meeting of the French Society of Astronomy and Astrophysics*, 103
- Mathis, J. S., Rimpl, W., & Nordsieck, K. H. 1977, *ApJ*, 217, 425
- Mathis, J. S., Whitney, B. A., & Wood, K. 2002, *ApJ*, 574, 812
- McGregor, P., Hart, J., Stevanovic, D., et al. 2004, in *Ground-based Instrumentation for Astronomy*, eds. A. F. M. Moorwood, & M. Iye, *SPIE Conf. Ser.*, 5492, 1033
- Megeath, S. T. 1996, *A&A*, 311, 135
- Miralles-Caballero, D., Colina, L., Arribas, S., & Duc, P.-A. 2011, *AJ*, 142, 79
- Monty, S., Puzia, T. H., Miller, B. W., et al. 2018, *ApJ*, 865, 160
- Neichel, B., Rigaut, F., Vidal, F., et al. 2014, *MNRAS*, 440, 1002
- Parmentier, G., de Grijs, R., & Gilmore, G. 2003, *MNRAS*, 342, 208
- Pastorelli, G., Marigo, P., Girardi, L., et al. 2019, *MNRAS*, 485, 5666
- Pflamm-Altenburg, J., González-Lópezlira, R. A., & Kroupa, P. 2013, *MNRAS*, 435, 2604
- Piqueras López, J., Colina, L., Arribas, S., Alonso-Herrero, A., & Bedregal, A. G. 2012, *A&A*, 546, A64
- Piqueras López, J., Colina, L., Arribas, S., Pereira-Santaella, M., & Alonso-Herrero, A. 2016, *A&A*, 590, A67
- Portegies Zwart, S. F., McMillan, S. L. W., & Gieles, M. 2010, *ARA&A*, 48, 431
- Privon, G. C., Aalto, S., Falstad, N., et al. 2017, *ApJ*, 835, 213
- Randriamanakoto, Z. 2015, Ph.D. Thesis, Department of Astronomy, University of Cape Town, Private Bag X3, Rondebosch 7701, South Africa
- Randriamanakoto, Z., Escala, A., Väisänen, P., et al. 2013a, *ApJ*, 775, L38
- Randriamanakoto, Z., Väisänen, P., Ryder, S., et al. 2013b, *MNRAS*, 431, 554
- Randriamanakoto, Z., Väisänen, P., Ryder, S. D., & Ranaivomanana, P. 2019, *MNRAS*, 482, 2530
- Reines, A. E., Johnson, K. E., Goss, W. M. 2008a, *AJ*, 135, 2222
- Reines, A. E., Johnson, K. E., & Hunt, L. K. 2008b, *AJ*, 136, 1415
- Reines, A. E., Nidever, D. L., Whelan, D. G., & Johnson, K. E. 2010, *ApJ*, 708, 26
- Ricci, C., Bauer, F. E., Treister, E., et al. 2017, *MNRAS*, 468, 1273
- Rigaut, F., Neichel, B., Boccas, M., et al. 2014, *MNRAS*, 437, 2361
- Robin, A. C., Reylé, C., Derrière, S., & Picaud, S. 2003, *A&A*, 409, 523
- Sanders, D. B., & Mirabel, I. F. 1996, *ARA&A*, 34, 749
- Sanders, D. B., Mazzarella, J. M., Kim, D. C., Surace, J. A., & Soifer, B. T. 2003, *AJ*, 126, 1607
- Santos, J. F. C., Dottori, H., & Grosbøl, P. 2013, *A&A*, 553, A74
- Schlafly, E. F., & Finkbeiner, D. P. 2011, *ApJ*, 737, 103
- Siebenmorgen, R., Voshchinnikov, N. V., & Bagnulo, S. 2014, *A&A*, 561, A82
- Skrutskie, M. F., Cutri, R. M., Stiening, R., et al. 2006, *AJ*, 131, 1163
- Solomon, P. M., Rivolo, A. R., Barrett, J., & Yahil, A. 1987, *ApJ*, 319, 730
- Stierwalt, S., Armus, L., Charmandaris, V., et al. 2014, *ApJ*, 790, 124
- Sun, W., de Grijs, R., Fan, Z., & Cameron, E. 2016, *ApJ*, 816, 9
- Tody, D. 1986, in *Instrumentation in Astronomy VI*, ed. D. L. Crawford, *SPIE Conf. Ser.*, 627, 733
- Tody, D. 1993, in *Astronomical Data Analysis Software and Systems II*, eds. R. J. Hanisch, R. J. V. Brissenden, & J. Barnes, *ASP Conf. Ser.*, 52, 173
- Torres-Albà, N., Iwasawa, K., Díaz-Santos, T., et al. 2018, *A&A*, 620, A140
- Turri, P., McConnachie, A. W., Stetson, P. B., et al. 2017, *AJ*, 153, 199
- Vavilkin, T. 2011, PhD Thesis, Department of Physics & Astronomy, Stony Brook University, Stony Brook, NY 11794-3800, USA
- Whelan, D. G., Johnson, K. E., Whitney, B. A., Indebetouw, R., & Wood, K. 2011, *ApJ*, 729, 111
- Whitmore, B. C., Allam, S. S., Budavári, T., et al. 2016, *AJ*, 151, 134
- Yuan, T. T., Kewley, L. J., & Sanders, D. B. 2010, *ApJ*, 709, 884

2.2 Analytical versus Starfinder PSF photometry

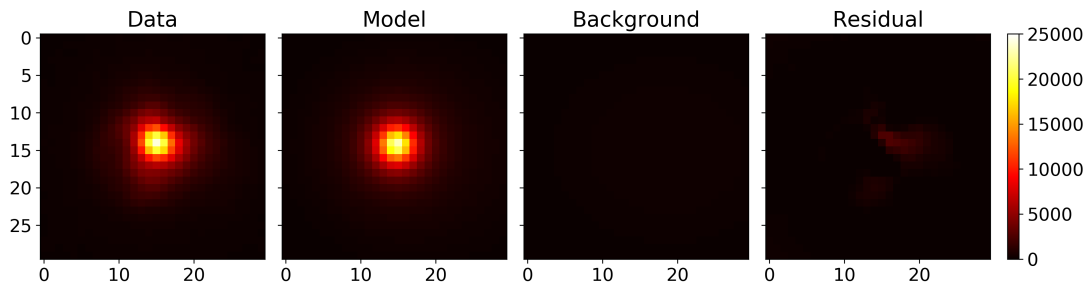


Figure 2.1 – Original data, best-fit compound model, best-fit background and residual for a 2MASS source in K_s band.

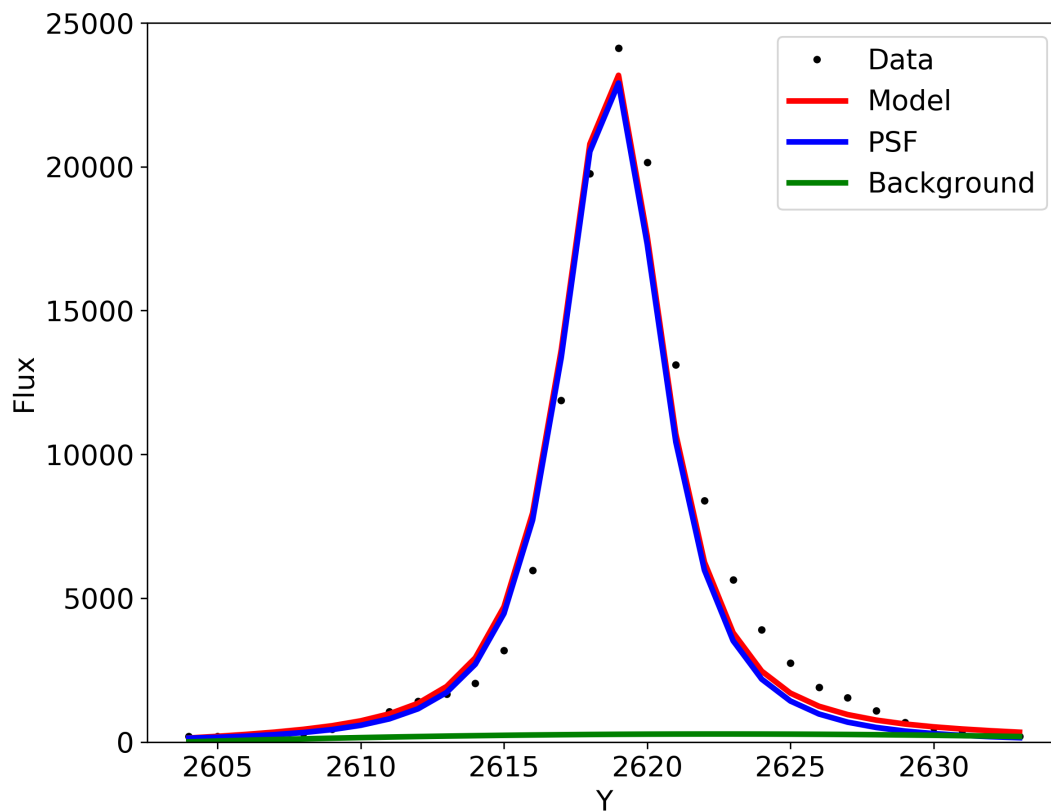


Figure 2.2 – Projection of original data (black dots), best-fit compound model (red line), Moffat PSF (blue line) and background (green line) for the same 2MASS source in K_s band as in Fig. 2.1.

For comparison to STARFINDER photometry, which is based on empirical PSF, we built analytical PSF models and fitted them to the sources, then compared photometric measurements from the two methods. In particular, each 2D compound model consists of one or multiple Mof-fat functions representing the sources (Eq. 2.1), and a second-order polynomial representing the background (Eq. 2.2) as follows:

$$M(x, y) = A \left(1 + \frac{(x - x_0)^2 + (y - y_0)^2}{\gamma^2} \right)^{-\alpha} \quad (\alpha > 1) \quad (2.1)$$

$$P(x, y) = c_{00} + c_{10}x + c_{20}x^2 + c_{01}y + c_{02}y^2 + c_{11}xy \quad (2.2)$$

First we calibrated the parameters α , γ and the zero points using the same 2MASS stars as for STARFINDER. Then we fitted the compound models above to 109 objects extracted and cross-matched by STARFINDER, using windows of 30×30 pixels. An example of fitted source is presented in Fig. 2.1 and Fig. 2.2. We also tested different window sizes on the same source as shown in Fig. 2.3. Finally, the photometric measurements from analytical PSF models and STARFINDER are compared in Fig. 2.4, which shows consistency.

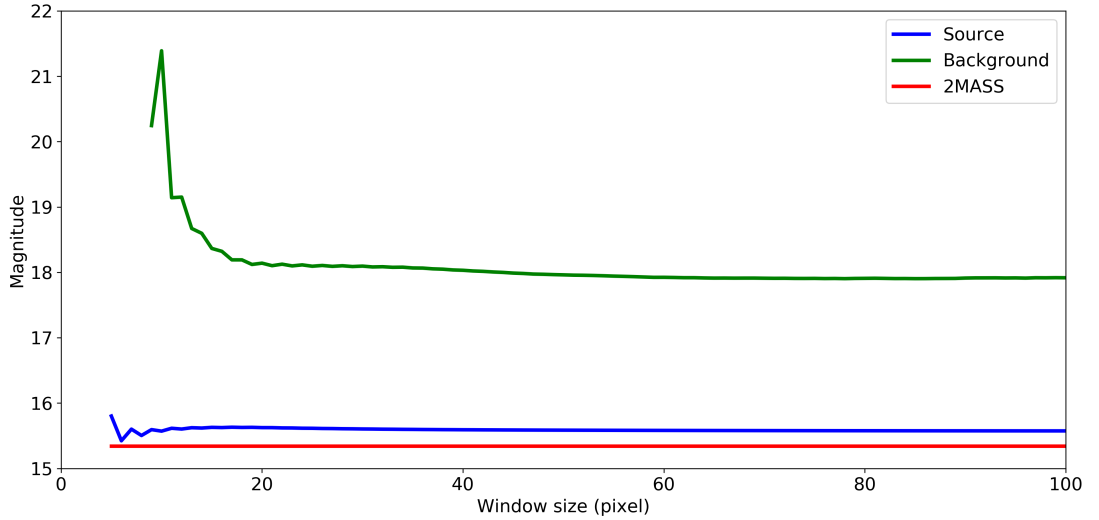


Figure 2.3 – Measured source (blue) and background (green) magnitudes using different window sizes for the same 2MASS source in K_s band as in Fig. 2.1. The 2MASS magnitude (red) is also plotted for comparison.

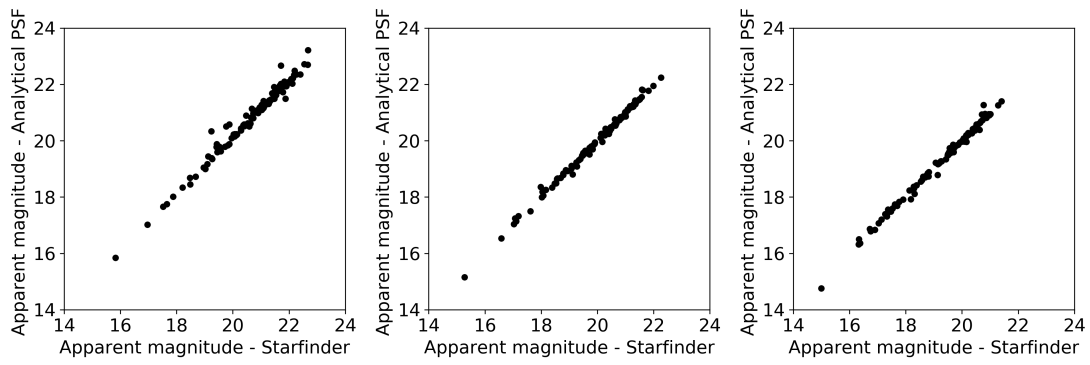


Figure 2.4 – Photometric measurements of 109 extracted and cross-matched sources in [Lam et al. \(2020\)](#) using analytical PSF models versus STARFINDER.

Chapter 3

Modelling super star clusters with the radiative transfer code MontAGN

3.1 Radiative transfer code MontAGN

In this chapter, we describe in detail the radiative transfer code MontAGN that was used to simulate the SSCs in IRAS 17138-1017. Originating from "Monte Carlo for Active Galactic Nuclei", at the beginning the code was built to interpret AGN observations (Marin et al. 2016; Grosset et al. 2016, 2018; Grosset 2019). Basically, definitions of dust species, dust structures, sources, simulation grid and number of photon packets are required to launch simulations. To simulate the SSCs, I have included the polycyclic aromatic hydrocarbons (PAHs) and the hierarchically clumpy structure, which are presented in detail in Sect. 3.2. Users may also toggle re-emission by dust, impose or limit the wavelength of the photons, fine-tune the resolutions of the phase functions and grain size distribution or customize the outputs. Parallel calculation is also supported. We aim to release the source code to the community in the future.

3.1.1 Input parameters

Currently MontAGN supports four types of particles interacting with photons: silicate, graphite grains (orthogonal and parallel components), PAHs and electron. The silicate, graphite and PAH grains are considered to be spherical with radii a following the power-law distribution:

$$\frac{dn}{da} \propto a^\alpha \quad (3.1)$$

Usually the MRN (Mathis et al. 1977) distribution with $\alpha = -3.5$ is adopted. The resolution of grain sizes may be adjusted if necessary. Silicate and graphite optical properties are from Draine (1985), while PAH absorption cross sections are from Siebenmorgen et al. (2014). In the following sections we will use the term *grain* for any interacting particle. Their behaviors during the simulation will be described in Sect. 3.1.2 below.

The overall simulation grid is defined by its size and resolution. Each simulation cell is characterized by its grain densities, temperature and number of absorbed photon packets. MontAGN provides various geometries to distribute grains inside the grid: spherical power law, vertically

decaying spherical power law, Gaussian profile, bump function, circumstellar disk, torus, cone, cylinder, spherical shell, hierarchically clumpy (fractal) structure, simple AGN and [Murakawa \(2010\)](#) torus. Each geometry is constructed based on a set of parameters. Particularly for SSC simulations we used the spherical shell and the fractal structure described in Sect. 3.2. In addition, sublimation radii with respect to the central sources are defined for each dust population and updated in accordance with cell temperatures. The corresponding dust grains inside these limits are ignored. Users may also define an ionization cone where all cells inside are considered empty of dust grains but may contain electrons.

Point sources are placed at the center of the simulation grid given their spectra, luminosities L and emission properties including emission direction, initial polarization orientation and components. By default, source emission is isotropic, unpolarized and initial polarization angle is set to random. Users may also impose a particular wavelength or a maximum wavelength on the emission spectra. Finally, the number of photon packets to be launched N_{phot} and the energy of each packet E are required parameters.

3.1.2 Photon propagation and interaction

MontAGN propagates photons in the form of energy packets, each one is characterized by the parameters in Table 3.1 and illustrated in Fig. 3.1. An extra tag indicates whether the packet will be recorded.

Table 3.1 – Photon packet attributes

Attribute	Symbol	Unit
Number	i	
Wavelength	λ	m
Energy	E	J
Inclination angle of propagation	θ	degree
Azimuthal angle of propagation	ϕ	degree
Direction vector of propagation	\vec{p}	
Normal vector of last scattering plane	\vec{u}	
Normalized Stokes parameters of polarization	$\vec{S} = [1, Q, U, V]^T$	
Polarization orientation angle before exit	ϕ_{QU}	degree
Penetrable optical depth	τ	
Last interaction position	(x, y, z)	pc
Last interacted object	<i>label</i>	
Number of interaction	$n_{interact}$	pc
Number of re-emission	n_{reem}	pc
Packet emission time	δt	s
Total emission time (for first packet only)	Δt	s

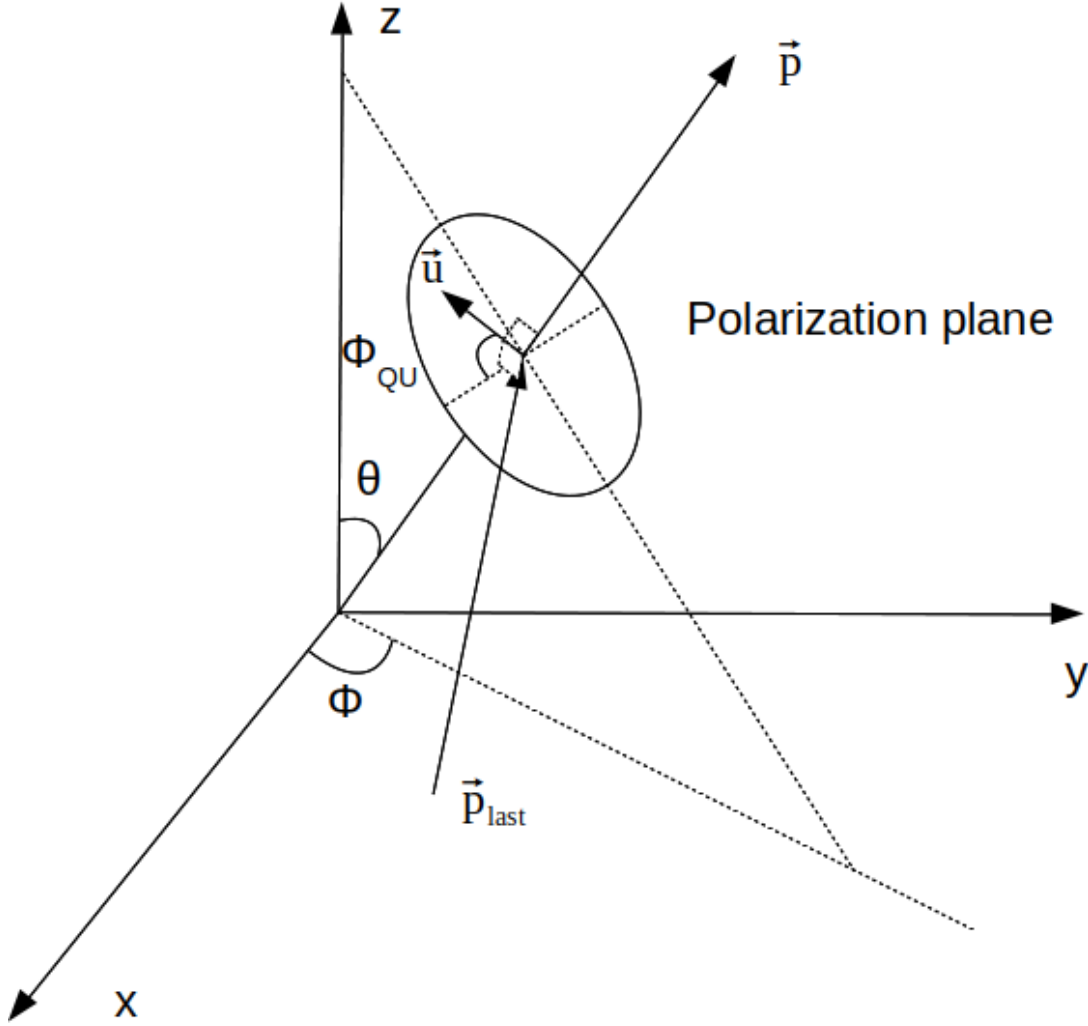


Figure 3.1 – Geometrical attributes of photon packets in MontAGN.

For each emission, MontAGN randomly selects a source with the probability proportional to the luminosity L (W), then uses its SED to randomly generate a wavelength λ for the photon packet, so that the number of photon packets $n_{\text{phot}}(\log \lambda)$ in a bin $\log \lambda$ follows the distribution:

$$n_{\text{phot}}(\lambda) \approx \frac{f_{\text{in}}(\lambda)\Delta\lambda}{L} \times \Sigma n_{\text{phot}} \quad (3.2)$$

where $f_{\text{in}}(\lambda)$ is the input flux (W/m), $\Delta\lambda$ is the bin size (m) and Σn_{phot} is the total number of photon packets. However users may apply a monochromatic filter to the sources. All packets have the same fixed energy E defined by the user and independent of the wavelength λ . The emission times are only calculated theoretically as $\delta t = E/L$ and $\Delta t = n_{\text{phot}} \times \delta t$ and none of them represent the real execution times of the program. The polarization state of each photon packet is described using the normalized Stokes parameters \vec{S} and the respective orientation referred from the normal vector of last scattering plane \vec{u} . Initially each packet is emitted in the

direction \vec{p} corresponding to the inclination θ and azimuth ϕ . Users may specify these parameters or use default values (see Sect. 3.1.1).

Similar to Robitaille (2011), after an interaction (absorption or scattering) or emission, each photon packet is assigned a random transmittance T uniformly distributed between 0 and 1. It corresponds to the optical depth $\tau = -\ln T$ that the packet may penetrate before interaction. The value of τ is reduced by the optical depths of the cells it crosses and when τ reaches 0 at a particular position (x, y, z) , interaction occurs. The interacting grain type *label* is randomly chosen with the probability corresponding to the contributed optical depth. The grain size a is also randomly selected from the distribution described by Eq. 3.1. The albedo is then interpolated given the wavelength λ and the grain size a . An interaction event is then executed, either with or without re-emission depending on the user's choice. If indicated, photons above a particular wavelength may be excepted from interaction.

In the case of an event without re-emission, only scattering is considered and the photon energy is decreased according to the albedo similar to Murakawa (2010) young stellar object (YSO) simulations. The corresponding phase function (see Fig. 3.2), scattering angles, and Mueller matrix are derived from the wavelength λ and grain size a , returning a new Stokes vector \vec{S} , a new polarization orientation \vec{u} and a new propagation direction \vec{p} . It is possible to tune the steps of the phase function. For silicate, graphite and PAH grains, Mie and Rayleigh scattering are applied while electrons produce Thomson scattering instead. Due to absorption, the remaining energy of the scattered packet is:

$$E_{out} = \text{albedo} \times E_{in} \quad (3.3)$$

Users may limit the maximum number of scattering to avoid long simulations with low energy output packets.

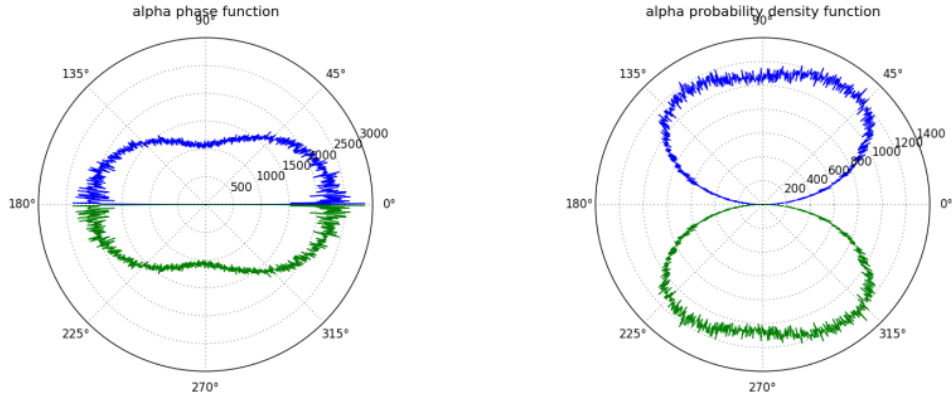


Figure 3.2 – Averaged phase (*left*) and probability density (*right*) functions in the case of Mie scattering generated by MontAGN (400 000 photons) for MRN-distributed silicates (Grosset 2019).

In the case of applying re-emission and temperature update, the packet is either scattered or absorbed at random, with the probability of scattering matching the albedo. If scattering occurs, the process is the same as if without re-emission but the energy is conserved. If absorption occurs, for silicate and graphite grains, the local cell is heated to a new temperature T and immediately re-emits the packet at a different wavelength λ randomly chosen following a black body law, assuming local thermodynamic equilibrium (Bjorkman & Wood 2001). For PAHs, the packet is

re-emitted at a new wavelength λ following the precomputed re-emission scheme of [Draine & Li \(2007\)](#).

3.1.3 Output

After a photon packet exits the simulation grid, MontAGN records all of its parameters in Table 3.1, except for \vec{p} and \vec{u} which are redundant given the angles θ , ϕ and ϕ_{QU} . The packets are grouped into bins of $\Delta\theta = 10^\circ$ for storage purposes. Users may perform different analyses and statistics on the list of output packets, for examples polarization and scattering maps, as well as output SEDs. In particular, we convert the number of photon packets in a bin $\log \lambda$ into the corresponding output flux $f_{\text{out}}(\lambda)$ using an inverted version of Eq. 3.2:

$$f_{\text{out}}(\lambda) = \frac{n_{\text{phot}}(\lambda)}{\Sigma n_{\text{phot}}} \times \frac{L}{\Delta\lambda} \quad (3.4)$$

Furthermore, MontAGN also tracks cell information including dust density, temperature states and updates over time. It is possible to reconstruct these information in 3D or 2D projections, for example dust and temperature distribution maps. These features are demonstrated in Sect. 3.3 and 3.4 below.

3.2 Hierarchically clumpy structure

3.2.1 Formulation

Observations of intermolecular clouds show that their distributions of size L and mass M follow the power laws ([Elmegreen & Falgarone 1996](#), and references therein):

$$\frac{dN}{dL} \propto L^{-\alpha_L} \quad (3.5)$$

$$\frac{dN}{dM} \propto M^{-\alpha_M} \quad (3.6)$$

$$M \propto L^{-\kappa} \quad (3.7)$$

where $\alpha_L = 3.3 \pm 0.3$ and $\alpha_M \approx 1.8$ on average. For individual cloud surveys, $2.4 \lesssim \kappa \lesssim 3.5$ and:

$$1 - \alpha_M \approx \frac{1 - \alpha_L}{\kappa} \quad (3.8)$$

Combining cloud surveys over a wide range of mass from $10^{-3} M_\odot$ to $10^7 M_\odot$ gives:

$$\kappa \approx \alpha_L - 1 \approx 2.3 \quad (3.9)$$

To explain these relations, [Elmegreen & Falgarone \(1996\)](#) suggest a fractal origin, in which the size distribution of substructures on a scale $\lambda > L$ is ([Mandelbrot 1983](#)):

$$N(\lambda > L) \propto L^{-D} \quad (3.10)$$

$$\Leftrightarrow \frac{dN}{dL} \propto L^{-(1+D)} \quad (3.11)$$

where D is the fractal dimension, which may also be defined as:

$$M \propto L^{-D} \quad (3.12)$$

The value $D \sim 2.3$ may stem from the turbulent random motion, similar to turbulent diffusion in an incompressible fluid with a Kolmogorov velocity spectrum ($D \approx 2 + \xi$ for $\Delta v \propto L^\xi$; Meneveau & Sreenivasan 1990). In addition, the observed size and mass distributions of interstellar clouds have invariant power-law slopes over different distances and angular resolutions. This may be explained if all cloud populations share the same fractal pattern. For any original size L and mass M , at a given distance the angular resolution will blend a same number of n clouds into a cloud of size $L' = nL$ and mass $M' = nM$. Due to this blending effect, their size and mass distributions become:

$$\frac{dN'}{dL'} = \frac{1}{n^2} \frac{dN}{dL} \propto \frac{dN}{dL} \quad (3.13)$$

$$\frac{dN'}{dM'} = \frac{1}{n^2} \frac{dN}{dM} \propto \frac{dN}{dM} \quad (3.14)$$

where the power-law slopes are constant. The prevalence of fractal structure may also explain other scaling relations spanning over a wide range, including velocity dispersion and molecular cloud density from 0.01 pc to over 100 pc (Larson 1981) and the star formation duration from 0.1 pc to over 1 kpc (Elmegreen & Efremov 1996).

For embedded SSCs, observations also suggest that their envelopes are porous, the reason why they leak out significant UV radiation (e.g., Reines et al. 2008; Johnson et al. 2009). Moreover, molecular hydrogen in a BCD galaxy is also found to be clumpy, explaining why it emits in the near-IR but not in the UV (Thuan et al. 2005). Thus Whelan et al. (2011) propose a hierarchically clumped density structure based on the description of Elmegreen (1997) to simulate the SSC envelopes.

3.2.2 Implementation

We adopted the algorithm from Mathis et al. (2002) to generate the clumpy dust distribution as follows:

- First generate a random set of N cells with coordinates $(x_i, y_i, z_i)_{i=1}^N$ from the 3D simulation grid of size $S \times S \times S$.
- Given the fractal dimension D and the fractal length $L = \sqrt[D]{N}$, for each cell i above, generate N sets of random distances $\{\Delta x_j, \Delta y_j, \Delta z_j\} \subset (0, \frac{S}{2L})$ and return N new cells of coordinates $(x_i + \Delta x_j, y_i + \Delta y_j, z_i + \Delta z_j)_{j=1}^N$. As a result, there are N^2 new cells in total.
- Execute the above step recursively to obtain N^H cells corresponding to H hierarchical levels.
- If any cell falls outside the grid $\{x_i, y_i, z_i\} \not\subset (0, S)$, adjust its coordinates by a multiple of S so that it is inside: $\{x_i + kS, y_i + mS, z_i + nS\} \subset (0, S)$ where $\{k, m, n\} \subset \mathbb{Z}$.
- Retain the cells inside the spherical shell of given R_{in} and R_{out} only.

- Assign proper dust densities based on the given total mass and dust ratio.

We adopted $N = 32$, $H = 5$ and $D = 2.6$ from [Whelan et al. \(2011\)](#) to create a reasonable fractal structure given the sizes of the envelopes and the simulation grid. Fine-tuning the parameters is unnecessary since extragalactic SSCs are not resolved and our major interest is to simulate the porosity of their envelopes only. Fig. 3.3 demonstrates a fractal envelope generated by MontAGN.

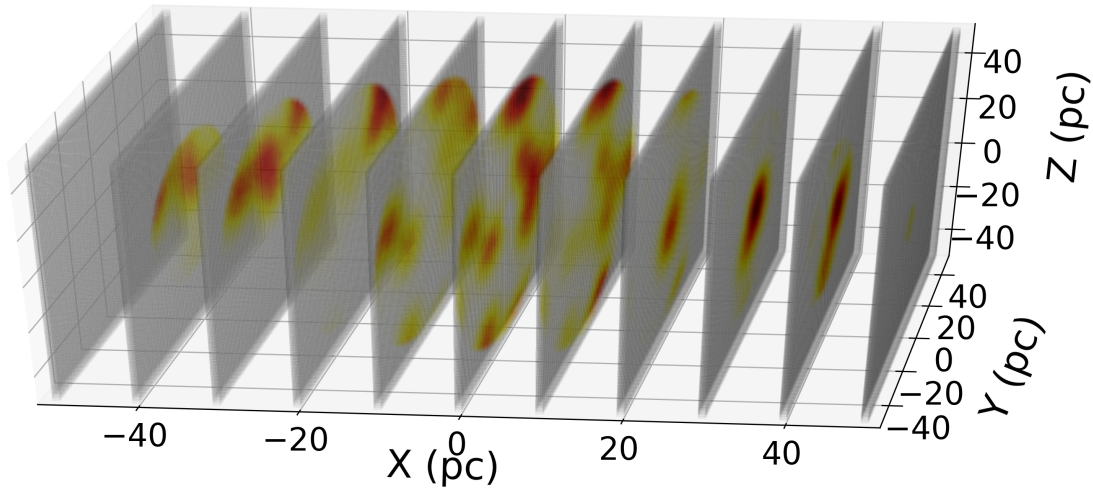


Figure 3.3 – Fractal dust shell of $R_{in} = 5$ pc, $R_{out} = 50$ pc, $N = 32$, $H = 5$ and $D = 2.6$ containing a total dust mass of $10^6 M_{\odot}$ with 75% silicate, 13.33% ortho-graphite, 6.67% para-graphite, 5% PAH and MRN size distribution.

3.3 Preliminary models

In this section we created some preliminary SSC models with MontAGN. Details are presented in the paper below. There were some misunderstanding among the developers of the code concerning the conversion between the flux and the number of photon packets, which caused the input spectrum to be misinterpreted. Nevertheless our major goals was to test the role of PAHs in the spectrum and the effect of the fractal structure, and in conclusion they behaved as expected.

Modelling Super Star Clusters with MontAGN - A 3D Radiative Transfer Code

Nguyen Tung-Lam, Lucas Grosset, Daniel Rouan, and Damien Gratadour
*LESIA, Observatoire de Paris, Université PSL, CNRS, Sorbonne Université,
Univ. Paris Diderot, Sorbonne Paris Cité, 5 place Jules Janssen, 92195
Meudon, France; lam.nguyen@obspm.fr*

Abstract. We present super star cluster (SSC) models in infrared generated by MontAGN (Monte Carlo for Active Galactic Nuclei), a 3-dimensional radiative transfer code written in Python 2.7. The code propagates photons in form of packets taking into account of scattering, absorption, re-emission, temperature update and polarisation. Hierarchically clumpy dust envelopes containing silicate, parallel and perpendicular graphite grains, polycyclic aromatic hydrocarbons (PAHs) with varying parameters are considered in our models. MontAGN is capable of constructing spectral energy distributions (SEDs), maps and 3D visualisations from the output. We compare our results with Whelan et al. 2011 and show that the code has successfully reproduced major features, although several upgrades and improvements are still needed in the future.

1. Introduction

Super star clusters (SSCs) are young, massive and compact clusters that exhibit extreme star formation rate, often resulting from the merging and interaction of galaxies (Portegies Zwart et al. 2010). Such systems involve luminous and ultraluminous infrared galaxies (LIRGs and ULIRGs) with $L_{IR} = 10^{11} - 10^{12} L_{\odot}$ and $L_{IR} = 10^{12} - 10^{13} L_{\odot}$ respectively (Sanders & Mirabel 1996). However, large distance to ULIRGs/LIRGs (median distance ~ 140 Mpc; Haan et al. (2011)) represents a major challenge for the study of SSCs, and their evolution and dynamics have not been described in detail. At early stages, SSCs are enveloped by dust and thus emit strongly in mid-infrared. With unprecedented spatial resolution in this wavelength range, the future James Webb Space Telescope (JWST) will be able to revolutionize our understandings of SSCs. Radiative transfer codes play an important role in interpreting as well as predicting astronomical observations. We introduce MontAGN (Monte Carlo for Active Galactic Nuclei) as a powerful tool to study not only active galactic nuclei (AGNs) but also SSCs.

2. Description of the code

Developed in Python 2.7, MontAGN allows users to define a variety of input parameters or launch pre-existing models. Initially, a 3-dimensional Cartesian grid of cubic cells is constructed. Each cell is characterized by dust particle densities, cell temperature and number of absorbed photon packets. Silicate, graphite grains with parallel and perpendicular components, polycyclic aromatic hydrocarbons (PAHs), as well as electrons can be used and mixed. We adopt grain properties of silicate and graphite from

Draine (1985). Dust size distribution follows Mathis et al. (1977). Several geometries are available: radial and spherical power laws, torus geometries, constant density cylinders, cones, shells and hierarchically clumped (fractal) density structures. Photons are propagated through the grid in form of packets, of a given total energy, with optional thermal re-emission. If enabled, besides scattering and absorption, re-emission and temperature update at each cell are also taken into account following the scheme of Lucy (1999) and Bjorkman & Wood (2001). For polarisation of photons, MontAGN employs the Stokes vectors formalism. When photons exit the simulation grid, their properties are recorded and can be used to plot spectral energy distributions (SEDs). Density and temperature maps in 2D and 3D can also be constructed using Matplotlib (Hunter 2007). Simulations can also be launched in parallel on clusters of processors.

Originally, montAGN was optimized for polarimetric observations of AGNs, as demonstrated by Grosset et al. (2016), Marin et al. (2016) and Grosset et al. (2018). For the simulations of SSCs, we include PAHs into our models by applying the absorption and emission scheme of Draine & Li (2007), with absorption cross sections calculated by Siebenmorgen et al. (2014). Hierarchically clumped density structures (Elmegreen 1997) are constructed based on the algorithm described by Mathis et al. (2002): (1) N cells in the simulation grid are randomly selected, (2) for each cells above, another N cells within a distance of $S/(2L)$ in each x and y axis are randomly selected, where S is the size of the grid and L is the fractal length corresponding to the fractal dimension $D = \log N / \log L$; this step is recursively implemented so that the total number of hierarchical levels is H and there are N^H cells selected, (3) each cell is translated by a multiple of S in each x and y axis until it falls inside the grid, (4) cells inside an envelope of determined inner and outer radii are retained and assigned corresponding dust densities.

3. Modelling SSCs

In this paper, we adopt SSC models from Whelan et al. (2011) as benchmarks for comparison and validation. We assume a central point source with a mass of $10^6 M_\odot$, an age of 1 Myr, a luminosity of $1.6 \times 10^9 L_\odot$, Salpeter IMF (Salpeter 1955) and solar metallicity, with its spectrum generated by Starburst99 (Leitherer et al. 1999). For each simulation, 10^5 photon packets are launched, each has an energy of $1.6 \times 10^9 L_\odot s$.

This central SSC is enshrouded by a spherical dust envelope. The inner radius was increased gradually from 5 pc to 40 pc to simulate cluster evolution, while the outer radius remains constant at 50 pc as illustrated in Figure 1. In addition to a smooth dust distribution, the envelope also contains a clumpy dust distribution with $N = 32$, $D = 2.6$, $H = 5$, accounting for 0%, 50%, and 99% of total dust mass. We apply a standard dust-to-gas ratio of 0.01 and star forming efficiencies (SFEs) of 5%, 15%, and 50%, which is the proportion of star mass in the cluster (Ashman & Zepf 2001).

Whelan et al. (2011) used a dust composition including astronomical silicate and graphite grains with a layer of water ice, PAHs and very small grains, with their distribution following Kim et al. (1994) that fits an extinction curve with $R_V = 4$ using a maximum entropy method solution from Cardelli et al. (1989). We use an ISM dust composition of 75% silicate, 13.33% ortho-graphite, 6.67% para-graphite and 5% PAH in term of mass (Joblin et al. 2011), following classical MRN grain size distribution (Mathis et al. 1977) instead.

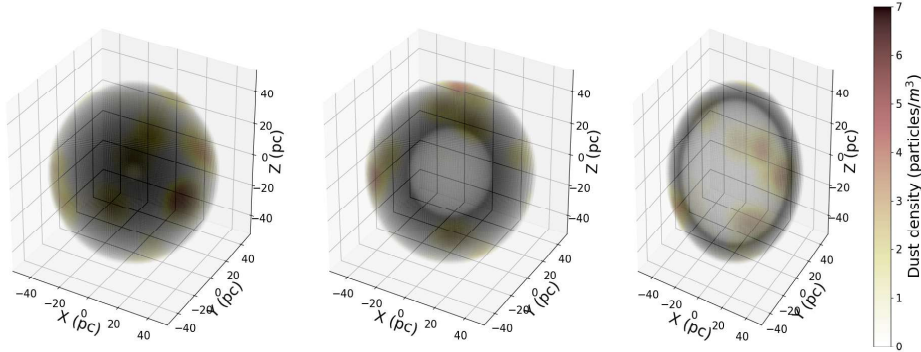


Figure 1. Density maps modelling early evolutionary stages of an embedded SSC with $R_{out} = 50$ pc, $R_{in} = 5$ pc, 25 pc, 40 pc, SFE = 5% and clumpiness = 99%.

4. Results

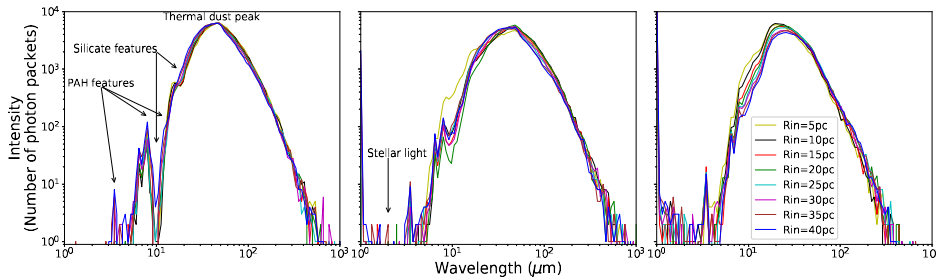


Figure 2. SEDs of models with $R_{out} = 50$ pc, SFE=5%, smooth dust (*left*), $R_{out} = 50$ pc, SFE= 5%, clumpiness = 99% (*middle*) and $R_{out} = 50$ pc, SFE=50%, clumpiness = 99% (*right*).

Similar to Whelan et al. (2011), the SEDs in Figure 2 show the attenuated stellar light from the central source, the thermal emission from the dust envelope, silicate and PAH features. In addition, smooth and optically thick models with high densities (i.e., low SFEs) and small inner radius values tend to significantly absorb the starlight in near IR and create deep silicate absorption. Higher optical depth also shifts the thermal dust peak to shorter wavelength as the envelope is heated to a larger extent. On the other hand, PAH features are more prominent in optically thin models as UV photons are able to reach and excite PAHs.

Although Whelan et al. (2011) did not present detailed calculations of temperature, we have been able to confirm their arguments. Figure 3 shows the averaged final temperature distributions relative to distances in cylindrical coordinate system, with the central source located in the lower left corner. Low optical depth allows the envelope to be heated more homogeneously and reach higher temperature. In contrast, UV flux can only heat the interior of optically thick envelopes, thus our regions are much colder.

Acknowledgments. Tung-Lam was supported by Sorbonne Université’s Doctoral Contract. We would like to thank Ralf Siebenmorgen for kindly providing us with the PAH cross sections in electronic form.

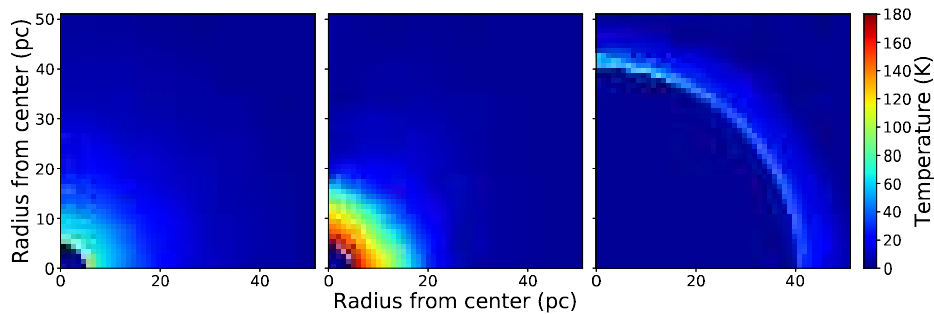


Figure 3. Averaged temperature distributions of model with: $R_m = 5$ pc, $R_{out} = 50$ pc, SFE = 5%, smooth dust (left), $R_m = 5$ pc, $R_{out} = 50$ pc, SFE = 50%, clumpiness = 99% (middle) and $R_m = 40$ pc, $R_{out} = 50$ pc, SFE = 50%, clumpiness = 99% (right).

References

- Ashman, K. M., & Zepf, S. E. 2001, *The Astronomical Journal*, 122, 1888
- Bjorkman, J. E., & Wood, K. 2001, *The Astrophysical Journal*, 554, 615
- Cardelli, J. A., Clayton, G. C., & Mathis, J. S. 1989, *The Astrophysical Journal*, 345, 245
- Draine, B. 1985, *The Astrophysical Journal Supplement Series*, 57, 587
- Draine, B. T., & Li, A. 2007, *The Astrophysical Journal*, 657, 810
- Elmegreen, B. G. 1997, *The Astrophysical Journal*, 477, 196
- Grosset, L., Marin, F., Gratadour, D., Goosmann, R., Rouan, D., Clénet, Y., Pelat, D., & Rojas Lobos, P. A. 2016, in *SF2A-2016: Proceedings of the Annual meeting of the French Society of Astronomy and Astrophysics*, edited by C. Reylé, J. Richard, L. Cambrésy, M. Deleuil, E. Pécontal, L. Tresse, & I. Vauglin, 57. 1610.05177
- Grosset, L., Rouan, D., Gratadour, D., Pelat, D., Orkisz, J., Marin, F., & Goosmann, R. 2018, *Astronomy & Astrophysics*, 612, A69
- Haan, S., Surace, J., Armus, L., Evans, A., Howell, J., Mazzarella, J., Kim, D., Vavilkin, T., Inami, H., Sanders, D., et al. 2011, *The Astronomical Journal*, 141, 100
- Hunter, J. D. 2007, *Computing In Science & Engineering*, 9, 90
- Joblin, C., Tielens, A., & Draine, B. 2011, *European Astronomical Society Publications Series*, 46, 29
- Kim, S.-H., Martin, P., & Hendry, P. D. 1994, *The Astrophysical Journal*, 422, 164
- Leitherer, C., Schaerer, D., Goldader, J. D., Delgado, R. M. G., Robert, C., Kune, D. F., de Mello, D. F., Devost, D., & Heckman, T. M. 1999, *The Astrophysical Journal Supplement Series*, 123, 3
- Lucy, L. 1999, *Astronomy and Astrophysics*, 344, 282
- Marin, F., Grosset, L., Goosmann, R., Gratadour, D., Rouan, D., Clénet, Y., Pelat, D., & Rojas Lobos, P. A. 2016, in *SF2A-2016: Proceedings of the Annual meeting of the French Society of Astronomy and Astrophysics*, edited by C. Reylé, J. Richard, L. Cambrésy, M. Deleuil, E. Pécontal, L. Tresse, & I. Vauglin, 103. 1610.05031
- Mathis, J. S., Rumpl, W., & Nordsieck, K. H. 1977, *The Astrophysical Journal*, 217, 425
- Mathis, J. S., Whitney, B. A., & Wood, K. 2002, *The Astrophysical Journal*, 574, 812
- Portegies Zwart, S. F., McMillan, S. L., & Gieles, M. 2010, *Annual review of astronomy and astrophysics*, 48, 431
- Salpeter, E. E. 1955, *The Astrophysical Journal*, 121, 161
- Sanders, D., & Mirabel, I. 1996, *Annual Review of Astronomy and Astrophysics*, 34, 749
- Siebenmorgen, R., Voshchinnikov, N., & Bagnulo, S. 2014, *Astronomy & Astrophysics*, 561, A82
- Whelan, D. G., Johnson, K. E., Whitney, B. A., Indebetouw, R., & Wood, K. 2011, *The Astrophysical Journal*, 729, 111

3.4 Modelling super star clusters in IRAS 17138-1017

In Lam et al. (2020) we have simulated the SSCs in IRAS 17138-1017 in order to quantify the effects of scattering and thermal emission and compare them with observations. Although we have chosen sensible physical parameters for the SSCs, some of them are only indicative since SSCs are unresolved in our observations. To better characterize the SSC populations in IRAS 17138-1017, we have selected a representative sample and elaborated our model grids for parameter fitting as follows.

3.4.1 SSC sample

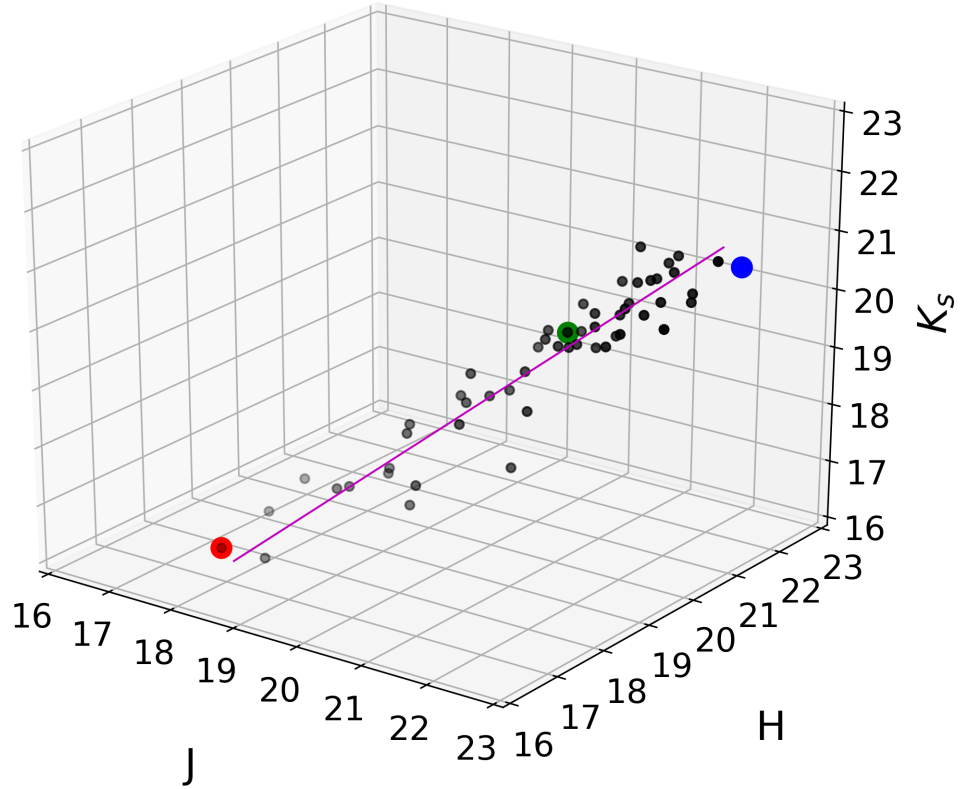


Figure 3.4 – JHK_s magnitudes of the SSC population in IRAS 17138-1017 (black circles) and their first principal component (magenta line). The red, green and blue circles represent the brightest, median and faintest SSCs respectively in terms of their projected values on the first principal component.

Using principal component analysis (PCA), we projected the JHK_s magnitudes of the SSC population in IRAS 17138-1017 on their first principal component and identified the maximum, median and minimum values representing the bright, median and faint SSCs in our sample (see

Fig. 3.4). In addition to the parameters measured in Lam et al. (2020), we fitted each of these SSCs in the K_s -band image with a compound model, which is the sum of a Moffat (1969) function accounting for the source and a second order polynomial accounting for the background. Although these SSCs are unresolved, their half widths at half maximum (HWHMs) indicate some upper limits for their radii R_{out} . Their physical parameters are described in Table 3.2.

Table 3.2 – Properties of sampled SSCs in IRAS 17138-1017

Properties	Bright SSC	Median SSC	Faint SSC
m_J	17.87 ± 0.04	20.97 ± 0.05	22.68 ± 0.11
m_H	17.07 ± 0.02	20.27 ± 0.03	21.61 ± 0.06
m_{K_s}	16.38 ± 0.02	19.74 ± 0.05	20.81 ± 0.08
A_V	$5.35^{+0.10}_{-0.33}$	$3.7^{+0.62}_{-0.69}$	$6.45^{+0.87}_{-0.78}$
$\log(\tau/\text{yr})$	$6.62^{+0.02}$	$6.64^{+0.07}_{-0.02}$	$6.64^{+0.13}_{-0.02}$
$\log(M/M_\odot)$	$7.26^{+0.01}_{-0.16}$	$5.67^{+0.2}_{-0.09}$	$5.35^{+0.27}_{0.15}$
R_{out} (pc)	~ 25	~ 15	~ 15

3.4.2 Model grid

For each SSC, we constructed a grid of models similar to Lam et al. (2020), but adopted the source age, mass and shell outer radius from Table 3.2 and varied the shell inner radius and fractal dust ratio (clumpiness) as in Table 3.3 instead. All models in the same grid use a common Starburst99 (SB99, Leitherer et al. 1999, 2014) spectrum as input for the stellar populations assumed to be concentrated at the center of the models (see Fig. 3.5). Each model represents a combination of the shell inner radius R_{in} and the clumpiness. As proposed by Whelan et al. (2011), these parameters are expected to increase as the central SSC evolves, considering the effects of a stationary stellar wind (Tenorio-Tagle et al. 2007).

Table 3.3 – Parameter grid for the sampled SSCs in IRAS 17138-1017

Parameter	Bright SSC	Median SSC	Faint SSC
R_{in} (pc)	5, 10, 15, 20	5, 10	5, 10
Clumpiness	0, 0.5, 0.99	0, 0.5, 0.99	0, 0.5, 0.99

We plot the total dust density maps of the model grid for the median SSC in Fig. 3.6. Beside 2D projections, we developed a 3D visualization code for MontAGN, which is especially useful in the case of random and asymmetrical structures like fractal. Compared to the smooth dust shell (clumpiness = 0), the most clumpy shells (99%) have highly dense regions interlacing with voids, which illustrates the fractal structure constructed in Sect. 3.2.

For the bright SSC, at first we launched six models, each with 100 000 photon packets for screening purposes. The first three have the largest shell inner radius $R_{\text{in}} = 20$ pc and all selected clumpiness values. The other three have the highest clumpiness value (99%) and all selected R_{in}

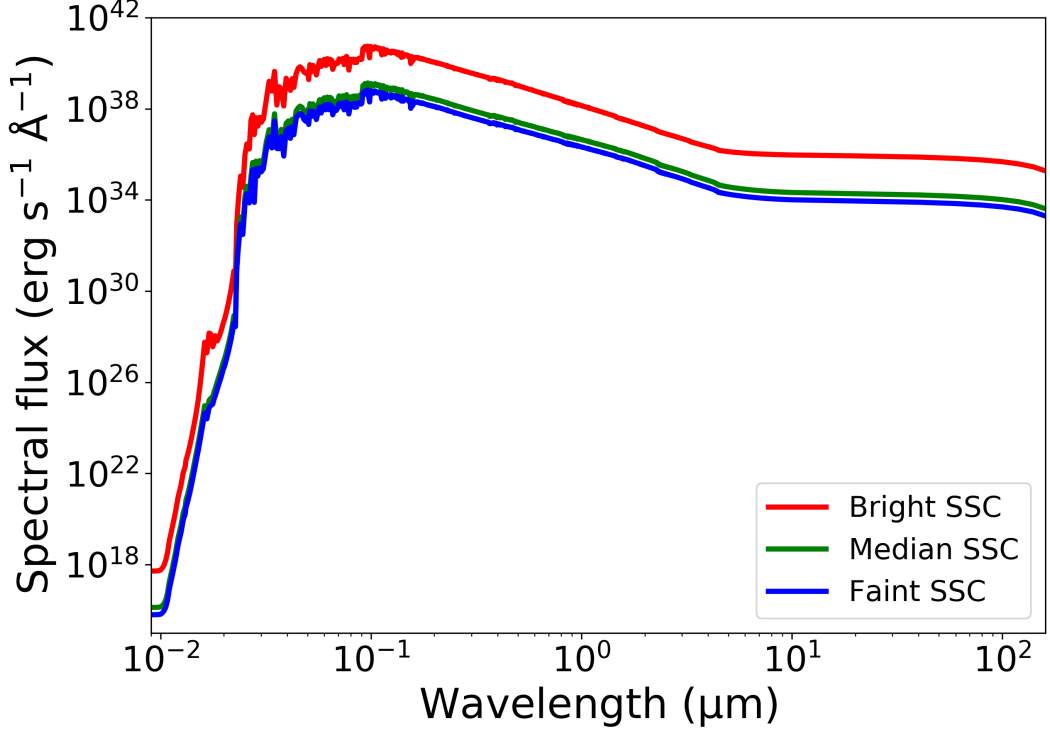


Figure 3.5 – Input SB99 spectra used in the model grids for the sampled SSCs in IRAS 17138-1017

< 20 pc. The resulting spectra are plotted in Fig. 3.7. We can see that even for the thinnest shell of $R_{\text{in}} = 20$ pc, almost no photon is detected in JHK_s bands for the clumpiness of 0 or 0.5, and thus not in agreement with the observations. The same situation happens with $R_{\text{in}} = 5$ pc and clumpiness = 99%. Therefore we ignored these extreme cases and any other models with thicker optical depths for the bright SSC, leaving models with clumpiness = 99% and $R_{\text{in}} = 10, 15, 20$ pc for further consideration. We performed similar screenings for the median and faint SSCs but could not exclude any models. Finally, we simulated each remaining model with four parallel threads of 250 000 photon packets, which are equivalent to 1 000 000 packets in total. The output spectra are plotted in Fig. 3.8. Generally higher clumpy ratios and thinner shells allow more stellar light to escape as expected. In contrast, the models with thicker shells and lower clumpy ratios exhibit more prominent PAH features at $6.2 \mu\text{m}$ and $7.7 \mu\text{m}$, as well as deeper silicate absorption at $9.7 \mu\text{m}$. If the second result is expected, the former one is not so obvious, since PAH excitation requires UV photons that propagate more easily in a clumpy and optical thin medium. On the other hand, the thermal emission only shows subtle changes across models.

3.4.3 Model fitting

For comparison, we also plot the observed fluxes in the JHK_s of the sampled SSCs in Fig. 3.10. Practically, it is possible to select the best-fit models visually based on this plot. However, we would like to fit the SEDs quantitatively using the same method presented in Lam et al.

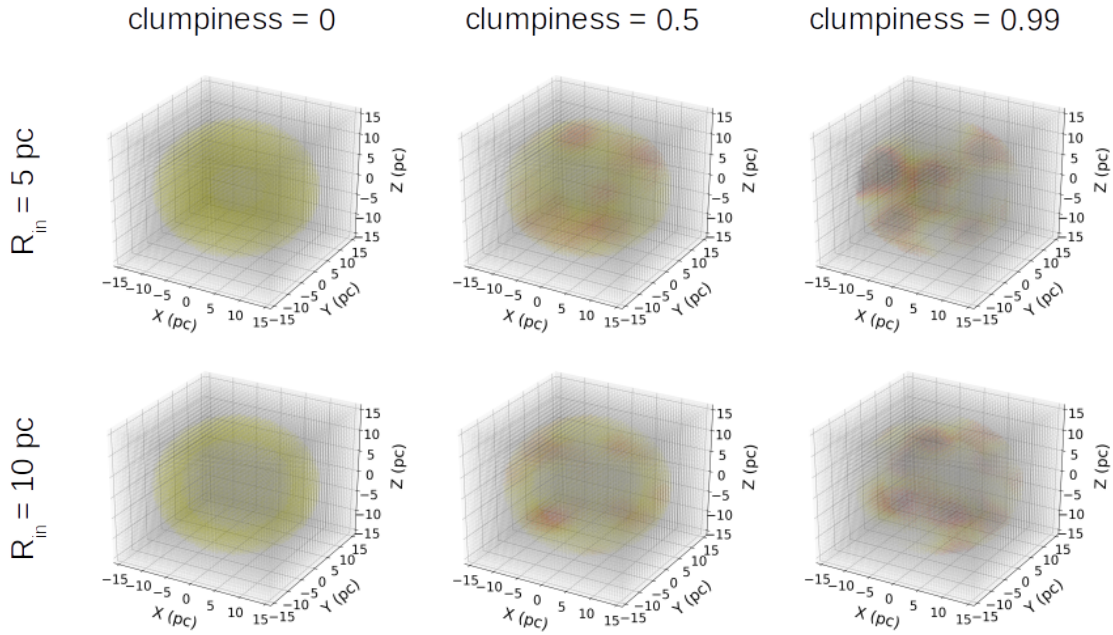


Figure 3.6 – Total dust density maps of the model grid for the median SSC in IRAS 17138-1017. Darker colors represent thicker optical depth.

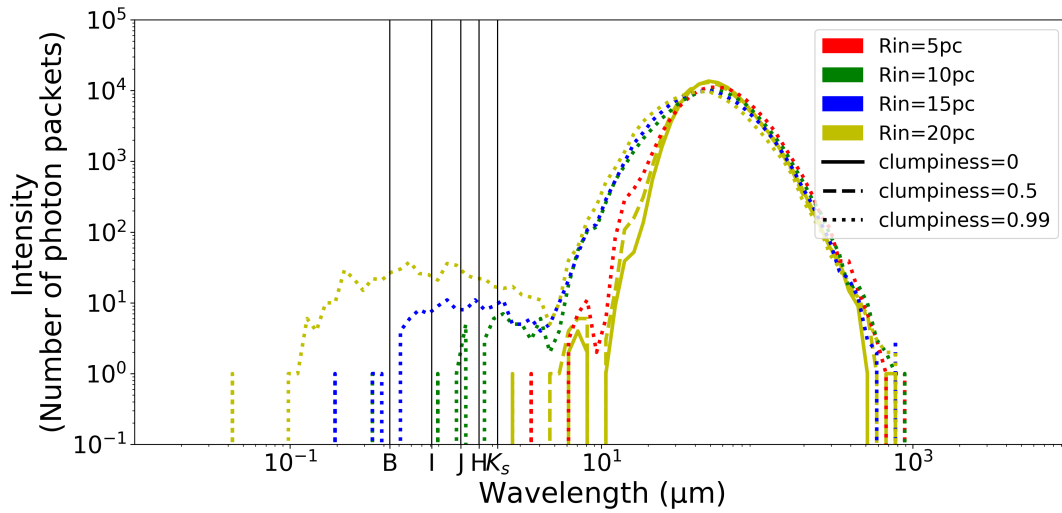


Figure 3.7 – Spectral energy distributions equivalent to 100 000 photon packets of the bright SSC models with the largest shell inner radius R_{in} or highest clumpiness (99%). The position of the $BIJHK_s$ bands are denoted.

(2020). The best-fit models should attain the minimum values of the following quantity:

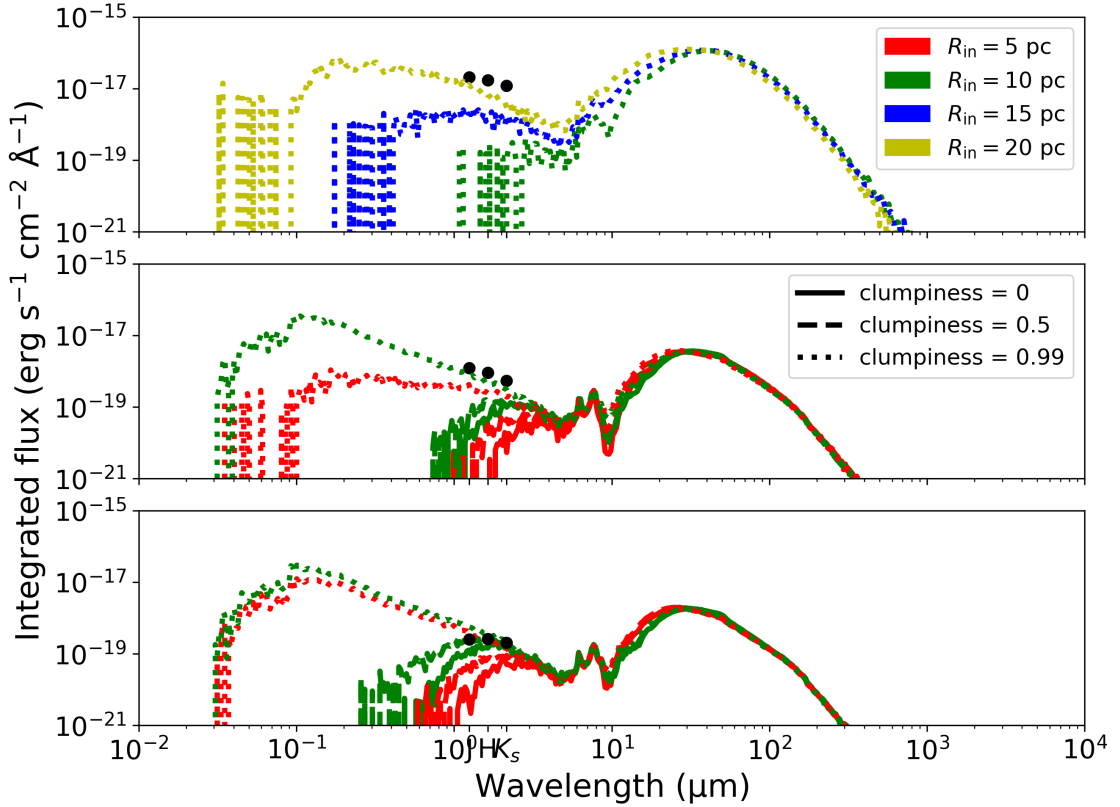


Figure 3.8 – Spectral energy distributions of the bright (top), median (middle) and faint (bottom) SSC models generated using 1 000 000 photon packets. The observed fluxes in the JHK_s bands are marked as black circles.

$$\chi^2(R_{\text{in}}, \text{clumpiness}) = \sum_{\lambda=J,H,K_s} \frac{(m_{\text{obs},\lambda} - m_{\text{MontAGN},\lambda})^2}{\sigma_\lambda^2} \quad (3.15)$$

where $m_{\text{obs},\lambda}$ and $m_{\text{MontAGN},\lambda}$ are the apparent magnitudes from the observations and the MontAGN models, respectively, and σ_λ are the photometric errors.

This method is more robust and practical for finer grids as well as larger parameter spaces, especially when there are more filters or spectral data.

3.4.4 Results and discussions

The fitting results are presented in Table 3.4, which are consistent with the visual comparison in Fig. 3.10. As seen in Fig. 3.9, the best-fit models are relatively optically thin, implying that the dust envelopes have almost dispersed. This agrees well with the cluster ages of over 4 Myr, which are around the emergence timescale of SSCs (e.g., Leisawitz et al. 1989; Eggleton 2006; Portegies Zwart et al. 2010; Morales et al. 2013). Notably, the shell inner radius is larger for the bright SSC. This is also consistent with the idea that the more luminous the star cluster is, the more efficient the dispersion of the shell is. Fainter SSCs have better fitted models. Considering

the bright SSC, the best-fit model still underestimates the observed magnitudes by a large χ^2 value, although it is the optically thinnest model. For reference, we also calculated χ^2 in the case of no dust shell and the central SSC is totally exposed, producing an output spectrum identical to the SB99 input. In terms of the χ^2 value, the no dust scenario better fits the observed magnitudes of the bright SSC. However, since we have found this particular SSC highly extinct in [Lam et al. \(2020\)](#), we still kept the dusty model in Table 3.4. For clarity, we replot the SEDs of the best-fit models in Fig. 3.10.

Table 3.4 – Fitted parameters of the sampled SSCs in IRAS 17138-1017

Properties	Bright SSC	Median SSC	Faint SSC
$R_{\text{in}}(pc)$	20	10	10
clumpiness	0.99	0.99	0.5
χ^2	6664.34	722.03	18.06

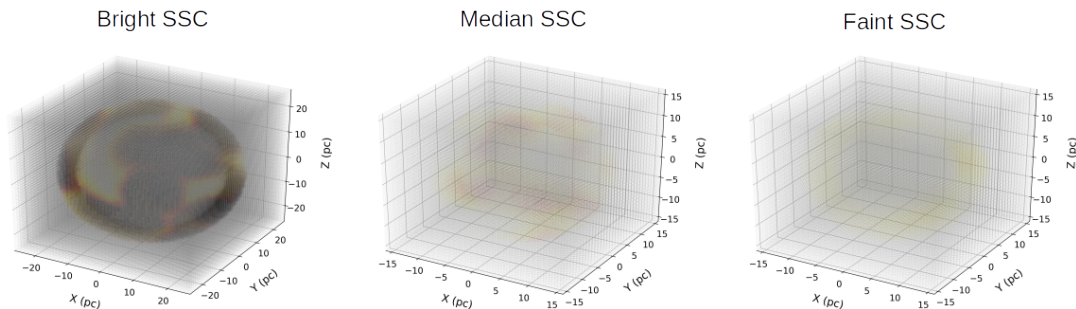


Figure 3.9 – Total dust density maps of the best-fit models for the bright (*left*), median (*middle*) and faint (*right*) sampled SSCs in IRAS 17138-1017. Darker colors represent thicker optical depth.

We also plot the temperature distributions inside the sampled SSCs in Fig. 3.11. In overall brighter SSCs have higher temperatures and their thermal radiations also peak at shorter wavelengths as seen in Fig. 3.10, which is consistent with their stronger input fluxes. Conversely, regions with higher densities or farther to the source tend to have lower temperatures. [Whelan et al. \(2011\)](#) explain that high optical depth quickly attenuates the UV light and limits its heating effect. Nevertheless, our observations are not sufficiently in the thermal infrared domain to compare or validate these models.

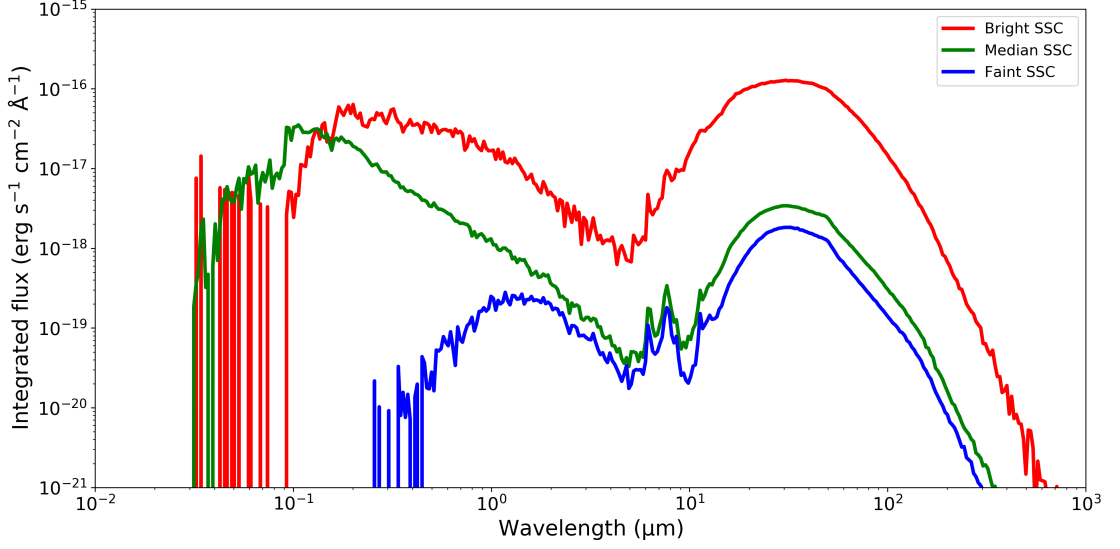


Figure 3.10 – Spectral energy distributions of the best-fit models for the bright (red), median (green) and faint (blue) sampled SSCs in IRAS 17138-1017.

Additionally, we verified the relation between the source luminosity L and the median dust temperature T using the SSC models in Lam et al. (2020). For any given cell, the absorbed energy E_{abs} during the total simulation time Δt is calculated as:

$$E_{\text{abs}} = E \times n_{\text{abs}} = L\Delta t \times \frac{n_{\text{abs}}}{n_{\text{phot}}} \quad (3.16)$$

where n_{abs} is the total number of absorbed photons. The emitted energy is calculated as:

$$E_{\text{em}} = n_{\text{grain}}\Delta t \times \int 4\pi Q_{\text{abs}}(\lambda)\sigma_{\text{cc}}B_{\lambda}(T)d\lambda \quad (3.17)$$

where n_{grain} is the number of grains inside the cell, $Q_{\text{abs}}(\lambda)$ is the absorption efficiency, σ_{cc} is the geometrical cross-section and $B_{\lambda}(T)$ is the black body emission at temperature T . Since we simulated in the mid-IR range:

$$Q_{\text{abs}}(\lambda) \propto \lambda^{-2} \quad (3.18)$$

$$\Rightarrow E_{\text{em}} \propto T^6 \quad (3.19)$$

Assuming local thermodynamic equilibrium, we have:

$$E_{\text{abs}} = E_{\text{em}} \quad (3.20)$$

$$\Rightarrow L \propto T^6 \quad (3.21)$$

This relation is confirmed in Fig. 3.12 below.

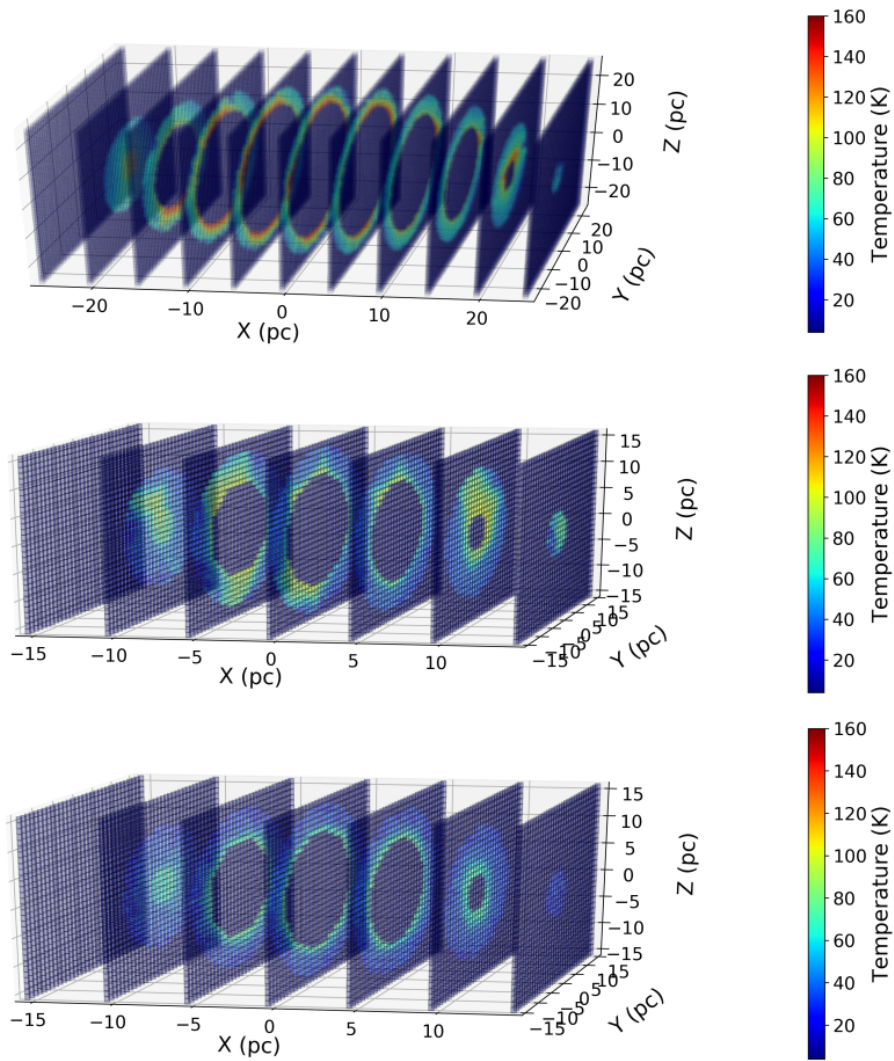


Figure 3.11 – Temperature distributions inside the best-fit models for the bright (*top*), median (*middle*) and faint (*bottom*) sampled SSCs in IRAS 17138-1017.

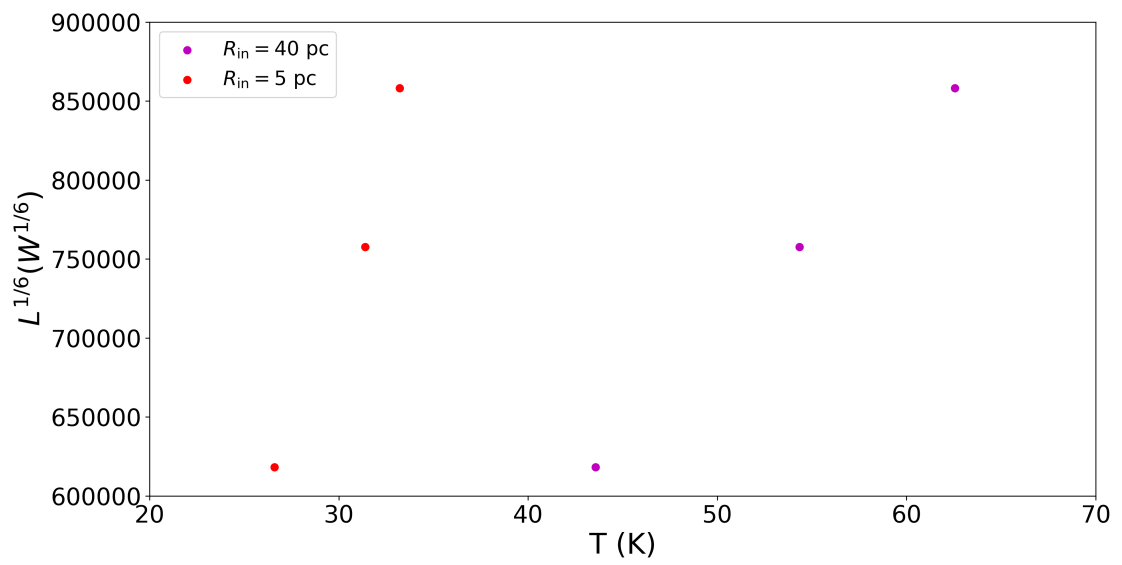


Figure 3.12 – Relation between the source luminosity and the median temperature in SSC models presented in [Lam et al. \(2020\)](#) with the same dust parameters.

Chapter 4

Preparing a JWST Program: Observing extreme star formation in external galaxies

4.1 Scientific justification

Star formation is primarily manifested in the form of clusters (e.g., [Lada & Lada 2003](#)). In extreme cases when two galaxies interact, that is notably the cases of (U)LIRGs, the induced gravitational potential perturbations drag gas and dust together, increase their densities and trigger violent starbursts. The SFR may then reach up to 1000 times the one of the Milky Way ([Kennicutt & Evans 2012](#)), resulting in numerous SSCs. These populations are much younger (< 100 Myr) than globular clusters, but more massive ($\gtrsim 10^4 M_{\odot}$) than open clusters, and highly compact ($\gtrsim 10^3 M_{\odot} \text{ pc}^{-1}$ at core) ([Portegies Zwart et al. 2010](#)). SSCs play a major role in the structural and chemical evolution of those galaxies through the efficient conversion of gas in stellar mass, the production and dissemination of heavy elements by supernovae, the feeding super massive black holes, the injection of turbulence in the interstellar medium (ISM). In their infancy SSCs are enshrouded in the molecular cloud from which they formed, radiating most of their power at IR wavelengths and that is why mid-IR imaging is so crucial to study this early phase. They can be bright enough to be detected beyond Local Group.

The formation and evolution of SSCs are reflected in their distributions of luminosity, mass, size, age, stellar content, dust and gas content, supernovae rate, etc. Their demographics need to be established on a significant sample in order to construct and refine the overall picture, including the connections to the local environments (gas density, proximity of an AGN, interaction with nearby galaxies) and the possible propagation of the burst. However, only a limited sample of SSCs exists in the Local Group ([Portegies Zwart et al. 2010](#); [Krumholz et al. 2019](#), and references therein), while they are much more abundant in LIRGs (e.g., [Vavilkin 2011](#); [Miralles-Caballero et al. 2011](#); [Randriamanakoto et al. 2013a,b](#); [Linden et al. 2017](#); [Lam et al. 2020](#)). Even though extensive surveys of LIRGs have been performed, their SSC populations remain elusive due to the large distances. Even if a good angular resolution has been reached using HST or 8m class telescopes, most of them only provide global analyses of the starburst at the galaxy scale (e.g., [Davies et al. 2003](#); [Piqueras López et al. 2012](#)). The GOALS survey ([Armus et al. 2009](#)) is especially noteworthy since it contains a large sample of 200 galaxies (median distance ~ 94.8 Mpc) and combines imaging and spectroscopic data in different wavelength

ranges from various ground-based and space-borne observatories. The visible and H -band survey by Haan et al. (2011), part of GOALS, is particularly of interest since it corresponds to a large sample (88 galaxies); however this ground-based program is limited within the IR to the H -band, and obviously the deeply dust-enshrouded populations of SSCs are missed at such wavelengths. It also includes the future JWST ERS Program 1328 studying the starburst-AGN connection (Armus et al. 2017). Nevertheless, only a subsample of 22 galaxies have their SSC populations studied using optical data from the HST (Linden et al. 2017). In fact, there are several JWST GTO programs studying nearby archetypical galaxies representing various environments that may host SSCs, including LIRGs (GTO 1204, GTO 1223, GTO 1234, GTO 1265, GTO 1266, GTO 1267, GTO 1268, GTO 1269). Furthermore, JWST will also observe resolved analogs of SSCs in Local Group (GTO 1225, GTO 1226, GTO 1227, GTO 1235). These pilot programs will provide excellent demonstrations and scientific bases for later studies of SSCs in LIRGs with JWST. Nevertheless, currently most of the GTO programs are not aiming at individualizing SSCs themselves, and establishing their demographics. This is what we would like to focus on with this short GO program of 24 hours.

Our goal is to take benefit of the unique convergence of three features offered by MIRI on JWST: the access to a broad range of the thermal IR at a good spectral resolution, the unique spatial resolution at these wavelengths and the unbeatable sensitivity, to study in details SSCs in the peculiar LIRG galaxy IRAS 17138-1017, where the SSC population has been successfully identified (not less than 55 clusters) and analyzed in the near-IR (Miralles-Caballero et al. 2011; Piqueras López et al. 2012; Randriamanakoto et al. 2013a,b; Randriamanakoto 2015; Lam et al. 2020). The LIRG IRAS 17138-1017 is a late-stage merger (Stierwalt et al. 2013), with $\log(L_{\text{IR}}/L_{\odot}) = 11.42$, at a distance of 76 Mpc (Sanders et al. 2003). There is no evidence that favors the presence of a Seyfert-like active nucleus. The SSC population is especially young (3 - 4.5 Myr) in this galaxy (Randriamanakoto 2015; Lam et al. 2020) and still deeply enshrouded in the progenitor molecular clouds as indicated by the large extinction (Depoy et al. 1988). For instance, the galaxy exhibits the most extinct supernovae so far, with $A_V = 15.7$ mag for SN2008cs (Kankare et al. 2008). This youth and the still deep burying of embedded clusters make this LIRG a particularly interesting target to study in the mid-IR the very early phase of a starburst. The good angular resolution is indeed required to separate SSCs and avoid as far as possible confusion that would lead to bias the properties of individual SSCs - such as luminosity - towards high values (see Randriamanakoto et al. 2013b). A typical separation of 200 pc between two SSCs corresponds to 600 mas at 75 Mpc, a resolution reached by JWST at least up to 20 μm .

The mid-IR domain offers several assets: the continuum is essentially due to the heated dust, there are several lines and bands of interest and the effects of extinction will be minimized. In conjunction with the near-IR data, broad-band imaging and spectroscopy from 5 to 28 μm will thus improve further our understanding of the SSCs by bringing several important pieces of information (e.g., Galliano et al. 2005, 2008; Martín-Hernández et al. 2005). In particular, we aim at identifying individual SSCs and derive the following quantities:

- The cluster mid-IR photometry and extinction-corrected bolometric luminosities, essential quantities to establish the luminosity function;
- The temperature of dust and some constrain on its range of variation by comparing the observed continuum to results of radiative transfer models (Whelan et al. 2011). This temperature is directly related to the stellar cluster luminosity and to the structure of the dusty envelope (e.g., internal radius) in which the SSC can be still partly or fully embedded.

- The mass of dust and thus the mass of gas, allowing to derive the mass function of the envelope.
- An unbiased estimation of the extinction based on the the 9.7 μm silicate absorption features that allows to de-redden in a proper way the near-IR photometry.
- By comparison to predictions from radiative transfer codes and stellar evolution models, the cluster age will be constrained through the analysis of the shape of the continuum, the relative intensity of PAH features and de-reddened near-IR colors (Whelan et al. 2011; Lam et al. 2019).
- The warm molecular gas content through the access to pure rotational lines of H_2 (S(7) @ 5.51 μm ; S(6) @ 6.11 μm ; S(5) @ 6.91 μm ; S(4) @ 8.03 μm ; S(3) @ 9.66 μm ; S(2) @ 12.28 μm ; S(1) @ 17.04 μm) that trace the warm gas.
- Indications on the UV radiation field and thus on the young stellar population thanks to PAH line intensities and ratios, and recombination lines of hydrogen (H I (7-6) @ 12.37 μm , H I (9-7) @ 11.32 μm , H I (8-7) @ 19.06 μm). For instance, the PAH line ratio 11.3 μm /7.7 μm can be used as a diagnostic for PAH ionization and, in turn, for UV field intensity.
- Hardness of the ionizing spectrum and/or the existence of shocks will be estimated thanks to forbidden lines such as [Ar III] @ 9.0 μm , [Ar II] @ 7.0 μm , [Ne III] @ 15.5 μm , [Ne II] @ 12.8 μm , and [S IV] @ 10.5 μm . All correspond to species with ionization potentials above 13.6 eV. One notes that the two-line ratio for Ar and Ne can break the degeneracy between the density of ionizing photon and the hardness of the radiation and thus give good estimates of those two quantities.
- Supernova content will be traced through various forbidden lines, notably iron lines [Fe II] @ 5.34, 17.9, 24.5 and 25.9 μm as well as [Ne III] @ 15.5 μm and [Ne II] @ 12.8 μm , whose ratio is an indicator of shock velocity (Rho et al. 2001).

The influence of the galactic environment on those various cluster properties will also be investigated by examining their evolution with respect to the location of the SSCs (spiral arms, nuclear region, tails). This will also give indications on the history of the burst throughout the galaxy and on a possible burst propagation.

4.2 Roadmap

In order to plan a JWST proposal for IRAS 17138-1017, we followed the roadmap suggested by the JWST Documentation¹ (STScI 2016–).

- Mind the important dates:

After delaying many times due to changing circumstances, the deadline for Cycle 1 GO/Archival Research (AR) proposal is 8pm Eastern Time (ET) on November 24, 2020. The JWST TAC will convene in February 2021 and announce the results in March 2021.

1. <https://jwst-docs.stsci.edu/>

The deadline for funding request is May 20, 2021. The JWST is expected to be launched on October 31, 2021 and the commissioning period will last 6 months. After that, the Cycle 1 will be implemented during one year.

- Study JWST and its tools:

We studied the JWST Documentation ([STScI 2016–](#)) to understand JWST instruments, their performance and usage, in particular MIRI. We also learned to use the proposal planning toolbox, particularly the General Target Visibility Tool (GTVT), the JWST Interactive Sensitivity Tool (JIST), the JWST Backgrounds Tool (JBT), the MIRI Simulation tool MIRISim, the Exposure Time Calculator (ETC), the Astronomer’s Proposal Tool (APT). Available configurations and recommended strategies were considered thoroughly for our observations. Example science programs and published proposals were also referred.

- Perform a quick check on the proposal feasibility:

We used the JWST GTVT, the JIST, the JBT to quickly assess the schedulability, visibility and observability of our target.

- Determine exposure parameters with the ETC:

We set up scenes for observations, instrument parameters and calculated the resulting signal-to-noise ratios (SNRs) to derive the best configuration.

- Create the proposal using the APT for submission to STScI.

4.3 Mid-Infrared Instrument (MIRI)

The JWST Mid-Infrared Instrument (MIRI; [Rieke et al. 2015b](#); [Wright et al. 2015](#)) consists of an imager and an integral field spectrograph covering the wavelength range from 4.9 to 28.8 μm . There are four available observing modes with the respective capabilities summarized in the Table 4.1 below. For the observation of IRAS 17138-1017, we are interested in the imaging and medium-resolution spectrometer (MRS) modes, with the aim of extracting the photometry and spectra of SSCs in the mid-IR.

4.3.1 Imaging

The MIRI imager ([Bouchet et al. 2015](#)) is equipped with nine different filters, all allowing to reach diffraction limit with PSF FWHMs of $\sim \lambda/D$ rad (where $D = 6.5$ m) and Strehl ratios $> 90\%$. Table 4.2 lists the characteristics of each filter and Fig. 4.1 plots their bandpasses.

Compared to the FWHM of $0.08''$ in the Gemini K_s band the PSF sizes of MIRI are much larger, so we do not expect to resolve SSCs. We will observe the SSCs in eight filters F560W, F770W, F1000W, F1130W, F1500W, F1800W, F2100W and F2550W, which maximize the spectral coverage and also help calibrating the MRS spectra. In addition, it is possible to trace the dust content and SFR with these filters ([Shipley et al. 2016](#); [Senarath et al. 2018](#)).

The MIRI detectors used by the imager and the MRS are arsenic-doped silicon impurity band conduction (Si:As IBC) ([Rieke et al. 2015a](#)). Their excellent performance in the IR range has

Table 4.1 – MIRI observing modes and their characteristics (STScI 2016–)

Observing mode	Wavelength coverage (μm)	FOV ¹ / Slit size (arcsec/pixel)	Pixel scale (arcsec)	Resolving power ($R = \lambda/\Delta\lambda$)	FWHM ² (arcsec)
Imaging	5.6 – 25.5	74×113	0.11	3.5 – 16.1	0.22 @ 6.25 μm
4-quadrant phase-mask (4QPM) coronagraphic imaging	10.65, 11.4, 15.5	24×24	0.11	14.1 – 17.2	0.22 @ 6.25 μm
Lyot coronagraphic imaging	23	30×30	0.11	4.1	0.22 @ 6.25 μm
Low-resolution spectroscopy	5 – 12	0.51×4.7 (slit size)	0.11	≈ 100 @ 7.5 μm	0.286 @ 7.7 μm
Medium-resolution spectroscopy	4.9 – 28.8	3.9 – 7.7	0.196 – 0.273	≈ 1550 – 3250	0.22 @ 6.2 μm

⁽¹⁾ Field of view. ⁽²⁾ Full width at half maximum.

Table 4.2 – MIRI filter characteristics (STScI 2016–)

Filter	λ_0 (μm)	$\Delta\lambda$ (μm)	FWHM (arcsec)	Diagnostic
F560W	5.6	1.2	0.22	[Fe II], H ₂ S(7) emissions, broadband imaging
F770W	7.7	2.2	0.25	PAH emission, broadband imaging
F1000W	10.0	2.0	0.32	H ₂ S(3), [S IV] emissions, silicate absorption, broadband imaging
F1130W	11.3	0.7	0.36	PAH emission
F1280W	12.8	2.4	0.41	[Ne II] emission, broadband imaging
F1500W	15.0	3.0	0.48	[Ne III] emission, broadband imaging
F1800W	18.0	3.0	0.58	[Fe II], [S III] emissions, silicate absorption, broadband imaging
F2100W	21.0	5.0	0.67	Broadband imaging
F2550W	25.5	4.0	0.82	[O IV], [Fe II] emissions, broadband imaging

already been demonstrated in the Spitzer instruments IRAC (Hora et al. 2008), IRS (Van Cleve et al. 1995; Houck et al. 2004), and MIPS (Gordon et al. 2004), as well as other missions: WISE (Mainzer et al. 2008), MSX (Mill et al. 1994), and Akari (Onaka et al. 2007). The pixel scale of 0.11'' provides Nyquist-sampling or better (FWHM > 2 pixels) in all filters except for the F560W band. Detail specifications are listed in Table 4.3.

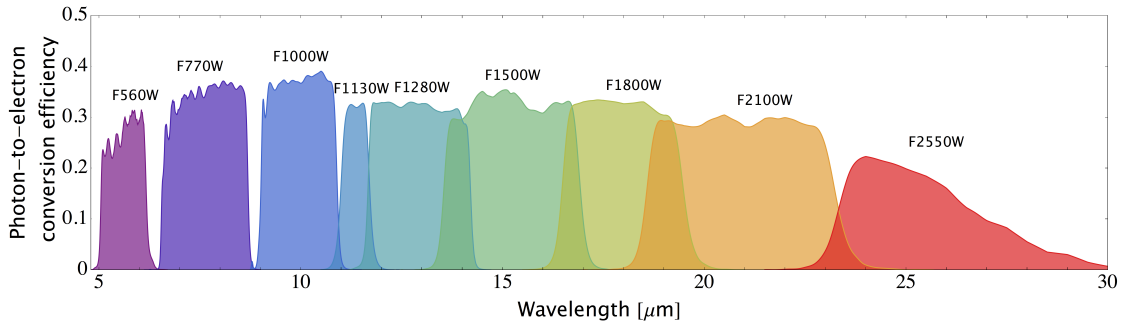


Figure 4.1 – MIRI imaging filter bandpasses (STScI 2016–).

Table 4.3 – MIRI detector specifications (STScI 2016–)

Type	Si:As IBC
Wavelength range	5 – 28 μm
Array size	1024 \times 1024
Pixel size	25 μm
Plate scale	0.11"/pixel
Nominal operating temperature	≤ 6.7 K
Dark current	< 0.2 e $^-$ /s/pix (median value)
Read noise	~ 14 e $^-$ correlated double sampling (CDS)
Latent images	$\sim 0.5\%$
Full well capacity	$\sim 250\,000$ e $^-$
Conversion gain	5.5 e $^-$ /DN

Table 4.4 – MIRI subarrays (STScI 2016–)

Subarray	Size (pixels)	First row corner	First column corner	Usable size (arcsec)
FULL	1024 \times 1032	1	1	74 \times 113
BRIGHTSKY	512 \times 512	51	457	56.3 \times 56.3
SUB256	256 \times 256	51	413	28.2 \times 28.2
SUB128	128 \times 136	889	1	14.1 \times 14.1
SUB64	64 \times 72	779	1	7 \times 7

MIRI imaging offers subarrays of various sizes for bright-target imaging without saturation (Ressler et al. 2015). Fig. 4.2 indicates their locations and Table 4.4 describes their properties in detail. It is possible to cover IRAS 17138-1017 with the subarray SUB128 only and mosaicking is not required. The choice of subarray will be considered later with the ETC.

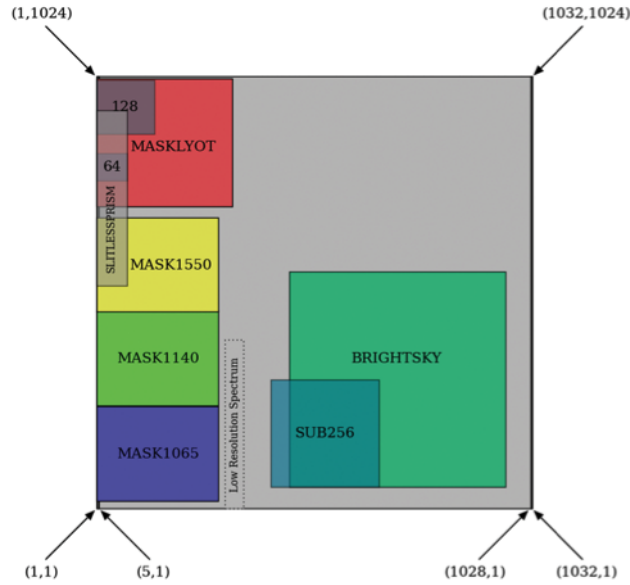


Figure 4.2 – Subarray arrangement on the MIRI imager detector (Ressler et al. 2015).

STScI (2016–) highly recommends and requires dithering for better sampling, detector defect correction, background subtraction and optimal self-calibration (Arendt et al. 2000). Several dither patterns are available for different science cases and listed in the Table 4.6. We will select the 4-point dither pattern for extended sources. The particular pattern will be determined later depending on the choice of subarray if necessary.

Table 4.6 – MIRI dithering patterns (STScI 2016–)

Dither patterns	Description	Application
4-Point-Sets	Various sets of four dithering points optimized for point and extended sources, short and long wavelength ranges, and different subarrays (Fig. 4.4). Mirror parity also available. PSF subsampling in all subarrays/bands.	Best choice for most science cases.
CYCLING	311 points representing a random Gaussian distribution. Starting point and number of points defined by the user.	Good option for many science cases.

2-Point	Two separated exposures on the array with the PSF peaks on different rows and columns for simple background subtraction and detector defect mitigation.	Justification required regarding the science use and data quality.
REULEAUX	Sets of 12-point dithers forming a reuleaux triangle with optimal pointing distance and slew time, limiting the PSF peaks on the same row or column and reducing bright source persistence (Fig. 4.3). Different sizes available for different subarrays.	For observations of unresolved or barely resolved sources with complex designs.
Coordinated Parallels	Customized dither patterns with two, three, four, and nine steps for different filters, correcting bad pixel and sampling subpixel for both instruments.	Parallel observations

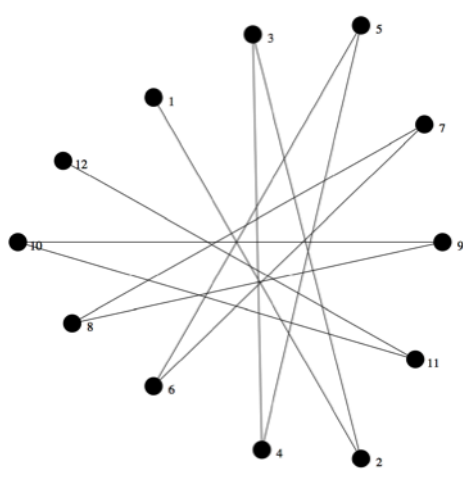


Figure 4.3 – REULEAUX dither pattern (STScI 2016–).

If we observe IRAS 17138-1017 with any subarray larger than SUB128, an off-source region may be used for background subtraction instead of a dedicated background observation. It is also possible to use MIRI MRS Simultaneous Imaging for this purpose. Target acquisition is also not required and not supported for MIRI imaging.

4-Point Extended on BRIGHTSKY

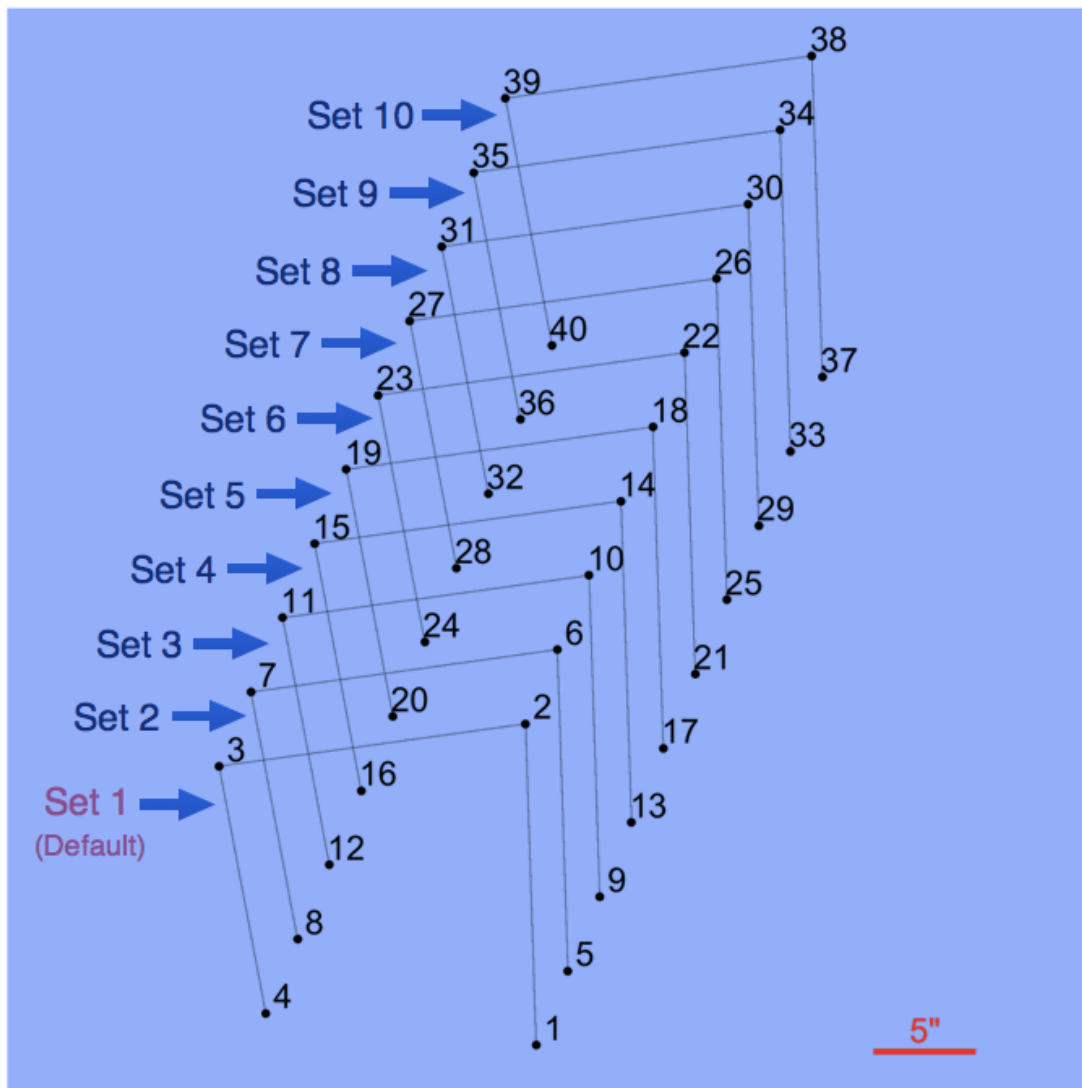


Figure 4.4 – Sets of 4-point dither pattern for extended sources on the BRIGHTSKY subarray (STScI 2016–).

4.3.2 Medium-resolution integral field unit spectroscopy

The MIRI medium-resolution spectrometer (MRS; Wells et al. 2015) splits the FOV into multiple image slices, disperses their spectra then combines them into a 3D data cube containing two spatial and one spectral dimension as illustrated in Fig. 4.5. These are implemented by four integral field unit (IFU) channels, each has three grating settings SHORT (A), MEDIUM (B), and LONG (C) and a different FOV size. A MRS exposure observes simultaneously four channels but with only one grating setting, covering disjointed wavelength ranges. Using all three grating settings and four channels produces a continuous spectrum from 4.9 to 28.3 μm . Their characteristics are described in Table. 4.7 and Fig. 4.6. We would like to observe IRAS 17138-1017 in the entire spectral range from 4.9 to 28.3 μm using all three grating settings and four channels. Previous Spitzer IRS studies of IRAS 17138-1017 at lower resolutions have revealed fine structure and molecular hydrogen lines, PAH and silicate features, as well as continuum emission in this wavelength range, providing valuable insights on the star formation, AGN and black hole activities (Pereira-Santaella et al. 2010; Alonso-Herrero et al. 2012, 2013). We also want to extract the SSC spectra and compare them to MontAGN models.

Table 4.7 – MIRI IFU channels (STScI 2016–)

Channel	Sub-band	Wavelength range (μm)	Resolving power ($\lambda/\Delta\lambda$)	FOV (arcsec)	Pixel scale (arcsec)	Number of slices	Slice width (arcsec)
Channel 1	SHORT (A)	4.88–5.75	3320–3710	3.2×3.7	0.196	21	0.176
	MEDIUM (B)	5.63–6.63	3190–3750				
	LONG (C)	6.41–7.52	3100–3610				
Channel 2	SHORT (A)	7.48–8.76	2990–3110	4.0×4.8	0.196	17	0.277
	MEDIUM (B)	8.71–10.23	2750–3170				
	LONG (C)	10.02–11.75	2860–3300				
Channel 3	SHORT (A)	11.52–13.49	2530–2880	5.5×6.2	0.245	16	0.387
	MEDIUM (B)	13.36–15.65	1790–2640				
	LONG (C)	15.43–18.08	1980–2790				
Channel 4	SHORT (A)	17.65–20.94	1,460–1,930	6.9×7.9	0.273	12	0.645
	MEDIUM (B)	20.41–24.22	1680–1770				
	LONG (C)	23.88–28.34	1630–1330				

The MIRI MRS is undersampled in terms of both the PSF and the spectral line spread function (LSF). Fig. 4.7 plots the spatial resolution and sampling of the MIRI MRS over its spectral range. If half-integer dithering offsets are performed in all four channels and both directions, diffraction limit (solid black line) is almost attained for $\lambda \geq 8 \mu\text{m}$. For $\lambda < 8 \mu\text{m}$, the along-slice FWHM $\approx 0.31''$ (dashed black line). In reality, the across-slice (solid colored lines) and along-slice (dashed colored lines) sampling vary around the ideal Nyquist-sampling (dotted

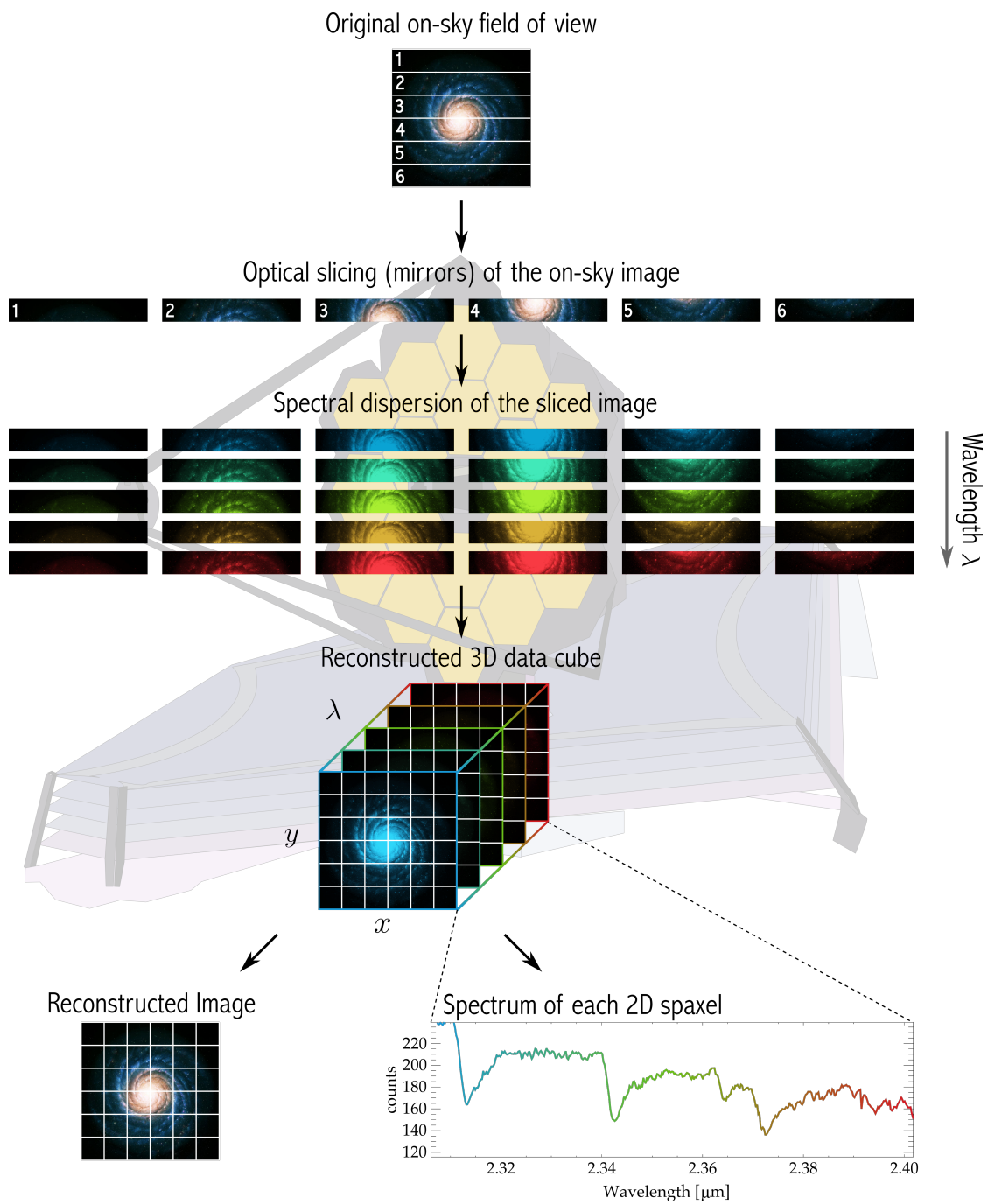


Figure 4.5 – Working principle of the MIRI MRS IFU (STScI 2016–).

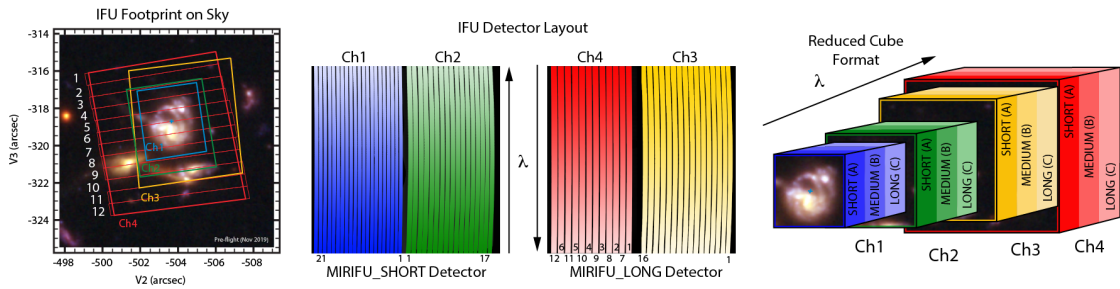


Figure 4.6 – Left: FOVs of IFU channels on the sky. Middle: Spectral dispersion onto the MRS detectors from IFU channels. Right: Reduced data cube containing two spatial and one spectral dimension (STScI 2016–).

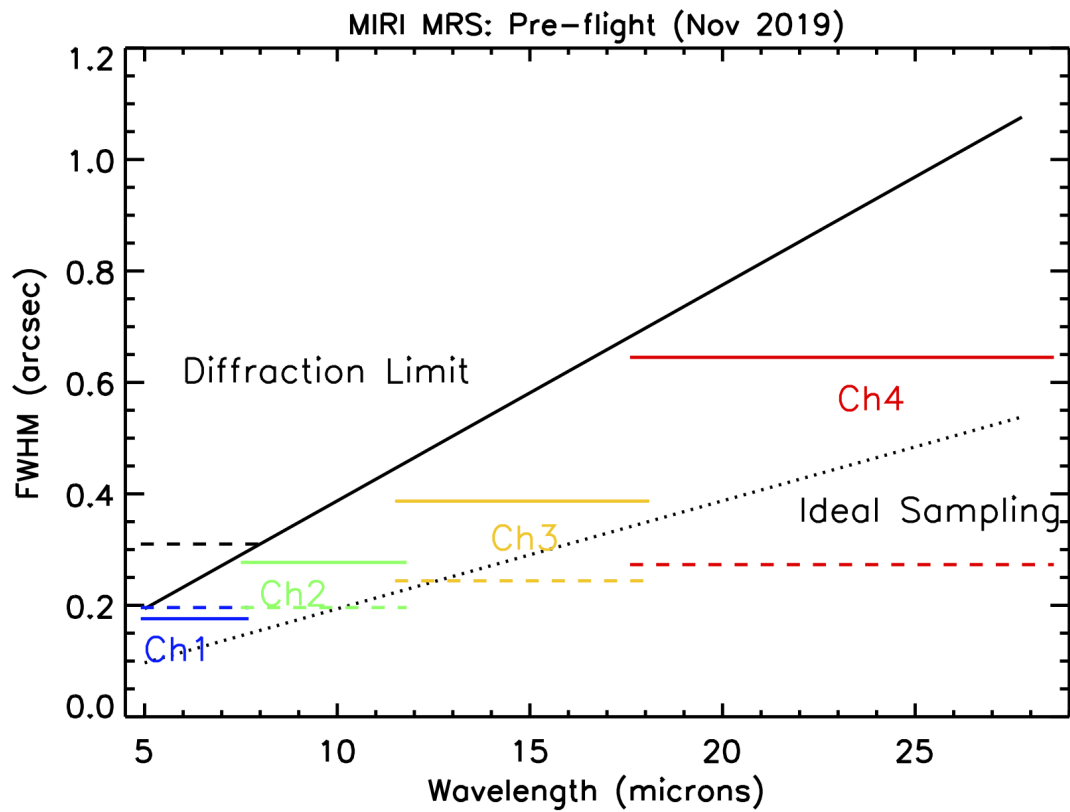


Figure 4.7 – MIRI MRS PSF and sampling (STScI 2016–).

black line). Given the spatial resolution of the MIRI MRS, we do not expect to isolate individual SSCs. However the Gemini images will help us locate SSC-populated regions and compare their spectra to the galaxy background.

Table 4.8 – Performance of MIRI MRS dither patterns (STScI 2016–)

Target	Channel	Number of points	PSF separation (FWHM)				Overlap area (arcsec ²)				Sampling quality				
			1	2	3	4	1	2	3	4	1	2	3	4	
Point sources	ALL	2	7.3	6.6	4.3	2.8	3.9	8.8	20.7	38.2	Fair	Fair	Good	Good	
		4	7.7	6.9	4.5	2.9	3.5	8.2	19.8	37.1	Good	Good	Good	Good	
	1	2	7.3	6.6	4.3	2.8	3.9	8.8	20.7	38.2	Fair	Fair	Good	Good	
		4	7.7	6.9	4.5	2.9	3.5	8.2	19.8	37.1	Good	Good	Good	Good	
	2	2	11.4	10.3	6.7	4.3	1.1	4.4	13.1	28.2	Fair	Fair	Good	Good	
		4	12.0	10.8	7.0	4.5	0.9	3.9	12.2	27.0	Good	Good	Good	Good	
	3	2	15.9	14.3	9.3	6.0	0.0	0.7	6.5	18.5	Poor	Fair	Fair	Fair	
		4	16.6	14.9	9.7	6.3	0.0	0.4	5.8	17.2	Poor	Good	Good	Good	
	4	2	21.9	19.6	12.8	8.3	0.0	0.0	1.6	9.3	Poor	Poor	Fair	Fair	
		4	22.9	20.6	13.4	8.7	0.0	0.0	1.1	8.0	Poor	Poor	Good	Good	
	Extended sources	ALL	2	3.1	2.8	1.8	1.2	9.3	16.1	30.7	51.4	Fair	Fair	Good	Good
			4	3.1	2.8	1.8	1.2	9.2	15.9	30.5	50.6	Good	Good	Good	Good
1		2	0.4	0.4	0.2	0.2	12.3	19.8	36.2	57.8	Fair	Fair	Fair	Poor	
		4	0.4	0.4	0.2	0.2	12.3	19.8	36.1	57.6	Good	Fair	Fair	Poor	
2		2	0.5	0.5	0.3	0.2	12.1	19.6	35.9	57.4	Fair	Fair	Fair	Fair	
		4	0.5	0.5	0.3	0.2	12.1	19.5	35.8	57.2	Fair	Good	Fair	Fair	
3		2	0.7	0.7	0.4	0.3	11.9	19.3	35.4	56.9	Poor	Fair	Good	Fair	
		4	0.7	0.7	0.4	0.3	11.8	19.2	35.3	56.6	Poor	Fair	Good	Fair	
4		2	1.1	1.0	0.7	0.4	11.4	18.7	34.6	55.9	Poor	Poor	Poor	Good	
		4	1.1	1.0	0.7	0.4	11.3	18.5	34.3	55.4	Poor	Poor	Poor	Good	

As a result, dithering is required for optimal sampling, as well as bad-pixel removal and decent PSF separation between exposures (STScI 2016–). Dither patterns are defined by their primary channel, number of points, spatial extend of the sources and the direction on the sky. Their expected performance in terms of the PSF separation between exposures, the exposure overlap area and the spatial sampling quality in each channel are described in Table 4.8. We selected a dither pattern optimized for extended sources, maximizing the field overlap in each

band to cover the galaxy. Due to the field distortions and discontinuities, 2-point dithering does not provide sufficient spatial and spectral sampling as theoretically expected, thus we adopted a 4-point pattern. Finally we chose ALL for the Primary Channel since it is the only pattern with good sampling quality in all channels. In addition to dithering, given the FOVs of MRS channels, we also considered to create a mosaic to better cover our target. The particular size will be determined later using the APT.

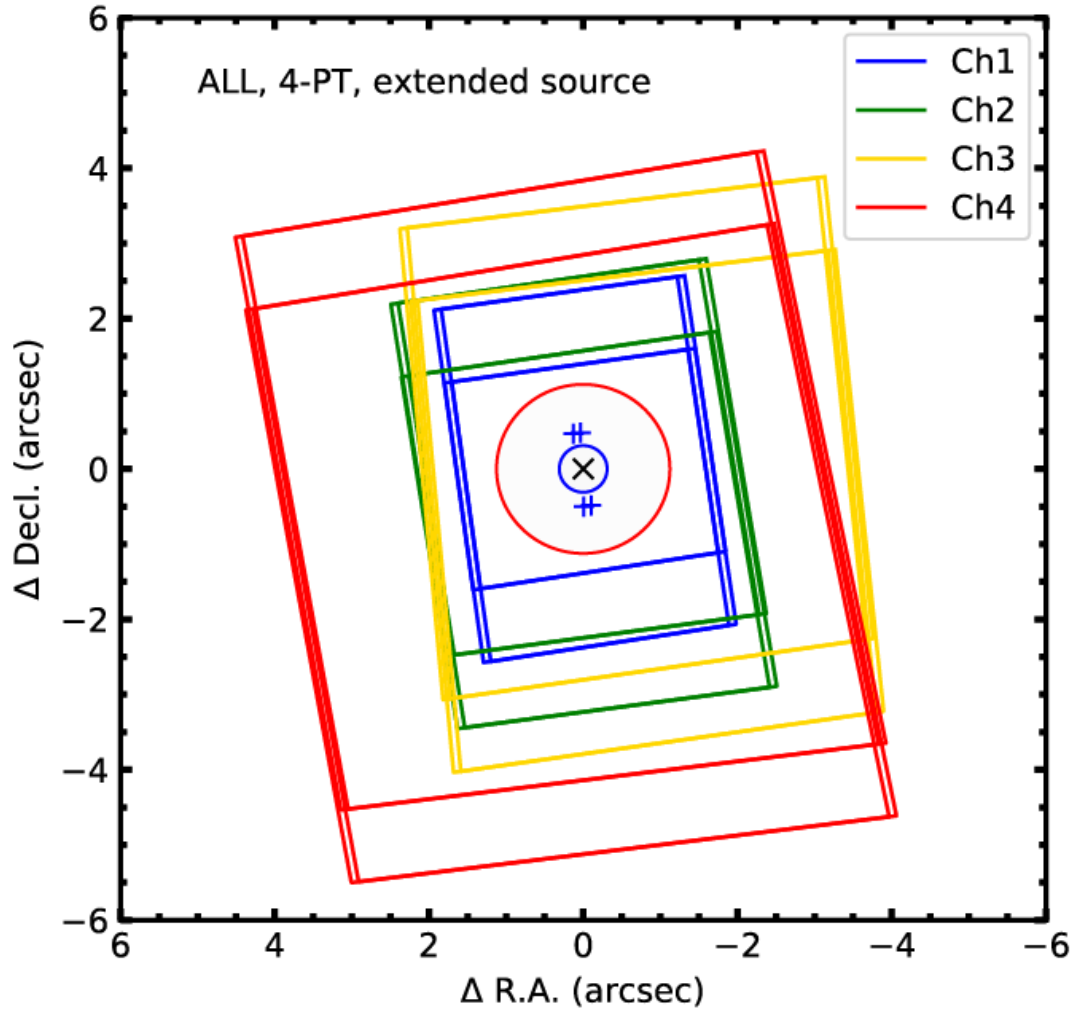


Figure 4.8 – Example dither pattern for the ALL, 4-point and extended source configuration. Circle sizes correspond to twice the PSF FWHM at 8 (blue) and 28 μm (red) (STScI 2016–).

As discussed in section 4.4.3 below, various types of background signal affect JWST observations, especially the substantial thermal emission from JWST itself at $\lambda \geq 15\mu\text{m}$. Therefore background subtraction is necessary. However, since we expect IRAS 17138-1017 to extensively occupy the MRS scene even with mosaicking, a dedicated background observation should be considered in the APT. On the other hand, target acquisition is unnecessary since the blind pointing accuracy of $0.10''$ (1σ radial) is enough for our extended target.

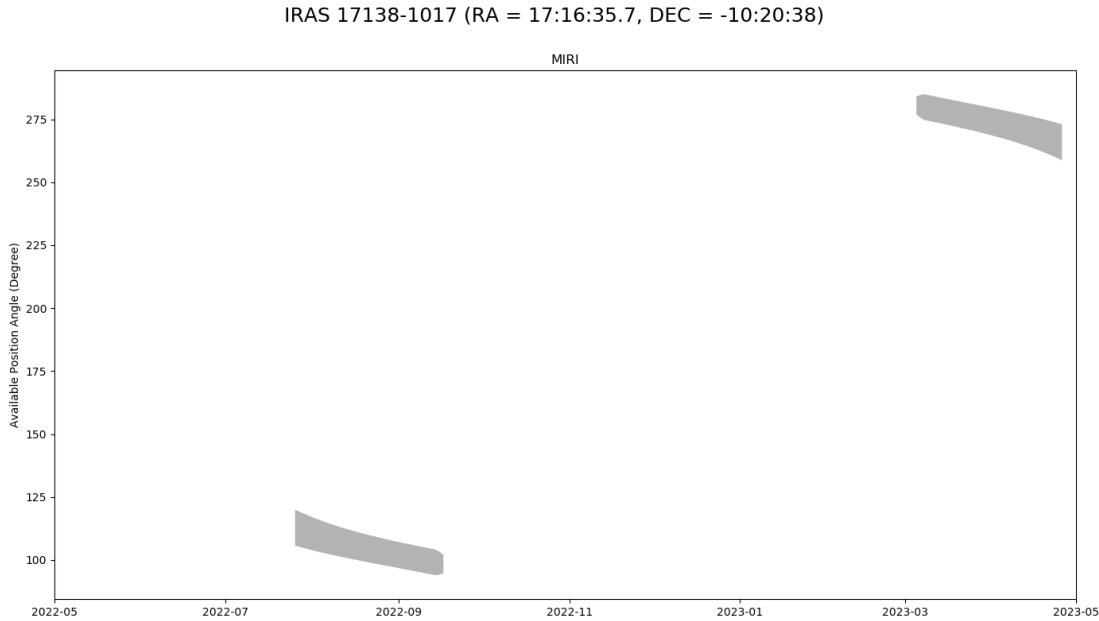


Figure 4.9 – Visibility of IRAS 17138-1017 for MIRI during Cycle 1.

We are also interested in simultaneous imaging if there is no problem with the data volume and saturation, in particular with the filters F560W, F770W and F1000W. Besides improving the MRS astrometry, we may use these images as dedicated backgrounds for imaging data, as well as control fields to remove foreground stars and background galaxies from the SSC sample. It is also promising to study their nature and distribution compared to models. Detailed configuration will be specified later in the APT.

4.4 Feasibility of observations

Before going deeper into a full proposal, in this section we will use several proposal planning tools to perform a quick test on the feasibility of our observations. These tools are for exploratory purposes only and detailed analyses will be available later in the ETC and the APT.

4.4.1 JWST General Target Visibility Tool (GTVT)

Although there is no specific requirement on the observation time and position angle (PA) for our proposal, we would like to have a quick look on the visibility of our targets. The General Target Visibility Tool (GTVT; [STScI 2016](#)) written in Python provides an overview of available temporal windows and corresponding PAs for a given target. The program assumes the orbital ephemeris for the expected launch date of October 2021.

Figure 4.9 plots the visibility of the galaxy IRAS 17138-1017 during Cycle 1 for the instrument MIRI. We expect JWST to be launched on October 31, 2021. The Cycle 1 will start 6 months later after commissioning and last one year, from May 2022 to May 2023. The JWST viewing is constrained by its sun shield and the target visibility is highly dependent on its ecliptic latitude. Given the low ecliptic latitude of IRAS 17138-1017, we could see that the available PAs are

restricted to two narrow ranges near 110° and 270° only, with the nominal roll flexibility of $\pm 5^\circ$. Each window lasts for about 50 days. Nevertheless, the final schedulability will be determined by the APT.

4.4.2 JWST Interactive Sensitivity Tool (JIST)

The JWST Interactive Sensitivity Tool (JIST; STScI 2016–)² allows users to quickly trace out SNRs across filters, for different observing modes and varied settings of source flux density and exposure time. Basically, JIST provides pre-calculated and interpolated results from the ETC, given several assumptions for simplicity and speed. Particularly, the scene contains a single point source with a flat SED only and 120% of the minimum zodiacal background on June 19, 2019 at $RA = 17^{\text{h}}26^{\text{m}}44^{\text{s}}$, $Dec = -73^\circ 19^{\text{m}}56^{\text{s}}$. A single integration is applied. Advanced settings and calculations will be performed later with the ETC.

For our proposal, we will consider two extreme cases: the faintest SSC (Fig. 4.10) and the brightest SSC (Fig. 4.11). In the wavelength range of the MIRI imaging mode, the flux of the SSCs generally increases towards longer wavelength. For the faintest SSC, the flux is in the order of $-2.5 \lesssim \log(\text{mJy}) \lesssim -0.5$. Varying the source flux in this range shows promising SNRs even for a short exposure time, for example 50.55 seconds as seen in Fig. 4.11. We may also scale up the SNRs by the square root of the number of dithered exposures. On the other hand, the flux of the brightest SSC is in the order of $-0.9 \lesssim \log(\text{mJy}) \lesssim 2.4$. Even for the shortest exposure time of 5.55 seconds, saturation starts appearing at $\log(\text{mJy}) = 0.6$ and affects all filter at $\log(\text{mJy}) = 2$. As a result, we will consider using a subarray to mitigate this problem.

4.4.3 JWST Backgrounds Tool (JBT)

Multiple sources of infrared background emission, both in-field and scattered, affect JWST observations: the zodiacal cloud, Milky Way Galaxy, and the JWST Observatory itself (thermal emission). There are spatial and temporal variability, as well as uncertainty in the background level. The JWST Backgrounds Tool (JBT; STScI 2016–) is a Python and command line tool that provides and visualizes the total background intensity and its components depending on the sky position, the day of the year and the wavelength. Calculations are retrieved from a background model precompiled by STScI and cached on the Mikulski Archive for Space Telescopes (MAST). This model is also shared with the JWST ETC and the JWST scheduling system.

Figure 4.12 plots the background levels over one year at the sky position of IRAS 17138-1017 for the MIRI imaging filters. There are 106 observable days as determined by the GTVT. The backgrounds change over time by different magnitudes depending on the filter. The low ecliptic latitude of our target leads to high minimum backgrounds and seasonal variability. The maximum background is on Day 63 and the minimum background is on Day 207 for all filters. We plot the background intensity spectrum and its components on Day 63 in Fig. 4.13. At wavelengths shorter than $15 \mu\text{m}$, the zodiacal emission dominates the background and its strong variation is manifested. At longer wavelengths, the thermal self-emission takes over and is assumed to be constant over time.

We should consider whether our observations would be background-limited, in other words whether the SNR would be sensitive to the background levels. The Background Limited special requirement in the APT allows scheduling observations at periods of low background. We will verify this issue later using the ETC.

2. <https://jist.stsci.edu/>

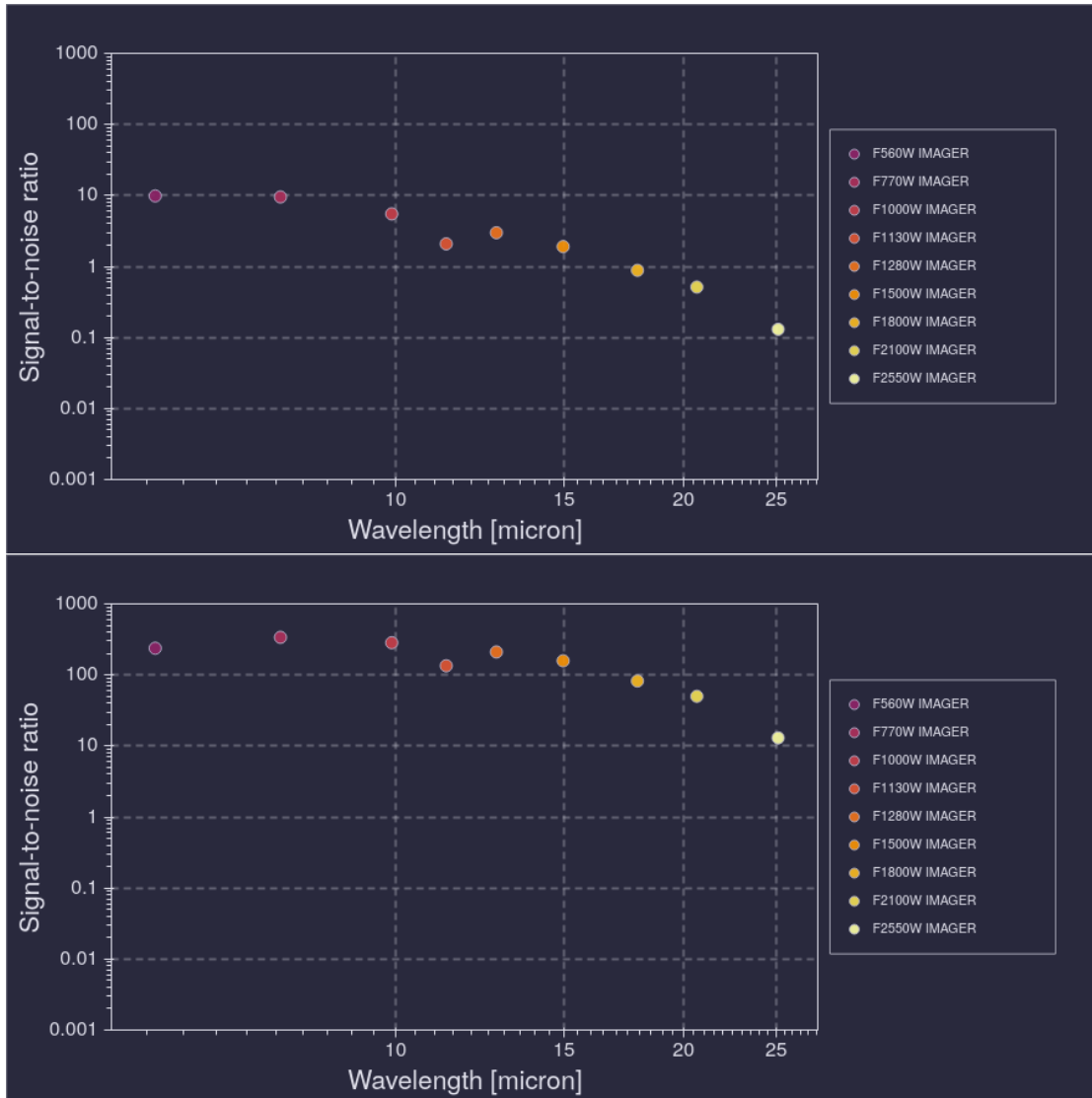


Figure 4.10 – SNRs for the faintest SSC assuming the minimum ($\log(\text{mJy}) \approx -2.5$, upper panel) and maximum ($\log(\text{mJy}) \approx -0.5$, lower panel) flux values in the wavelength range of the MIRI imaging mode. The exposure time is set at 50.55 seconds.

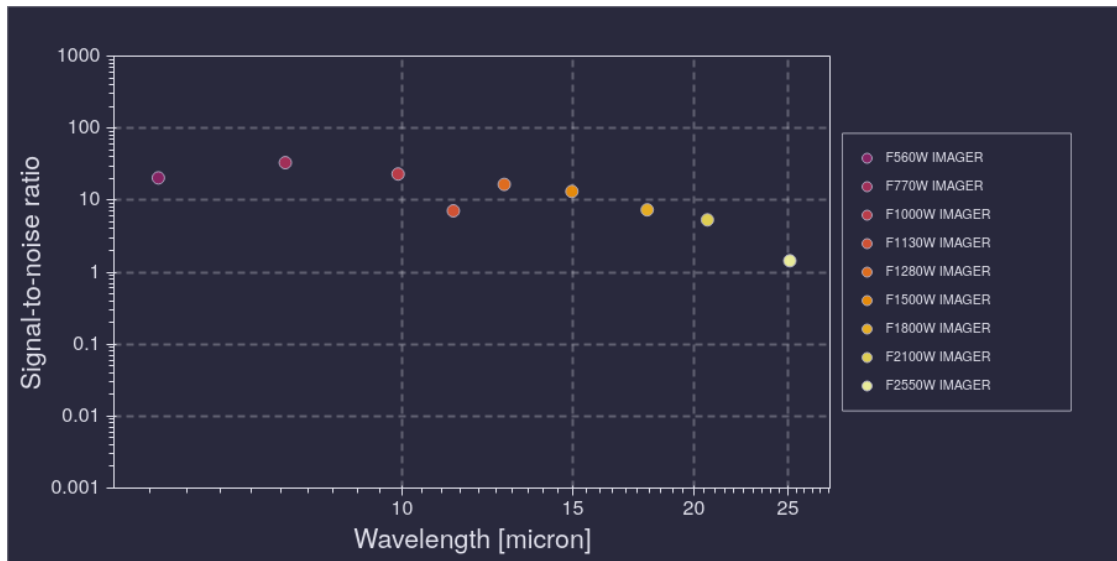


Figure 4.11 – SNRs for the brightest SSC assuming the minimum flux value ($\log(\text{mJy}) \approx -0.9$) in the wavelength range of the MIRI imaging mode. The exposure time is set at 5.55 seconds.

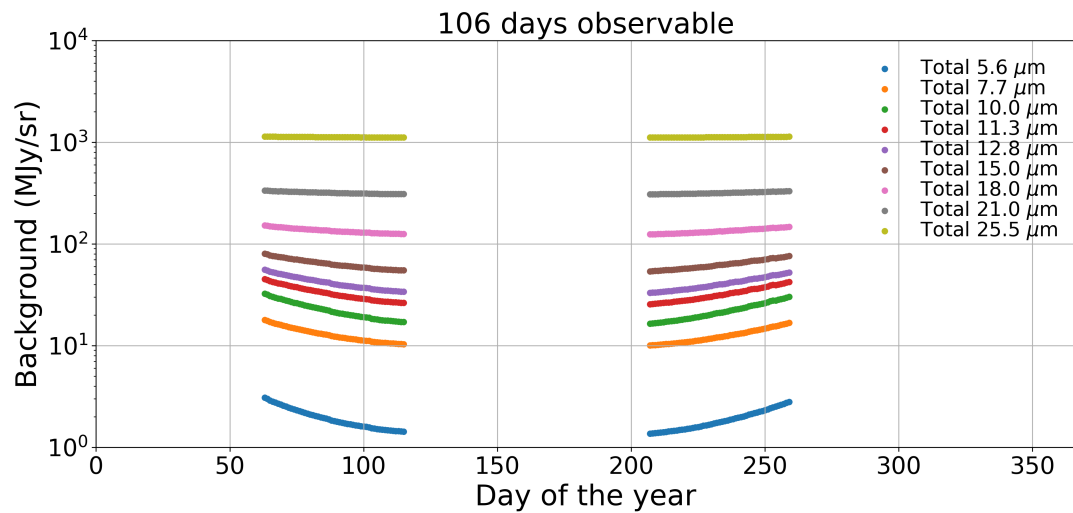


Figure 4.12 – Total background levels over one year at the sky position of IRAS 17138-1017 for the MIRI imaging filters.

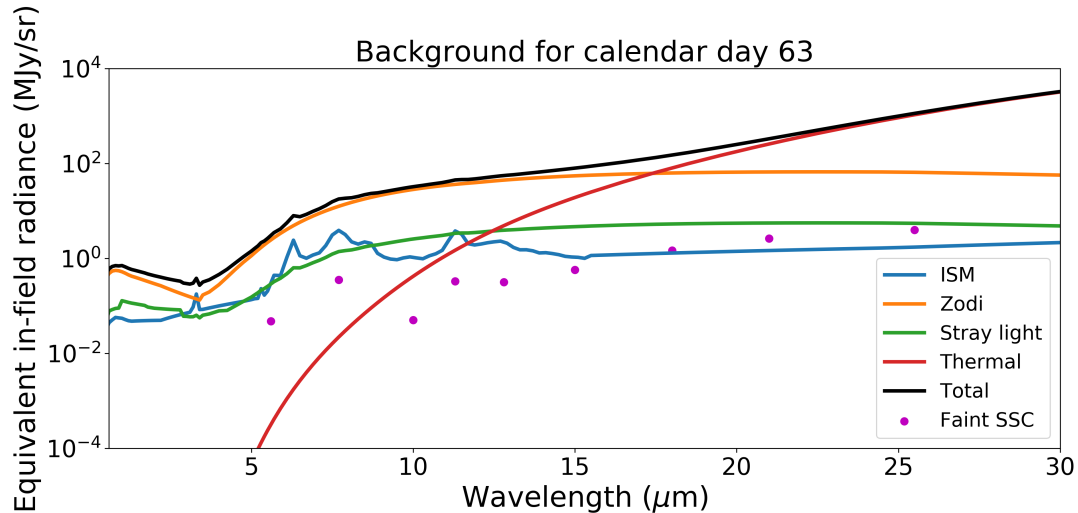


Figure 4.13 – Background intensity spectrum and its components on Day 63 at the sky position of IRAS 17138-1017.

4.5 Exposure Time Calculator (ETC)

In order to select the best exposure settings for our observations in terms of SNR, we use the graphical user interface³ of the JWST Exposure Time Calculator (ETC; STScI 2016–). Users may specify sources, construct scenes from them and perform calculations with different JWST instruments and observing modes. Sources and scenes may be shared across calculations, together they are organized in the form of workbooks. The ETC facilitates the "copy and modify" approach for sources, scenes, calculations, workbooks and automatically updates results following changes, which can be plotted and compared to each other.

In detail, the ETC's underlying engine Pandeia (Pontoppidan et al. 2016) models both the spatial and spectral dimensions of individual detector pixels taking account of correlated read noise, inter-pixel capacitance and saturation. Realistic PSFs for each instrument mode are generated from WebbPSF (Perrin 2011; Perrin et al. 2012, 2014). In addition, Pandeia also simulates both data acquisition and data post-processing, but essentially it is not an observation simulator and does not model the full detector with higher-order effects such as field distortion. To fully simulate MIRI observations, we will instead use MIRISim in Chapter 5.

4.5.1 Scenes and sources

To determine the proper number of groups and integrations for each filter, we considered two extreme scenes: the brightest SSC and the faintest SSC. Our goal is to achieve the highest possible SNRs for the faintest SSC without saturating the brightest SSC.

The scene of each SSC consists of a point source representing the SSC and a flat, extended, circular source representing the galaxy background as depicted in Fig. 4.14. The SSC SEDs are adopted from the MontAGN simulations in Chapter 3 and plotted in Fig. 3.10. The radius of the galaxy background was set to 2 arcsec to facilitate the imaging aperture photometry only,

3. <https://jwst.etc.stsci.edu/>

in practice we would use PSF photometry with STARFINDER instead. To simulate the galaxy background SEDs (Fig. 4.16), we normalized the SED model of IRAS 17138-1017 from [Herrero-Illana et al. \(2017\)](#) to $m_K = 11.81$ for the bright and $m_K = 13.77$ for the faint SSC based on measurements of the data in [Lam et al. \(2020\)](#). Then we reddened them using the [Weingartner & Draine \(2001\)](#) Milky Way $R_V = 3.1$ extinction law with $A_V = 1.88$ based on [Schlafly & Finkbeiner \(2011\)](#) measurements from the NASA/IPAC Extragalactic Database (NED).

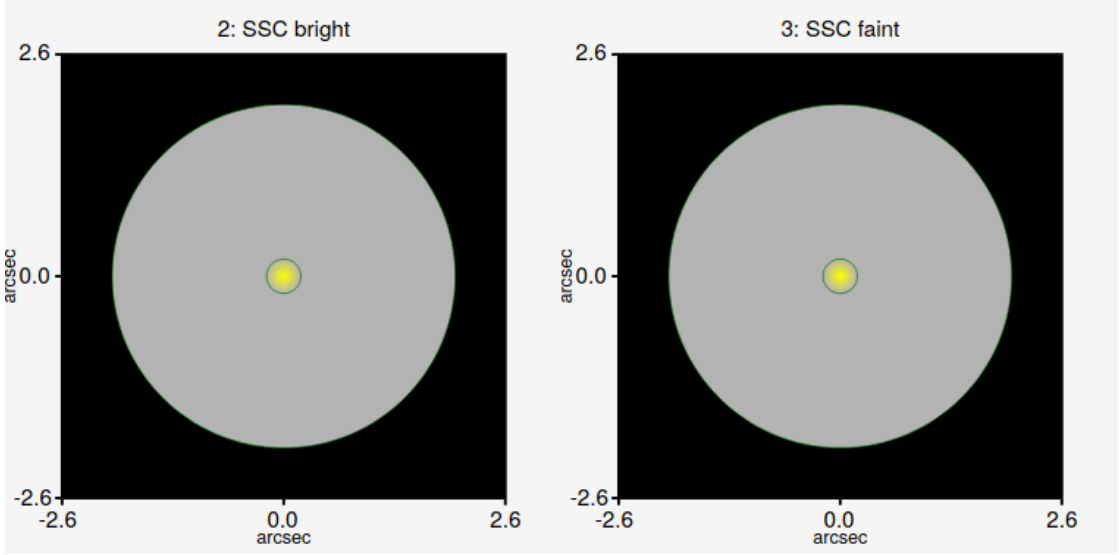


Figure 4.14 – Scenes of the bright (*left*) and faint (*right*) SSCs in IRAS 17138-1017 used in the ETC.

4.5.2 Calculations

For each scene, we built four MIRI imaging calculations corresponding to eight filters F560W, F770W, F1000W, F1130W, F1500W, F1800W, F2100W, F2550W and 12 MIRI MRS calculations covering the entire spectral range. We adopted the medium background at position RA = 17:16:35.7, Dec = -10:20:38 for the backgrounds, which is based on the JWST background model (see Section 4.4.3). For MIRI imaging calculations, we selected the Imaging Aperture Photometry strategy with the circular aperture centered on the SSCs. By default, the aperture radius was set to 0.3 arcsec. We performed the background subtraction using a background region, with the inner and outer radii of the sky annulus of 0.45 and 0.7 arcsec respectively. For MIRI MRS calculations, we selected the IFU Nod Off Scene strategy to represent the dedicated background observation with a circular aperture centered on the SSCs. Its radius was set to 0.3 arcsec by default.

All JWST detectors adopt a non-destructive up-the-ramp sampling technique called MULTIACCUM ([Ressler et al. 2015](#)). Fig. 4.17 demonstrates the readout scheme. In particular, each pixel is sampled $N_{samples}$ times at intervals of $t_d = 10 \mu s$. It takes a frame time of t_1 to sample all the pixels to make one frame. To save data volume and prevent saturation, the on-board flight software averages N_{frames} into a group before recording and downlinking. For MIRI $N_{frames} = 1$ and each frame is equivalent to a group, the delta time between groups $t_2 = 0$. N_{groups} are integrated before the array resets, making an integration. An exposure consists of

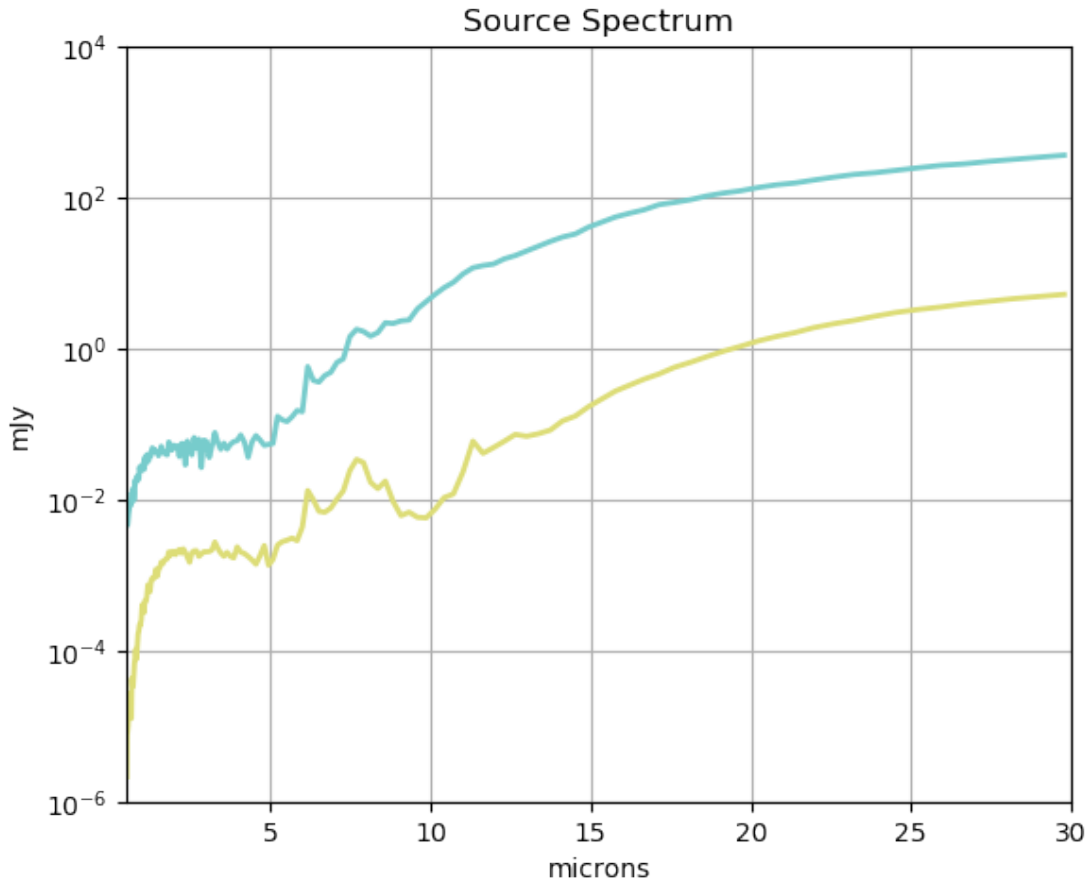


Figure 4.15 – SEDs of the bright (cyan) and faint (yellow) SSCs in IRAS 17138-1017.

N_{int} integrations. The total exposure time T_{exp} for N_{exp} exposures is calculated as:

$$T_{exp} = N_{exp} \times N_{int} \times N_{groups} \times t_1 \quad (4.1)$$

Besides the number of integrations N_{int} and number of exposures N_{exp} , users may select between two available readout patterns for MIRI, which are presented in Table 4.9 below. Following the recommendation of STScI (2016–), we selected the FAST readout mode for all MIRI imaging observations.

For each integration, STScI (2016–) recommends at least five groups for a reasonable calibration and at maximum 360 groups in FAST/FULL mode (~ 1000 s) to avoid the total impact of cosmic rays. The number of integrations should be minimized to mitigate the reset switch charge decay (RSCD) effect (see Section 5.2.1). In some cases, saturation at the end of an integration is acceptable since the count rate may still be derived from the unsaturated groups, although persistence should be concerned. In particular, we started with one integration and varied the number of groups in the brightest SSC scene to determine the upper limit, then applied it to the faintest SSC scene. For MIRI MRS calculations, the same exposure parameters were set to all four channels of the same grating setting. We also adjusted the number of groups taking the data volume constraint into account. For all calculations, we set the number of exposures to four

to mimic the 4-pt dithering.

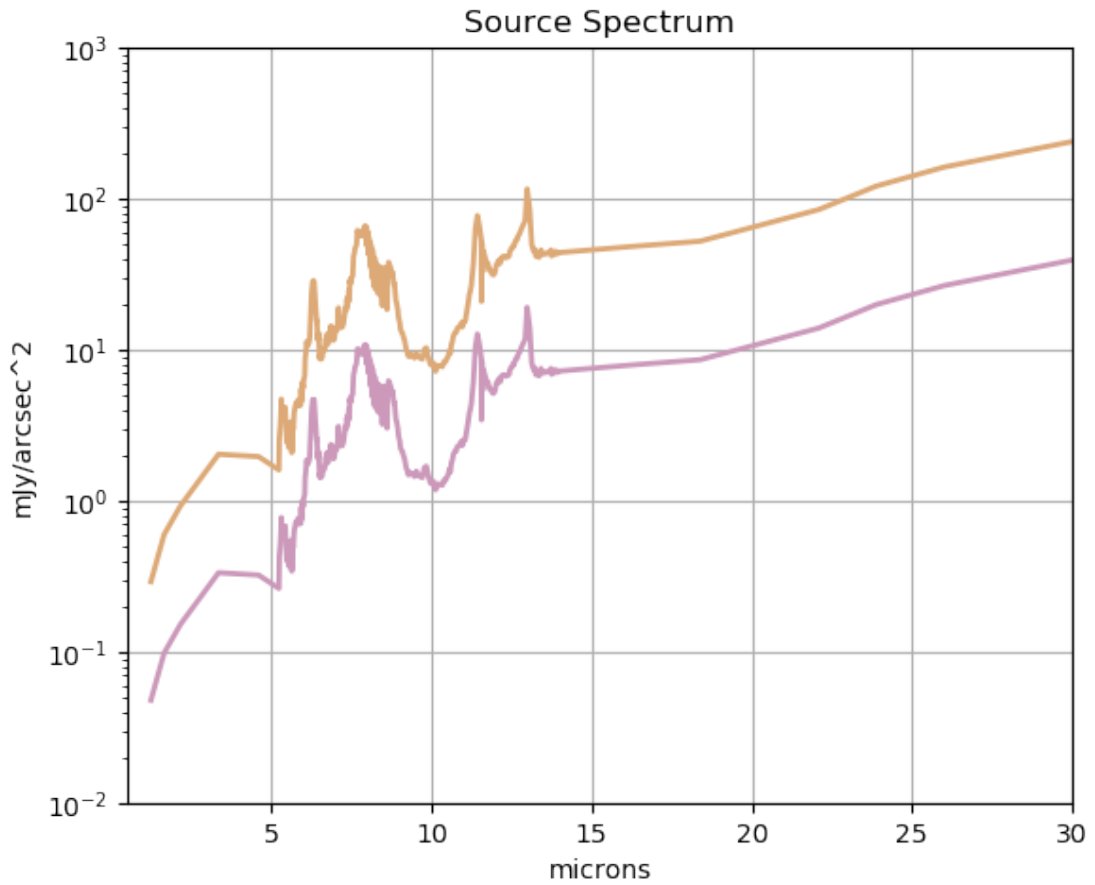


Figure 4.16 – SEDs of the bright (brown) and faint (purple) galaxy backgrounds in IRAS 17138-1017.

Table 4.9 – MIRI readout patterns (STScI 2016–)

	FAST	SLOW
$N_{samples}$	1	9
t_1 (full array)	2.755 s	23.890 s
Readout direction	Horizontal across the rows	Vertical along the columns
Advantages	<ul style="list-style-type: none"> – High dynamic range and low noise in case of background domination – More frequent sampling for detector defect and cosmic ray correction 	<ul style="list-style-type: none"> – Minimize detector effects and noise – Nine times smaller data size

Usage	<ul style="list-style-type: none"> - Default for imaging and LRS slit spectroscopy - Only option for coronagraphy, LRS slitless spectroscopy and sub-array imaging - Recommended for all MIRI prime observations 	<ul style="list-style-type: none"> - Faint source MRS spectroscopy with low sky backgrounds - Parallel observations
-------	---	---

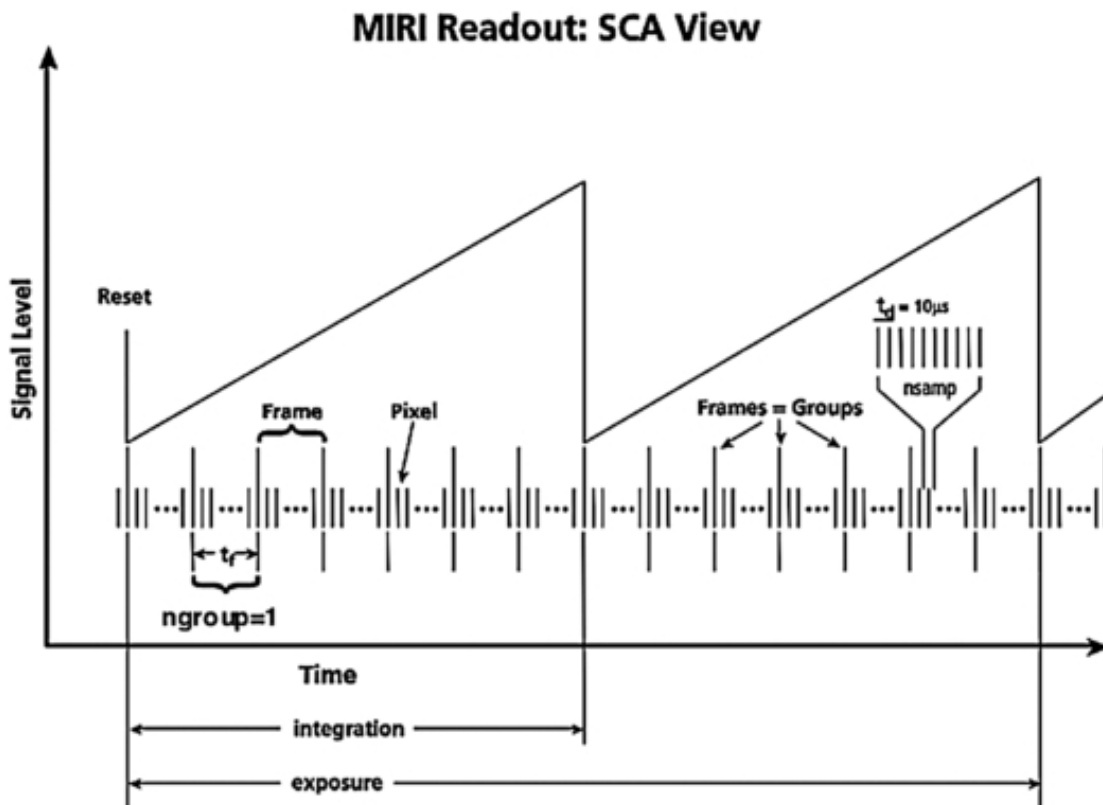


Figure 4.17 – MULTIACCUM readout scheme (Ressler et al. 2015).

4.5.3 Results

The calculation results for the MIRI imaging and MRS modes are listed in Table 4.10 and 4.11 respectively. Fig. 4.18 and Fig. 4.19 plot the SNR versus wavelength for the brightest and faintest SSC scenes respectively.

Table 4.10 – MIRI imaging ETC calculation results

Filter	λ of interest (μm)	Subarray	Readout pattern	N_{groups}	N_{int}	N_{exp}	T_{exp} (sec)	SNR	
								Brightest SSC	Faintest SSC
F560W	5.84	SUB256	FAST	150	1	4	179.71	45.68	6.89
F770W	7.81	SUB256	FAST	35	1	4	41.93	190.85	8.49
F1000W	9.95	SUB256	FAST	55	1	4	65.89	1027.57	6.84
F1130W	11.41	SUB256	FAST	80	1	4	95.85	952.37	14.20
F1500W	14.25	SUB256	FAST	10	1	4	11.98	1258.86	19.40
F1800W	17.96	SUB256	FAST	10	1	4	11.98	1465.79	32.67
F2100W	20.95	SUB256	FAST	5	1	4	5.99	888.53	23.78
F2550W	25.27	SUB256	FAST	15	1	4	17.97	1096.17	44.30

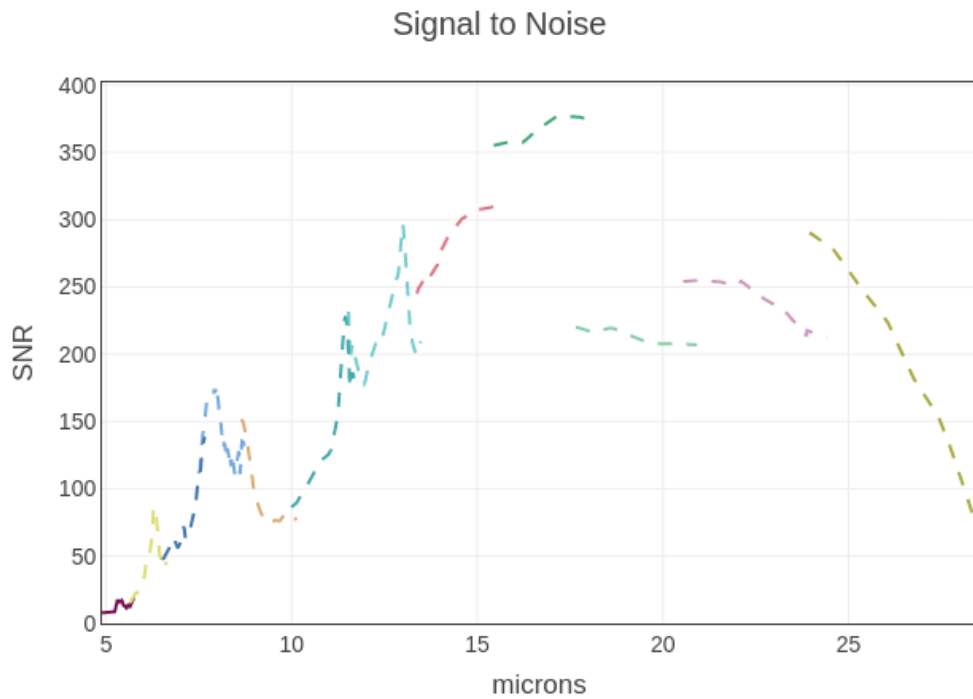


Figure 4.18 – SNR over the entire wavelength range of the MIRI MRS for the scene of the bright SSC.

Table 4.11 – MIRI MRS ETC calculation results

λ range	Channel	λ slice (μm)	Subarray	Readout pattern	N_{groups}	N_{int}	N_{exp}	T_{exp} (sec)	SNR	
									Brightest SSC	Faintest SSC
SHORT	1	5.34 [Fe II]	FULL	FAST	40	1	4	144.01	15.76	2.70
	2	7.70 PAH							163.98	50.43
	3	12.60 PAH							229.94	57.08
	4	18.71 [S III]							218.61	35.84
MEDIUM	1	6.20 PAH	FULL	FAST	40	1	4	144.01	55.19	11.65
	2	9.70 silicate							76.69	10.38
	3	14.20 PAH							286.96	60.94
	4	24.32 [Ne V]							213.15	35.10
LONG	1	6.98 [Ar II]	FULL	FAST	40	1	4	144.01	58.82	12.15
	2	11.30 PAH							175.67	37.22
	3	16.40 PAH							362.13	65.58
	4	25.99 [Fe II]							227.32	38.44

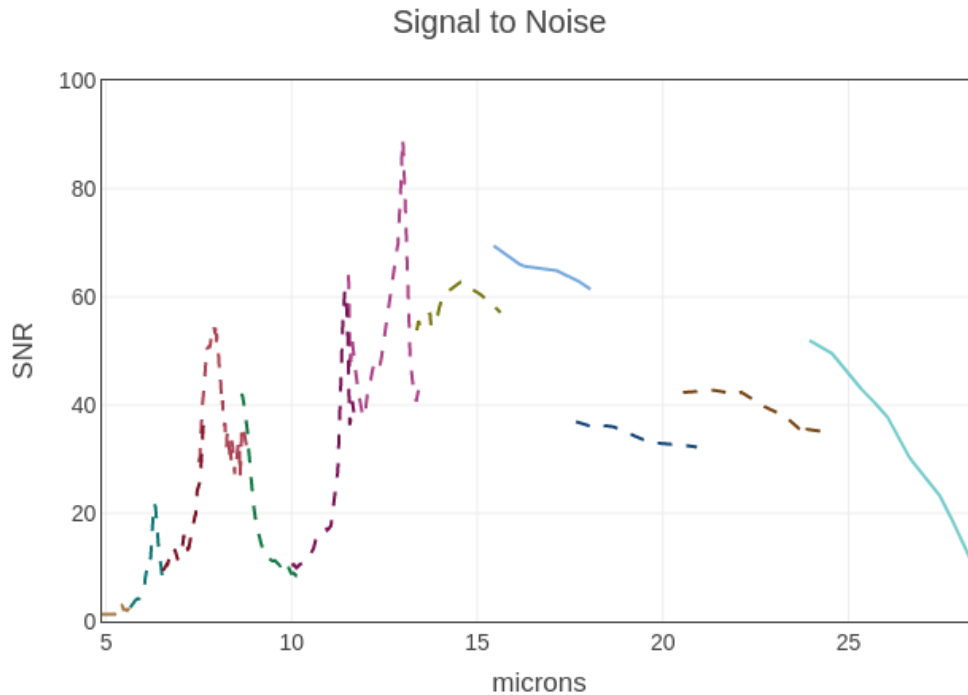


Figure 4.19 – SNR over the entire wavelength range of the MIRI MRS for the scene of the faint SSC.

4.6 JWST Astronomer’s Proposal Tool (APT)

After having tested and established the best configurations for our observations, we created our proposal using the Astronomer’s Proposal Tool (APT; [STScI 2016](#)), the official proposal submission tool for the JWST. The same object IRAS 17138-1017 is defined as two separate fixed targets: LEDA-59990-IMG for the imaging mode and LEDA-59990-MRS for the MRS mode, which requires a dedicated background observation with the target LEDA-59990-BKG. The capacity of the solid state recorder onboard JWST is 58.8 GB. These data are downlinked twice a day, thus the APT warns users to limit the data volume of their observations lower than 29 GB. As a result, we limit our MRS mosaic to 3×3 and simultaneous imaging to the BRIGHTSKY subarray only. On the other hand, it is possible to use a 20-point CYCLING dither pattern for all filters in the imaging mode without passing the data limit. Thus we decided to use this pattern instead, which should provide higher SNRs than the 4-pt dither pattern. The sky footprints of our observations are plotted in Fig. 4.20, 4.21 and 4.22. Finally, all of our visits are schedulable as plotted in Fig. 4.23.

Studying the very young embedded super star cluster population of IRAS 17138-1017 with MIRI

Scientific Category: Galaxies

Scientific Keywords: Luminous Infrared Galaxies, Star Clusters, Star Formation, Starburst Galaxies, Stellar Populations

Alternate Category: Stellar Populations and the Interstellar Medium

Instruments: MIRI

Proposal Size: SMALL

Exclusive Access Period: 12 months

Allocation Information (in hours):

Science Time: 7.3

Charged Time: 24.0

Abstract

Super star clusters represent extreme star formation and are often found in large number in (ultra)luminous infrared galaxy ((U)LIRGs). The LIRG IRAS 17138-1017 exhibits many such SSCs (>50) which are very young (3-5 Myr) and still deeply enshrouded in their progenitor molecular clouds. It is a particularly interesting target to study at mid-IR the very early phase of a starburst. We aim to characterize the super star cluster population of the LIRG IRAS 17138-1017 with combined MIRI imaging and MRS IFU observations, which will overcome the dust extinction seen in previous studies in near-infrared. In particular, by extracting photometry and tracing multiple spectroscopic diagnostics (ionized gas, molecular hot/warm gas, dust emission, dust and PAH features), we aim at deriving the cluster ages, luminosities, masses and extinction in conjunction with the interstellar medium they formed from. The distribution functions of those quantities and the spatial distributions will provide valuable insight into the star formation and evolution history of the galaxy.

Studying the very young embedded super star cluster population of IRAS 17138-1017 with
MIRI

Target Summary:

Target	RA	Dec
LEDA-59990-IMG	17 16 35.7896	-10 20 38.07
LEDA-59990-MRS	17 16 35.7896	-10 20 38.07
LEDA-59990-BKG	17 16 34.8000	-10 19 57.00

Observing Summary:

Target	Observing Template	Flags	Allocation *
LEDA-59990-IMG	MIRI Imaging <i>F560W, F770W, F1000W, F1130W, F1500W, F1800W, F2100W, F2550W</i>	<i>NOPAR</i>	2,200 / 23,486
LEDA-59990-MRS	MIRI Medium Resolution Spectroscopy <i>F560W, F770W, F1000W</i>		12,096 / 31,528
LEDA-59990-BKG	MIRI Medium Resolution Spectroscopy <i>F560W, F770W, F1000W</i>		12,096 / 31,483

* Science duration / charged duration (sec)

Total Prime Science Time in Hours:	7.3
Total Charged Time in Hours:	24.0

Observing Description

Super star clusters (SSCs) are the sites of extreme star formation in (ultra)luminous infrared galaxy. The LIRG IRAS 17138-1017 at 76 Mpc exhibits many such SSCs (>50 detected) which are very young (3-5 Myr) and still deeply enshrouded in their progenitor molecular clouds. IRAS 17138-1017 is thus a particularly interesting target to study at mid-IR the very early phase of a starburst. In the mid-IR, there are many tracers of the star formation activity that MIRI will be able to observe even for the faint clusters, thanks to its sensitivity and the negligible extinction by dust. With MIRI imaging, we will observe IRAS 17138-1017 in F560W, F770W, F1000W, F1130 F1500W, F1800, F2100W, F2500W. These filters provide the highest resolutions, and trace the star formation rate through the thermal dust emission and PAH signature, provide extinction by silicate features. The subarray SUB256 together with a 4-pt dither pattern for extended source provide good spatial coverage and sampling of the galaxy with background regions included.

Several spectroscopic diagnostics on ionized gas (H recombination lines), molecular hot/warm gas (H₂ rotational lines), dust emission (continuum), extinction by dust (silicate absorption), stellar irradiation (PAH features), Supernovae (forbidden lines) will be available in the 5-28 microns range of MRS. For MIRI MRS, we will obtain full spectral coverage over all channels and wavelength ranges from 4.9 to 28.3 μ m. To achieve good spatial coverage and sampling of the galaxy, we employ a mosaic of 3 \times 3 and 4-pt dither pattern for extended source. Similar dedicated MRS background observations are requested and linked to the science observations as a non-interruptible sequence. Simultaneous imaging of neighbor regions in F560W, F770W, F1000W are also obtained and may be used for imaging background subtraction and as control fields for cluster selection.

For both observation modes, the FAST readout mode is applied, with the exposure times adjusted to achieve the highest possible SNRs for the faintest SSC without saturating the brightest SSC.

Investigators:

Investigators and Team Expertise are included in this preview for your team to review. These will not appear in the version of the proposal given to the TAC, to allow for a dual anonymous review.

Investigator	Institution	Country
A Ciurlo	University of California - Los Angeles	USA/CA
* Y Clenet	Observatoire de Paris	FRA
* D Gratadour	Observatoire de Paris - Section de Meudon	FRA
L Grosset	Universities Space Research Association	USA/MD
* L Nguyen	Observatoire de Paris	FRA
* D Rouan	Observatoire de Paris	FRA
* P Vermot	Observatoire de Paris	FRA

Number of investigators: 7

* ESA investigators: 5

Team Expertise:

Studying the very young embedded super star cluster population of IRAS 17138-1017 with MIRI

The team is involved in MIRI development since the beginning, as the provider of the set of coronagraphs. Members of the team are involved in the science team of MIRI.

The team has an expertise in science based on near-IR imaging of central regions of galaxies, especially AGNs and starburst galaxies : more than 35 refereed papers since 2000.

In fact, we have studied the super star cluster population in IRAS 17138-1017 in the near-infrared using the ground-based adaptive optics instrument GeMS/GSAOI on the Gemini telescope (Lam et al. 2020). We have developed the three-dimensional radiative transfer code MontAGN (Monte Carlo for Active Galactic Nuclei) to predict and interpret observations of AGNs (Grosset et al. 2016, 2018; Marin et al. 2016) as well as super star clusters (Lam et al. 2019,2020). Preliminary simulations with MIRISim (Geers et al. 2019) and data reduction have also been implemented.

Studying the very young embedded super star cluster population of IRAS 17138-1017 with MIRI

Scientific Category: Galaxies

Scientific Keywords: Luminous Infrared Galaxies, Star Clusters, Star Formation, Starburst Galaxies, Stellar Populations

Alternate Category: Stellar Populations and the Interstellar Medium

Instruments: MIRI

Proposal Size: SMALL

Exclusive Access Period: 12 months

Allocation Information (in hours):

Science Time: 7.3

Charged Time: 24.0

Abstract

Super star clusters represent extreme star formation and are often found in large number in (ultra)luminous infrared galaxy ((U)LIRGs). The LIRG IRAS 17138-1017 exhibits many such SSCs (>50) which are very young (3-5 Myr) and still deeply enshrouded in their progenitor molecular clouds. It is a particularly interesting target to study at mid-IR the very early phase of a starburst. We aim to characterize the super star cluster population of the LIRG IRAS 17138-1017 with combined MIRI imaging and MRS IFU observations, which will overcome the dust extinction seen in previous studies in near-infrared. In particular, by extracting photometry and tracing multiple spectroscopic diagnostics (ionized gas, molecular hot/warm gas, dust emission, dust and PAH features), we aim at deriving the cluster ages, luminosities, masses and extinction in conjunction with the interstellar medium they formed from. The distribution functions of those quantities and the spatial distributions will provide valuable insight into the star formation and evolution history of the galaxy.

Studying the very young embedded super star cluster population of IRAS 17138-1017 with
MIRI

Target Summary:

Target	RA	Dec
LEDA-59990-IMG	17 16 35.7896	-10 20 38.07
LEDA-59990-MRS	17 16 35.7896	-10 20 38.07
LEDA-59990-BKG	17 16 34.8000	-10 19 57.00

Observing Summary:

Target	Observing Template	Flags	Allocation *
LEDA-59990-IMG	MIRI Imaging <i>F560W, F770W, F1000W, F1130W, F1500W, F1800W, F2100W, F2550W</i>	<i>NOPAR</i>	2,200 / 23,486
LEDA-59990-MRS	MIRI Medium Resolution Spectroscopy <i>F560W, F770W, F1000W</i>		12,096 / 31,528
LEDA-59990-BKG	MIRI Medium Resolution Spectroscopy <i>F560W, F770W, F1000W</i>		12,096 / 31,483

* Science duration / charged duration (sec)

Total Prime Science Time in Hours:	7.3
Total Charged Time in Hours:	24.0

Observing Description

Super star clusters (SSCs) are the sites of extreme star formation in (ultra)luminous infrared galaxy. The LIRG IRAS 17138-1017 at 76 Mpc exhibits many such SSCs (>50 detected) which are very young (3-5 Myr) and still deeply enshrouded in their progenitor molecular clouds. IRAS 17138-1017 is thus a particularly interesting target to study at mid-IR the very early phase of a starburst. In the mid-IR, there are many tracers of the star formation activity that MIRI will be able to observe even for the faint clusters, thanks to its sensitivity and the negligible extinction by dust. With MIRI imaging, we will observe IRAS 17138-1017 in F560W, F770W, F1000W, F1130 F1500W, F1800, F2100W, F2500W. These filters provide the highest resolutions, and trace the star formation rate through the thermal dust emission and PAH signature, provide extinction by silicate features. The subarray SUB256 together with a 4-pt dither pattern for extended source provide good spatial coverage and sampling of the galaxy with background regions included.

Several spectroscopic diagnostics on ionized gas (H recombination lines), molecular hot/warm gas (H₂ rotational lines), dust emission (continuum), extinction by dust (silicate absorption), stellar irradiation (PAH features), Supernovae (forbidden lines) will be available in the 5-28 microns range of MRS. For MIRI MRS, we will obtain full spectral coverage over all channels and wavelength ranges from 4.9 to 28.3 μ m. To achieve good spatial coverage and sampling of the galaxy, we employ a mosaic of 3 \times 3 and 4-pt dither pattern for extended source. Similar dedicated MRS background observations are requested and linked to the science observations as a non-interruptible sequence. Simultaneous imaging of neighbor regions in F560W, F770W, F1000W are also obtained and may be used for imaging background subtraction and as control fields for cluster selection.

For both observation modes, the FAST readout mode is applied, with the exposure times adjusted to achieve the highest possible SNRs for the faintest SSC without saturating the brightest SSC.

Investigators:

Investigators and Team Expertise are included in this preview for your team to review. These will not appear in the version of the proposal given to the TAC, to allow for a dual anonymous review.

Investigator	Institution	Country
A Ciurlo	University of California - Los Angeles	USA/CA
* Y Clenet	Observatoire de Paris	FRA
* D Gratadour	Observatoire de Paris - Section de Meudon	FRA
L Grosset	Universities Space Research Association	USA/MD
* L Nguyen	Observatoire de Paris	FRA
* D Rouan	Observatoire de Paris	FRA
* P Vermot	Observatoire de Paris	FRA

Number of investigators: 7

* ESA investigators: 5

Team Expertise:

Studying the very young embedded super star cluster population of IRAS 17138-1017 with MIRI

The team is involved in MIRI development since the beginning, as the provider of the set of coronagraphs. Members of the team are involved in the science team of MIRI.

The team has an expertise, mainly based on high angular resolution imaging and spectroscopy in the near-IR (adaptive optics and interferometry), centred on the study of central regions of galaxies, especially AGNs and starburst galaxies, as well as the Galactic Center.

The members of the team have contributed to more than 35 refereed papers on these topics since 2000.

More specifically, as regards this proposal, we have studied the super star cluster population in IRAS 17138-1017 in the near-infrared using the ground-based adaptive optics instrument GeMS/GSAOI on the Gemini telescope (Lam et al. 2020). We have developed the three-dimensional radiative transfer code MontAGN (Monte Carlo for Active Galactic Nuclei) to predict and interpret observations of AGNs (Grosset et al. 2016, 2018; Marin et al. 2016) as well as super star clusters (Lam et al. 2019,2020). Preliminary simulations with MIRISim (Geers et al. 2019) and data reduction have also been implemented.

■ Scientific Justification

Star formation is primarily manifested in the form of clusters (e.g., Lada & Lada 2003). In extreme cases when two galaxies interact, that is notably the case of (ultra)luminous infrared galaxies ((U)LIRGs, $L_{\text{IR}} > 10^{11} L_{\odot}$; Sanders & Mirabel 1996), the induced gravitational potential perturbations drag gas and dust together, increase their densities and trigger violent starbursts. The star formation rate (SFR) may then reach up to 1000 times the one of the Milky Way (Kennicutt & Evans 2012), resulting in numerous super star clusters (SSCs). These populations are much younger (< 100 Myr) than globular clusters, but more massive ($\gtrsim 10^4 M_{\odot}$) than open clusters, and highly compact ($\gtrsim 10^3 M_{\odot} \text{ pc}^{-3}$ at core) (Portegies Zwart et al. 2010). Given their masses and densities, many studies suggest that SSCs may finally evolve into globular clusters (Portegies-Zwart et al. 2010, Krumholz et al. 2019). SSCs play a major role in the structural and chemical evolution of those galaxies through the efficient conversion of gas in stellar mass, the production and dissemination of heavy elements by supernovae, the feeding super massive black holes, the injection of turbulence in the ISM. In their infancy SSC are enshrouded in the molecular cloud from which they formed, radiating most of their power at IR wavelengths and that is why mid-IR imaging is so crucial to study this early phase. They can be bright enough to be detected beyond Local Group.

The formation and evolution of SSCs are reflected in their distributions of luminosity, mass, size, age, stellar content, dust and gas content, supernova rate, etc. Their demographics need to be established on a significant sample in order to construct and refine the overall picture, including the connections to the local environments (gas density, proximity of an AGN, interaction with nearby galaxies) and the possible propagation of the burst. However, only a limited sample of SSCs exists in the Local Group (Portegies-Zwart et al. 2010, Krumholz et al. 2019 and references therein), while they are much more abundant in LIRGs (e.g., Vavilkin 2011; Miralles-Caballero et al. 2011; Randriamanakoto et al. 2013a,b; Linden et al. 2019, Lam et al. 2020). Even though extensive surveys of LIRGs have been performed, their SSC populations remain elusive due to the large distances. Even if a good angular resolution has been reached using the HST or 8m class telescopes, most of them only provide global analyses of the starburst at the galaxy scale (e.g. Davies et al. 2003, Piqueras-Lopez et al. 2012). The Great Observatories All-sky LIRG Survey (GOALS; Armus et al. 2009) is especially noteworthy since it contains a large sample of 200 galaxies (median distance ~ 94.8 Mpc) and combines imaging and spectroscopic data in different wavelength ranges from various ground-based and space-borne observatories. The visible and H-band survey by Haan et al. (2011), part of GOALS, is particularly of interest since it corresponds to a large sample (88 galaxies); however this ground based program is limited in IR to the H band, and obviously the deeply dust-enshrouded population of SSCs is missed at such wavelengths. The program of GOALS also includes the JWST Early Release Science (ERS) Program 1328 studying the starburst-AGN connection (Armus et al. 2017). Nevertheless, only a subsample of 22 galaxies have their SSC populations studied using optical data from the Hubble Space Telescope (HST) (Linden et al. 2017). In fact, there are several JWST

Guaranteed Time Observations (GTO) programs studying nearby archetypical galaxies representing various environments that may host SSCs, including LIRGs (GTO 1204, GTO 1223, GTO 1234, GTO 1265, GTO 1266, GTO 1267, GTO 1268, GTO 1269). Furthermore, JWST will also observe resolved analogs of SSCs in Local Group (GTO 1225, GTO 1226, GTO 1227, GTO 1235). These pilot programs will provide excellent demonstrations and scientific bases for later studies of SSCs in LIRGs with JWST. Nevertheless, currently most of the GTO programs are not aiming at individualizing SSCs themselves, and establishing their demographics. This is what we would like to focus on with this short GO program of 20 hours.

Our goal is to take benefit of the unique convergence of three features offered by MIRI on JWST: the access to a broad range of the thermal infrared at a good spectral resolution, the unique spatial resolution at these wavelengths and the unbeatable sensitivity, to study in details SSCs in the peculiar LIRG galaxy IRAS 17138-1017, where the SSCs population has been successfully identified (not less than 55 clusters) and analyzed in the near-IR (Miralles-Caballero et al., 2011; Piqueras Lpez et al. 2012, Randriamanakoto et al. 2013, 2015; Lam et al. 2020, see Fig. 1). The LIRG IRAS 17138-1017 is a late-stage merger

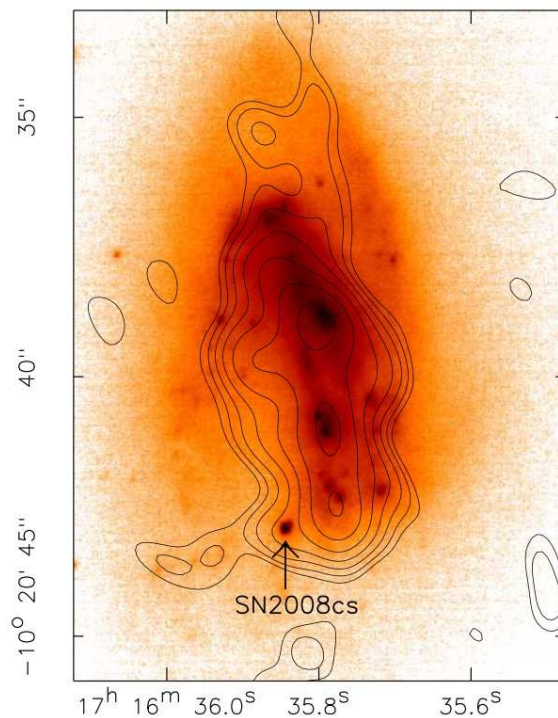


Figure 1: K-band Gemini ALTAIR/NIRI image, with 22.4 GHz VLA-C contours. Taken from Kankare 2008.

(Stierwalt et al. 2014), with $\log(LIR/L)=11.42$, at a distance of 76 Mpc (Sanders et al.

2003). There is no evidence that favors the presence of a Seyfert-like active nucleus. The SSC population is especially young (3 - 4.5 Myr) in this galaxy (Randriamanakoto, 2013; Lam et al., 2020) and still deeply enshrouded in the progenitor molecular clouds as indicated by the large extinction (Depoy et al. 1988). For instance, the galaxy exhibits the most extinct supernovae so far, with $A_v = 15.7$ mag for SN2008cs (Kankare et al. 2008). This youth and the still deep burying of embedded clusters make this LIRG a particularly interesting target to study at mid-IR the very early phase of a starburst. The good angular resolution is indeed required to separate SSC and avoid as far as possible confusion that would lead to bias the properties of individual SSC - such as luminosity - towards high values (see Randriamanakoto, 2013). A typical separation of 200 pc between two SSC corresponds to 600 mas at 75 Mpc, a resolution reached by JWST at least up to $20 \mu\text{m}$.

The mid-IR domain offers several assets: the continuum is essentially due to the heated dust, there are several lines and bands of interest and the effects of extinction will be minimized. In conjunction with the near-IR data, broad-band imaging and spectroscopy from 5 to $28 \mu\text{m}$ will thus improve further our understanding of the SSCs by bringing several important pieces of information (e.g., Galliano et al 2005, 2008, Martin-Hernandez et al. 2005). In particular, we aim at identifying individual SSCs and derive for each the following quantities :

- The cluster mid-IR photometry and extinction-corrected bolometric luminosities, essential quantities to establish the luminosity function;
- The temperature of the dust and some constrain on its range of variation by comparing the observed continuum to results of radiative transfer model (Whelan et al. , 2011). This temperature is directly related to the stellar cluster luminosity and to the structure of the dusty envelope (e.g. internal radius) in which the SSC can be still partly or fully embedded.
- The mass of dust and thus the mass of gas, allowing to derive the mass function of the envelope.
- An unbiased estimation of the extinction based on the the $9.7 \mu\text{m}$ silicate absorption features that allows to de-redden in a proper way the near-IR photometry
- By comparison to predictions from radiative transfer code and stellar evolution models, the cluster age, will be constrained through the analysis of the shape of the continuum, the relative intensity of PAH features and de-reddened near-IR colors (Whelan et al. , 2011; Lam et al., 2019).
- The warm molecular gas content through the access to pure rotational lines of H_2 (S(7) @ $5.51 \mu\text{m}$; S(6) @ $6.11 \mu\text{m}$; S(5) @ $6.91 \mu\text{m}$; S(4) @ $8.03 \mu\text{m}$; S(3) @ $9.66 \mu\text{m}$; S(2) @ $12.28 \mu\text{m}$; S(1) @ $17.04 \mu\text{m}$) that trace the warm gas;
- Indication on the UV radiation field and thus on the young stellar population thanks to PAH lines intensity and ratio, and recombination lines of hydrogen (H I (7-6) $12.37 \mu\text{m}$, H I (9-7) $11.32 \mu\text{m}$, H I (8-7) $19.06 \mu\text{m}$). For instance, the PAH line ratio $11.3/7.7$ can be used as a diagnostic for PAH ionization and, in turn, for UV field intensity.
- Hardness of the ionizing spectrum and/or the existence of shocks will be estimated thanks to forbidden lines such as [Ar III] @ $9.0 \mu\text{m}$, [Ar II] @ $7.0 \mu\text{m}$, [Ne III] @ $15.5 \mu\text{m}$, [Ne II] @ $12.8 \mu\text{m}$, and [S IV] @ $10.5 \mu\text{m}$. All correspond to species with ionization potentials

above 13.6 eV. One notes that the two line ratio for Ar and Ne can break the degeneracy between the density of ionizing photon and the hardness of the radiation and thus give good estimates of those two quantities.

- SN content will be traced through various forbidden lines, notably iron lines [FeII] @ 5.34, 17.9, 24.5 and 25.9 μm as well as [Ne III] @ 15.5 μm and [Ne II] @ 12.8 μm , whose ratio is an indicator of shock velocity (Rho et al., 2001).

The influence of the galactic environment on those various properties will also be investigated by examining their evolution with respect to the location of the SSCs (spiral arms, nuclear region, tails). This will also give indications on the history of the burst throughout the galaxy and on a possible burst propagation.

■ Technical Justification

For MIRI imaging, we will use eight filters: F560W, F770W, F1000W, F1130W, F1500W, F1800W, F2100W, and F2500W cover efficiently the spectral range of MRS and will help calibrating the spectra, trace the PAH, silicate features and the star formation rate (Shipley et al. 2016, Senarath et al. 2018). For all filters, the subarray SUB256 together with a 20 points CYCLING pattern allow good spatial coverage and sampling of the galaxy as well as a fair estimate of the background. The FAST readout mode is the only option for subarray imaging. The number of groups for the four filters are between 150 and 35. Only one integration is used to mitigate the reset switch charge decay effect. The exposure times were chosen to maximize the signal-to-noise ratio (SNR) of the faintest SSC while avoiding saturation of the brightest SSC. The ETC scene was based on the near-IR photometry (Lam et al., 2020) to scale the flux of a bright, a medium and a faint SSC.

Using MIRI MRS, we will obtain full spectral coverage over all channels and wavelength ranges from 4.9 to 28.3 μm . As described in the science justification, the spectral range covers various signatures each contributing to a specific diagnostic: PAH bands, silicate absorption features, pure rotational lines of H_2 , forbidden lines of various elements and recombination lines of hydrogen. To achieve good spatial coverage and sampling of the galaxy, we employ a mosaic of 3×3 , the FULL array and 4-pt dither pattern for extended source. Dedicated MRS background observation are requested and linked to the science observations as a non-interruptible sequence. Simultaneous imaging of neighbour regions in F560W, F770W, F1000W are also obtained and may be used for imaging background subtraction and as control fields for cluster selection, but with the BRIGHTSKY subarray only to save data volume. Since the SSCs are dominated by the galaxy background, the FAST readout mode is chosen to maximise dynamic range and minimise noise. The number of groups are 40 for all channels. Only one integration to mitigate the reset switch charge decay effect. The exposure time were chosen to maximise the signal-to-noise ratio (SNR) of the faintest SSC while avoiding saturation of the brightest SSC, as well as to save data volume.

Furthermore, to verify the feasibility of our study, we constructed some SSC models using the radiative transfer code MontAGN (Grosset et al. 2018 from private consultation), and simulated MIRI observations using MIRISim (Geers et al. 2019). After reducing the

outputs with the JWST Data Reduction Pipeline (Bushouse et al. 2019) version 0.16.2, build 7.5, we extracted the photometry and spectra of these SSCs. Example of results for MIRI imaging is plotted in Fig. 2 Although there are several limitations in the present simulations and further calibrations are needed, it is clearly feasible to extract solid scientific results from MIRI data.

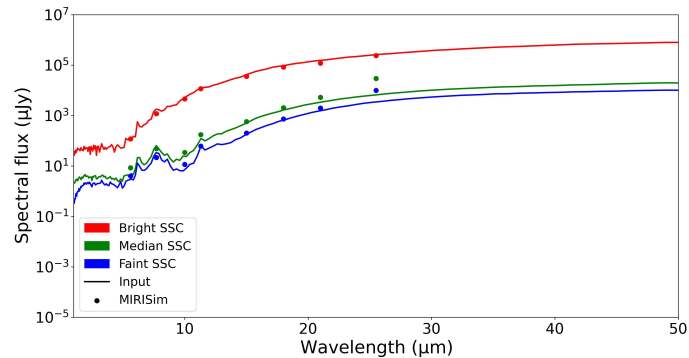


Figure 2: Recovered photometric measurements (dots) compared to the input spectra (lines) of some IRAS 17138-1017 SSC models at various magnitudes, after simulation using MIRISIM and reduction using the provisional JWST data reduction pipeline v0.16.2.

■ Special Requirements (if any)

■ Justify Coordinated Parallel Observations (if any)

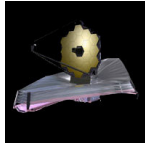
■ Justify Duplications (if any)

■ Analysis Plan (AR only)

References :

- Armus, L., Mazzarella, J. M., Evans, A. S., et al. 2009, *PASP*, 121, 559
- Bastian, N. 2008, *MNRAS*, 390, 759
- Bushouse, H. et al. 2019, *Astronomical Data Analysis Software and Systems XXVIII. ASP Conference Series*, Vol. 523, 243
- Davies, R. I. et al. 2003, *Astrop. J.*, 597, 907
- Depoy, D. L., Wynn-Williams, C. G., Hill, G. J., & Becklin, E. E. 1988, *AJ*, 95, 398
- Galliano, E. et al., 2005, *A&A*, 438, 803
- Geers, V. C. et al. 2019, *Astronomical Data Analysis Software and Systems XXVIII. ASP Conference Series*, Vol. 523, 641

- Grosset, L., Rouan, D., Gratadour, D., et al. 2018, *A&A*, 612, A69
- Kankare, E., Mattila, S., Ryder, S., et al. 2008, *Astrop. J.*, 689, L97
- Kennicutt, R. C. & Evans, N. J. 2012, *ARA&A*, 50, 531
- Krumholz, M. R., McKee, C. F., & Bland -Hawthorn, J. 2019, *ARA&A*, 57, 227
- Lada, C. J., & Lada, E. A. 2003, *ARA&A*, 41, 57
- Lam, N. T., et al., 2019, in *Radiative Signatures from the Cosmos*, ASP Conference Series, Vol. 519, 273
- Linden, S. T., Evans, A. S., Rich, J., et al. 2017, *Astrop. J.*, 843, 91
- Martn-Hernndez, N. L., Schaerer, D., Sauvage, M. 2005, *A&A*, 429, 449
- Miralles-Caballero, D., Colina, L., Arribas, S., & Duc, P.-A. 2011, *AJ*, 142, 79
- Piqueras Lpez, J., et al. 2016, *A&A*, 590, A67
- Piqueras Lpez, J., et al. 2012, *A&A*, 546, A64
- Portegies Zwart, S. F., McMillan, S. L. W., & Gieles, M. 2010, *ARA&A*, 48, 431
- Randriamanakoto, Z., Escala, A., Visnen, P., et al. 2013a, *Astrop. J.*, 775, L38
- Randriamanakoto, Z., Visnen, P., Ryder, S., et al. 2013b, *MNRAS*, 431, 554
- Randriamanakoto, Z. 2015, Ph.D. Thesis
- Rho, J., et al. 2001, *Astrop. J.*, 547, 885
- Senarath, M. R. 2018, *Astrop. J.*, 869, L26
- Shiple, H.V. 2016, *Astrop. J.*, 818, 60
- Whelan, D. G., et al. 2011, *Astrop. J.*, 729, 111
- Vavilkin, T. 2011, PhD Thesis,



1715 - Studying the very young embedded super star cluster population of IRAS 17138-1017 with MIRI

Cycle: 1, Proposal Category: GO

INVESTIGATORS

<i>Name</i>	<i>Institution</i>	<i>E-Mail</i>
Dr. Daniel Rouan (PI) (ESA Member)	Observatoire de Paris	daniel.rouan@obspm.fr
Dr. Damien Gratadour (CoI) (ESA Member) (CoPI)	Observatoire de Paris - Section de Meudon	damien.gratadour@obspm.fr
Dr. Lucas Grosset (CoI) (US Admin CoI)	Universities Space Research Association	lucas.grosset@obspm.fr
Mr. Lam Tung Nguyen (CoI) (ESA Member)	Observatoire de Paris	lam.nguyen@obspm.fr
Dr. Yann Clenet (CoI) (ESA Member)	Observatoire de Paris	yann.clenet@obspm.fr
Dr. Pierre Vermot (CoI) (ESA Member)	Observatoire de Paris	pierre.vermot@obspm.fr
Dr. Anna Ciurlo (CoI)	University of California - Los Angeles	ciurlo@astro.ucla.edu

OBSERVATIONS

<i>Folder</i>	<i>Observation</i>	<i>Label</i>	<i>Observing Template</i>	<i>Science Target</i>
Observation Folder				
	1	MIRI Imaging	MIRI Imaging	(1) LEDA-59990-IMG
	2	MIRI MRS	MIRI Medium Resolution Spectroscopy	(2) LEDA-59990-MRS
	3	MIRI MRS BKG	MIRI Medium Resolution Spectroscopy	(3) LEDA-59990-BKG

ABSTRACT

Super star clusters represent extreme star formation and are often found in large number in (ultra)luminous infrared galaxy ((U)LIRGs). The LIRG IRAS 17138-1017

exhibits many such SSCs (>50) which are very young (3-5 Myr) and still deeply enshrouded in their progenitor molecular clouds. It is a particularly interesting target to study at mid-IR the very early phase of a starburst.

We aim to characterize the super star cluster population of the LIRG IRAS 17138-1017 with combined MIRI imaging and MRS IFU observations, which will overcome the dust extinction seen in previous studies in near-infrared. In particular, by extracting photometry and tracing multiple spectroscopic diagnostics (ionized gas, molecular hot/warm gas, dust emission, dust and PAH features), we aim at deriving the cluster ages, luminosities, masses and extinction in conjunction with the interstellar medium they formed from. The distribution functions of those quantities and the spatial distributions will provide valuable insight into the star formation and evolution history of the galaxy.

OBSERVING DESCRIPTION

Super star clusters (SSCs) are the sites of extreme star formation in (ultra)luminous infrared galaxy. The LIRG IRAS 17138-1017 at 76 Mpc exhibits many such SSCs (>50 detected) which are very young (3-5 Myr) and still deeply enshrouded in their progenitor molecular clouds. IRAS 17138-1017 is thus a particularly interesting target to study at mid-IR the very early phase of a starburst. In the mid-IR, there are many tracers of the star formation activity that MIRI will be able to observe even for the faint clusters, thanks to its sensitivity and the negligible extinction by dust. With MIRI imaging, we will observe IRAS 17138-1017 in F560W, F770W, F1000W, F1130 F1500W, F1800, F2100W, F2500W. These filters provide the highest resolutions, and trace the star formation rate through the thermal dust emission and PAH signature, provide extinction by silicate features. The subarray SUB256 together with a 4-pt dither pattern for extended source provide good spatial coverage and sampling of the galaxy with background regions included.

Several spectroscopic diagnostics on ionized gas (H recombination lines), molecular hot/warm gas (H₂ rotational lines), dust emission (continuum), extinction by dust (silicate absorption), stellar irradiation (PAH features), Supernovae (forbidden lines) will be available in the 5-28 microns range of MRS. For MIRI MRS, we will obtain full spectral coverage over all channels and wavelength ranges from 4.9 to 28.3 μ m. To achieve good spatial coverage and sampling of the galaxy, we employ a mosaic of 3 \times 3 and 4-pt dither pattern for extended source. Similar dedicated MRS background observations are requested and linked to the science observations as a non-interruptible sequence. Simultaneous imaging of neighbor regions in F560W, F770W, F1000W are also obtained and may be used for imaging background subtraction and as control fields for cluster selection.

For both observation modes, the FAST readout mode is applied, with the exposure times adjusted to achieve the highest possible SNRs for the faintest SSC without saturating the brightest SSC.

Proposal 1715 - Targets - Studying the very young embedded super star cluster population of IRAS 17138-1017 with MIRI

Fixed Targets	#	Name	Target Coordinates	Targ. Coord. Corrections	Miscellaneous	
	(1)	LEDA-59990-IMG	RA: 17 16 35.7896 (259.1491233d) Dec: -10 20 38.07 (-10.34391d) Equinox: J2000	Epoch of Position: 2015.5		
	<p><i>Comments: This object was generated by the targetselector and retrieved from the SIMBAD database.</i> <i>Category=Galaxy</i> <i>Description=[Infrared galaxies, Interacting galaxies, Spiral galaxies, Starburst galaxies, Ultraluminous infrared galaxies]</i> <i>Extended=YES</i></p>					
	(2)	LEDA-59990-MRS	RA: 17 16 35.7896 (259.1491233d) Dec: -10 20 38.07 (-10.34391d) Equinox: J2000	Epoch of Position: 2015.5		
<p><i>Comments: This object was generated by the targetselector and retrieved from the SIMBAD database. It is identical to the target LEDA-59990-IMG, but requires companion background observation(s).</i> <i>Category=Galaxy</i> <i>Description=[Infrared galaxies, Interacting galaxies, Spiral galaxies, Starburst galaxies, Ultraluminous infrared galaxies]</i> <i>Extended=YES</i></p>						
(3)	LEDA-59990-BKG	RA: 17 16 34.8000 (259.1450000d) Dec: -10 19 57.00 (-10.33250d) Equinox: J2000				
<p><i>Comments:</i> <i>Category=Calibration</i> <i>Description=[Telescope/sky background]</i> <i>Extended=YES</i></p>						

Proposal 1715 - Observation 1 - Studying the very young embedded super star cluster population of IRAS 17138-1017 with MIRI

Fri Dec 04 14:31:34 GMT 2020

Observation	Proposal 1715, Observation 1: MIRI Imaging Diagnostic Status: No Diagnostics Observing Template: MIRI Imaging										
Fixed Targets	#	Name	Target Coordinates			Targ. Coord. Corrections		Miscellaneous			
	(1)	LEDA-59990-IMG	RA: 17 16 35.7896 (259.1491233d) Dec: -10 20 38.07 (-10.34391d) Equinox: J2000			Epoch of Position: 2015.5					
	<i>Comments: This object was generated by the targetselector and retrieved from the SIMBAD database.</i> <i>Category=Galaxy</i> <i>Description=[Infrared galaxies, Interacting galaxies, Spiral galaxies, Starburst galaxies, Ultraluminous infrared galaxies]</i> <i>Extended=YES</i>										
Template	Subarray										
	SUB256										
Dithers	#	Dither Type	Starting Point	Number of Points	Points	Starting Set	Number of Sets	Optimized For	Direction	Pattern Size	
	1	CYCLING	1	20		1	1			DEFAULT	
Spectral Elements	#	Filter	Readout Pattern	Groups/Int	Integrations/Exp	Exposures/Dith	Dither	Total Dithers	Total Integrations	Total Exposure Time	ETC Wkbk.Calc ID
	1	F560W	FAST	150	1	1	Dither 1	20	20	898.56	42530.1
	2	F770W	FAST	35	1	1	Dither 1	20	20	209.664	42530.2
	3	F1000W	FAST	55	1	1	Dither 1	20	20	329.472	42530.3
	4	F1130W	FAST	80	1	1	Dither 1	20	20	479.232	42530.4
	5	F1500W	FAST	10	1	1	Dither 1	20	20	59.904	42530.6
	6	F1800W	FAST	10	1	1	Dither 1	20	20	59.904	42530.7
	7	F2100W	FAST	5	1	1	Dither 1	20	20	29.952	42530.8
	8	F2550W	FAST	15	1	1	Dither 1	20	20	89.856	42530.9
Special Requirements	No Parallel										

Proposal 1715 - Observation 2 - Studying the very young embedded super star cluster population of IRAS 17138-1017 with MIRI

Observation	Proposal 1715, Observation 2: MIRI MRS Fri Dec 04 14:31:34 GMT 2020 Diagnostic Status: No Diagnostics Observing Template: MIRI Medium Resolution Spectroscopy Background Observations:[MIRI MRS BKG (Obs 3)]												
Fixed Targets	#	Name	Target Coordinates				Targ. Coord. Corrections			Miscellaneous			
	(2)	LEDA-59990-MRS	RA: 17 16 35.7896 (259.1491233d) Dec: -10 20 38.07 (-10.34391d) Equinox: J2000				Epoch of Position: 2015.5						
	<i>Comments: This object was generated by the targetselector and retrieved from the SIMBAD database. It is identical to the target LEDA-59990-IMG, but requires companion background observation(s).</i> Category=Galaxy Description=[Infrared galaxies, Interacting galaxies, Spiral galaxies, Starburst galaxies, Ultraluminous infrared galaxies] Extended=YES												
Acquisition	#	Target											
	1	NONE											
Template	AcqFilter		Primary Channel				Simultaneous Imaging			Imager Subarray			
	F560W		ALL				YES			BRIGHTSKY			
Mosaic	Rows	Columns	Row Overlap %			Column Overlap %		Row shift	Column shift		Tile Order		
	3	3	10.0			10.0		0.0	0.0		DEFAULT		
Dithers	#	Dither Type				Optimized For			Direction				
	1	4-Point				EXTENDED SOURCE			NEGATIVE				
Spectral Elements	#	Wavelength Range	Detector	Filter	Readout Pattern	Groups/Int	Integrations/Exp	Exposures/Dith	Dither	Total Dithers	Total Integrations	Total Exposure Time	ETC Wkbk.Calc ID
	1		IMAGER	F560W	FAST	40	1	1	Dither 1	4	4	138.445	42530
	1	SHORT(A)	MRSLONG		FAST	40	1	1	Dither 1	4	4	444.006	42530.23
	1	SHORT(A)	MRSSHORT		FAST	40	1	1	Dither 1	4	4	444.006	42530.21
	2		IMAGER	F770W	FAST	40	1	1	Dither 1	4	4	138.445	42530
	2	MEDIUM(B)	MRSLONG		FAST	40	1	1	Dither 1	4	4	444.006	42530.27
	2	MEDIUM(B)	MRSSHORT		FAST	40	1	1	Dither 1	4	4	444.006	42530.25
	3		IMAGER	F1000W	FAST	40	1	1	Dither 1	4	4	138.445	42530
	3	LONG(C)	MRSLONG		FAST	40	1	1	Dither 1	4	4	444.006	42530.31
	3	LONG(C)	MRSSHORT		FAST	40	1	1	Dither 1	4	4	444.006	42530.29

Proposal 1715 - Observation 2 - Studying the very young embedded super star cluster population of IRAS 17138-1017 with MIRI

Special Requirements

Sequence Observations 2, 3, Non-interruptible

Proposal 1715 - Observation 3 - Studying the very young embedded super star cluster population of IRAS 17138-1017 with MIRI

Fri Dec 04 14:31:34 GMT 2020

Observation	Proposal 1715, Observation 3: MIRI MRS BKG Diagnostic Status: No Diagnostics Observing Template: MIRI Medium Resolution Spectroscopy Background Observation For: [MIRI MRS (Obs 2)]												
Fixed Targets	#	Name	Target Coordinates				Targ. Coord. Corrections			Miscellaneous			
Acquisition	#	Target											
Template	AcqFilter	Primary Channel				Simultaneous Imaging			Imager Subarray				
Mosaic	Rows	Columns	Row Overlap %		Column Overlap %		Row shift		Column shift		Tile Order		
Dithers	#	Dither Type				Optimized For			Direction				
Spectral Elements	#	Wavelength Range	Detector	Filter	Readout Pattern	Groups/Int	Integrations/E xp	Exposures/Dit h	Dither	Total Dithers	Total Integrations	Total Exposure Time	ETC Wbk.Calc ID
	1		IMAGER	F560W	FAST	40	1	1	Dither 1	4	4	138.445	42530
	1	SHORT(A)	MRSLONG		FAST	40	1	1	Dither 1	4	4	444.006	42530
	1	SHORT(A)	MRSSHORT		FAST	40	1	1	Dither 1	4	4	444.006	42530
	2		IMAGER	F770W	FAST	40	1	1	Dither 1	4	4	138.445	42530
	2	MEDIUM(B)	MRSLONG		FAST	40	1	1	Dither 1	4	4	444.006	42530
	2	MEDIUM(B)	MRSSHORT		FAST	40	1	1	Dither 1	4	4	444.006	42530
	3		IMAGER	F1000W	FAST	40	1	1	Dither 1	4	4	138.445	42530
	3	LONG(C)	MRSLONG		FAST	40	1	1	Dither 1	4	4	444.006	42530
	3	LONG(C)	MRSSHORT		FAST	40	1	1	Dither 1	4	4	444.006	42530

Proposal 1715 - Observation 3 - Studying the very young embedded super star cluster population of IRAS 17138-1017 with MIRI

Special Requirements

Sequence Observations 2, 3, Non-interruptible

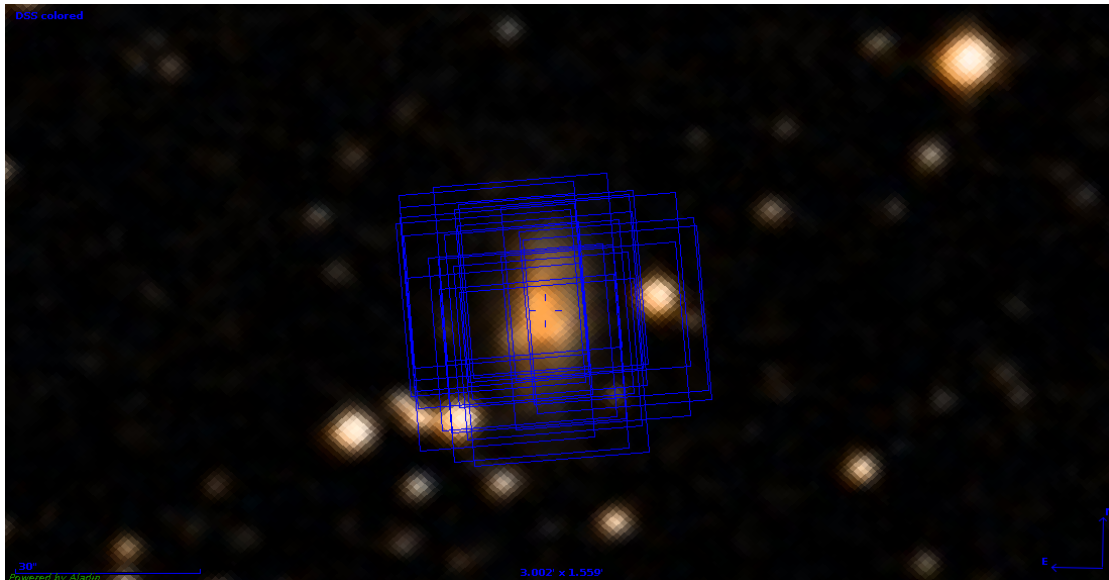


Figure 4.20 – Footprint of the MIRI imaging observation plotted on the 2MASS sky.

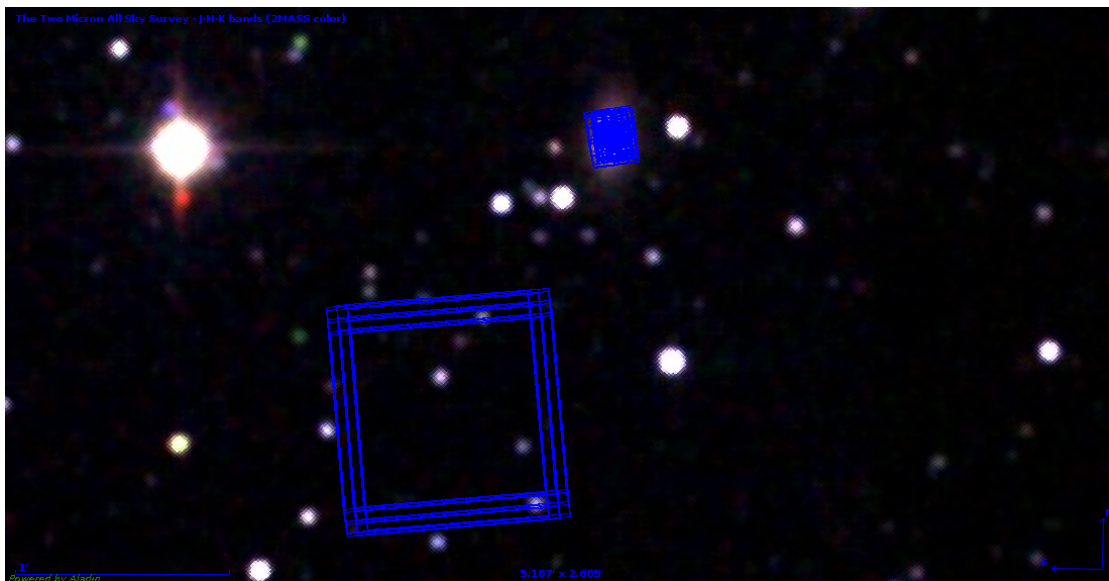


Figure 4.21 – Footprint of the MIRI MRS observation and simultaneous imaging plotted on the 2MASS sky.

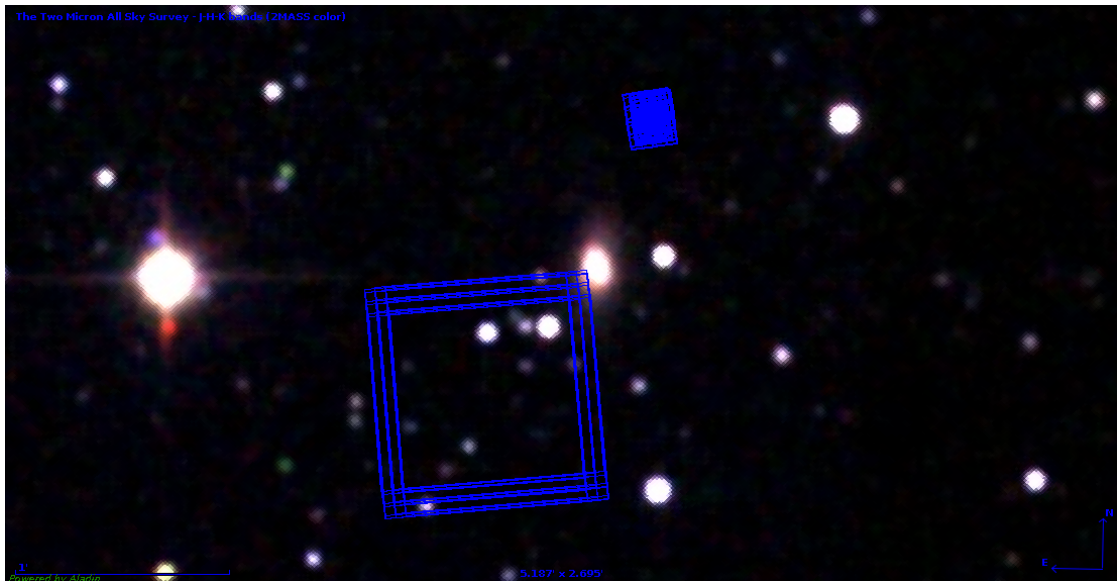


Figure 4.22 – Footprint of the MIRI dedicated background observation and simultaneous imaging plotted on the 2MASS sky.

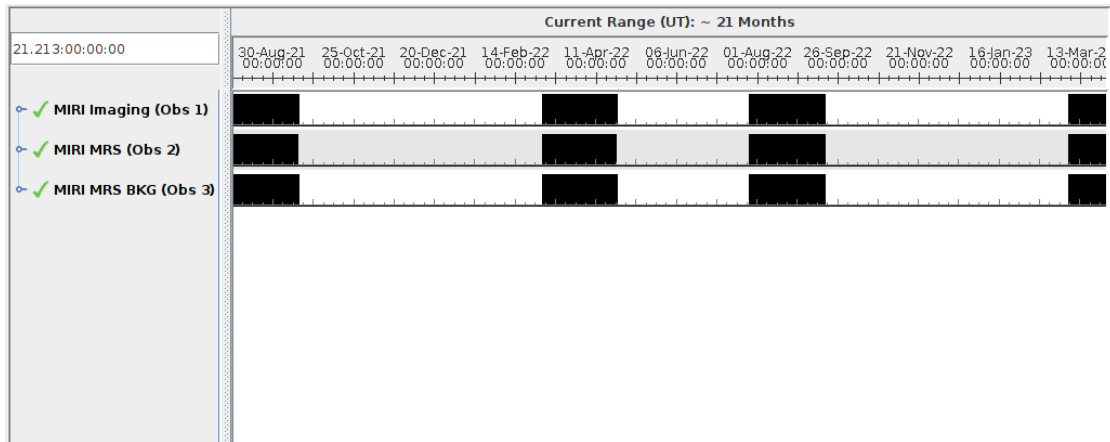


Figure 4.23 – Visit schedule of our observations.

Chapter 5

MIRI data simulation and analysis

The purpose of this chapter is to assess the projected performance of MIRI/JWST with respect to our scientific goal of studying the SSC population of IRAS 17138-1017 in the mid-IR. Although the ETC provides some SNR calculations, we would like to simulate realistic MIRI data in the finest details in Sect. 5.1, accounting for the instrumental behaviors including detector characteristics and defects, cosmic-ray impacts, optical distortions, instrumental background and transmission, etc. In the next section Sect. 5.2, we describe the JWST calibration pipeline applied to the simulated MIRI data and the output products. Finally in Sect. 5.3, we analyzed the reduced simulated data and tried to recover some pertinent astrophysical information, such as dust temperatures and distributions, cluster ages and masses, along with their uncertainties.

5.1 MIRISim

5.1.1 Introduction

We simulated MIRI observations with MIRISim (Geers et al. 2019) version 2.3.0, a Python 3 simulator package developed by the MIRI European Consortium¹. MIRISim produces detector outputs from input astronomical scenes based on the best knowledge of MIRI performance. The workflow of MIRISim and its components are illustrated in Fig. 5.1 and Fig. 5.2 and described in detail below.

ObsSim is the central processing module of MIRISim that handles input, output and calibration files, coordinates simulator components, organizes and executes simulations. Initially, it parses target parameters from the user and provides them to **SkySim**. It also parses instrument and simulator parameters for either **ImSim**, **LRSSim** or **MAISIE**.

SkySim creates an astronomical scene from the scene properties or queries interpreted by **ObsSim**. Users may specify targets in the form of a FITS (Flexible Image Transport System) file or through sets of spatial and spectral parameters. The resulting sampled scene will be fed into either **ImSim** or **LRSSim** corresponding to the imaging or LRS mode. In the MRS mode, **ObsSim** converts it into a SkyCube for **MAISIE**.

ImSim takes the sampled scene from **SkySim** and simulates the instrumental transmission, response, distortions and PSFs for different imager array sizes. A detector illumination model is returned to **ObsSim** and subsequently provided to **SCASim**. A separated module for the LRS mode **LRSSim** is available, which includes image slicing and dispersion. However coronagraphy is not yet supported.

1. <https://miricle.org/>

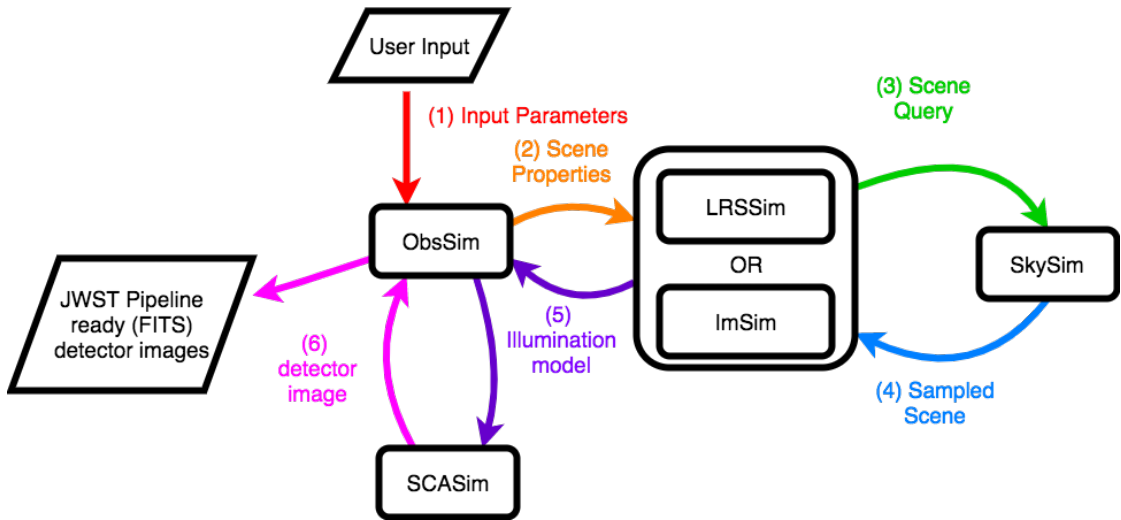


Figure 5.1 – MIRISim Workflow for the imaging and LRS modes (MIRI European Consortium 2020)

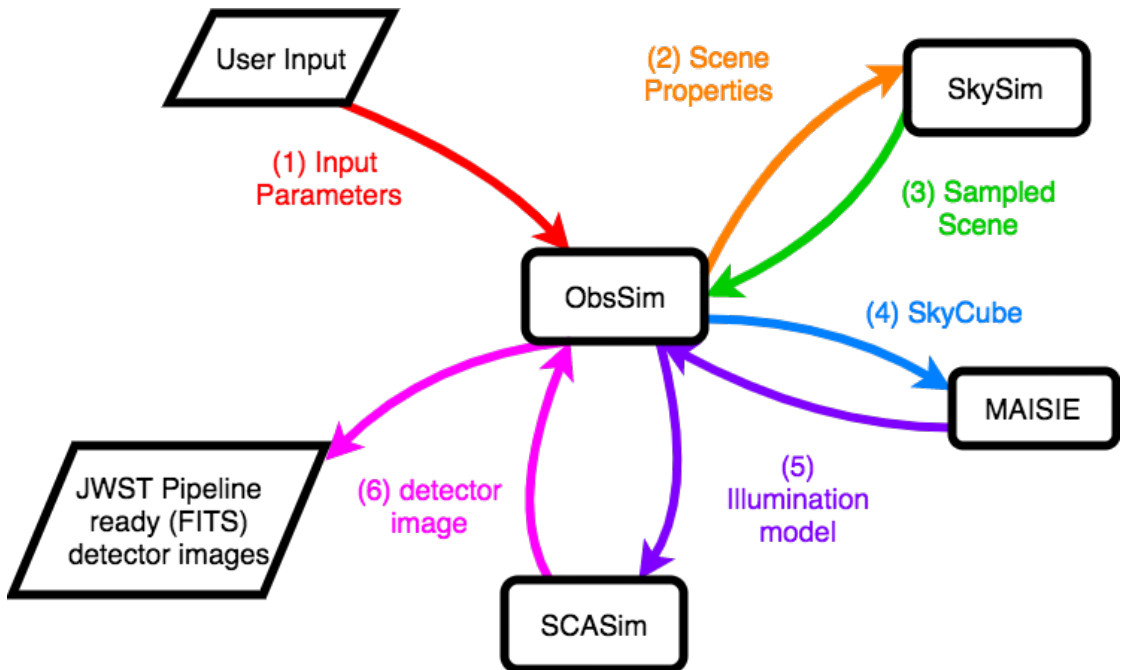


Figure 5.2 – MIRISim Workflow for the MRS mode (MIRI European Consortium 2020)

MIRI-MAISIE is built from the MIRI SpecSim simulator (Lorente et al. 2006) and Multi-purpose Astronomical Instrument Simulator (MAISIE; O’Brien et al. 2016) to simulate MRS observations. It slices and disperses the SkyCube from ObsSim, applies the thermal contamination, distortions, fringing effects, pixel response and gain to each channel then combines into an illumination model for the detector. ObsSim stores this model for later SCASim processing.

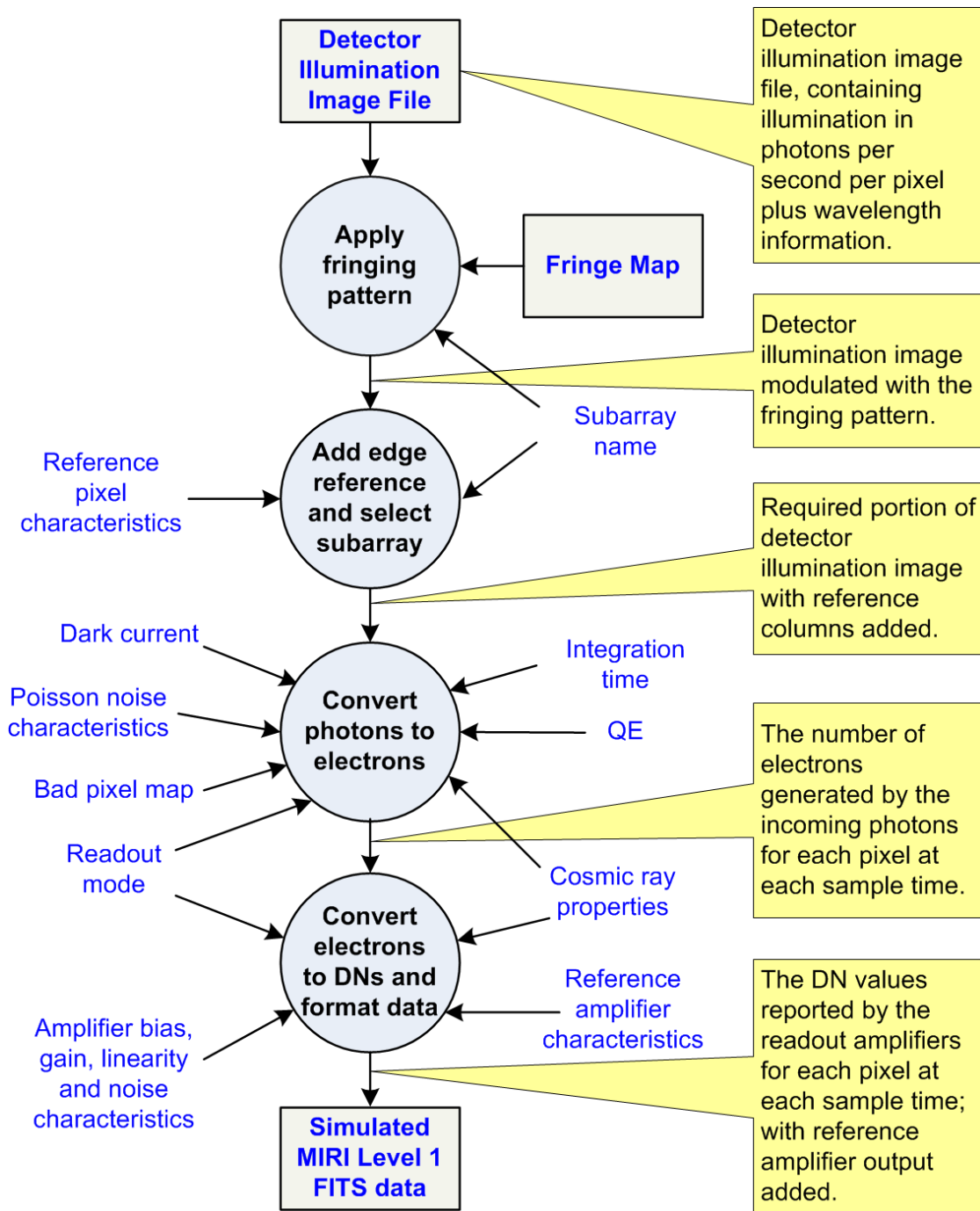


Figure 5.3 – SCASim workflow (MIRI European Consortium 2020)

SCASim is the Sensor Chip Assembly (SCA) simulator (Beard et al. 2012). Through ObsSim, it receives the illumination model created by either ImSim, LRSSim or MAISIE and simulates the detector effects as presented in Fig. 5.3. Finally the detector images produced by SCASim are written to FITS files by ObsSim, which are compatible with the JWST data reduction pipeline.

MIRISim operates based on the Calibration Data Products (CDPs), which are the best description of MIRI instrument performance as known by the MIRI European Consortium. These files are delivered to STScI, taking part in the Calibration Reference Data System (CRDS) of the JWST Data Calibration Pipeline (Bushouse et al. 2017). Currently MIRISim 2.2.0 uses the CDP-7 as baseline and is compatible with the build 7.2.1 of the JWST pipeline.

5.1.2 Input scenes

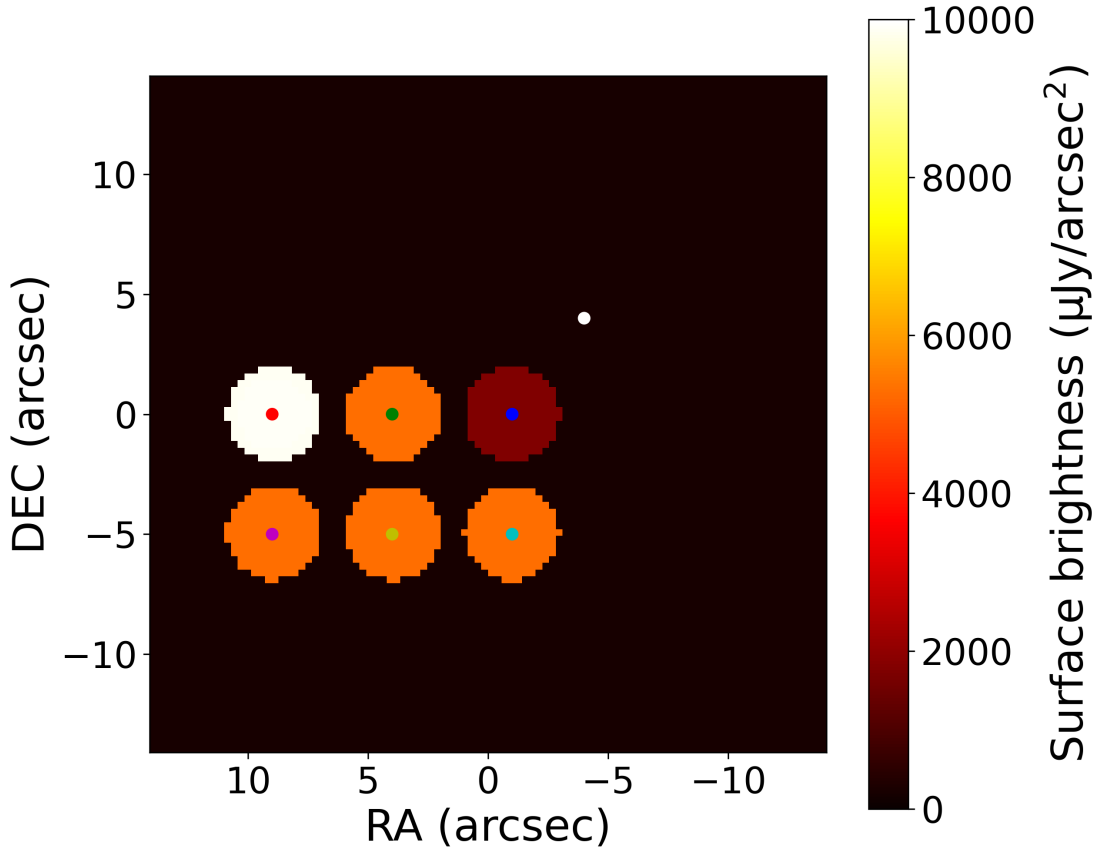


Figure 5.4 – MIRI imaging simulation scene at $10 \mu\text{m}$. Six SSC models with their local galaxy backgrounds are depicted: the bright (red), median (green) and faint (blue) SSCs described in Chapter 3 and the SSCs from Lam et al. (2020) with the same inner radius for the dust envelope $R_{\text{in}} = 5 \text{ pc}$ and the ages $\tau = 1$ (magenta), 5 (yellow), 10 Myr (cyan). A Vega star (white) normalized at $m = 12.5$ is also added for calibration purposes.

MIRISim allows users to construct scenes with point sources, extended sources in the forms of exponential and Sersic disks, as well as sky backgrounds. However, MIRISim does not support

flat extended sources as in the ETC. Alternatively, users may import an external FITS cube or image.

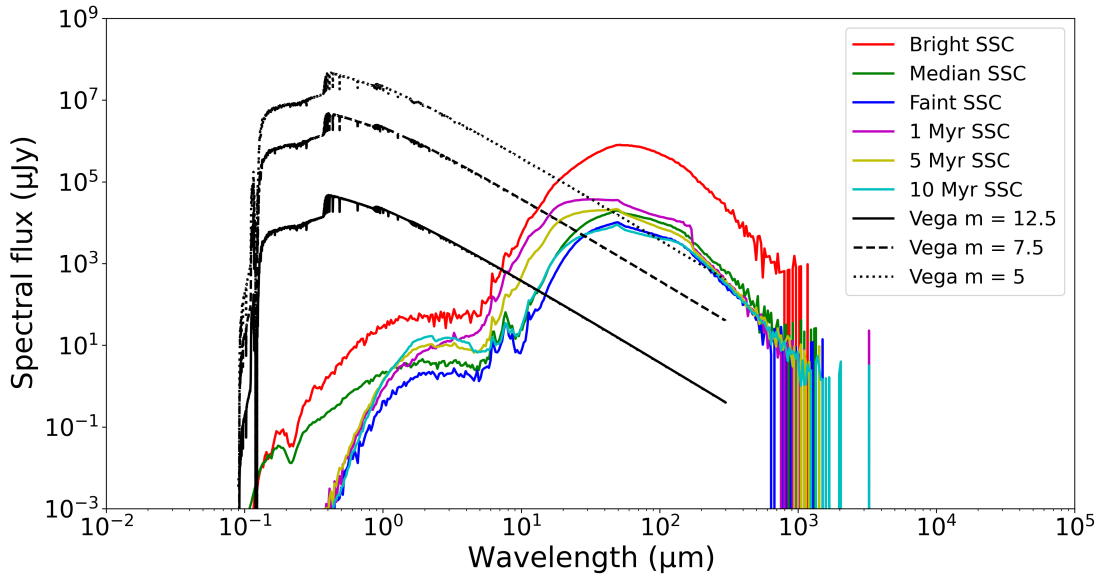


Figure 5.5 – Input SEDs of point sources for MIRISim.

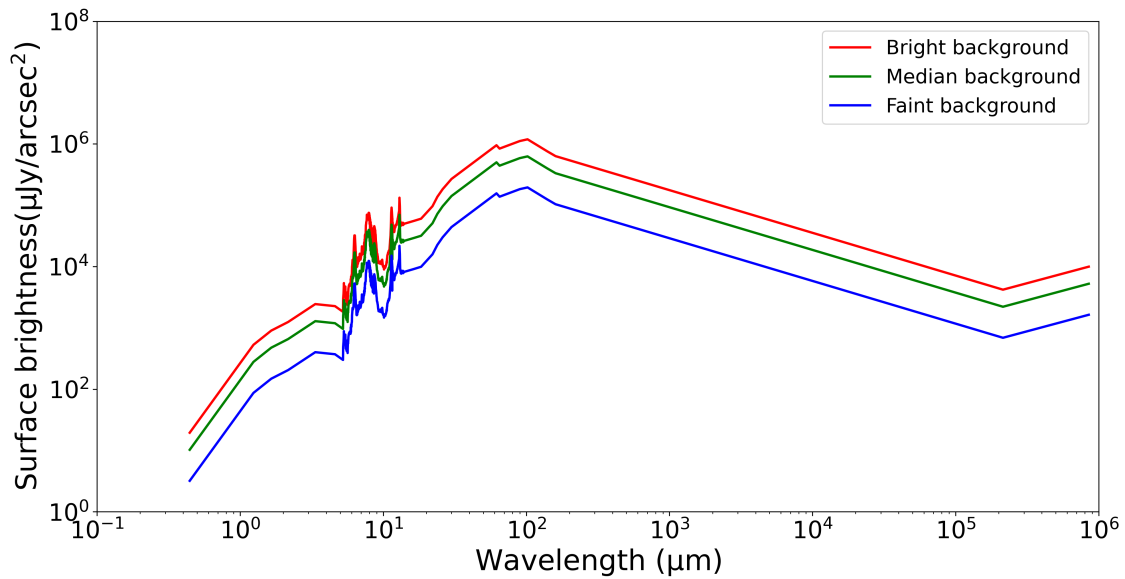


Figure 5.6 – Input SEDs of galaxy backgrounds for MIRISim.

For MIRI imaging, we built a scene as shown in Fig. 5.4 to simulate the SSCs in IRAS 17138-1017. Six point sources at the centers of the circular disks are the bright, median and faint SSCs described in Chapter 3 and Chapter 4, and the SSC models from [Lam et al. \(2020\)](#) with the same

inner radius for the dust envelope $R_{\text{in}} = 5$ pc and the ages $\tau = 1, 5, 10$ Myr. In the ETC, we used flat circular disks to represent local galaxy backgrounds. However in MIRISim, we worked around by using exponential disks in the form of $I = I_0 e^{-r/h}$ with a very large scale radius $h = 1000''$ and a truncation radius of $2''$. For the SSCs in Chapter 3, their local galaxy backgrounds share the same SED as of IRAS 17138-1017, but normalized to the K_s -band surface brightness values measured around them respectively. We adopted the median SSC galaxy background for the SSC models from Lam et al. (2020). To simulate the foreground Galactic extinction, we reddened the SSC and background SEDs by $A_V = 1.88$ based on the Fitzpatrick (1999) reddening law and Schlafly & Finkbeiner (2011) measurements from NED. The galaxy background SEDs are shown in Fig. 5.6. For calibration purposes, we also included in the scene a Vega star, which is normalized to $m = 12.5$ for the filters F560W, F770W, F1000W, F1130W, $m = 7.5$ for the filters F1500W, F1800W, F2100W and $m = 5$ for the filter F2550W. The point source SEDs are shown in Fig. 5.5. Finally we arbitrarily set up a low-level background with a gradient of 5% over $1'$ and a PA of 45° .

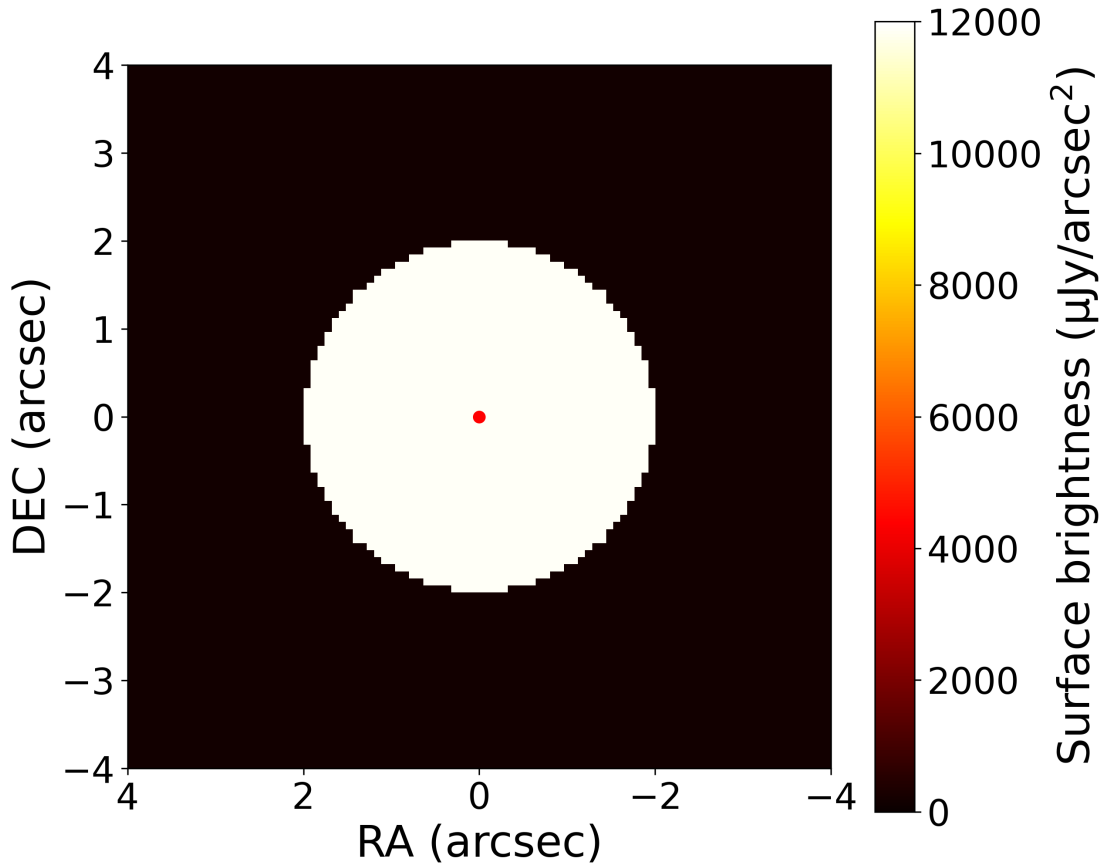


Figure 5.7 – MIRI MRS simulation scene at $10 \mu\text{m}$ containing the bright SSC (red dot) on its local galaxy background (white disk).

For MIRI MRS simulations, given the FOVs of the channels, we could only observe SSC scenes one by one, particularly the three SSC models from Lam et al. (2020) and their corresponding galaxy backgrounds. A low-level background with a gradient of 5% over $1'$ and a PA of 45° was

also present. The MRS simulation scene is plotted in Fig. 5.7.

5.1.3 Instrumental configuration

To simulate MIRI imaging in eight filters F560W, F770W, F1000W, F1130W, F1500W, F1800W, F2100W and F2550W, we adopted the corresponding readout patterns, subarrays, numbers of groups and numbers of integrations described in Table 4.10, but only one exposure for each observation since dithering is defined separately in MIRISim. The optical paths are configured in accordance with the above subarrays in the imaging mode, assuming the observation date at launch. While we would like to use a 4-point dither pattern for extended source, MIRISim only offers the large CYCLING dither pattern. Nevertheless, we implemented it with four dither positions, starting from the first position in the recommended pattern.

For MIRI MRS spectroscopy, we simulated individual IFU detectors (channels 1,2 or channels 3,4) in combination with each disperser (SHORT, MEDIUM and LONG). Thus each scene requires six simulations to cover the entire spectral range. We also applied the corresponding readout patterns, subarrays, number of groups and number of integrations from Table 4.11 and only one exposure for each observation. The optical paths were set for the channel of shortest wavelengths in each observation in the MRS mode, assuming the observation date at launch. Contrary to the imaging mode, we did not dither since MIRISim only provides MRS dither patterns optimized for point sources.

5.1.4 Simulator configuration

For the imaging mode, we used default parameters for the internal components of the MIRISim presented in Section 5.1.1. In fact [MIRI European Consortium \(2020\)](#) recommends general users not to change these settings. However, the current version of MIRISim is known to overproduce noise on the integration ramps in the MRS simulations with the FAST readout mode². As a consequence, excess cosmic ray flagging may occur during pipeline reduction and subsequently affect slope images, cubes, and extracted spectra. While this effect is still being investigated, the MIRISim team recommend users to exclude the read noise in MRS FAST mode simulations.

5.1.5 Output

MIRISim produces detector images conforming to the MIRI data product requirements and the JWST pipeline. Each detector image corresponds to a single exposure and its science extension is a 4D cube in the form of $n_{cols} \times n_{rows} \times n_{groups} \times n_{ints}$. Fig. 5.8 and Fig. 5.9 are two examples of detector images in the MIRI imaging and MRS modes respectively.

Furthermore, MIRISim also produces illumination models generated by the simulators. These models are immediate products illustrating how the specified MIRI detector would be illuminated given the inputs from the user. Subsequently they are processed by SCASim to produce the detector images above. Fig. 5.10 and Fig. 5.11 illustrate the illumination models for Fig. 5.8 and Fig. 5.9 respectively.

2. https://wiki.miricle.org/Public/MIRISimPublicRelease2dot3#Simulation_of_some_detector_effects_is_approximate

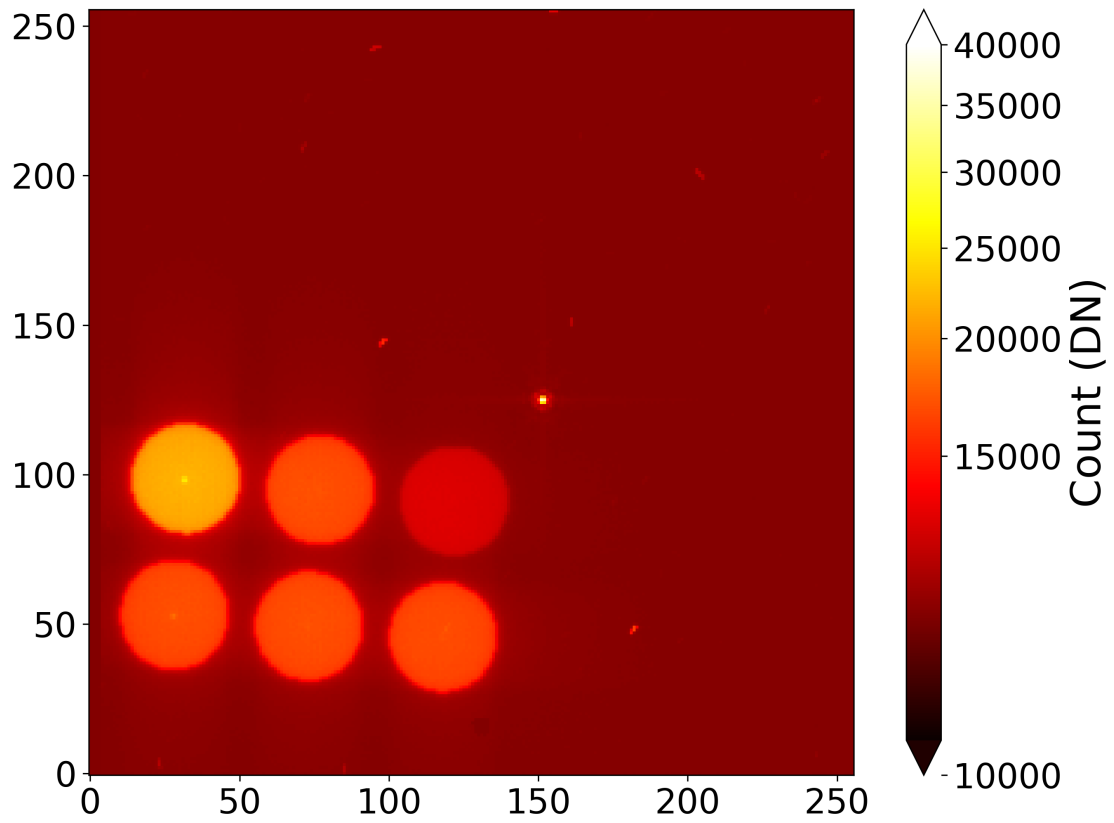


Figure 5.8 – Detector image of the scene in Fig. 5.4 observed through the F560W filter. The last frame of the first exposure is shown for maximum signal levels.

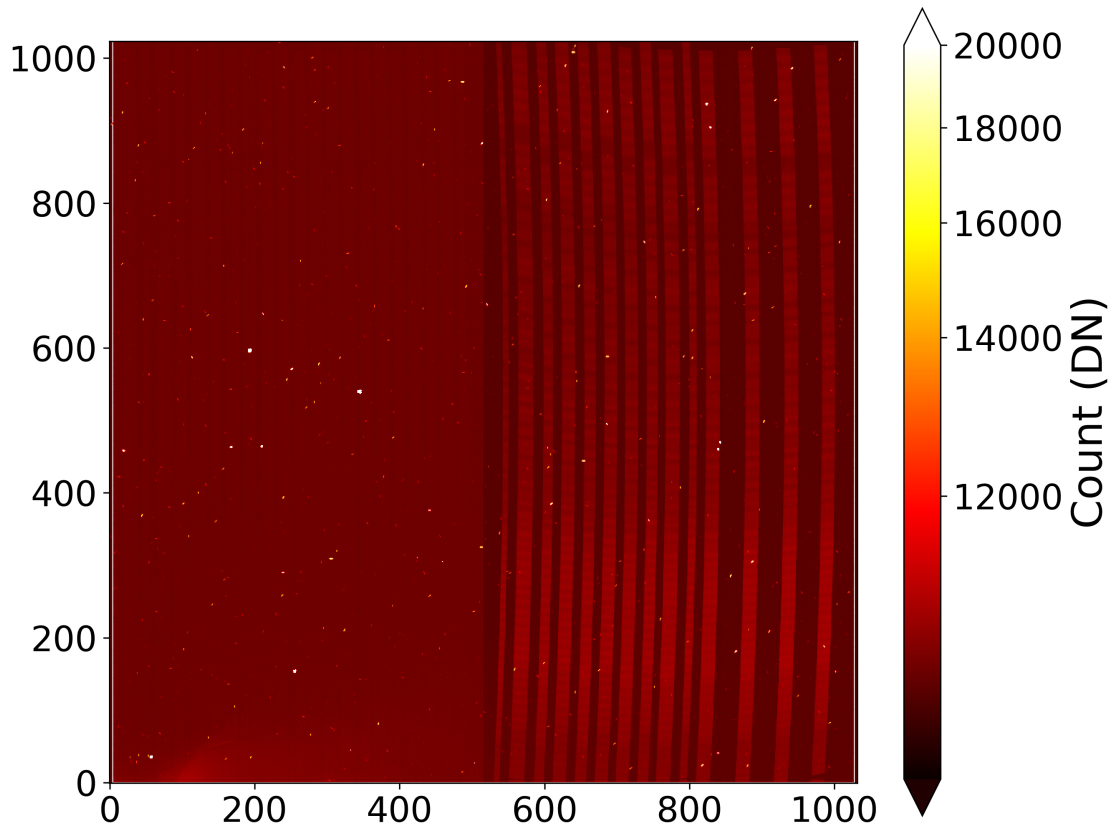


Figure 5.9 – Detector image of the scene in Fig. 5.7 for the 1 Myr SSC observed through channels 12SHORT. The last frame of the exposure is shown for maximum signal levels.

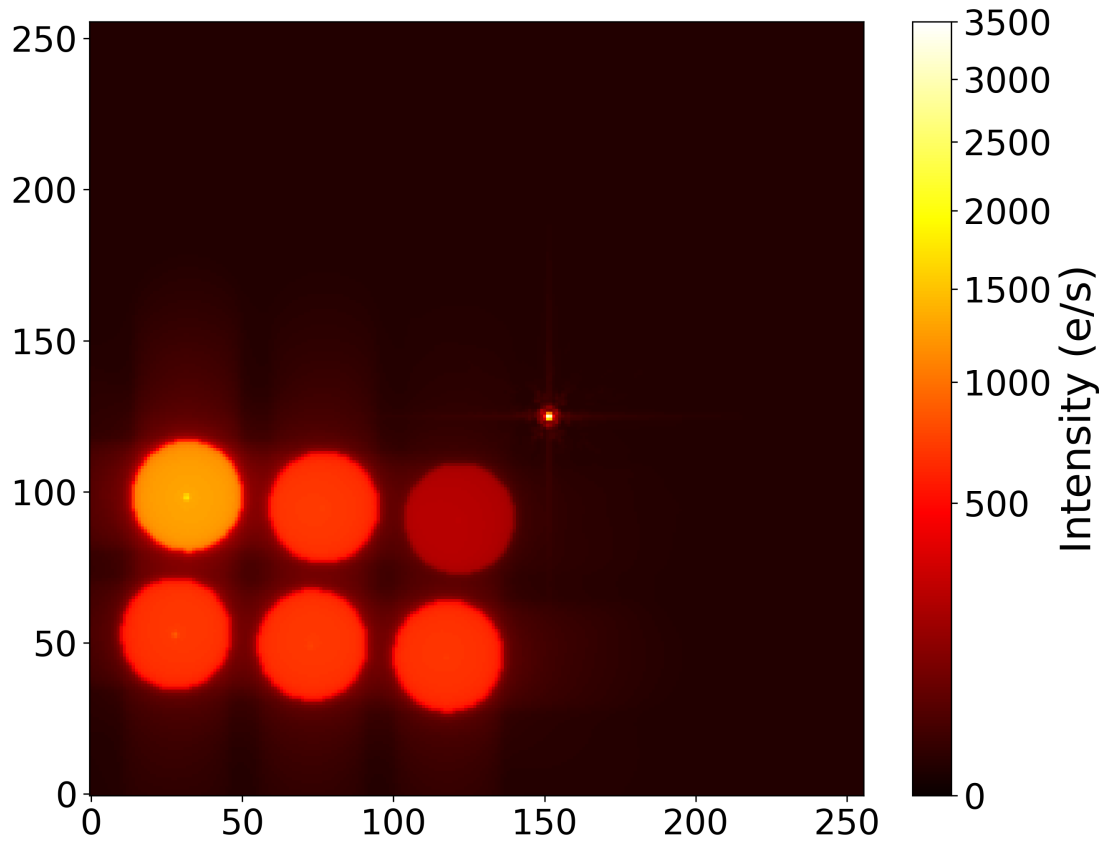


Figure 5.10 – Illumination model through the F560W filter for the scene in Fig. 5.4.

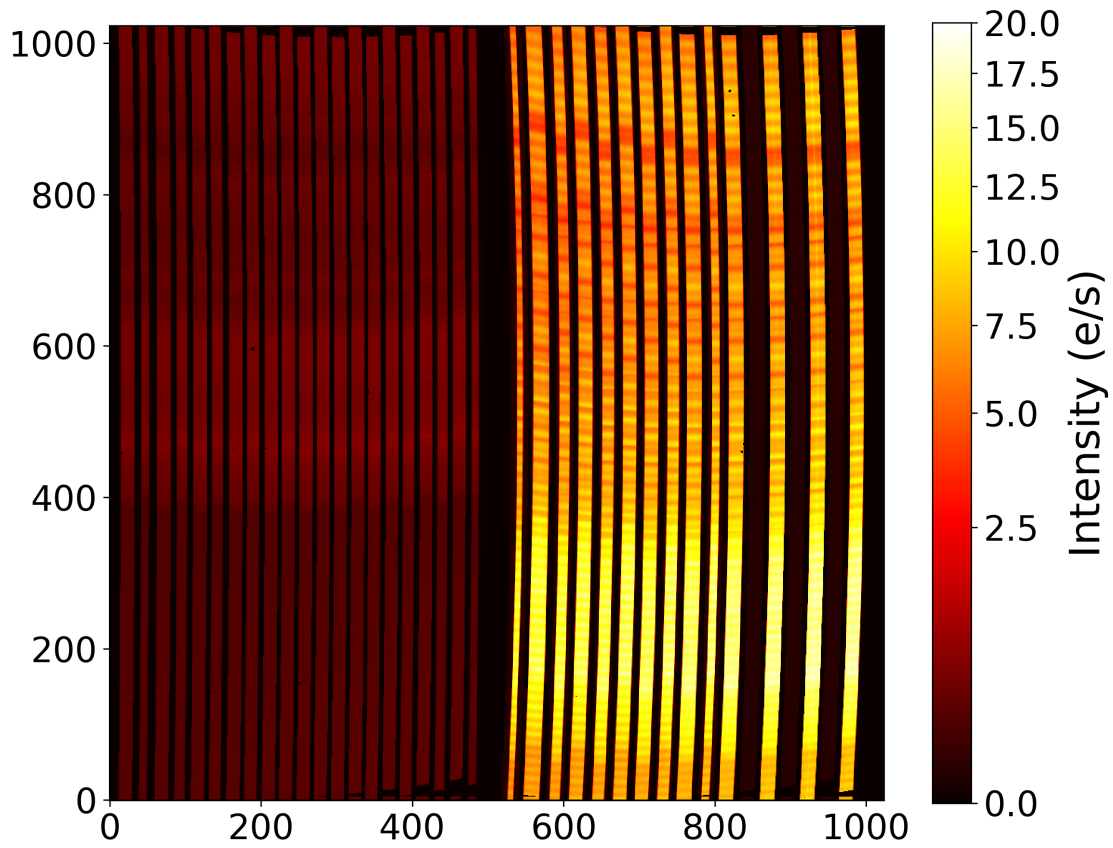


Figure 5.11 – Illumination model through channels 12SHORT for the scene in Fig. 5.7 with the 1 Myr SSC.

5.2 Data reduction

The JWST Data Reduction Pipeline (Bushouse et al. 2017) is a Python package that helps users process and remove as far as possible instrumental artefacts from observations, in order to retrieve single calibrated exposures as well as combined data and high-level products. Currently the software is being actively developed and has not been released for public use yet. It is on an as-is basis only without any guarantee or support. Nevertheless, we obtained a fully tested and tagged release version (0.16.2, build 7.5) from GitHub³ and reduced the output files from MIRISim as they are ready for ingest.

The full calibration pipeline consists of 3 main stages (STScI 2020):

- Stage 1 processes individual raw exposures at detector-level and generates count rate images.
- Stage 2 corrects and calibrates count rate data in accordance with the instrument and observing mode, producing fully calibrated exposures.
- Stage 3 creates combined products from individual calibrated exposures.

The specific pipeline module for each stage may vary depending on the instrument and observing mode. Each module includes multiple calibration steps, many of them require reference files in accordance with the instrument in order to process data. The JWST Instrument Teams create, test and validate these files, then deliver them to the Reference Data for Calibration and Tools (ReDCaT) Management Teams. Finally these files will be distributed to the pipeline team or any other ground subsystem through the JWST CRDS. They are regularly updated following the evolution of the data processing and the knowledge of the instruments. In addition, the CRDS also provides configuration files containing parameter values for pipelines or steps. Details on the calibration process of the MIRISim outputs are described below.

5.2.1 Stage 1: Detector processing

We executed the stage 1 pipeline to process individual dithered imaging and MRS exposures using the common `calwebb_detector1` configuration for non-time-series observation (TSO) modes. The following steps were automatically executed in sequence:

- Data quality initialization:

The `dq_init` step creates the data quality mask using a static MASK reference file from CRDS. The reference flags are assumed to reflect pixel conditions persisting in all groups and integrations.

- Saturation detection:

The `saturation` step identifies saturated pixels. For each pixel, it compares the SCI values on a group-by-group basis with predetermined limits in a saturation reference file from CRDS. The group reaching the saturation threshold will be flagged SATURATED in the GROUPDQ array, so will the subsequent ones.

3. <https://github.com/spacetelescope/jwst>

- First frame correction:

The `firstframe` step designates the first group in every integration as `DO_NOT_USE` in the `GROUPDQ` array if there are more than three groups per integration, excluding it from subsequent steps. It is required to correct for the reset anomaly of MIRI arrays as the initial sampling of an integration after a reset does not behave linearly (Ressler et al. 2015).

- Last frame correction:

Similar to the `firstframe` step above, the `lastframe` step designates the last group in every integration as `DO_NOT_USE` in the `GROUPDQ` array, but only if there are more than two groups per integration, excluding it from subsequent steps. It is required to correct for the last-frame effect of MIRI. In particular, pixel rows are reset in pairs and in the last frame of an integration they interfere the adjacent ones, causing unwanted offsets (Ressler et al. 2015).

- Linearity correction:

The `linearity` step corrects pixel-by-pixel, group-by-group and integration-by-integration within an exposure for the non-linearity of the detector. The algorithm is similar to the HST WFC3/IR instrument, where the corrected count in a pixel F_c (in DN) is calculated from the observed count F as follows:

$$F_c = c_0 + c_1F + c_2F^2 + \dots + c_nF^n \quad (5.1)$$

The polynomial coefficients c_i are retrieved from the linearity reference file.

- RSCD correction:

The `RSCD` step flags a number of initial groups in all integrations except the first one as `DO_NOT_USE`, in order to circumvent several non-ideal behaviors of the detectors. In detail, MIRI uses field effect transistors (FETs) to reset electronics but this process is actually exponential, not instantaneous. There is only one reset between integrations but several ones between exposures, thus from the second integration afterwards, the first frames will be affected by this reset decay. An algorithm to repair instead of removing those affected groups is being developed. For the subarray SUB256 the number of skipped groups is four. However we only use one integration for each exposure so there will be no change after this step despite of it being executed.

- Dark current subtraction:

The `dark_current` step subtracts dark current data from an exposure using a dark reference file. The reference files have been generated using one frame per group (`NFRAMES=1`), no dropped frame (`GROUPGAP=0`) and the maximum number of frames allowed for an integration. A direct frame-by-frame subtraction will be performed if the processed science exposure have the same parameters `NFRAMES=1` and `GROUPGAP=0`. This is the case of our exposures. Otherwise, the dark data will be frame-averaged and skipped similar to the processed data, then subtracted on a group-by-group basis.

- Reference pixel correction:

The `refpix` step corrects for the signal drifts caused by the readout electronics using the reference pixels. There are four columns of reference pixels corresponding to four amplifiers located at the left and right edges of each MIRI detector. Nevertheless, this step is skipped for subarray data from MIRI imaging simulations. On the other hand, the MIRISim team reports vertical striping in simulated MRS data due to an inconsistent handling of reference pixels in the DARK reference files and recommends users to disable this step⁴.

- Jump detection:

The `jump` step identifies jumps in the integration ramps of each pixel and flags their locations in the GROUPDQ array as JUMP_DET. This effect is generally caused by cosmic rays. In particular, the jump detection is based on the two-point difference method (Anderson & Gordon 2011):

For each pixel, the first differences (between adjacent groups) and their clipped median (without the largest one) are calculated. The total expected noise for each difference includes the read noise and the Poisson noise derived from the median. Then the ratios of the median-subtracted differences to their expected noise are computed. If the largest value exceeds the rejection threshold, the corresponding group will be flagged as jump-impacted. The algorithm runs iteratively on a pixel excluding flagged groups after each loop until no more jump is found. The gain and read noise used in this step are retrieved from the reference files.

There is an option to save the output of this step as a `_ramp` file, with the same dimensions as the raw input ($n_{cols} \times n_{rows} \times n_{groups} \times n_{ints}$). By default we did not selected this option.

- Ramp fitting:

The `ramp_fitting` derives the mean count rate for each pixel using ordinary least squares linear fitting. First, the linear fit is performed on individual segments. These segments are continuous ramp intervals that do not contain any saturation or cosmic ray as determined by the GROUPDQ array. Then the final slope for the exposure is calculated from all individual segment slopes and stored as a 2D `_rate` file. This is the primary output of the calibration stage 1. We only have one integration per exposure, but if there are multiple integrations, the count rates for individual integrations will be saved as a 3D `_rateints` file. In detail, the slope and variance calculations follow the weighting algorithm of Fixsen et al. (2000):

The read noise variance of a segment slope is calculated as follows, assuming the read noise from the corresponding reference file:

$$Var_s^R = \frac{12 R^2}{(ngroups_s^3 - ngroups_s)(tgroup^2)} \quad (5.2)$$

4. https://wiki.miricle.org/Public/MIRISimPublicRelease2dot3#Vertical_striping

where R is the read noise of the first differences between adjacent frames, $ngroups_s$ is the group number in the segment, and $tgroup$ is the group time TGROUP in the header (in seconds).

The Poisson noise variance of a segment slope is computed as:

$$Var_s^P = \frac{slope_{est}}{tgroup \times gain (ngroups_s - 1)} \quad (5.3)$$

where $slope_{est}$ is the median of the first differences of non-saturated and cosmic-ray-free groups in all integrations, which is considered as a robust pixel slope estimate, and $gain$ is the pixel gain from the corresponding reference file.

The total variance of a segment slope is simply:

$$Var_s^C = Var_s^R + Var_s^P \quad (5.4)$$

The read noise variance of an integration slope is:

$$Var_i^R = \frac{1}{\sum_s \frac{1}{Var_s^R}} \quad (5.5)$$

The Poisson noise variance of an integration slope is:

$$Var_i^P = \frac{1}{\sum_s \frac{1}{Var_s^P}} \quad (5.6)$$

The total variance of an integration slope is:

$$Var_i^C = \frac{1}{\sum_s \frac{1}{Var_s^R + Var_s^P}} \quad (5.7)$$

The integration slope is weighted from the segment slopes as follows:

$$slope_i = \frac{\sum_s \frac{slope_s}{Var_s^C}}{\sum_s \frac{1}{Var_s^C}} \quad (5.8)$$

These slopes are recorded in the `_rateints` file.

The read noise variance of an exposure slope is:

$$Var_o^R = \frac{1}{\sum_i \frac{1}{Var_i^R}} \quad (5.9)$$

The Poisson noise variance of an exposure slope is:

$$Var_o^P = \frac{1}{\sum_i \frac{1}{Var_i^P}} \quad (5.10)$$

The total variance of a segment slope is simply:

$$Var_o^C = Var_o^R + Var_o^P \quad (5.11)$$

Finally the output exposure slope is calculated as:

$$slope_o = \frac{\sum_{i,s} \frac{slope_{i,s}}{Var_{i,s}^C}}{\sum_{i,s} \frac{1}{Var_{i,s}^C}} \quad (5.12)$$

These slopes will be recorded in the `_rate` file.

In the end of this stage, we obtained output `_rate` files as demonstrated in Fig. 5.12 and 5.13.

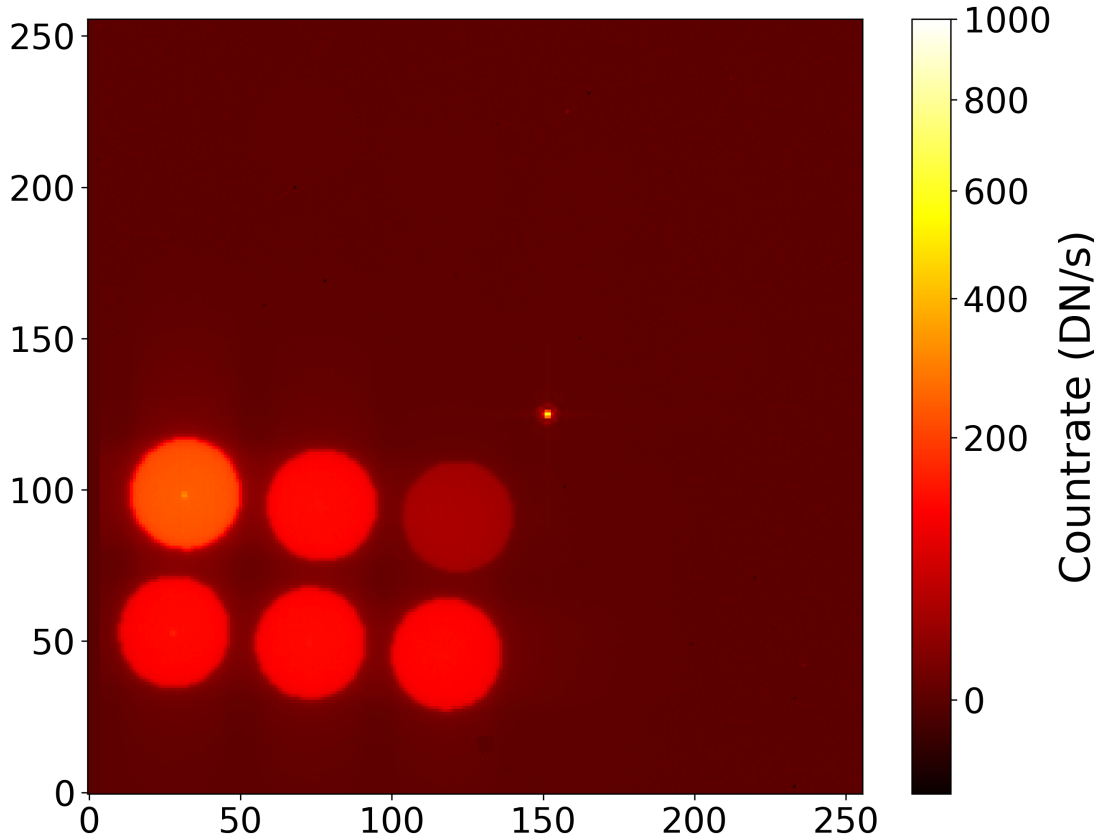


Figure 5.12 – Count rate data retrieved from the detector image in Fig. 5.8.

5.2.2 Stage 2: Instrument-mode processing for imaging

We continued to run the stage 2 pipeline to process the imaging count rate data produced by stage 1 using the `calwebb_image2` configuration for non-TSO imaging modes. This stage consists of the following steps in chronological order:

- Assign world coordinate system (WCS):

Starting the stage 2 pipeline, the `assign_wcs` assigns a WCS object to each SCI exposure as an ASDF (Advanced Scientific Data Format) extension. It provides the transforma-

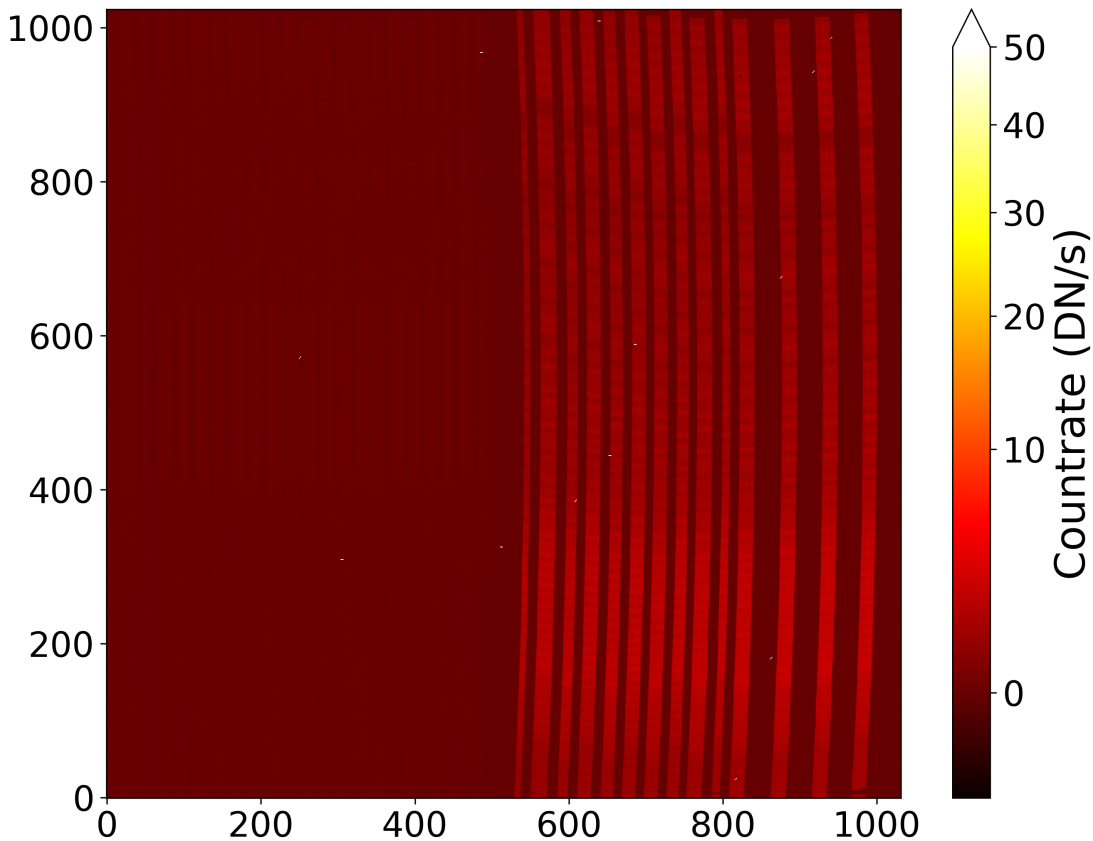


Figure 5.13 – Count rate data retrieved from the detector image in Fig. 5.9.

tion from the detector frame `v2v3` to the `world` coordinate frame with zero-based input positions. Some instruments may have intermediate coordinate frames, such as the detector frame for the MIRI imaging mode. In particular, the following WCS keywords in the SCI header define the transformation: `RA_REF` and `DEC_REF` defining a fiducial point on the sky in International Celestial Reference System (ICRS) degree, `V2_REF` and `V3_REF` defining that point in the V2V3 system in arcsec, `ROLL_REF` providing the corresponding roll angle in degree and `RADESYS` specifying the standard coordinate system ICRS. For the MIRI imaging mode, the transformation is constructed from the distortion and filter-offset reference files from CRDS. Nevertheless, the WCSs of the MIRISim outputs are for cosmetic purposes only.

— Flat field correction:

The `flat_field` step divides the science data by a flat-field reference data from CRDS. For our MIRI imaging data, the subarray region corresponding to SUB256 is extracted from the flat-field image.

— Photometric calibration:

The `photom` step calibrates flux units from count rate to surface brightness or flux density using photometric and pixel area reference files from CRDS. The photometric reference data provides the flux conversions for various instrument configurations. Particularly for MIRI imaging the photometry information includes the flux density (PHOTMJSR in MJy/sr or PHOTUJA2 in $\mu\text{Jy}/\text{arcsec}^2$) producing 1 DN/s as well as the average pixel area (PIXAR_SR in sr^5 or PIXAR_A2 in arcsec^2). The pixel area reference data is transferred to the output as an AREA extension.

After this step, the pipeline will produce a fully calibrated but unrectified output with the suffix `_cal` as demonstrated in Fig. 5.14, which will be fed to the stage 3 pipeline later.

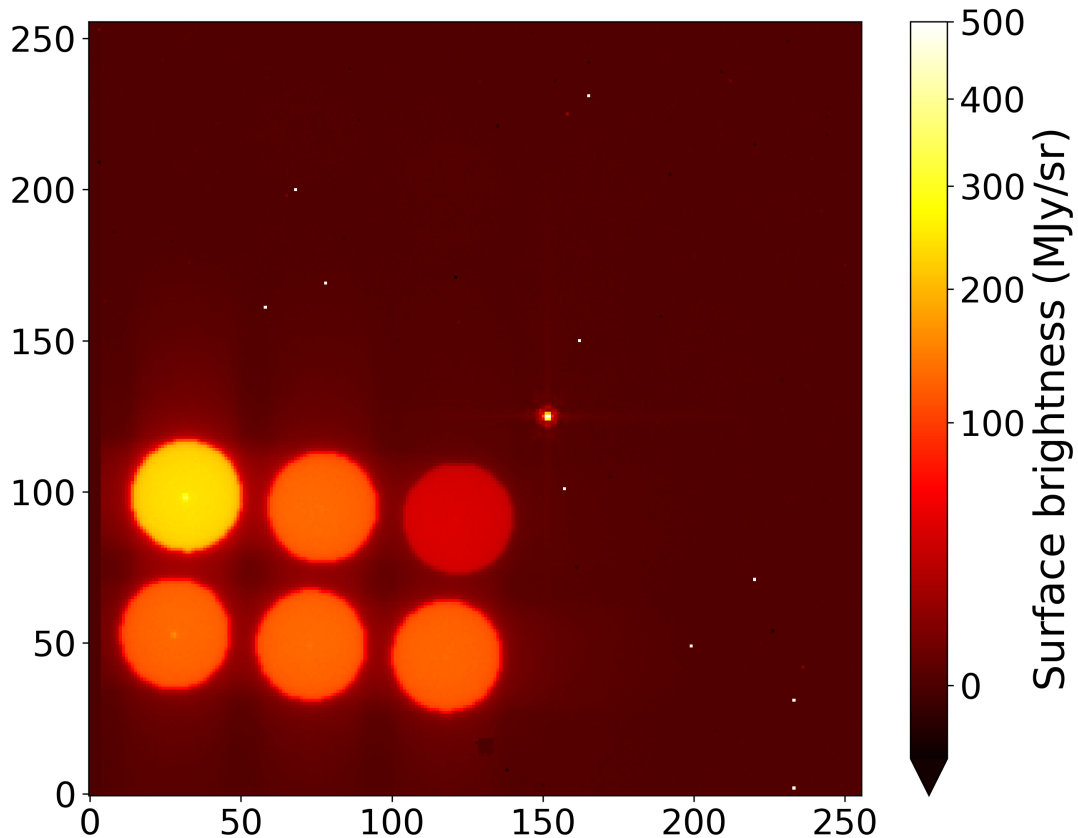


Figure 5.14 – Calibrated data retrieved from the detector image in Fig. 5.8. The pixel values are in MJy/sr.

— Resampling:

The `resample` step uses the WCS and distortion information to resample each input 2D exposure, then combines them into a single output using the drizzling algorithm⁶. Parameters are retrieved from the CRDS drizzling reference file. However, at stage 2

5. We have detected a bug in the pipeline, possibly a typo, concerning the value of PIXAR_SR. It is incorrectly specified as 8.4403609523084E-14, whereas it should be 2.84403609523084E-13 instead.

6. <https://www.stsci.edu/scientific-community/software/drizzlepac.html>

this step is implemented for quick-look purposes only and there is no combination. The rectified `_i2d` outputs are demonstrated in Fig. 5.15 below.

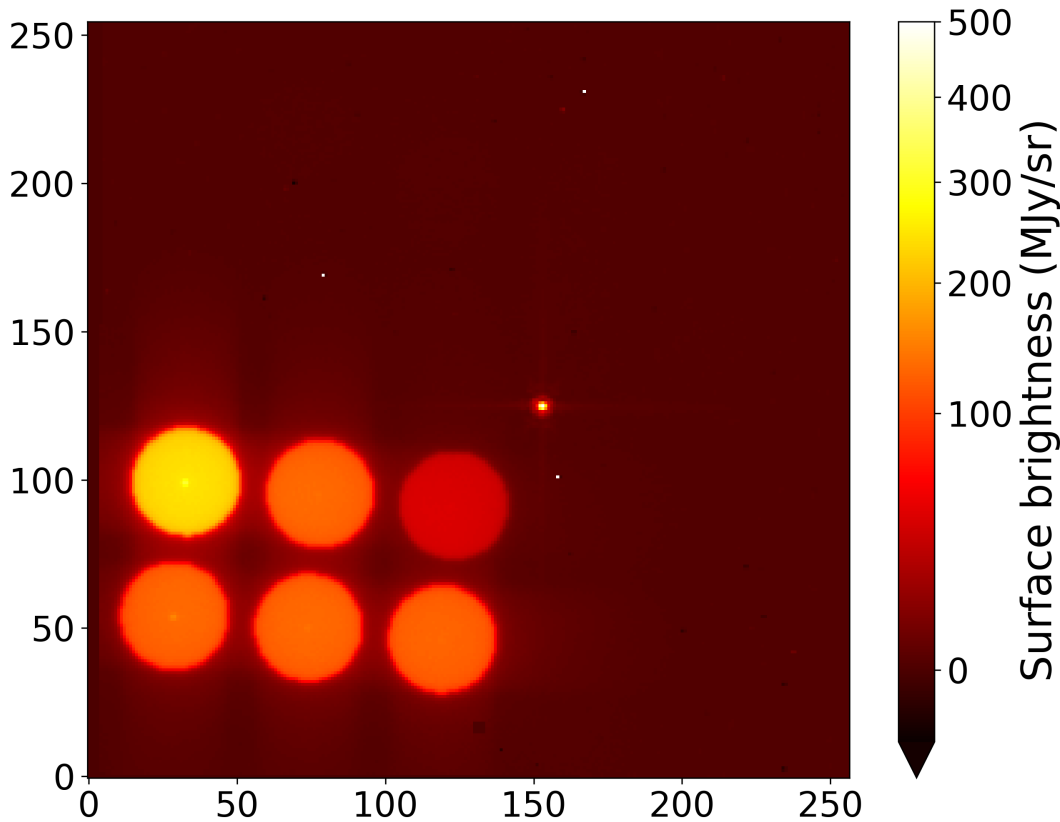


Figure 5.15 – Resampled 2D data retrieved from the detector image in Fig. 5.8. The pixel values are in MJy/sr.

5.2.3 Stage 3: Multiple exposure combination for imaging

Finally, for each filter, in order to combine the four dithered exposures into a single rectified output, we ran the stage 3 pipeline using the `calwebb_image3` configuration for non-TSO direct imaging modes. In particular, the steps below were successively executed:

— `TweakReg`:

The step `tweakreg` extracts point source catalogs from the input images and aligns their WCSs by matching these catalogs. It is based on the algorithm of the `tweakwcs` package⁷. First, sources in each input exposures are detected using the `photutils`⁸ implementation of the DAOFIND algorithm (Stetson 1987). Given a 2D Gaussian kernel (FWHM = 2.5 pixels by default) and a SNR threshold (10.0 above the background by default), it looks

7. <https://tweakwcs.readthedocs.io/en/latest/>

8. <https://photutils.readthedocs.io/>

for local density maxima in a convolved image and compares their sizes and shapes to the kernel. At maximum 100 brightest objects will be kept by default. By default, catalog matching is performed using at least 15 objects, with a searching radius of 1.0 arcsec, a minimum separation for distinct sources of 1.0 arcsec, a matching tolerance of 0.5 arcsec and initial offset from 2D histogram. General affine coordinate transformations are fitted to the catalogs using 3 clipping iterations at 3.0σ limit. Finally the corresponding tangent-plane corrections are applied to the input image WCS.

— SkyMatch:

The step `skymatch` equalizes sky values in the input images. The default algorithm is as follows. Using the mode statistic with 5.0 clipping iterations at 4.0σ limits, the minimum sky value of all the images is calculated and taken as the baseline value. The total signal levels in the overlap regions between image pairs are assumed to be dominated by pure sky and equal to that baseline. This step calculates the sky value adjustments required for each image to minimize the least-square mismatch of these signals. However they are not subtracted from the input.

— Outlier detection:

The step `outlier_detection` finds and flags any bad pixels, cosmic-rays or other artifacts that have been overlooked in the previous steps. For non-TSO MIRI imaging data, by default all input images are first resampled into a common WCS using the exposure time for weighting. A median image is derived from this stack, adopting 70% of maximum weight as the lower-limit for valid data. This median image is then resampled back to match each input image. The differences in their pixel values are calculated and compared with two thresholds to detect outliers. These thresholds are constructed from the resampled median, its derivative and the error data, given two SNRs (4.0 and 3.0 by default) and two derivative scaling factors (0.5 and 0.4 by default). In addition, a neighbor rejection of 1-pixel radius is also applied. Finally the outliers are flagged in the DQ arrays, resulting in `_crf` files similar to the calibrated data `_cal` but with DQ extensions updated.

— Resampling:

This is the same `resample` step described in the stage 2 pipeline for non-TSO imaging mode, but this time the combination of four dithered exposures was implemented, producing the final rectified `_i2d` output as illustrated in Fig. 5.16.

— Source Catalog:

The `source_catalog` step builds a source catalog containing various photometric and morphological properties. First, it extracts sources from the data using image segmentation from `photutils`. By default, it smooths the image by a 5×5 Gaussian kernel with a FWHM of 3.0 pixels, then looks for sources containing at least 5 connected pixels with values greater than 3σ above the background. If enabled, it can also deblend sources by multi-thresholding in combination with watershed segmentation. After identifying sources, it calculates their aperture photometry in three apertures encircling 30%, 50% and 70% of energy value, as well as the total aperture-corrected flux and magnitudes using the aperture correction reference file. The segmentation also derives the centroids,

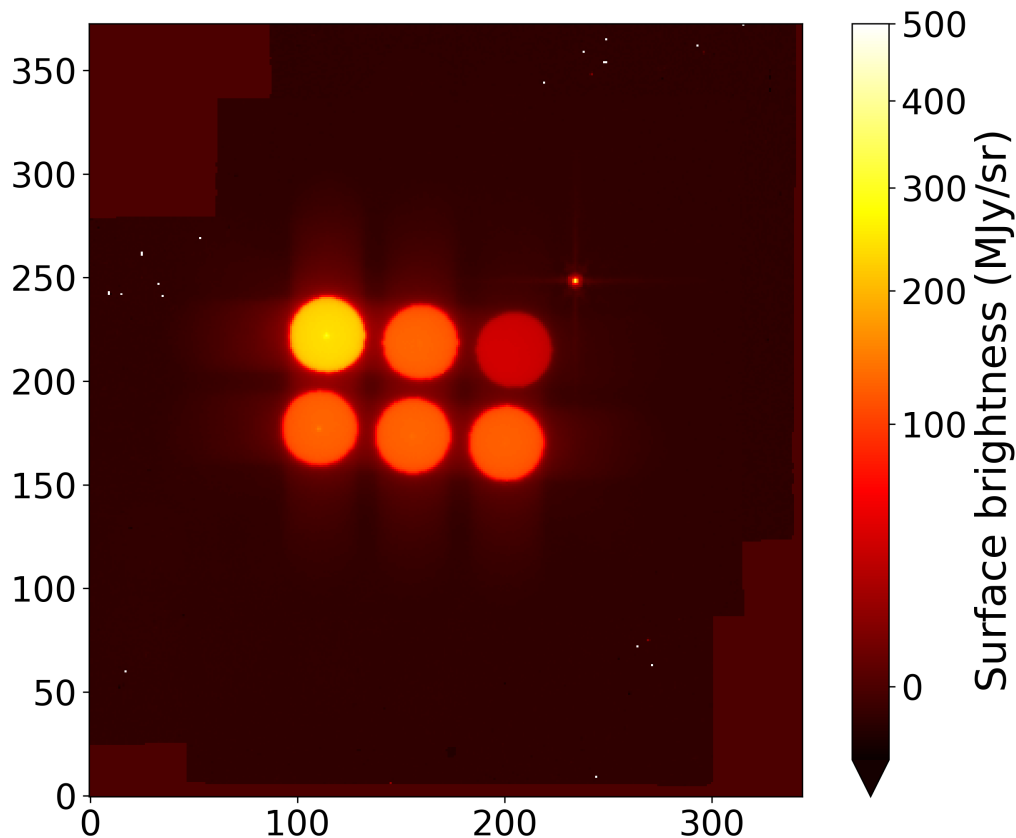


Figure 5.16 – Resampled 2D data retrieved by processing and combining four dithered F560W exposures of the scene in Fig. 5.4.

isophotal photometry, isophotal areas, semimajor and semiminor axes, orientation and the minimal bounding box of the sources. Both AB and Vega magnitudes are provided using the corresponding offset reference file. In the end, an output catalog `_cat` in the ECSV format is created. However, for post-pipeline data analysis, we prefer to use the PSF photometry by `STARFINDER` instead as image segmentation is not efficient in our case.

5.2.4 Stage 2: Instrument-mode processing for spectroscopy

The MRS count rate data produced by stage 1 was processed using the `calwebb_spec2` configuration for non-TSO spectroscopic modes. In particular, the pipeline consecutively executed following steps:

- Assign WCS:

This step is similar to the one implemented in the stage 2 `calwebb_image2` configuration for non-TSO imaging modes.

- Source type determination:

The `srctype` step assigns an appropriate value to the `SRCTYPE` keyword for subsequent calibrations based on the spatial extension of the target: either `POINT`, `EXTENDED` or `UNKNOWN`. For `MIRISim` MRS simulations without dithering, `SRCTYPE` is set to `EXTENDED` by default. In practice, the source type will be specified by the user in the `APT` and passed to `SRCTYPE`.

- Flat field correction:

This step is similar to the one implemented in the stage 2 `calwebb_image2` configuration for non-TSO imaging modes, but with the `FULL` array instead.

- Stray light correction:

The `straylight` step decontaminates MIRI MRS channel 1 and 2 spectra which are exposed to scattered signal from the Spectrometer Main Optics (SMO). This signal spreads over detector rows, decreasing from 1% in Channel 1A to a negligible level in Channel 2B compared to bright illuminated regions of the spectral image. The stray light comprises a smooth and a structured component, only the former is corrected. Theoretically, the regions between slices on the detector are shielded from sky signals and records the stray light only. Their locations are referred from the `REGIONS` reference file, assuming a 20% throughput threshold. Their signals are used to interpolate the stray light on the slice pixels based on the Modified Shepard's Method (MSM), building a 2D model for the entire detector. In particular, the stray light s on each science pixel is calculated as:

$$s = \frac{\sum_{i=1}^n p_i w_i}{\sum_{i=1}^n w_i} \quad (5.13)$$

where p_i are the stray light fluxes in the gap pixels at distances of d_i within a radius of influence R and w_i are the corresponding weights:

$$w_i = \frac{\max(0, R - d_i)^k}{R d_i} \quad (5.14)$$

By default $R = 50$ pixels and the exponent $k = 1$.

- Fringe correction:

The `fringe` step divides the science data by a fringe reference image from `CRDS` for correction. The particular fringe model depends on the detector and wavelength grating.

- Photometric calibration:

The `photom` step converts flux units from count rate to surface brightness using a photometric reference file from `CRDS`. This file contains 2-D maps of sensitivity factors (in $(\text{MJy/pixel})/(\text{DN/s})$) and sizes (in arcsec^2) of individual pixels, which are multiplied into the science image, producing a fully calibrated but unrectified exposure with the suffix `_cal` for stage 3 processing. An example is shown in Fig. 5.17.

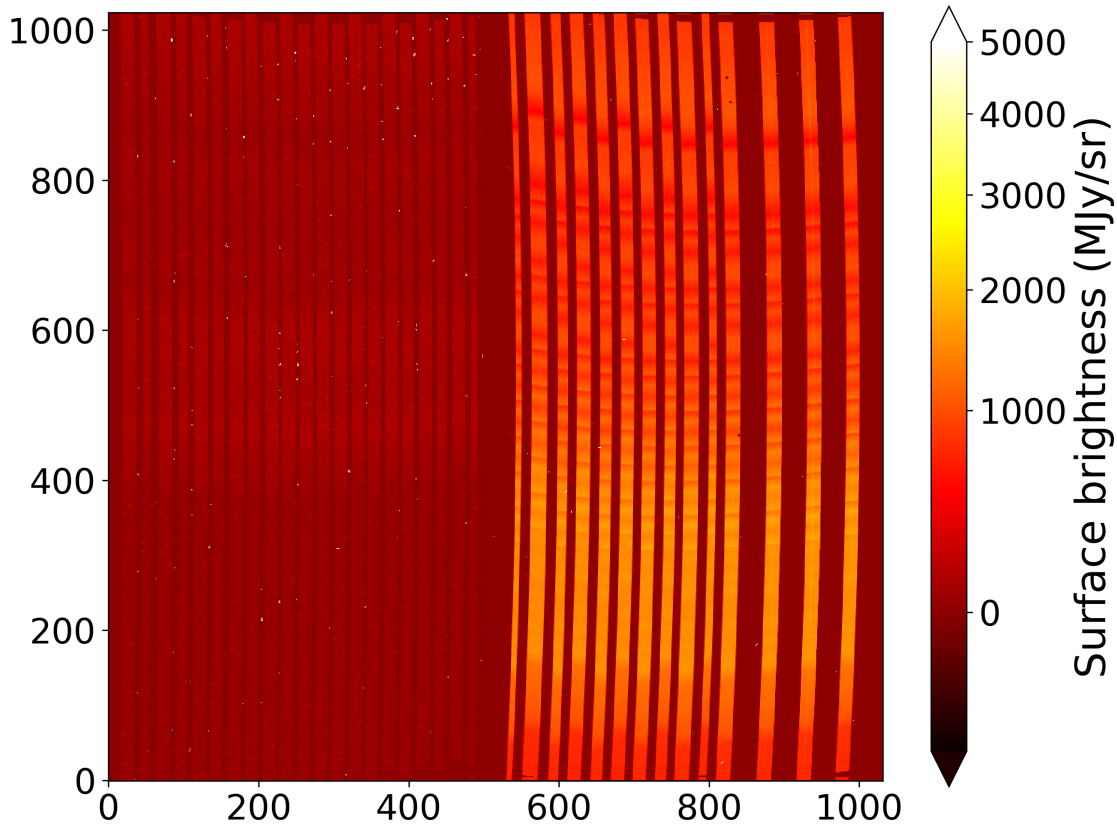


Figure 5.17 – Calibrated data retrieved from the detector image in Fig. 5.9. The pixel values are in MJy/sr.

— Cube Building:

The `cube_build` step rectifies and rearranges the calibrated 2D slice exposures above into 3D cubes with two spatial and one spectral axis. The WCS information from all input data is combined to completely cover their rectified sky footprints. The sampling scale in all three dimensions is retrieved from a CUBEPARS reference file. From the input WCSs and the spacecraft telemetry, pixels from individual exposures are rectified and registered into the common output WCS, resulting in a cloud of irregular sampling points. These points are transformed into a regular data cube using MSM. In particular, the flux of each spaxel is calculated as:

$$K = \frac{\sum_{i=1}^n Flux_i w_i}{\sum_{i=1}^n w_i} \quad (5.15)$$

where $Flux_i$ are the fluxes from the cloud points at distances of $(xdistance, ydistance, zdistance)$ along the x, y and wavelength axes, within radii of interest $rois$ and $roiw$ in the spatial and spectral dimensions respectively. These distances are normalized by the corresponding cube sample sizes $(cdelt1, cdelt2, cdelt3)$ to determine the weights w_i as below:

$$xnormalize = xdistance/cdelt1 \quad (5.16)$$

$$ynormalize = ydistance/cdelt2 \quad (5.17)$$

$$znormalize = zdistance/cdelt3 \quad (5.18)$$

$$w_i = \frac{1.0}{\sqrt{(xnormalized_i^2 + ynormalized_i^2 + znormalized_i^2)^p}} \quad (5.19)$$

By default, the sample sizes $cdelt1$, $cdelt2$, $cdelt3$, the radii of interest $rois$, $roiw$ and the exponent p for MSM-based MIRI cube building of individual MIRI bands are defined by the CUBEPARS reference file as in Table 5.1 below.

Table 5.1 – Parameters for MSM-based cube building of individual MIRI bands

Channel	Sub-channel	λ_{min} (μm)	λ_{max} (μm)	$cdelt1 = cdelt2$ (arcsec)	$cdelt3$ (μm)	$rois$ (arcsec)	$roiw$ (μm)	p
1	SHORT	4.89	5.74	0.13	0.001	0.1	0.001	2
	MEDIUM	5.64	6.62	0.13	0.001	0.1	0.001	2
	LONG	6.42	7.51	0.13	0.001	0.1	0.001	2
2	SHORT	7.49	8.75	0.17	0.002	0.15	0.002	2
	MEDIUM	8.72	10.22	0.17	0.002	0.15	0.002	2
	LONG	10.03	11.74	0.17	0.002	0.15	0.002	2
3	SHORT	11.53	13.48	0.2	0.003	0.2	0.003	2
	MEDIUM	13.37	15.64	0.2	0.003	0.2	0.003	2
	LONG	15.44	18.07	0.2	0.003	0.2	0.003	2
4	SHORT	17.66	20.93	0.35	0.006	0.4	0.006	2
	MEDIUM	20.42	24.21	0.35	0.006	0.4	0.006	2
	LONG	23.89	28.33	0.35	0.006	0.4	0.006	2

At this stage, the output cube `_s3d` contains both channels with the same grating that are projected onto the same detector. The output spatial scale is the minimum between the channels, while a varying spectral scale from the CUBEPARS reference file is applied. This cube serves the quick-look purpose only.

— Extract 1D Spectra:

The `extract_1d` step uses aperture photometry to acquire a 1D spectrum from a 2D or 3D JWST spectroscopic data. For the output cube `_s3d` above, since we did not

specified the spatial extension of the target in MIRISim, by default it was considered to be extended. The entire image was extracted using rectangular aperture photometry without background subtraction. Aperture correction was applied based on a reference file from CRDS. Extracted spectra are stored in `_x1d` file, as plotted in Fig. 5.18.

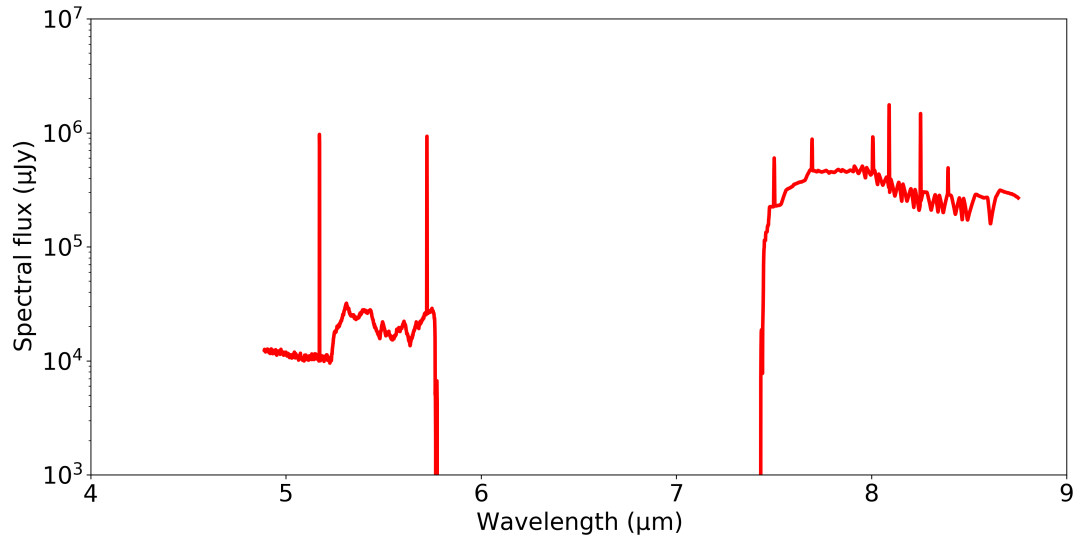


Figure 5.18 – Spectrum extracted from the detector image in Fig. 5.9 containing two disjointed segments for channels 1SHORT (4.88 μm – 5.75 μm) and 2SHORT (7.48 μm – 8.76 μm).

5.2.5 Stage 3: Multiple exposure combination for spectroscopy

This stage combines multiple calibrated exposures into a single 2D or 3D spectral output and a combined 1D spectrum. However, since dithering was not performed in MIRISim, we ran this stage for demonstration purposes only using the `calwebb_spec3` configuration for non-TSO spectroscopic modes. The following steps were performed in order:

- MIRI MRS sky matching:

The `mrs_imatch` step reconciles pixel values in the input 2D MIRI MRS images. Since we only had one exposure, it was run nominally only. First it sigma-clips any sources in the matching region, then calculates the background corrections for each image that minimize the least-square mismatch of their intensities. In particular, the background polynomial $P_n(k)$ for the pixel $k = (k_1, k_2, \dots)$ in the image n is defined as:

$$P_n(k_1, k_2, \dots) = \sum_{d_1=0, d_2=0, \dots}^{D_1, D_2, \dots} c_{d_1, d_2, \dots}^n \cdot k_1^{d_1} \cdot k_2^{d_2} \cdot \dots \quad (5.20)$$

where $d = (d_1, d_2, \dots)$ are the polynomial degrees, by default set to 1. The coefficients $c_{d_1, d_2, \dots}^n$ would be solved to minimize the following quantity:

$$L = \sum_{n,m=1,n \neq m}^N \sum_k \frac{[I_n(k) - I_m(k) - P_n(k) + P_m(k)]^2}{\sigma_n^2(k) + \sigma_m^2(k)} \quad (5.21)$$

where $I_n(k)$ and $I_m(k)$ are the intensities of pixel k in the images n and m respectively, $\sigma_n^2(k)$ and $\sigma_m^2(k)$ are the corresponding errors.

— Cube building:

This step is similar to the one performed in stage 2, but separate `_s3d` cubes are built for each band instead.

— Extract 1D spectra:

This step is similar to the one performed in stage 2, but there are separate `_x1d` spectra for each band instead.

5.3 Post-pipeline data analysis

5.3.1 MIRI imaging simulations

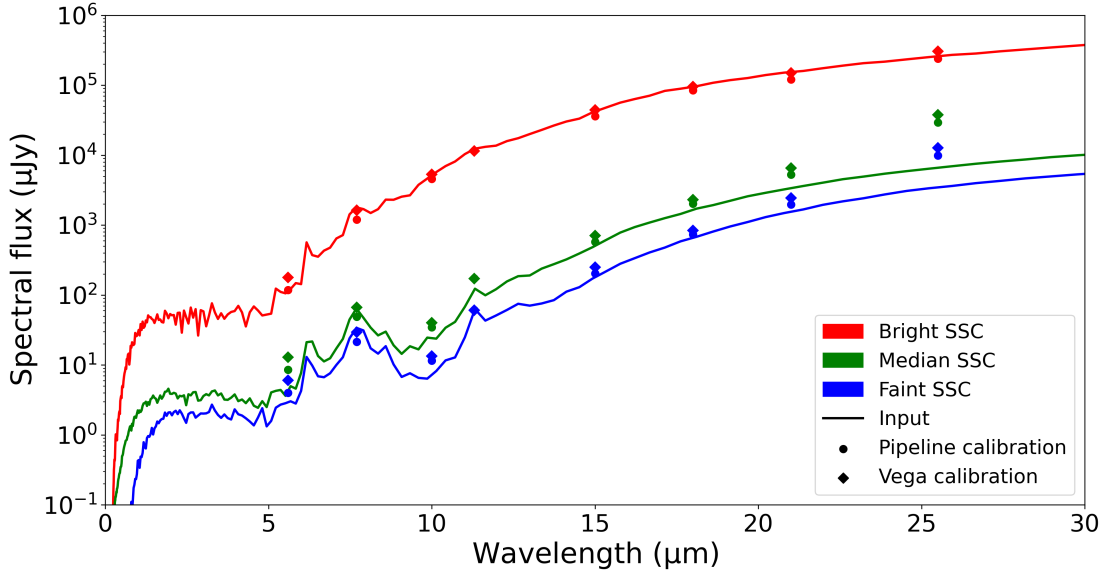


Figure 5.19 – Recovered photometric measurements using pipeline (dots) and Vega (diamonds) calibrations compared to the input spectra (lines) of the bright (red), median (green) and faint (blue) SSCs described in Chapter 3.

After three calibration stages, we obtained eight resampled `_i2d` images corresponding to the filters F560W (Fig. 5.16), F770W, F1000W, F1130W, F1500W, F1800W, F2100W, F2550W. Similar to Lam et al. (2020), we extracted the SSCs in these images using STARFINDER. We

selected the normalized Vega star as the empirical PSF template then applied circular masking, principal component extraction, halo smoothing and normalization. By fine-tuning the signal and correlation thresholds, we were able to recover the SSCs as well as the normalized Vega star. Although the `photom` step provide conversions from count rates to surface brightness values (MJy/sr), for comparison we recalibrated the extracted fluxes from STARFINDER against the normalized Vega star. Results are plotted in Fig. 5.19 and Fig. 5.20.

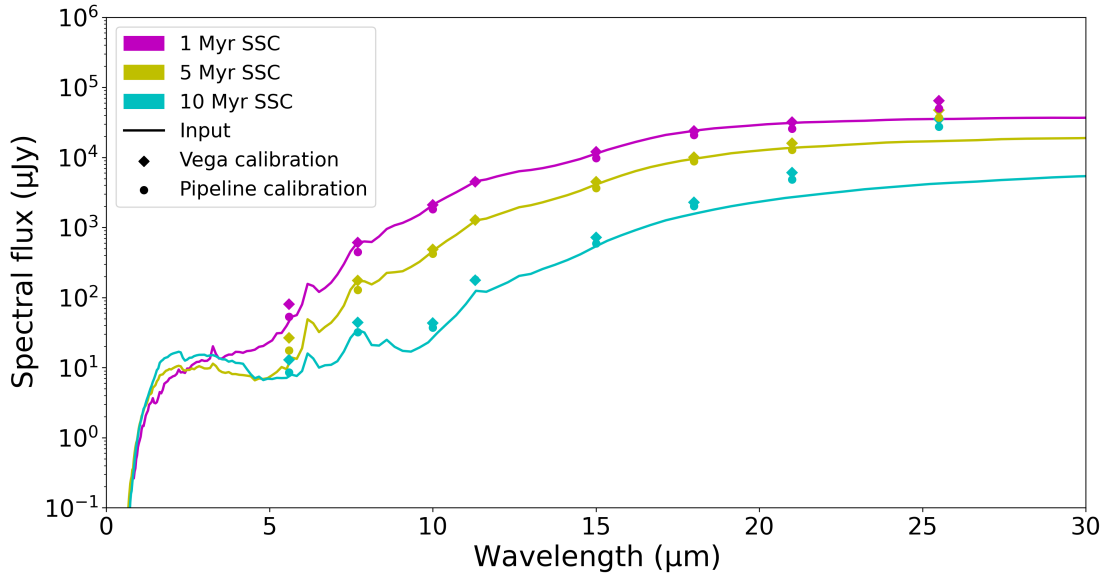


Figure 5.20 – Recovered photometric measurements using pipeline (dots) and Vega (diamonds) calibrations compared to the input spectra (lines) of the SSCs with the same inner radius for the dust envelope $R_{\text{in}} = 5\text{pc}$ and ages $\tau = 1$ (magenta), 5 (yellow), 10 Myr (cyan) described in Lam et al. (2020).

In both figures, except for the filter F2550W, photometric measurements using pipeline calibration show better performance and agree well with the input spectra. Although the error bars are plotted, they are barely visible in the logarithmic scale. Given the results for the SSC sample in Fig. 5.19, it is possible to detect the SSCs found in Lam et al. (2020). Fig. 5.20 shows that the eight chosen filters in the mid-IR are the better choice for age-dating the SSCs sharing the same other parameters compared to the near-IR range. Notably, Lin et al. (2020) find a tight anticorrelation between the mass-normalized dust-only $8\ \mu\text{m}$ luminosity and the age of young stellar clusters from the Legacy Extragalactic UV survey (LEGUS; Calzetti et al. 2015). We also see a similar trend in our SSC sample despite of its small number (Fig. 5.21).

On the other hand, in Fig. 5.22 we replot the SSC models in Fig. 3.8 but overlay the mid-IR photometric measurements instead. Each model grid has the same age and mass but varied dust geometry. In this case, given the close mid-IR flux values of these models, we should use the near-IR filters in Chapter 3 to select the best-fit ones. Thus by combining observations in both near and mid-IR, we could better constrain the parameters of the SSCs in IRAS 17138-1017. These filters are also useful for the calibration of the IFU spectra in the next section. Furthermore, it is also possible to constrain the SFR (Senarath et al. 2018) or discriminate SSCs from other objects (Jones et al. 2017) using JWST mid-IR filters.

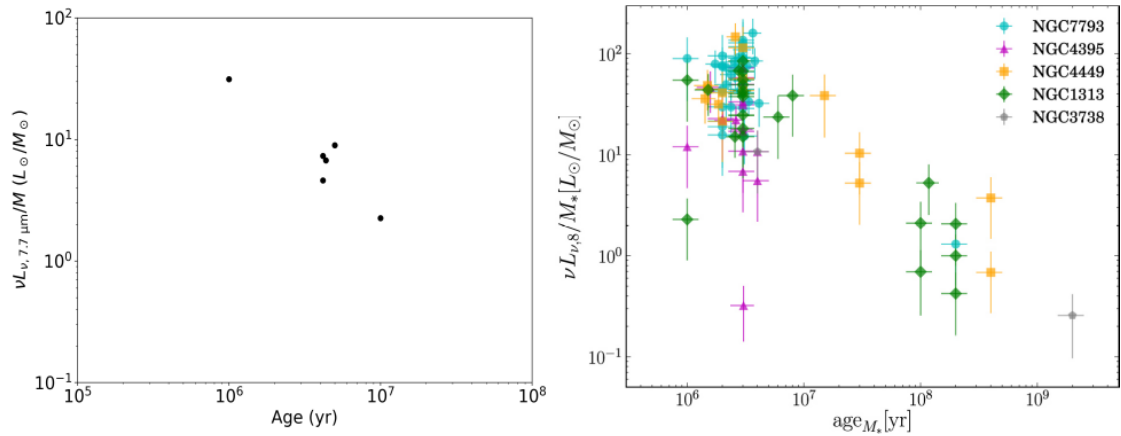


Figure 5.21 – Relation between the mass-normalized 8 μm luminosity and the cluster age in our sample (*left*) compared to Lin et al. (2020) (*right*).

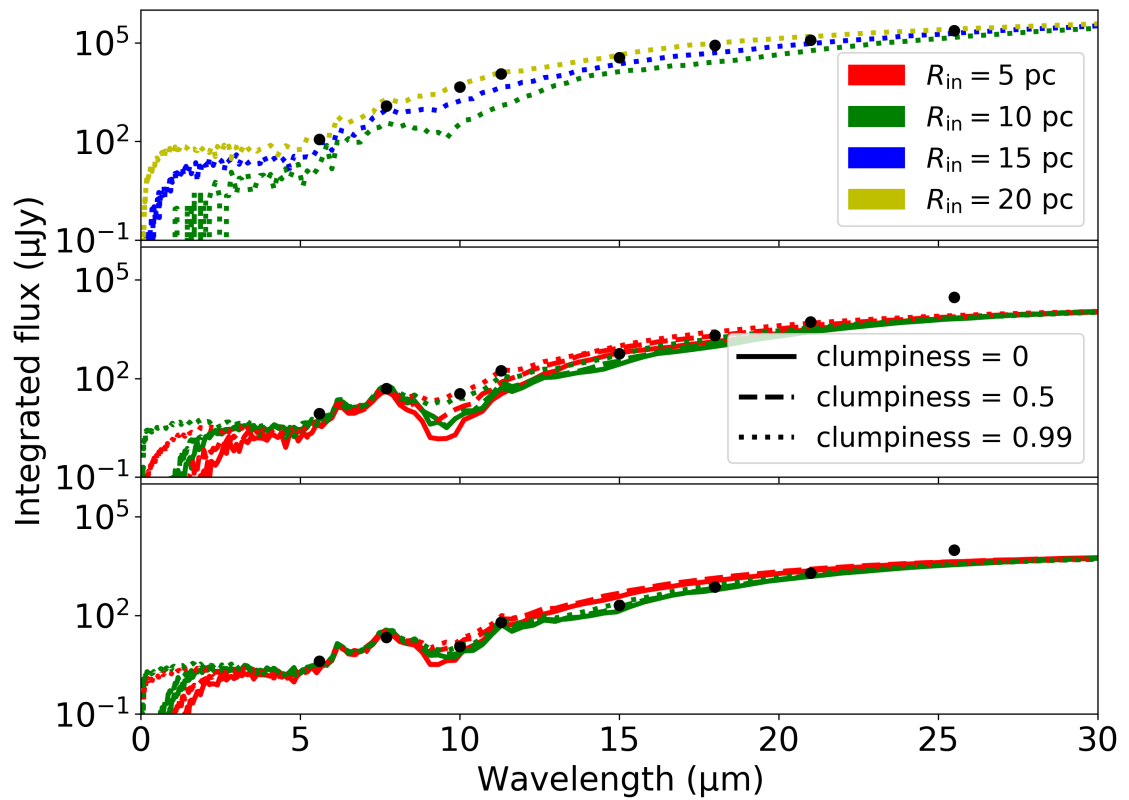


Figure 5.22 – Spectral energy distributions of the bright (top), median (middle) and faint (bottom) SSC models generated by MontAGN using 1 000 000 photon packets. The observed fluxes in the mid-IR filters are marked as black circles.

5.3.2 MIRI MRS simulations

After three calibration stages, for each SSC scene we obtain 12 `_s3d` cubes corresponding to 12 subchannels. As noted by the MIRISim team, MIRISim may enlarge the PSF core by $\sim 25\%$ in RA, $\sim 35\%$ in Dec than expected⁹. In addition, the local galaxy backgrounds in our simulations are also extended significantly for simplicity. Consequently, for the demonstrative purposes, we used aperture extraction to recover SSC spectra from MIRISim simulations. In practice, advance extraction methods are required to account for the varying PSF and galaxy background.

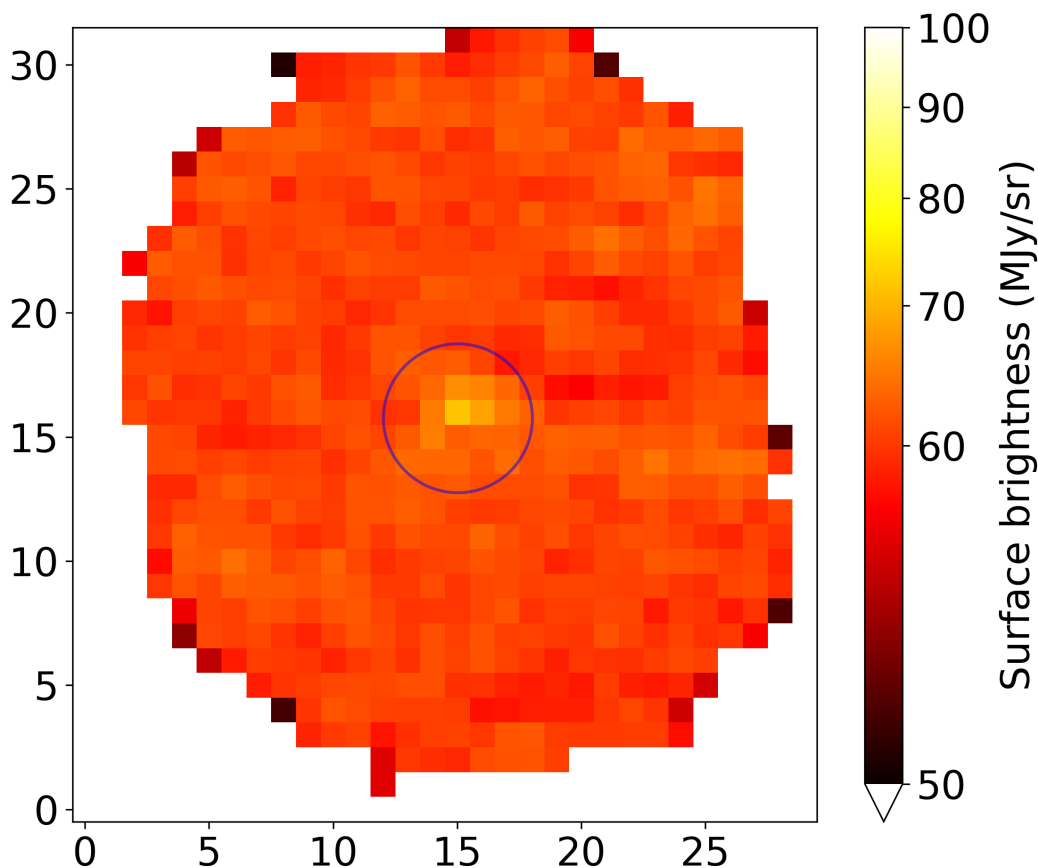


Figure 5.23 – Detected SSC and the extraction aperture in the 1SHORT median continuum image, which is retrieved from the detector image in Fig. 5.9.

First, we identified SSCs in the scenes. Again in principle, we should use the same source detection method as in Lam et al. (2020) and Sect. 5.3.1. However, given the PSF defects as well as the simplicity of the scene, we used the DAOFIND algorithm (Stetson 1987) implemented by `photutils`¹⁰ to identify SSCs on the median continuum images, then selected the sources closest

9. https://wiki.miricle.org/Public/MIRISimPublicRelease2dot3#MRS_PSF_is_oversized

10. <https://photutils.readthedocs.io/en/stable/index.html>

to the center instead. Since the MRS is undersampled by nearly a factor of two at the shortest wavelengths in each channel (STScI 2016–, see Fig. 4.7), we used a circular aperture with a radius of 3 pixels for spectrum extraction and an annulus with radii within 4 to 5 pixels for background subtraction. For example, Fig. 5.23 and Fig. 5.24 show the extraction aperture around a detected SSC and the extracted spectra respectively. The entire spectra as extracted from the pipeline products for the 1 Myr, 5 Myr and 10 Myr SSCs are plotted in Fig. 5.25. Another known issue with MIRISim is that output fluxes in the MRS channel 4 exhibit abnormal signal drops and excess noise¹¹.

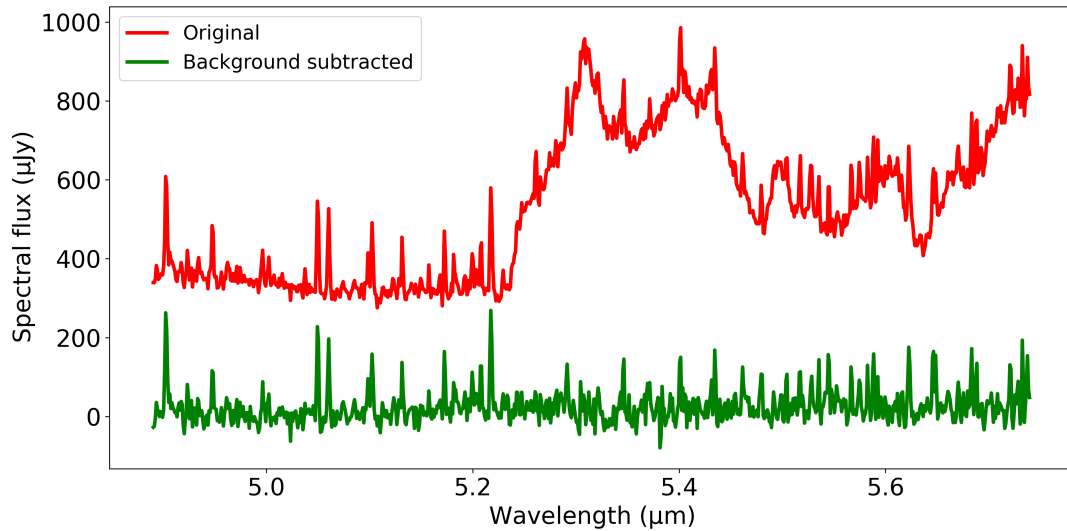


Figure 5.24 – Original (red) and background-subtracted (green) spectra extracted from the SSC in Fig. 5.23.

For each SSC, first we applied a 25-pixel boxcar smoothing to channel 1 and 5-pixel boxcar smoothings to the other channels. Then we applied additional 15-pixel median smoothings to all channels and rescaled the spectra to match the photometric measurements in Sect. 5.3.1. Results are plotted in Fig. 5.26, which well match the input spectra.

We used `specutils`¹², a dedicated JWST post-pipeline data analysis tool under development, to analyze the spectra. First of all, we removed the foreground Galactic extinction in Sect. 5.1.2. For each SSC, we fitted local continua under these features with Chebyshev polynomials after additional 3-pixel median smoothing (see Fig. 5.27 for example). Then we normalized the features by their local continua and subtracted the continua from the corresponding features. Finally, we fitted Gaussian models to the features and derived their strengths (see Fig. 5.28 for example). In addition to the mid-IR filters, PAH emission features are also good tracers of the SFR (Shingley et al. 2016). Moreover, the relation between the 11.3/7.7 μm and the 6.2/7.7 μm PAH ratios (Fig. 5.29) can be used to constrain dust parameters (e.g., Draine & Li 2001).

11. https://wiki.miricle.org/Public/MIRISimPublicRelease2dot3#Output_fluxes_in_MRS_channel_4_are_not_consistent_with_the_JWST_ETC

12. <https://specutils.readthedocs.io/en/stable/index.html>

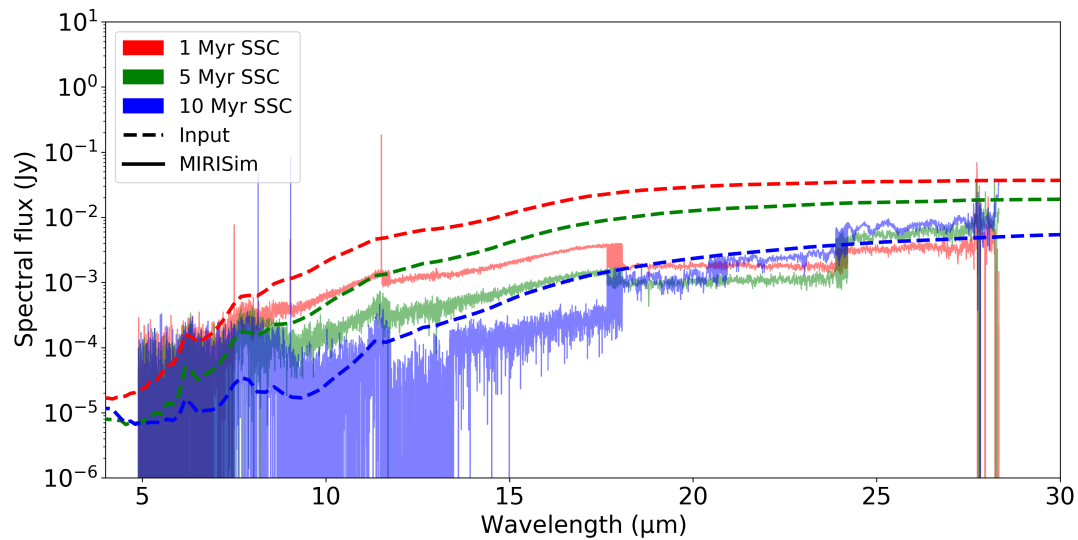


Figure 5.25 – Extracted (solid lines) compared to the input spectra (dashed lines) of the SSCs with the same inner radius for the dust envelope $R_{\text{in}} = 5$ pc and ages $\tau = 1$ (magenta), 5 (yellow), 10 Myr (cyan) described in Lam et al. (2020).

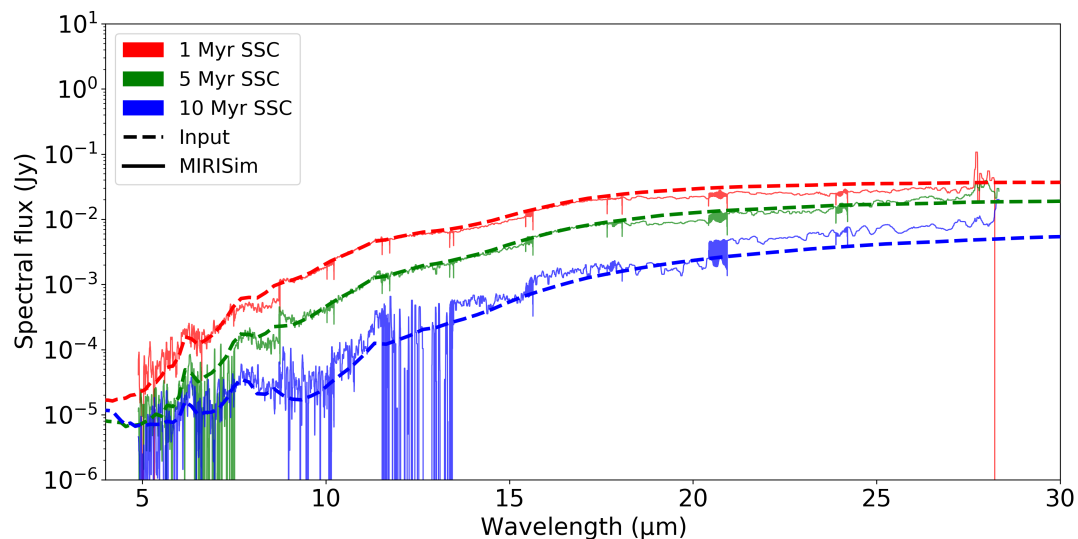


Figure 5.26 – Smoothed and joined (solid lines) compared to the input spectra (dashed lines) of the SSCs with the same inner radius for the dust envelope $R_{\text{in}} = 5$ pc and ages $\tau = 1$ (red), 5 (green), 10 Myr (blue) described in Lam et al. (2020).

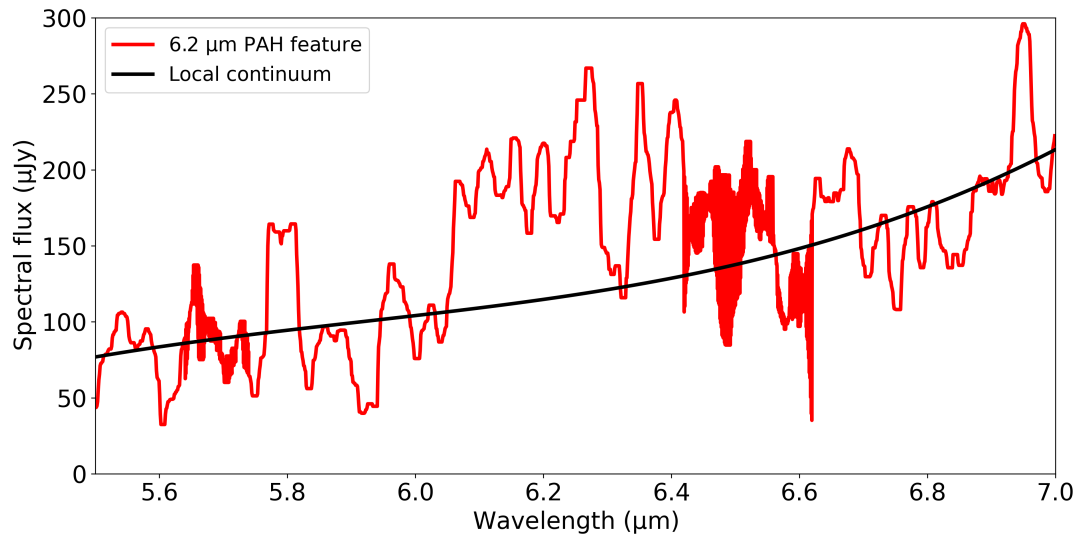


Figure 5.27 – 6.2 μm feature (red) of the 1 Myr SSC and its fitted local continuum (black).

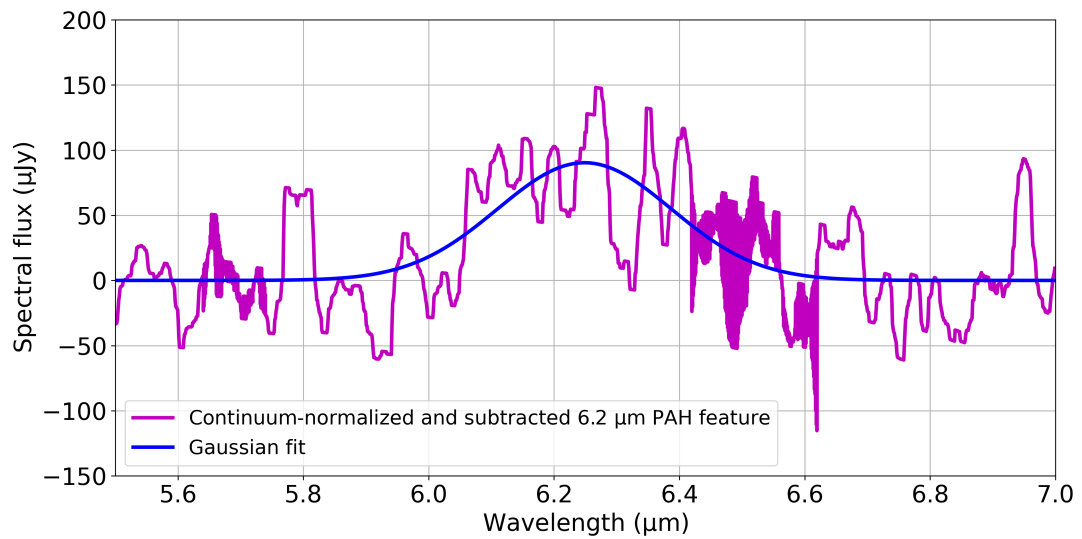


Figure 5.28 – Continuum-normalized and subtracted 6.2 μm feature (magenta) of the 1 Myr SSC and its Gaussian fit (blue).

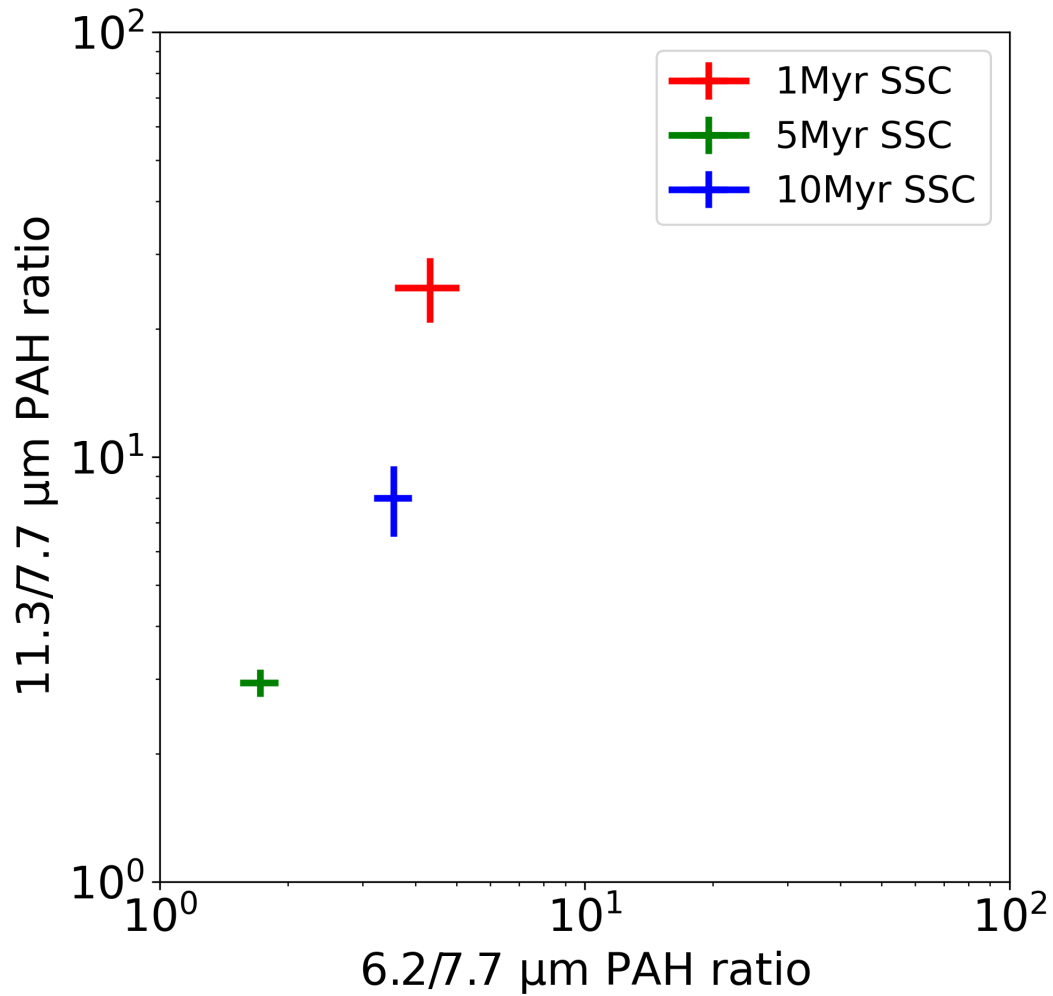


Figure 5.29 – Relation between the 11.3/7.7 μm and the 6.2/7.7 μm PAH ratios of the SSCs with the same inner radius for the dust envelope $R_{\text{in}} = 5$ pc and ages $\tau = 1$ (red), 5 (green), 10 Myr (blue) described in Lam et al. (2020).

In summary, despite of several limitations, our MontAGN and MIRISim simulations show the feasibility and advantages of characterizing the SSCs in IRAS 17138-1017 with MIRI/JWST. In particular, with the tools we have developed, the population at very young ages (≤ 10 Myr) with m_{K_s} between 16 mag and 21 mag as already observed in Lam et al. (2020) can be extracted and analyzed in details in the mid-IR, promising new insights on the formation and evolution of SSCs.

Chapter 6

Conclusions and prospectives

The main product of star formation is star clusters, in fact at least 80% of stars are produced in some forms of clustered or associated groups (e.g., Meurer et al. 1995; Lada & Lada 2003). Star formation requires large reservoirs of gas that are accompanied by large quantities of dust (1% in mass), such that the earliest phases are completely obscured at UV, optical, and even near-IR wavelengths. Nonetheless the investigation of the very young phase of star formation is crucial. Notably, embedded stellar clusters are evolving through this important stage and deserve thorough attention, given that stars have already formed inside the molecular cloud without radically altering it. To quantify their properties and address open issues, it is necessary to study them at IR wavelengths and at the best angular resolution.

This work has illustrated some of the possibilities offered by ground-based near-IR adaptive optics (AO) imaging, as well as expected from mid-IR spectro-imaging and broadband imaging with MIRI/JWST. Remarkably, SSC populations may be resolved into individual components and separated from the surrounding environment. Thanks to advancements in terms of instrumental resolution and sensitivity, an overall model of star cluster formation and evolution is gradually emerging, in which SSCs are fundamental building blocks. However, several puzzles remain to be addressed by future studies, especially with JWST. This chapter summarizes the scientific results produced throughout my PhD, outlines unresolved issues and paves way for promising results to be obtained in the era of JWST.

6.1 Observations and analyses in near-IR with adaptive optics

Beside the global properties of galaxies, only a small number of studies focus on their SSC populations due to large distances and limited angular resolutions. For example, among a total of 202 galaxies in the GOALS survey, high resolution ($\sim 0.1''$) and large field of view ($3.4' \times 3.4'$) HST *BI*-band images are only available for a complete sample of 87 galaxies, which allows Vavilkin (2011) to study their optically-visible SSC populations in his thesis. Nevertheless with only two bands his results suffered from several degeneracies so they were not published on a peer-reviewed journal. Later in Linden et al. (2017), far-UV (F140LP) data with an FOV of $30'' \times 30''$ are included, providing more robust estimations of cluster parameters, but only for 22 systems containing more than 100 *B*-band SSCs within the central $30'' \times 30''$ region.

This research has made use of GSAOI/GeMS, a ground-based AO system in the near-IR on the Gemini South telescope. Even compared to HST, GSAOI provides imaging data at superior

angular resolution and sensitivity, which help separating individual SSCs with minimal confusion. One major challenge for extragalactic SSC studies is to extract clusters themselves on a highly varying background and in a crowded field. Among many source extraction algorithms (see Masias et al. 2012), we find that STARFINDER shows the best performance. It is dedicated to AO images of crowded fields with an user-friendly interface, combining both visual inspection and automated extraction. STARFINDER has also worked on MIRISim data and could be used in parallel with JWST-dedicated tools. However, it is important to distinguish SSCs from other objects such as foreground stars and background galaxies. Comparison to control fields has proved to be efficient, while models counting stars and galaxies are to be used with caution. Nevertheless, we have constructed a cluster catalog with high confidence for IRAS 17138-1017, which contains 54 SSCs with m_{K_s} between 16 mag and 21 mag with a median instrumental uncertainty of 0.05 mag.

Based on a Starburst99 stellar evolutionary model and cluster colors, we have developed a fitting method to derive cluster ages, masses and extinctions. However, there are several outliers exhibiting red excess and they could not be explained by the evolutionary models. We find two recent starbursts at 2.8 and 4.5 Myr containing highly extinct SSCs. Their luminosities and masses are power-law distributed but exhibit shallower slopes than the canonical values in LIRGs. Nonetheless, analyses of cluster demographics require accurate measurements of those quantities, which may be improved with additional filters and better evolutionary models.

Eventually, it appears that IRAS 17138-1017 hosts two of the youngest starbursts ever observed as thus deserves special attention. This is the rationale of our follow-up program with MIRI/JWST described in Chapter 4 and Chapter 5. Moreover, ALMA studies would certainly bring additional important insights on the dense molecular gas at earlier stages of star formation prior to the embedded phase, when the parent molecular cloud is forming cores and protostars.

Furthermore, it is possible to apply the analysis process above to archival images of other galaxies, especially AO and HST data, to maximize their scientific returns. For example, the Gemini archive also contains GSAOI $JHK_sBr\gamma$ images of II Zw 40, GSAOI JHK_s images of NGC 3110, as well as Flamings 2 JHK_s images of NGC 5331, which have not been fully exploited. Additionally, we can extend the Grosbøl & Dottori (2012) study of SSCs in spiral galaxies by deriving cluster ages and masses, given their observations in $YJHKBr\gamma$ bands with the HAWK-I instrument on the Very Large Telescope (VLT).

6.2 Simulations

We have successfully developed an extension to MontAGN, a radiative transfer code initially dedicated to AGNs, in particular in the mid-IR. We have explored various cluster parameters and shown that the thermal dust emission and scattered radiation in the K_s band are insignificant and could not explain the red excess found in several SSCs. It is also possible to derive SSC properties by fitting model grids to observations. There are several limitations and further improvements to be implemented in the future:

- Some of the cluster parameters have been assumed (e.g., metallicity, star-forming efficiency (SFE)) or derived in advance (age, mass and extinction) using the color-fitting method. For consistency and comprehensiveness, we should include all of them in the parameter space of the MontAGN models. However additional filters or spectral data are required to derive those parameters independently and robustly. Greater accuracy may also be achieved with finer parameter grids, but at the cost of computation time. It is also necessary to evaluate the uncertainties associated with various filter combinations in

order to select the most relevant and useful ones for a given sets of estimated parameters (see e.g., [Anders et al. 2004](#)).

- MontAGN uses user-supplied input spectra, which depend on external stellar population synthesis models in our case. [de Grijs et al. \(2005\)](#) notice non-negligible discrepancies between SSP models, resulting in uncertainties up to 0.1 mag in optical-near-IR and 0.2 mag in UV filters, largely due to different input physics and treatments of evolutionary phases. Thus these models should be considered carefully for better MontAGN outputs.
- Since we do not have any observation data in the mid-IR, the modelling capability of MontAGN in this wavelength range have not been explored and validated, especially the PAH, silicate features and the thermal emission. It is particularly useful for predicting and interpreting MIRI/JWST observations of SSCs, as presented in Chapter 5. Future JWST observations of well-characterized sources could be used for calibration.
- Besides spectral and dust distribution information, MontAGN also allows users to investigate the temperature inside clusters, which have been demonstrated in [Lam et al. \(2019\)](#). Currently this information is not available, but we aim to gain access using mid-IR spectroscopic data from MIRI/JWST (see Chapter 5).
- Radiative transfer simulations require substantial computational resources and time. For example, to simulate the SSC with the inner radius for the dust envelope $R_{\text{in}} = 5$ pc and the ages $\tau = 1$ Myr in [Lam et al. \(2020\)](#), we used 10^7 photons, but divided into 40 jobs of 250 000 photons and launched them in parallel on the tycho cluster of the Paris Observatory. It took over two days to finish a job of 250 000 photons on a node with 24 cores of 2.20 GHz Intel Xeon E5-2650 v4. As a consequence, we could only test a limited number of models. Therefore it would be beneficial to adapt MontAGN to high-performance and parallel computing architectures, for example using Graphical Processor Units (GPUs) or Grand Équipement National de Calcul Intensif (GENCI, Big National Equipment Intensive Computing) infrastructures.

Subsequently, the spectra of best-fit MontAGN models have been used as inputs to MIRISim simulations. Despite of various known issues with MIRISim, we have been able to simulate some simple SSC scenes with the actual parameters from our JWST proposal. Thus MontAGN has proved to be a valuable program for preparing future proposals beside available tools from the JWST community.

6.3 Era of James Webb Space Telescope

6.3.1 Preparing the MIRI/JWST proposal

During the development of this thesis, the launch date of JWST has undergone many delays, followed by its GO program. Nevertheless, we have completed our GO proposal for "Studying the very young embedded super star cluster population of IRAS 17138-1017 with MIRI" and submitted it to the STScI. We have familiarized ourselves with the MIRI instrument, adopting the best configurations and strategies for our proposed observations based on the JWST Documentation ([STScI 2016-](#)).

To validate our proposal, we have used various proposal planning tools developed by the JWST community, including the ETC and MIRISim. ETC calculations show that we can observe

the faintest SSC in IRAS 17138-1017 with fair SNRs while avoiding saturation on the brightest SSC. Moreover, while the JWST calibration pipeline is still being developed and not yet publicly supported, we have successfully used it to reduce the output data from MIRISim and performed some preliminary analyses, confirming the feasibility of our proposal.

For post-pipeline analysis of JWST data, the STScI proposes various Python packages included within `AstroConda`¹. Although they are still under development and at various maturity levels, we have used several of them throughout this thesis as listed in Table 6.1. Additionally, STARFINDER is also a versatile software for source extraction and photometry as demonstrated above.

Table 6.1 – JWST post-pipeline data analysis tools already used frequently in this work

Package	Usage
astropy	A common core Python package for astronomy
photutils	Tools for source extraction and photometry
specutils	Tools for astronomical spectroscopic analysis
synphot	Toolkits for synthetic photometry from simulated observations and input spectra

Finally, to maximize the science potential and help the community familiarize with JWST, the STScI created the ERS program with no exclusive access period. Retrieved datasets will be released immediately to the community for demonstration and representation purposes. Among those programs, we are particularly interested in the ERS program 1328 which studies the starburst-AGN connection in a sample of merging LIRGs (Armus et al. 2017). It will provide MIRI MRS and imaging data as well as introduce some early results from which we can learn and practice before applying to our own dataset.

6.3.2 Perspective for SSC studies

Certainly, Chapter 5 only provide a glimpse at potential SSC studies using MIRI/JWST, starting from photometry and spectra at fairly good SNRs for a large set of SSCs. The opened perspectives cover a broad range of subjects, each requiring some preparatory work through simulations, analyses of theoretical work and physical modelling as well as comparisons with results already obtained in the Milky Way and nearby galaxies, or in more distant galaxies but at lower resolution with Spitzer and Herschel.

As an example, nebular lines (i.e. [NeIII] 15.5 μm , [NeII] 12.8 μm , [SIV] 10.5 μm , [SIII] 18.7 μm , [NeV] 14.3 μm , [SIV] 10.5 μm , and [OIV] 25.9 μm) provide important diagnostics on the hardness of the ionizing radiation field and the effective temperature of the ionizing stars. Then those results will be compared with population synthesis models such as Starburst99 to derive cluster ages, temperatures, densities, and extinctions.

Here is a non-exhaustive list of open questions requiring such preparatory work to constrain the physical processes under study. Specifically the most relevant diagnostics and quantities derived from observations need to be identified, together with their behaviors with respect to some parameters.

1. <https://astroconda.readthedocs.io/>

- Compactness of clusters: What are the scales of star formation, particularly the sizes of the produced clusters? Which factors (SFR, gas density, galaxy type, environment, interaction, location in the galaxy, AGN, metallicity, etc.) determine them? Since the resolving power will not be enough to resolve each SSC, it is through the comparison of the dust mass (thermal emission) and of the warm molecular gas mass (H_2 rotational lines) with models of embedded cluster formation and evolution as well as radiative transfer codes such as MontAGN, that some clues should be obtained.
- Embedded timescale: How long does it take for a cluster to escape from its natal cloud, and how does this timescale depend on the properties of the cluster itself (luminosity, supernova rate, winds, etc.) and the environment (metallicity, gas and dust concentrations, dynamical conditions, etc.)? Estimating the dust mass still associated to the cluster will be the key to evaluate the mass of gas, and thus the degree of embedding. The quantity of warm molecular gas measured through H_2 rotational lines will also be important. In both cases, confrontation to physical models will be necessary.
- Propagation of starburst: How successive generations of stars may be chained through some triggering mechanism? What are the temporal and spatial scales of such propagation? Accurate estimation of cluster ages from near-IR color-color diagrams, as proposed in [Lam et al. \(2020\)](#), with extinction-free diagnostics provided by nebular lines will be crucial for this study.
- Cluster disruption: Which parameters among those previously mentioned determine the *infant mortality* of stellar clusters? [Lada & Lada \(2003\)](#); [Portegies Zwart et al. \(2010\)](#) show that 90% of clusters are destroyed within 10 Myr of their early life, but the detailed physics behind this phenomenon remains to be established. Even if clusters survive the gas expulsion process, they may still dissolve later due to tidal perturbation, stellar or dynamical evolution. How is the dissolution timescale determined? Does it depend on the cluster mass and the environment? The answer may come from complete surveys of SSCs in different environments, which may vary across galaxies and even within each galaxy. Cluster ages, masses and densities must be determined with high precision for validation or rejection of various proposed models.

Last but not least, complementary studies at other wavelengths will also appreciably enrich the picture. For instance, ALMA will probe star formation at an even earlier stage than embedded cluster, when the gas in the parent molecular cloud is forming cores and protostars. Near-IR imaging will also be the key access to the stars themselves. Thus studying SSCs in the era of JWST will not be accomplished without concurrent facilities.

Bibliography

- Adamo, A. & Bastian, N. 2018, *The Lifecycle of Clusters in Galaxies*, ed. S. Stahler, Vol. 424, 91
- Adamo, A., Östlin, G., Zackrisson, E., & Hayes, M. 2011a, *MNRAS*, 414, 1793
- Adamo, A., Östlin, G., Zackrisson, E., et al. 2010, *MNRAS*, 407, 870
- Adamo, A., Östlin, G., Zackrisson, E., et al. 2011b, *MNRAS*, 415, 2388
- Adamo, A., Ryon, J. E., Messa, M., et al. 2017, *ApJ*, 841, 131
- Adamo, A., Zeidler, P., Kruijssen, J. M. D., et al. 2020, *Space Sci. Rev.*, 216, 69
- Alonso-Herrero, A., Pereira-Santaella, M., Rieke, G. H., et al. 2013, *ApJ*, 765, 78
- Alonso-Herrero, A., Pereira-Santaella, M., Rieke, G. H., & Rigopoulou, D. 2012, *ApJ*, 744, 2
- Alonso-Herrero, A., Rieke, G. H., Rieke, M. J., et al. 2006, *ApJ*, 650, 835
- Anders, P., Bissantz, N., Fritze-v. Alvensleben, U., & de Grijs, R. 2004, *MNRAS*, 347, 196
- Andersen, M., Zinnecker, H., Moneti, A., et al. 2009, *ApJ*, 707, 1347
- Anderson, R. E. & Gordon, K. D. 2011, *PASP*, 123, 1237
- Arendt, R. G., Fixsen, D. J., & Moseley, S. H. 2000, *ApJ*, 536, 500
- Armus, L., Evans, A. S., Appleton, P. N., et al. 2017, *A JWST Study of the Starburst-AGN Connection in Merging LIRGs*, JWST Proposal ID 1328. Cycle 0 Early Release Science
- Armus, L., Mazzarella, J. M., Evans, A. S., et al. 2009, *PASP*, 121, 559
- Ascenso, J. 2018, *Embedded Clusters*, ed. S. Stahler, Vol. 424, 1
- Banerjee, S. & Kroupa, P. 2012, *A&A*, 547, A23
- Banerjee, S. & Kroupa, P. 2018, *Formation of Very Young Massive Clusters and Implications for Globular Clusters*, ed. S. Stahler, Vol. 424, 143
- Banerjee, S., Kroupa, P., & Oh, S. 2012, *MNRAS*, 426, 1416
- Bastian, N. 2008, *MNRAS*, 390, 759
- Bastian, N., Adamo, A., Gieles, M., et al. 2012, *MNRAS*, 419, 2606
- Bastian, N. & Lardo, C. 2018, *ARA&A*, 56, 83

- Baumgardt, H. 1998, *A&A*, 330, 480
- Baumgardt, H., Kroupa, P., & Parmentier, G. 2008, *MNRAS*, 384, 1231
- Beard, S., Morin, J., Gastaud, R., et al. 2012, in *Astronomical Society of the Pacific Conference Series*, Vol. 461, *Astronomical Data Analysis Software and Systems XXI*, ed. P. Ballester, D. Egret, & N. P. F. Lorente, 169
- B ethermin, M., Dole, H., Lagache, G., Le Borgne, D., & Penin, A. 2011, *A&A*, 529, A4
- Bigiel, F., Leroy, A., Walter, F., et al. 2008, *AJ*, 136, 2846
- Bjorkman, J. E. & Wood, K. 2001, *ApJ*, 554, 615
- Bouchet, P., Garc a-Mar n, M., Lagage, P. O., et al. 2015, *PASP*, 127, 612
- Boutloukos, S. G. & Lamers, H. J. G. L. M. 2003, *MNRAS*, 338, 717
- Brodie, J. P. & Strader, J. 2006, *ARA&A*, 44, 193
- Brown, M. J. I., Moustakas, J., Kennicutt, R. C., et al. 2017, *ApJ*, 847, 136
- Bushouse, H., Droettboom, M., & Greenfield, P. 2017, in *Astronomical Society of the Pacific Conference Series*, Vol. 512, *Astronomical Data Analysis Software and Systems XXV*, ed. N. P. F. Lorente, K. Shorridge, & R. Wayth, 355
- Calzetti, D., Armus, L., Bohlin, R. C., et al. 2000, *ApJ*, 533, 682
- Calzetti, D., Lee, J. C., Sabbi, E., et al. 2015, *AJ*, 149, 51
- Caputi, K. I., Lagache, G., Yan, L., et al. 2007, *ApJ*, 660, 97
- Chandar, R., Fall, S. M., Whitmore, B. C., & Mulia, A. J. 2017, *ApJ*, 849, 128
- Crowther, P. A., Caballero-Nieves, S. M., Bostroem, K. A., et al. 2016, *MNRAS*, 458, 624
- Davies, R. I., Sternberg, A., Lehnert, M., & Tacconi-Garman, L. E. 2003, *ApJ*, 597, 907
- de Grijs, R., Anders, P., Lamers, H. J. G. L. M., et al. 2005, *MNRAS*, 359, 874
- Depoy, D. L., Wynn-Williams, C. G., Hill, G. J., & Becklin, E. E. 1988, *AJ*, 95, 398
- Draine, B. T. 1985, *ApJS*, 57, 587
- Draine, B. T. & Li, A. 2001, *ApJ*, 551, 807
- Draine, B. T. & Li, A. 2007, *ApJ*, 657, 810
- Eggleton, P. 2006, *Evolutionary Processes in Binary and Multiple Stars*
- Elbaz, D., Cesarsky, C. J., Chanical, P., et al. 2002, *A&A*, 384, 848
- Elmegreen, B. G. 1997, *ApJ*, 477, 196
- Elmegreen, B. G. 2006, *ApJ*, 648, 572
- Elmegreen, B. G. 2011, *ApJ*, 731, 61
- Elmegreen, B. G. 2018, *ApJ*, 869, 119

- Elmegreen, B. G. & Efremov, Y. N. 1996, *ApJ*, 466, 802
- Elmegreen, B. G. & Efremov, Y. N. 1997, *ApJ*, 480, 235
- Elmegreen, B. G. & Falgarone, E. 1996, *ApJ*, 471, 816
- Elmegreen, B. G. & Hunter, D. A. 2010, *ApJ*, 712, 604
- Fall, S. M. 2006, *ApJ*, 652, 1129
- Fall, S. M., Chandar, R., & Whitmore, B. C. 2005, *ApJ*, 631, L133
- Fall, S. M., Chandar, R., & Whitmore, B. C. 2009, *ApJ*, 704, 453
- Fall, S. M. & Zhang, Q. 2001, *ApJ*, 561, 751
- Fitzpatrick, E. L. 1999, *PASP*, 111, 63
- Fixsen, D. J., Offenberg, J. D., Hanisch, R. J., et al. 2000, *PASP*, 112, 1350
- Fleck, Robert C., J. 1996, *ApJ*, 458, 739
- Galliano, E., Alloin, D., Pantin, E., et al. 2008, *A&A*, 492, 3
- Galliano, E., Alloin, D., Pantin, E., Lagage, P. O., & Marco, O. 2005, *A&A*, 438, 803
- García-Marín, M., Colina, L., Arribas, S., & Monreal-Ibero, A. 2009, *A&A*, 505, 1319
- Geers, V. C., Klaassen, P. D., Beard, S., & European Consortium, M. 2019, in *Astronomical Society of the Pacific Conference Series*, Vol. 523, *Astronomical Data Analysis Software and Systems XXVII*, ed. P. J. Teuben, M. W. Pound, B. A. Thomas, & E. M. Warner, 641
- Gennaro, M., Brandner, W., Stolte, A., & Henning, T. 2011, *MNRAS*, 412, 2469
- Gieles, M. 2009, *MNRAS*, 394, 2113
- Gieles, M., Bastian, N., Lamers, H. J. G. L. M., & Mout, J. N. 2005, *A&A*, 441, 949
- Gieles, M., Larsen, S. S., Bastian, N., & Stein, I. T. 2006a, *A&A*, 450, 129
- Gieles, M., Portegies Zwart, S. F., Baumgardt, H., et al. 2006b, *MNRAS*, 371, 793
- Gordon, K. D., Engelbracht, C. W., Muzerolle, J., et al. 2004, in *Society of Photo-Optical Instrumentation Engineers (SPIE) Conference Series*, Vol. 5487, *Optical, Infrared, and Millimeter Space Telescopes*, ed. J. C. Mather, 177–185
- Górski, M., Zgirski, B., Pietrzyński, G., et al. 2020, *ApJ*, 889, 179
- Gratton, R., Bragaglia, A., Carretta, E., et al. 2019, *A&A Rev.*, 27, 8
- Grosbøl, P. & Dottori, H. 2008, *A&A*, 490, 87
- Grosbøl, P. & Dottori, H. 2012, *A&A*, 542, A39
- Grosset, L. 2019, PhD thesis, LESIA, Observatoire de Paris, PSL Research university
- Grosset, L., Marin, F., Gratadour, D., et al. 2016, in *SF2A-2016: Proceedings of the Annual meeting of the French Society of Astronomy and Astrophysics*, 57–60

- Grosset, L., Rouan, D., Gratadour, D., et al. 2018, *A&A*, 612, A69
- Haan, S., Surace, J. A., Armus, L., et al. 2011, *AJ*, 141, 100
- Haas, M. R., Gieles, M., Scheepmaker, R. A., Larsen, S. S., & Lamers, H. J. G. L. M. 2008, *A&A*, 487, 937
- Harris, W. E. 2001, *Globular Cluster Systems*, Vol. 28, 223
- Hénault-Brunet, V., Evans, C. J., Sana, H., et al. 2012, *A&A*, 546, A73
- Herrero-Illana, R., Pérez-Torres, M. Á., Randriamanakoto, Z., et al. 2017, *MNRAS*, 471, 1634
- Hopkins, P. F. 2013, *MNRAS*, 433, 170
- Hora, J. L., Carey, S., Surace, J., et al. 2008, *PASP*, 120, 1233
- Houck, J. R., Roellig, T. L., Van Cleve, J., et al. 2004, in *Society of Photo-Optical Instrumentation Engineers (SPIE) Conference Series*, Vol. 5487, *Optical, Infrared, and Millimeter Space Telescopes*, ed. J. C. Mather, 62–76
- Johnson, K. E., Hunt, L. K., & Reines, A. E. 2009, *AJ*, 137, 3788
- Jones, O. C., Meixner, M., Justtanont, K., & Glasse, A. 2017, *ApJ*, 841, 15
- Jordán, A., McLaughlin, D. E., Côté, P., et al. 2007, *ApJS*, 171, 101
- Kankare, E., Mattila, S., Ryder, S., et al. 2008, *ApJ*, 689, L97
- Kennicutt, Robert C., J. 1998, *ApJ*, 498, 541
- Kennicutt, R. C. & Evans, N. J. 2012, *ARA&A*, 50, 531
- Kharchenko, N. V., Piskunov, A. E., Schilbach, E., Röser, S., & Scholz, R. D. 2013, *A&A*, 558, A53
- Kim, D. C., Evans, A. S., Vavilkin, T., et al. 2013, *ApJ*, 768, 102
- Kruijssen, J. M. D. 2012, *MNRAS*, 426, 3008
- Kruijssen, J. M. D. 2014, *Classical and Quantum Gravity*, 31, 244006
- Kruijssen, J. M. D. & Bastian, N. 2016, *MNRAS*, 457, L24
- Kruijssen, J. M. D., Pelupessy, F. I., Lamers, H. J. G. L. M., Portegies Zwart, S. F., & Icke, V. 2011, *MNRAS*, 414, 1339
- Kruijssen, J. M. D., Pfeffer, J. L., Crain, R. A., & Bastian, N. 2019, *MNRAS*, 486, 3134
- Krumholz, M. R., McKee, C. F., & Bland-Hawthorn, J. 2019, *ARA&A*, 57, 227
- Kudritzki, R.-P. & Puls, J. 2000, *ARA&A*, 38, 613
- Kuhn, M. A., Feigelson, E. D., Getman, K. V., et al. 2014, *ApJ*, 787, 107
- Lada, C. J. & Lada, E. A. 2003, *ARA&A*, 41, 57
- Lam, N. T., Gratadour, D., Rouan, D., & Grosset, L. 2020, *A&A*, 639, A28

- Lam, N. T., Grosset, L., Rouan, D., & Gratadour, D. 2019, in *Astronomical Society of the Pacific Conference Series*, Vol. 519, *Radiative Signatures from the Cosmos*, ed. K. Werner, C. Stehle, T. Rauch, & T. Lanz, 273
- Lamers, H. J. G. L. M., Baumgardt, H., & Gieles, M. 2010, *MNRAS*, 409, 305
- Lamers, H. J. G. L. M., Gieles, M., Bastian, N., et al. 2005, *A&A*, 441, 117
- Larsen, S. S. 2009, *A&A*, 494, 539
- Larson, K. L., Sanders, D. B., Barnes, J. E., et al. 2016, *ApJ*, 825, 128
- Larson, R. B. 1981, *MNRAS*, 194, 809
- Le Floch, E., Papovich, C., Dole, H., et al. 2005, *ApJ*, 632, 169
- Lee, J. K., Rolleston, W. R. J., Dufton, P. L., & Ryans, R. S. I. 2005, *A&A*, 429, 1025
- Leisawitz, D., Bash, F. N., & Thaddeus, P. 1989, *ApJS*, 70, 731
- Leitherer, C., Ekström, S., Meynet, G., et al. 2014, *ApJS*, 212, 14
- Leitherer, C. & Heckman, T. M. 1995, *ApJS*, 96, 9
- Leitherer, C., Schaerer, D., Goldader, J. D., et al. 1999, *ApJS*, 123, 3
- Li, H., Gnedin, O. Y., & Gnedin, N. Y. 2018, *ApJ*, 861, 107
- Lin, Z., Calzetti, D., Kong, X., et al. 2020, *ApJ*, 896, 16
- Linden, S. T., Evans, A. S., Rich, J., et al. 2017, *ApJ*, 843, 91
- Longmore, S. N., Kruijssen, J. M. D., Bastian, N., et al. 2014, in *Protostars and Planets VI*, ed. H. Beuther, R. S. Klessen, C. P. Dullemond, & T. Henning, 291
- Lorente, N. P. F., Glasse, A. C. H., Wright, G. S., & García-Marín, M. 2006, in *Society of Photo-Optical Instrumentation Engineers (SPIE) Conference Series*, Vol. 6274, *Society of Photo-Optical Instrumentation Engineers (SPIE) Conference Series*, ed. H. Lewis & A. Bridger, 62741F
- Lu, J. R. 2018, *Massive Young Clusters Near the Galactic Center*, ed. S. Stahler, Vol. 424, 69
- Magnelli, B., Elbaz, D., Chary, R. R., et al. 2009, *A&A*, 496, 57
- Mainzer, A., Larsen, M., Stapelbroek, M. G., et al. 2008, in *Society of Photo-Optical Instrumentation Engineers (SPIE) Conference Series*, Vol. 7021, *High Energy, Optical, and Infrared Detectors for Astronomy III*, ed. D. A. Dorn & A. D. Holland, 70210X
- Mandelbrot, B. B. 1983, *The fractal geometry of nature /Revised and enlarged edition/*
- Marin, F., Grosset, L., Goosmann, R., et al. 2016, in *SF2A-2016: Proceedings of the Annual meeting of the French Society of Astronomy and Astrophysics*, 103–106
- Martín-Hernández, N. L., Schaerer, D., & Sauvage, M. 2005, *A&A*, 429, 449
- Masias, M., Freixenet, J., Lladó, X., & Peracaula, M. 2012, *MNRAS*, 422, 1674

- Mather, J. 2012, James Webb Space Telescope Project: Science Requirements Document (Rev. E), JWST-RQMT-002558, Goddard Space Flight Center, Greenbelt, MD
- Mathis, J. S., Rumpl, W., & Nordsieck, K. H. 1977, *ApJ*, 217, 425
- Mathis, J. S., Whitney, B. A., & Wood, K. 2002, *ApJ*, 574, 812
- McLaughlin, D. E. & Fall, S. M. 2008, *ApJ*, 679, 1272
- Megeath, S. T. 1996, *A&A*, 311, 135
- Meneveau, C. & Sreenivasan, K. R. 1990, *Phys. Rev. A*, 41, 2246
- Messa, M., Adamo, A., Calzetti, D., et al. 2018a, *MNRAS*, 477, 1683
- Messa, M., Adamo, A., Östlin, G., et al. 2018b, *MNRAS*, 473, 996
- Meurer, G. R., Heckman, T. M., Leitherer, C., et al. 1995, *AJ*, 110, 2665
- Mill, J. D., O'Neil, R. R., Price, S., et al. 1994, *Journal of Spacecraft and Rockets*, 31, 900
- Miralles-Caballero, D., Colina, L., Arribas, S., & Duc, P.-A. 2011, *AJ*, 142, 79
- MIRI European Consortium. 2020, MIRISim Documentation, revision 2.3.0
- Moffat, A. F. J. 1969, *A&A*, 3, 455
- Morales, E. F. E., Wyrowski, F., Schuller, F., & Menten, K. M. 2013, *A&A*, 560, A76
- Murakawa, K. 2010, *A&A*, 518, A63
- Nardini, E., Risaliti, G., Salvati, M., et al. 2008, *MNRAS*, 385, L130
- Nardini, E., Risaliti, G., Watabe, Y., Salvati, M., & Sani, E. 2010, *MNRAS*, 405, 2505
- O'Brien, A., Beard, S., Geers, V., & Klaassen, P. 2016, in *Society of Photo-Optical Instrumentation Engineers (SPIE) Conference Series*, Vol. 9913, *Software and Cyberinfrastructure for Astronomy IV*, ed. G. Chiozzi & J. C. Guzman, 991312
- Onaka, T., Matsuhara, H., Wada, T., et al. 2007, *PASJ*, 59, S401
- Östlin, G., Cumming, R. J., & Bergvall, N. 2007, *A&A*, 461, 471
- Pereira-Santaella, M., Alonso-Herrero, A., Rieke, G. H., et al. 2010, *ApJS*, 188, 447
- Peretto, N. & Fuller, G. A. 2009, *A&A*, 505, 405
- Pérez-González, P. G., Rieke, G. H., Egami, E., et al. 2005, *ApJ*, 630, 82
- Perrin, M. 2011, *Improved PSF Simulations for JWST: Methods, Algorithms, and Validation*, technical Report, JWST-STScI-002469, STScI
- Perrin, M. D., Sivaramakrishnan, A., Lajoie, C.-P., et al. 2014, in *Society of Photo-Optical Instrumentation Engineers (SPIE) Conference Series*, Vol. 9143, *Space Telescopes and Instrumentation 2014: Optical, Infrared, and Millimeter Wave*, ed. J. Oschmann, Jacobus M., M. Clampin, G. G. Fazio, & H. A. MacEwen, 91433X

- Perrin, M. D., Soummer, R., Elliott, E. M., Lallo, M. D., & Sivaramakrishnan, A. 2012, in *Society of Photo-Optical Instrumentation Engineers (SPIE) Conference Series*, Vol. 8442, *Space Telescopes and Instrumentation 2012: Optical, Infrared, and Millimeter Wave*, ed. M. C. Clampin, G. G. Fazio, H. A. MacEwen, & J. Oschmann, Jacobus M., 84423D
- Petric, A. O., Armus, L., Howell, J., et al. 2011, *ApJ*, 730, 28
- Pfeffer, J., Bastian, N., Kruijssen, J. M. D., et al. 2019, *MNRAS*, 490, 1714
- Pfeffer, J., Kruijssen, J. M. D., Crain, R. A., & Bastian, N. 2018, *MNRAS*, 475, 4309
- Piqueras López, J., Colina, L., Arribas, S., & Alonso-Herrero, A. 2013, *A&A*, 553, A85
- Piqueras López, J., Colina, L., Arribas, S., Alonso-Herrero, A., & Bedregal, A. G. 2012, *A&A*, 546, A64
- Piqueras López, J., Colina, L., Arribas, S., Pereira-Santaella, M., & Alonso-Herrero, A. 2016, *A&A*, 590, A67
- Piskunov, A. E., Just, A., Kharchenko, N. V., et al. 2018, *A&A*, 614, A22
- Pontoppidan, K. M., Pickering, T. E., Laidler, V. G., et al. 2016, in *Society of Photo-Optical Instrumentation Engineers (SPIE) Conference Series*, Vol. 9910, *Observatory Operations: Strategies, Processes, and Systems VI*, ed. A. B. Peck, R. L. Seaman, & C. R. Benn, 991016
- Portegies Zwart, S. F., McMillan, S. L. W., & Gieles, M. 2010, *ARA&A*, 48, 431
- Psychogyios, A., Charmandaris, V., Diaz-Santos, T., et al. 2016, *A&A*, 591, A1
- Randriamanakoto, Z. 2015, PhD thesis, Department of Astronomy, University of Cape Town, Private Bag X3, Rondebosch 7701, South Africa
- Randriamanakoto, Z., Escala, A., Väisänen, P., et al. 2013a, *ApJ*, 775, L38
- Randriamanakoto, Z., Väisänen, P., Ryder, S., et al. 2013b, *MNRAS*, 431, 554
- Reina-Campos, M. & Kruijssen, J. M. D. 2017, *MNRAS*, 469, 1282
- Reines, A. E., Johnson, K. E., & Hunt, L. K. 2008, *AJ*, 136, 1415
- Ressler, M. E., Sukhatme, K. G., Franklin, B. R., et al. 2015, *PASP*, 127, 675
- Rho, J., Jarrett, T. H., Cutri, R. M., & Reach, W. T. 2001, *ApJ*, 547, 885
- Rieke, G. H., Ressler, M. E., Morrison, J. E., et al. 2015a, *PASP*, 127, 665
- Rieke, G. H., Wright, G. S., Böker, T., et al. 2015b, *PASP*, 127, 584
- Robitaille, T. P. 2011, *A&A*, 536, A79
- Rolleston, W. R. J., Dufton, P. L., McErlean, N. D., & Venn, K. A. 1999, *A&A*, 348, 728
- Roman-Duval, J., Krumholz, M. R., Bolatto, A. D., et al. 2014, in *American Astronomical Society Meeting Abstracts*, Vol. 224, *American Astronomical Society Meeting Abstracts #224*, 220.03
- Russell, S. C. & Dopita, M. A. 1992, *ApJ*, 384, 508
- Salpeter, E. E. 1955, *ApJ*, 121, 161

- Sanders, D. B., Mazzarella, J. M., Kim, D. C., Surace, J. A., & Soifer, B. T. 2003, *AJ*, 126, 1607
- Sanders, D. B. & Mirabel, I. F. 1996, *ARA&A*, 34, 749
- Schechter, P. 1976, *ApJ*, 203, 297
- Schlafly, E. F. & Finkbeiner, D. P. 2011, *ApJ*, 737, 103
- Schmidt, M. 1959, *ApJ*, 129, 243
- Schneider, F. R. N., Ramírez-Agudelo, O. H., Tramper, F., et al. 2018, *A&A*, 618, A73
- Schweizer, F. & Seitzer, P. 1992, *AJ*, 104, 1039
- Senarath, M. R., Brown, M. J. I., Cluver, M. E., et al. 2018, *ApJ*, 869, L26
- Shiple, H. V., Papovich, C., Rieke, G. H., Brown, M. J. I., & Moustakas, J. 2016, *ApJ*, 818, 60
- Siebenmorgen, R., Voshchinnikov, N. V., & Bagnulo, S. 2014, *A&A*, 561, A82
- Silva-Villa, E., Adamo, A., Bastian, N., Fouesneau, M., & Zackrisson, E. 2014, *MNRAS*, 440, L116
- Spitzer, Lyman, J. 1958, *ApJ*, 127, 17
- Stemo, A., Comerford, J. M., Barrows, R. S., et al. 2020, *ApJ*, 888, 78
- Stetson, P. B. 1987, *PASP*, 99, 191
- Stierwalt, S., Armus, L., Surace, J. A., et al. 2013, *ApJS*, 206, 1
- STScI. 2016–, JWST User Documentation, [Published 2020 January 23], Baltimore, MD, <https://jwst-docs.stsci.edu/>
- STScI. 2020, JWST Pipeline Documentation, revision 0.17.1, <https://jwst-pipeline.readthedocs.io/>
- Surace, J. A., Sanders, D. B., Vacca, W. D., Veilleux, S., & Mazzarella, J. M. 1998, *ApJ*, 492, 116
- Tenorio-Tagle, G., Wunsch, R., Silich, S., & Palouš, J. 2007, *ApJ*, 658, 1196
- Thuan, T. X., Lecavelier des Etangs, A., & Izotov, Y. I. 2005, *ApJ*, 621, 269
- Toomre, A. 1964, *ApJ*, 139, 1217
- Toomre, A. & Toomre, J. 1972, *ApJ*, 178, 623
- Van Cleve, J. E., Herter, T. L., Butturini, R., et al. 1995, in *Society of Photo-Optical Instrumentation Engineers (SPIE) Conference Series*, Vol. 2553, *Infrared Spaceborne Remote Sensing III*, ed. M. S. Scholl & B. F. Andresen, 502–513
- Vansevičius, V., Kodaira, K., Narbutis, D., et al. 2009, *ApJ*, 703, 1872
- Vanzella, E., Calura, F., Meneghetti, M., et al. 2017, *MNRAS*, 467, 4304
- Vavilkin, T. 2011, PhD thesis, Department of Physics & Astronomy, Stony Brook University, Stony Brook, NY 11794-3800, USA

- Veilleux, S., Rupke, D. S. N., Kim, D. C., et al. 2009, *ApJS*, 182, 628
- Vesperini, E. & Heggie, D. C. 1997, *MNRAS*, 289, 898
- Vesperini, E. & Zepf, S. E. 2003, *ApJ*, 587, L97
- Weingartner, J. C. & Draine, B. T. 2001, *ApJ*, 548, 296
- Wells, M., Pel, J. W., Glasse, A., et al. 2015, *PASP*, 127, 646
- Whelan, D. G., Johnson, K. E., Whitney, B. A., Indebetouw, R., & Wood, K. 2011, *ApJ*, 729, 111
- Whitmore, B. C., Chandar, R., & Fall, S. M. 2007, *AJ*, 133, 1067
- Wright, G. S., Wright, D., Goodson, G. B., et al. 2015, *PASP*, 127, 595
- Zhang, Q. & Fall, S. M. 1999, *ApJ*, 527, L81

Abstract

Les super amas d'étoiles (SSCs) sont des objets jeunes, massifs et compacts résultant d'une formation extrême d'étoiles, qui se produit souvent lorsque les galaxies interagissent, comme dans le cas des galaxies (ultra)-lumineuses en infrarouge ((U)LIRGs). Ils sont des éléments fondamentaux d'une hiérarchie globale de la formation des étoiles dans l'univers. Néanmoins, la majorité des populations des SSCs restent inexplorées en raison de leurs lointains. Par conséquent, leurs propriétés globales et leur cycle de vie ne sont pas entièrement compris et nécessitent des études plus approfondies, en particulier dans le domaine de l'infrarouge (IR) où ils rayonnent la plupart de leur puissance sous forme d'émission de poussières thermiques.

Nous avons étudié la population des SSCs dans l'IRAS 17138-1017, un LIRG typique, en utilisant des images en bandes JHK_s d'optique adaptative basées au sol. Un catalogue de 54 SSCs de m_{K_s} entre 16 mag et 21 mag avec une incertitude de 0,05 mag a été construit. À partir de diagrammes couleur-couleur et couleur-magnitude accompagné d'une trajectoire d'évolution stellaire théorique, nous avons déduit les âges, les masses et les extinctions des amas. La plupart des SSCs sont très éteintes et appartiennent à deux épisodes récents de flambées d'étoiles à 2,8 et 4,5 millions d'années. Leurs distributions de luminosité et de masse sont bien décrites par les lois de puissance mais avec des pentes moins profondes que celles généralement observées dans les LIRGs. À titre de comparaison, nous avons construit plusieurs modèles de SSCs à différents stades d'évolution en utilisant MontAGN, un code de transfert radiatif spécialisé dans l'IR. Ces modèles montrent que l'émission thermique de la poussière et la lumière diffusée sont insignifiantes dans la bande K et ne pourraient pas expliquer l'excès de rouge de certains SSCs.

En utilisant le code de transfert radiatif MontAGN, nous avons conçu des modèles de SSC consistant en une population stellaire centrale simple et une enveloppe de poussière sous la forme d'une structure hiérarchiquement fragmentée. Les modèles les mieux adaptés pour trois SSCs représentatifs dans l'IRAS 17138-1017 à des magnitudes lumineuses, médianes et faibles ont été obtenus, y compris leurs spectres dans l'IR moyen.

Compte tenu de la supériorité dans l'IR moyen du Télescope Spatial James Webb (JWST), nous avons créé une proposition pour observer les SSCs de l'IRAS 17138-1017 en utilisant l'instrument MIRI. Nous obtiendrons des données d'imagerie dans huit filtres F560W, F770W, F1000W, F1130W, F1500W, F1800W, F2100W, F2550W et des données Spectroscopiques à Moyenne Résolution (MRS) sur tous les canaux et dans toutes les gammes de longueurs d'onde de 4,9 à 28,3 μm , ainsi que des observations de fond dédiées et des images parallèles dans F560W, F770W et F1000W. Nous avons défini les paramètres d'exposition pour obtenir les rapports signal sur bruit les plus élevés possibles pour le SSC le plus faible sans saturer le SSC le plus brillant dans l'IRAS 17138-1017.

Enfin, nous avons utilisé MIRISim, un progiciel fourni par l'équipe MIRI, pour simuler les données du MIRI et les avons fait passer dans le pipeline d'étalonnage du JWST. Les analyses des données simulées réduites montrent que nos observations prévues sont capables de vérifier certaines prédictions du code de transfert radiatif MontAGN.

Keywords: super star clusters, lirg, starburst, infrared, radiative transfer, jwst

Laboratoire d'Études Spatiales et d'Instrumentation en Astrophysique

Observatoire de Paris, Section de Meudon – 5, place Jules Janssen – 92195 MEUDON Cedex
– France

Abstract

Super star clusters (SSCs) are young, massive and compact objects resulting from extreme star formation, which often occurs when galaxies interact, such as in the case of (ultra)luminous infrared galaxies ((U)LIRGs). They are fundamental parts of an overall star formation hierarchy throughout the universe. Nevertheless, a majority of SSC populations remain uncharted due to their large distances. Consequently, their global properties and lifecycle are not fully understood and require further studies, especially in the infrared (IR) range where they radiate most of their power in the form of thermal dust emission.

We studied the SSC population in IRAS 17138-1017, a typical LIRG, using ground-based adaptive optics JHK_s -band images. A catalogue of 54 SSCs of m_{K_s} between 16 mag and 21 mag with an uncertainty of 0.05 mag was constructed. From color-color and color-magnitude diagrams with a theoretical stellar evolutionary track, we derived the cluster ages, masses and extinctions. Most of the SSCs are highly extinct and belong to two recent starburst episodes at 2.8 and 4.5 Myr. Their luminosity and mass distributions are well described by power laws but with shallower slopes than those generally observed in LIRGs. For comparison, we constructed several SSC models at various evolution stages using MontAGN, a radiative transfer code specialized in the IR. These models show that dust thermal emission and scattered light are insignificant in K band and could not explain the red excess of some SSCs.

Using the radiative transfer code MontAGN, we designed SSC models consisting of a central simple stellar population and a dust envelope in the form of a hierarchically clumpy structure. Best-fit models for three representative SSCs in IRAS 17138-1017 at bright, median and faint magnitudes were obtained including their spectra in the mid-IR.

Given the superiority in the mid-IR of the James Webb Space Telescope (JWST), we created a proposal to observe the SSCs in IRAS 17138-1017 using the MIRI instrument. We will obtain imaging data in eight filters F560W, F770W, F1000W, F1130W, F1500W, F1800W, F2100W, F2550W and Medium Resolution Spectroscopic (MRS) data over all channels and wavelength ranges from 4.9 to 28.3 μm , along with dedicated background observations and parallel imaging in F560W, F770W and F1000W. We set the exposure parameters to achieve the highest possible signal-to-noise ratios for the faintest SSC without saturating the brightest SSC in IRAS 17138-1017.

Finally, we used MIRISim, a package provided by the MIRI team, to simulate MIRI data and passed them through the JWST calibration pipeline. Analyses of reduced simulated data show that our planned observations are able to verify some predictions from the radiative transfer code MontAGN.

Keywords: super star clusters, lirg, starburst, infrared, radiative transfer, jwst